Universitat Autònoma de Barcelona

Zn-Based Metal-Organic Frameworks Derived Materials for High-Efficient Carbon Dioxide Electrochemical Reduction

Ting Zhang

ADVERTIMENT. L'accés als continguts d'aquesta tesi queda condicionat a l'acceptació de les condicions d'ús establertes per la següent llicència Creative Commons: http://cat.creativecommons.org/?page_id=184

ADVERTENCIA. El acceso a los contenidos de esta tesis queda condicionado a la aceptación de las condiciones de uso establecidas por la siguiente licencia Creative Commons: http://es.creativecommons.org/blog/licencias/

WARNING. The access to the contents of this doctoral thesis it is limited to the acceptance of the use conditions set by the following Creative Commons license: https://creativecommons.org/licenses/?lang=en

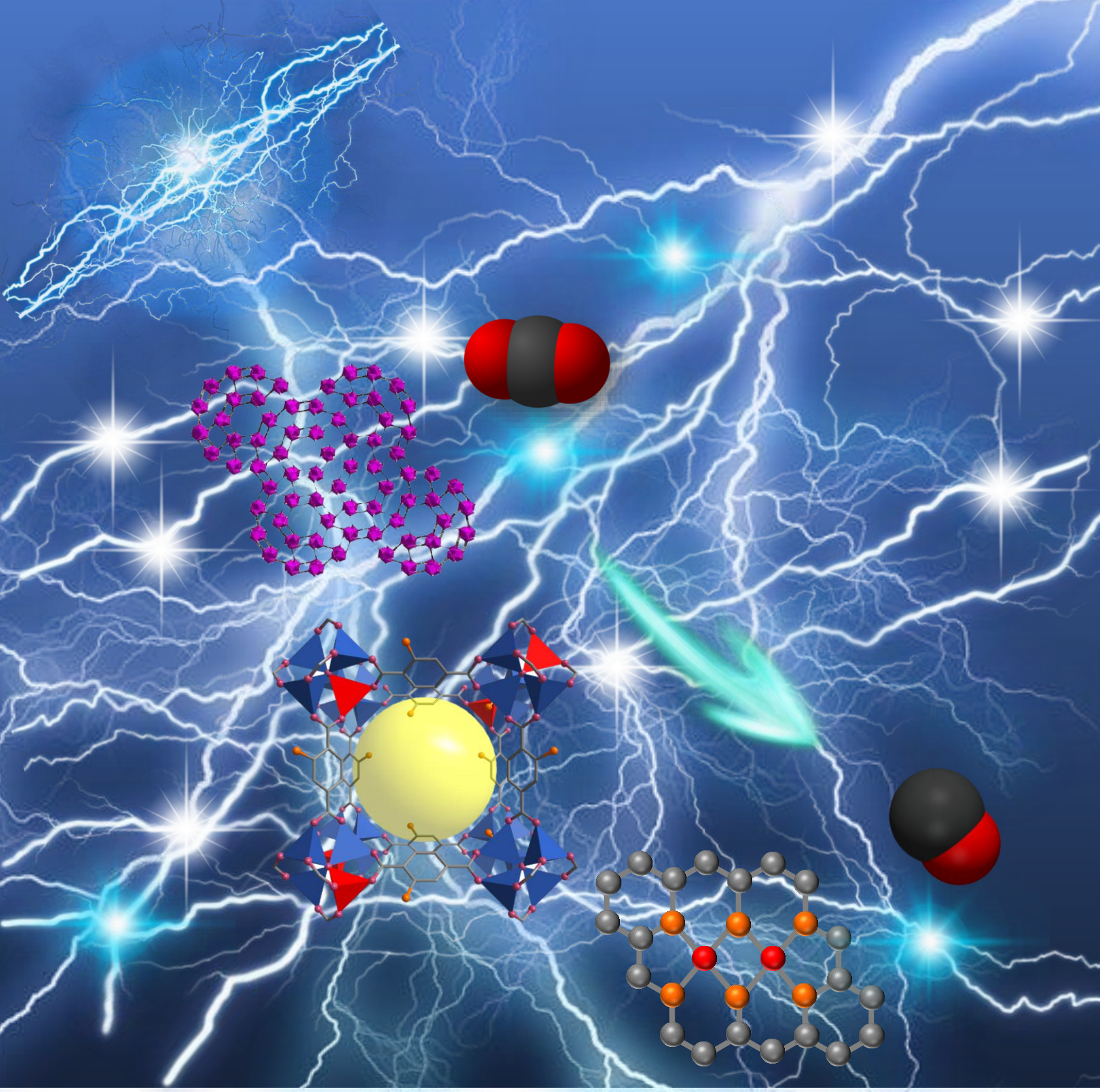

Zn-Based Metal-Organic Frameworks Derived Materials for High-Efficient Carbon Dioxide Electrochemical Reduction

Ting Zhang

Doctorate Program in Materials Science

PhD Thesis

Zn-Based Metal-Organic Frameworks Derived Materials for High-Efficient Carbon Dioxide Electrochemical Reduction

Ting Zhang

Director: Prof. Jordi Arbiol i Cobos

Co-Director: Prof. Joan Ramón Morante i Lleonart

Institut Català de Nanociència i Nanotecnologia (ICN2), CSIC & BIST

Institut de Recerca en Energia de Catalunya (IREC)

Department of Chemistry, Faculty of Sciences

Universitat Autònoma de Barcelona (UAB)

Jordi Arbiol i Cobos, ICREA Research Professor at Institut Català de Nanociència i Nanotecnologia (ICN2), CSIC & BIST, **Joan Ramón Morante i Lleonart**, Professor and Director at Institut de Recerca en Energia de Catalunya (IREC)

CERTIFY

that Mrs. **Ting Zhang**, MSc in Physical Chemistry, carried out the work entitled "**Zn-Based Metal-Organic Frameworks Derived Materials for High-Efficient Carbon Dioxide Electrochemical Reduction**" under their direction and qualifies for the degree of Doctor in Materials Science.

And for that record, sign this certificate.

Prof. Jordi Arbiol i Cobos, Prof. Joan Ramón Morante i Lleonart,

Ting Zhang

Bellaterra, May 2021

Table of Content

Acknowledgments

Here, I would like to express my thanks to all people who gave me their invaluable support on my dissertation and PhD process. Without your guidance and assistance, I could not have been finished this research presented in this dissertation.

First of all, I would like to thank my supervisor, Prof. Dr. Jordi Arbiol at Institut Català de Nanociència i Nanotecnologia (ICN2). Without his excellent guidance and advices, as well as endless encouragement, patience and supports during my PhD period, I would not have finished my PhD well, meanwhile, his positive research attitude will continue to affect me in my future research.

I would like to express my thanks to Prof. Dr. Joan Ramon Morante at Institut de Recerca en Energia de Catalunya (IREC). He gave me many excellent guidelines on my experiments. Meanwhile, his professional theory also broadened my horizons in the materials science and engineering world.

Thanks to all members in GAe^{-}N group (ICN2), Pengyi, Sara, Jérémy, Chiara, Ying, Xu, Zhifu, Marc and Christian, they gave me a comfortable scientific environment and a pleasant memory in the past years. I would express my thanks to my colleagues at IREC, Martí, Félix, Paolo, Teresa, Sebastián, Nina, Monalisa, Chaoqi, Mengyao, Congcong, Ruifeng, Xiaoting, Yong, Junshan, Yu, JunFeng, Xiang, Dawei and Ke. Meanwhile, thanks to Yunhui, Dr. Inhar Imaz and Prof. Dr. Daniel Masposh (ICN2) who provided the scientific support for me. I also express my thanks to Hong and Prof. Dr. Bo Yang from ShanghaiTech University (Shanghai, China) who provided the DFT support to my work. I would like to express my thanks to Prof. Dr. Lirong Zheng from institute of high energy physics, Chinese Academy of Sciences who provided the XAS support to my work. In addition, thanks to all the technical staff working at the different facilities, for their support, especially from the Electron Microscopy Division at ICN2 (Francisco Belarre, Marcos Rosado and Dr. Belen Ballesteros) and Dr. Diouldé Sylla at IREC. I also would like to express my thanks to all the collaborators that provided me with TEM samples, such as, Kai, Dr. Xuan Zhang and Prof. Dr. Jan Fransaer as well

as Dr. Mauro Epifani from Consiglio Nazionale delle Ricerche-Istituto per la Microelettronica ed i Microsistemi (Italy), who gave me strong support on my TEM characterization work.

I really appreciate to China Scholarship Council (CSC), for the financial support, which made all the work possible.

Finally, thanks to my parents who gave me great support and understanding during my PhD period, and to my dearest Xu for his love, patience and understanding in the past years.

Abstract - English

The excessive combustion of fossil fuels results in the emission of carbon dioxide (CO_2), which triggers increasing environmental problems, such as, global warming, rising sea levels, extreme weather, and species extinction. Therefore, the technologies for conversion of CO_2 into other value products plays a vital role in order to eliminate the CO_2 concentration in atmosphere. Thereinto, electrochemical conversion of CO_2 powered by renewable energy to useful chemicals is considered as an elegant solution to achieve the carbon cycle.

However, due to the innerness of CO_2 molecules and competitive hydrogen evolution reaction (HER), the main challenges in the field CO_2 RR are the high overpotential requirement that represents the unfavourable thermodynamics and low Faradaic efficiency (FE) for the target products. Therefore, searching for a high-efficient and cost-friendly electrocatalyst is sensible and necessary for practical applications. In the past decades, metal-organic frameworks (MOFs) engrossed the enormous considerations in the field of electrocatalysis because of their large specific surface area, rich pore structure, and uniformly dispersed active sites. Although they have a great potential in electrocatalysis, most MOFs materials still suffer from insufficient activity, low conductivity, and poor stability, which would hinder their practical applications. Especially, in the field of CO_2 RR, many important parameters, including high FE, low overpotential, large current density and robust stability among others, should be considered. Thus, the rational design of MOFs to fulfil the above requirements as much as possible is crucial for exploiting their future in CO_2 RR applications. Therefore, in this dissertation, we made many efforts to develop MOFs-based/derived catalysts with superior efficiency, activity, and stability for boosting the CO_2 RR performance.

This dissertation is divided into 5 chapters:

Chapter 1 is the insights on the fundamental concepts about electrochemical CO_2 RR, which includes the fundamental cell of electrochemical CO_2 RR, reviews the common

reduction products and their simple pathways. Meanwhile, the overview of important parameters affecting CO_2 RR, including different catalysts over the past years, electrolyte, and the relevant metrics evaluating the electrocatalysts as well as limitations of electrochemical CO_2 reduction are also presented in this chapter. In addition, this chapter summarizes the fundamental concepts about MOFs materials and their high-temperature pyrolysis derived materials as the electrocatalysts. This chapter also introduces some current characterization techniques for studies of CO_2 RR.

Specific synthesis procedures and experimental results for each studied material are presented in **Chapters 2-4**.

Chapter 2 deals with the fabrication of surface modified ZIF-8 as MOFs-based electrode for electrochemical CO_2 RR to generate CO. In this work, a surface modified ZIF-8 has been prepared through introducing a very small proportion 2,5-dihidroxyterephthalic acid (DOBDC) into ZIF-8, achieving a 2.5 times higher current density of CO (from −4 mA cm^{-2} to −10 mA m^{-2}) and a boosted Faradaic efficiency (from 56 % to 79 %).

In **Chapter 3**, a facile route is used to introduce axial bonded O-containing groups into a Fe-N-C catalyst through pyrolysis of Fe-doped Zn-based metal organic frameworks (IRMOF-3), forming highly dispersed Fe single atoms with HO-FeN_4 active sites. Due to the local environment modulation induced by such -OH groups, the D-Fe-N-C catalyst exhibits an enhanced CO_2 RR activity, including a high selectivity with CO Faradaic efficiency of 95 % at −0.50 V vs. RHE, and a robust stability, which is higher than that of the reported normal FeN_4 sites without -OH groups.

In **Chapter 4**, we proposed that introducing Fe atoms into Ni-N-C catalysts fabricates double metal (bimetallic) single-atom catalysts (Ni/Fe-N-C) towards CO_2 RR to achieve a high selectivity and activity simultaneously. The optimized double-metal Ni/Fe-N-C catalyst showed an excellent performance, obtaining a high selectivity with a high CO Faradaic efficiency (with a maximum FE (CO) of 98 %) at a low overpotential (390 mV vs. RHE). The performance obtained is superior to both single

metal counterparts (Ni-N-C and Fe-N-C catalysts) and other state-of-the-art M-N-C catalysts, proving that regulating single active sites with a second metal site potentially breaks the single metal-based activity benchmark to obtain the high selectivity and activity in CO_2 RR, simultaneously.

Finally, **Chapter 5** summarizes the general conclusions of this dissertation, along with a brief outlook.

Resum - Català

La combustió excessiva de combustibles fòssils té com a resultat l'emissió de diòxid de carboni (CO_2), que està desencadenant problemes ambientals creixents, com ara l'escalfament global, l'augment del nivell del mar, el clima extrem i l'extinció d'espècies. Per tant, les tecnologies per a la conversió de CO_2 en altres productes de valor estan jugant un paper vital per eliminar la concentració de CO_2 a l'atmosfera. En aquest sentit, la conversió electroquímica de CO_2, alimentat per energia renovable, en productes químics útils es considera una solució elegant per aconseguir el cicle del carboni.

Tanmateix, a causa de la interioritat de les molècules de CO_2 i de la reacció competitiva d'evolució d'hidrogen (HER), els principals reptes de CO_2 RR són l'elevat requeriment de sobrepotencial associat a una termodinàmica desfavorable i una baixa eficiència faradaica (FE) per a un producte concret. Per tant, buscar un electrocatalitzador d'alta eficiència i econòmic és raonable i necessari per a aplicacions pràctiques. En les darreres dècades, els marcs metal·lorgànics (MOF) van absorbir les enormes consideracions en el camp de l'electrocatàlisi a causa de la seva gran superfície específica, una rica estructura de porus i llocs actius uniformement dispersos. Tot i que tenen un gran potencial en electrocàlisi, la majoria dels materials MOF encara pateixen una activitat insuficient, baixa conductivitat i poca estabilitat, cosa que dificultaria les seves aplicacions pràctiques. Especialment, en el camp del CO_2 RR, s'han de tenir en compte molts paràmetres importants, inclosa una alta eficiència faradaica (FE), l'excessiu baix sobrepotencial, una gran densitat de corrent i una estabilitat robusta, entre d'altres. Per tant, el disseny racional dels MOF per complir els requisits anteriors tant com sigui possible és crucial per explotar el seu futur en aplicacions de CO_2 RR. Per tant, en aquesta dissertació, vam fer molts esforços per desenvolupar catalitzadors basats en MOFs/derivats amb una eficiència, activitat i estabilitat superiors per augmentar el rendiment del CO_2 RR.

Aquesta dissertació es divideix en 5 capítols:

El capítol 1 presenta les idees sobre els conceptes fonamentals sobre CO_2 RR electroquímic, que inclou la cèl·lula fonamental de CO_2 RR electroquímica, que revisa els productes de reducció comuns i les seves vies senzilles. En aquest capítol també es presenta la visió general de paràmetres importants que afecten el CO_2 RR, inclosos diferents catalitzadors dels darrers anys i electròlits, i les mètriques rellevants que avaluen els electrocatalitzadors, així com les limitacions de la reducció electroquímica de CO_2. A més, aquest capítol resumeix els conceptes fonamentals sobre els materials MOF i els seus materials derivats de la piròlisi a alta temperatura com els electrocatalitzadors. Aquest capítol també introdueix algunes tècniques de caracterització actuals per a estudis de CO_2 RR.

Els procediments de síntesi específics i els resultats experimentals per a cada material estudiat es presenten als **capítols 2-4**.

El **capítol 2** tracta de la fabricació de ZIF-8 modificat a la superfície com a elèctrode basat en MOFs per a un CO_2 RR electroquímic per generar CO. En aquest treball, hem modificat la superfície del MOF ZIF-8 a partir d'introduir un petita proporció d'àcid 2,5-dihidroxyterephthalic (DOBDC), aconseguint una densitat de corrent de CO 2,5 vegades superior (de -4 mA cm^{-2} a -10 mA cm^{-2}) i una eficiència faradaica augmentada (del 56% al 79%).

Al **capítol 3**, s'utilitza una ruta fàcil per introduir grups que contenen O enllaçats axialment en un catalitzador Fe-N-C mitjançant piròlisi de marcs orgànics metàl·lics basats en Zn dopats amb Fe (IRMOF-3), formant àtoms individuals de Fe molt dispersos amb llocs actius de HO-FeN_4. A causa de la modulació de l'entorn local induïda per aquests grups -OH, el catalitzador D-Fe-N-C presenta una activitat CO_2 RR millorada, que inclou una alta selectivitat amb una eficiència faradaica de CO del 95% a $-0{,}50$ V vs. RHE, i una estabilitat robusta , que és superior a la dels llocs FeN_4 normals reportats sense grups -OH.

Al **capítol 4**, vam proposar la introducció d'àtoms de Fe en catalitzadors de Ni-N-C per produir catalitzadors amb àtoms individualitzats (Ni/Fe-N-C) de doble metall

(bimetàl·lics) de cara al CO_2 RR per aconseguir una alta selectivitat i activitat simultàniament. El catalitzador Ni/Fe-N-C de doble metall optimitzat va mostrar un rendiment excel·lent, obtenint una alta selectivitat amb una alta eficiència faradaica de CO (amb un FE (CO) màxim del 98%) a un baix sobrepotencial (390 mV vs. RHE). El rendiment obtingut és superior als seus homòlegs metàl·lics (Ni-N-C i Fe-N-C catalitzadors) i a altres catalitzadors M-N-C d'última generació, demostrant que la regulació de llocs actius únics amb els segons llocs metàl·lics trenca el punt de referència únic d'activitat basat en metalls per obtenir una alta selectivitat i activitat en CO_2 RR, simultàniament.

Finalment, el **capítol 5** resumeix les conclusions generals d'aquesta dissertació, juntament amb una breu visió.

Resumen - Castellano

La combustión excesiva de combustibles fósiles da como resultado la emisión de dióxido de carbono (CO_2), que desencadenó crecientes problemas ambientales, como el calentamiento global, el aumento del nivel del mar, el clima extremo y la extinción de especies. Por lo tanto, las tecnologías para la conversión de CO_2 en otros productos de valor jugaron un papel vital para eliminar la concentración de CO_2 en la atmósfera. En ese sentido, la conversión electroquímica de CO_2 alimentado por energía renovable en productos químicos útiles se considera una solución elegante para lograr el ciclo del carbono.

Sin embargo, debido a la interioridad de las moléculas de CO_2 y la reacción competitiva de evolución de hidrógeno (HER), los principales desafíos en el campo CO_2 RR son el alto requerimiento de sobrepotencial que representa la termodinámica desfavorable y la baja eficiencia faradaica (FE) para los productos objetivo. Por lo tanto, la búsqueda de un electrocatalizador económico y de alta eficiencia es sensato y necesario para aplicaciones prácticas. En las últimas décadas, las estructuras organometálicas (MOF) absorbieron las enormes consideraciones en el campo de la electrocatálisis debido a su gran área de superficie específica, rica estructura de poros y sitios activos uniformemente dispersos. Aunque con grandes potenciales en electrocatálisis, la mayoría de los materiales MOF todavía sufren de actividad insuficiente, baja conductividad y poca estabilidad, lo que dificultaría sus aplicaciones prácticas. Especialmente, en el campo de CO_2 RR, se deben considerar muchos parámetros importantes, incluida la alta eficiencia faradaica (FE), bajo sobrepotencial, gran densidad de corriente y estabilidad robusta, etc. Por lo tanto, el diseño racional de MOF para cumplir con los requisitos anteriores tanto como sea posible es crucial para explotar sus futuras aplicaciones de CO_2 RR. Por lo tanto, en esta disertación, hicimos muchos esfuerzos para desarrollar catalizadores basados en MOFs / derivados de MOF con eficiencia, actividad y estabilidad superiores para aumentar el rendimiento de CO_2 RR.

Esta disertación se divide en 5 capítulos:

El **capítulo 1** es la información sobre los conceptos fundamentales sobre la CO_2 RR electroquímico, que incluye la celda fundamental de la CO_2 RR electroquímico, revisa los productos de reducción comunes y sus vías simples. Mientras tanto, la descripción general de los parámetros importantes que afectan la CO_2 RR, incluidos los diferentes catalizadores en los últimos años y el electrolito, y las métricas relevantes que evalúan los electrocatalizadores, así como las limitaciones de la reducción electroquímica de CO_2, también se presentan en este capítulo. Además, este capítulo resume los conceptos fundamentales sobre los materiales MOF y sus materiales derivados de la pirólisis a alta temperatura como electrocatalizadores. Este capítulo también presenta algunas técnicas de caracterización actuales para estudios de CO_2 RR.

Los procedimientos de síntesis específicos y los resultados experimentales para cada material estudiado se presentan en los **Capítulos 2-4**.

El **Capítulo 2** trata de la fabricación de ZIF-8 modificado en superficie como electrodo basado en MOF para CO_2 RR electroquímico para generar CO. En este trabajo, se preparó un ZIF-8 modificado en superficie mediante la introducción de una proporción muy pequeña de ácido 2,5-dihidroxitereftálico (DOBDC) en ZIF-8, logrando una densidad de corriente de CO 2,5 veces mayor (de -4 mA cm^{-2} a -10 mA m^{-2}) y una eficiencia Faradaica mejorada (de 56% a 79%).

En el **Capítulo 3**, se utiliza una ruta fácil para introducir grupos que contienen O con enlaces axiales en un catalizador de Fe-N-C a través de la pirólisis de estructuras orgánicas metálicas a base de Zn dopado con Fe (IRMOF-3), formando átomos únicos de Fe altamente dispersos con sitios activos HO-FeN_4. Debido a la modulación del ambiente local inducida por tales grupos -OH, el catalizador D-Fe-N-C exhibe una actividad CO_2 RR mejorada, incluida una alta selectividad con eficiencia de CO Faradaic del 95 % a $-0,50$ V frente a RHE, y una estabilidad sólida, que es más alto que el de los sitios FeN_4 normales reportados sin grupos -OH.

En el **capítulo 4**, proponemos que la introducción de átomos de Fe en catalizadores de Ni-N-C fabrica catalizadores de un solo átomo de metal doble (Ni/Fe-N-C) hacia CO_2

RR para lograr una alta selectividad y actividad simultáneamente. El catalizador de Ni/Fe-N-C de doble metal optimizado mostró excelentes rendimientos, obteniendo una alta selectividad con eficiencia faradaica CO (un máximo FE (CO) del 98 %) a un bajo sobrepotencial (390 mV vs RHE), que es superior a las contrapartes de un solo metal (Ni-N-C y Fe-N-C catalizadores) y otros catalizadores M-N-C de última generación, lo que demuestra que la regulación de sitios activos individuales con los sitios del segundo metal rompe potencialmente el punto de referencia de actividad basada en un solo metal para obtener una alta selectividad y actividad para CO_2 RR, simultáneamente.

Finalmente, el Capítulo 5 resume las conclusiones generales de esta disertación, junto con una breve perspectiva.

Chapter 1

Introduction: Fundamental Concepts of CO_2 Electrochemical Reduction and Metal-Organic Frameworks (MOFs)

1.1 Overview: Background of CO_2 Electrochemical Reduction

With the growth of combustion of traditional fuels (such as coal and crude oil), the excessive emission of greenhouse gases (e.g., carbon dioxide (CO_2)) amounted at *ca.* 30 000 Mt in 2010. As a result, the unprecedented concentration of CO_2 in the atmosphere trigged increasing concerns about global warming, rising sea levels, extreme weather, and species extinction.[1, 2] Thus, decreasing or eliminating emissions of atmospheric CO_2 becomes an imperative task. However, the fossil fuels will remain a long-term and major source in industrial developments, in view of the target for reducing atmospheric CO_2 concentration to 500 ppm by 2050,[3] a large number of technologies have been proposed in order to maintain the carbon cycle, following two major categories: 1) capture CO_2 from the atmosphere and then storage it forever; 2) convert CO_2 into other high-value products.[4-6] In comparison with the second route, however, more CO_2 emission will likely be caused during the CO_2 capture process, because of further separation, purification, compression, transportation, and storage processes.[7] Therefore, conversion of CO_2 to produce useful chemicals is widely considered as the most straightforward strategy to reduce atmospheric CO_2 concentration in hope for realizing a 'carbon cycling' pathway.[8, 9] To date, CO_2 conversion can be achieved by chemical methods, such as, photocatalytic,[10] biological[11] and electrocatalytic reduction,[12] and a few other means. Among them, electrochemical reduction of CO_2 (CO_2 RR) to some high-value products is especially desirable both in terms of energy efficiency and cost for 1) controllable electrode potentials and ambient reaction temperatures as well as pressures; 2) recycled electrolytes, minimizing overall chemical consumption; 3) reduced new CO_2-sources generation due to electricity as the driver; and 4) easy scale-up applications.[8, 13, 14] Therefore, many recent reports in the field of CO_2 RR are overwhelming in the Web of Science (WOS) (**Figure 1.1**). However, in order to widely utilize the electrochemical reduction of CO_2 technologies to obtain high efficiency, the first step is to understand the fundamentals of this process.

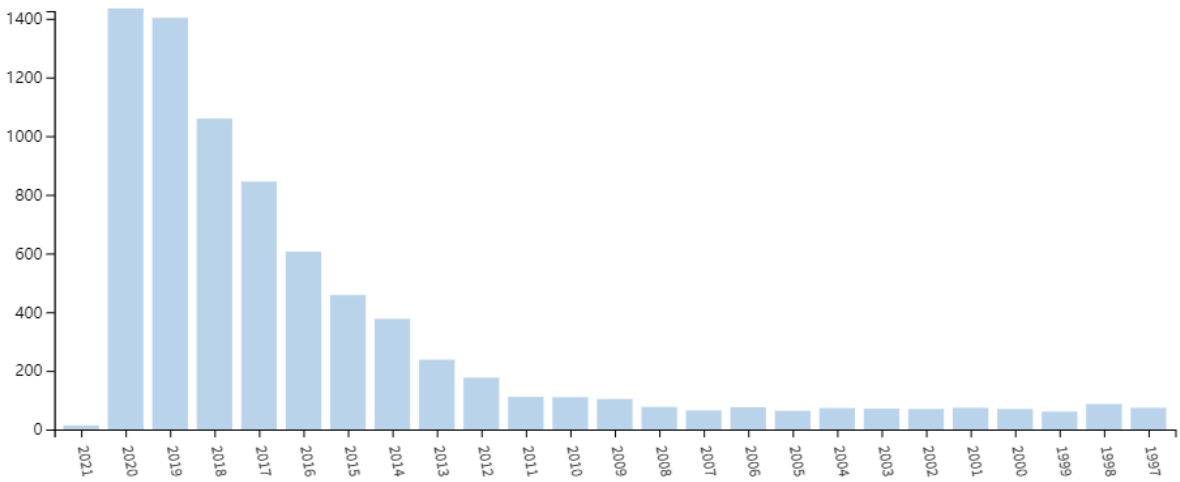

Figure 1.1 Number of publications in electrochemical CO_2 reduction research published per year. This Web of Science search was carried out on the 26th Nov. 2020.

1.2 Fundamental Concepts of CO_2 Electrochemical Reduction

1.2.1 Electrochemical Cell of CO_2 Electrochemical Reduction

Generally speaking, an electrochemical process involves an electrical and chemical interconversion, therefore, as a typical reduction process, CO_2 RR also have a similar situation that required a cathodic voltage to drive the reduction of CO_2 to produce other carbon-containing products. In a typical electrochemical CO_2 RR H-cell a standard three-electrode system is assembled, including a working electrode (WE) loaded with catalysts (cathode), a reference electrode to determine the applied potential, and a counter electrode (CE) to balance the charge and ion flow of reaction (anode). Meanwhile, the overall electrocatalytic device consists of two compartments separated by an ion-exchange membrane to prevent the mixing of the cathodic and anodic reaction products and further reoxidation of targeted products,[15-17] as illustrated in **Figure 1.2**. At the cathode, a myriad of products during CO_2 RR are produced over the electrocatalysts. And the oxygen (O_2) evolution reaction (OER) (E^{0}= 1.23 V vs. RHE) is performed over the anode. The overall process is driven by an external applied voltage, which is used to increase the electrochemical potential of the electrons liberated from the reducing agent so that they are capable of reducing CO_2 at the cathode, to produce different products, such as carbon monoxide ($E^{0}_{CO(g)}$= −0.106 V vs. RHE) and many others.[17]

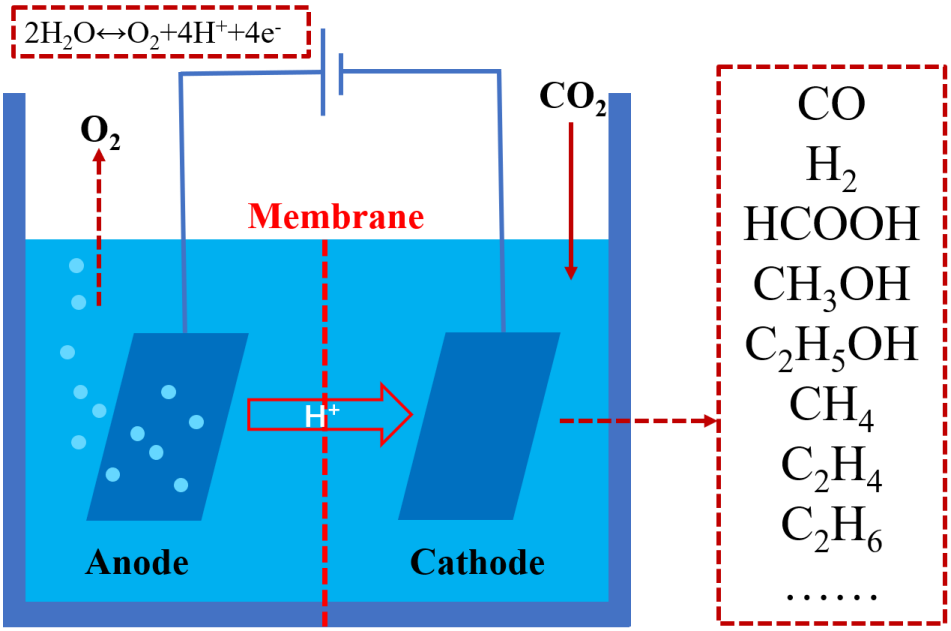

Figure 1.2 Schematic image of typical H-cell for CO_2 RR.

Electrochemical CO_2 reduction is also conducted in a gas-liquid flow cell (flow cell) (**Figure 1.3**), which allows the large scale applications in the industry.[15] This reactor is more suitable for practical applications, because the continuously circulated gas and liquid flow in this electrolysis reactors can optimize the mass transport limitations during the reaction process.[18] In addition, higher current densities (generally > 100 mA cm^{-2}) can be obtained in a flow cell simultaneously.[19] Nevertheless, future investigations will continue to focus on developing multilayer gas-liquid flow cells or large-scale industrial applications to achieve a market size and price of target CO_2 RR products.

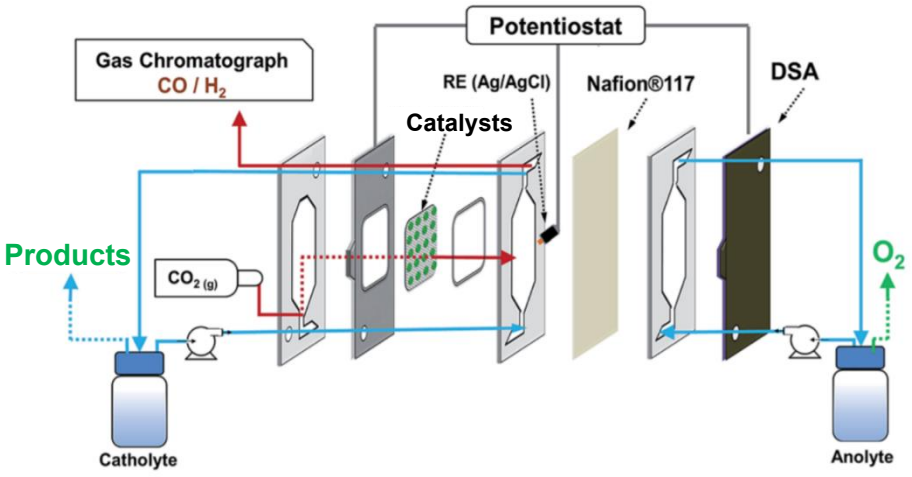

Figure 1.3 Scheme of the electrochemical flow cell. Reprinted with permission from ref[20].

1.2.2 Products of CO_2 Electrochemical Reduction

Electrochemical CO_2 reduction is driven by applied potential through two-, four-, six-, eight-, ten- and twelve-electron reduction pathways in different phases.[17, 21] Depending on carbon containing, the distribution of major reduction products (C1 or multi-carbon) for CO_2 RR is shown in **Table 1.1**. HCOOH, CO, HCHO, CH_3OH and CH_4 are the main C1 products. Other products, such as, C_2H_4, CH_3CH_2OH, are defined as multi-carbon products in CO_2 RR.[22] However, as methanol and ethanol or other C2 products, most of currently known electrocatalysts are unable to electrocatalytically generate them with a high selectivity, thus, potentially disqualifying these chemicals as viable CO_2 RR products.[23] Therefore, one of the most important criterion for the utility of the CO_2 RR is the selection of a targeted product. From a commercial point of view, formate and CO are considered as the attractive targeted products for CO_2 electrolysis because they can be produced with a high Faradaic efficiency (FE) hitherto exceeding 90 % and only require a simple two-electron/proton transfer pathway with low energy barriers.[24, 25] On the other hand, to date, CO, together with HCOOH, have been also considered as the most promising candidates due to their further commercial values.[26, 27] Especially, CO is most appealing because of a significant global demand for downstream products of syngas (CO, H_2), such as, synthetic methanol, which could pave the way for various fuels production.[22, 28] Therefore, many researches have widely focused on producing CO or HCOOH as well as investigating their reaction mechanisms using advanced characterization technologies in order to obtain a deeper understanding in this process. In addition, in those products beyond containing a single carbon, the reaction complexity increases significantly, as the addition of more proton/electron transfers. Thus, further advancing to our understanding of the reaction mechanisms of C-O bond cleavage and C-C bonds formation and designing high-efficient catalysts for generating multi-carbon products are imperative for further investigations.[29-31] All in all, the points mentioned above indicate that there is large a space to make the electrochemical carbon industry more profitable.

Table 1.1 Products of electrochemical CO_2 reduction and redox potential at pH=7. ref[32]

Half-reactions	Electrode Potentials (vs. RHE) at pH=7
$CO_2(g) + e^- \rightarrow CO_2^{\bullet -}$	−1.48
$CO_2(g) + 2e^- + 2H^+ \rightarrow HCOOH\ (l)$	−0.250
$CO_2(g) + 2e^- + 2H^+ \rightarrow CO(g) + H_2O(l)$	−0.106
$CO_2(g) + 2e^- + 4H^+ \rightarrow HCHO(l) + H_2O(l)$	−0.070
$CO_2(g) + 4e^- + 4H^+ \rightarrow C(s) + 2H_2O(l)$	0.21
$CO_2(g) + 6e^- + 6H^+ \rightarrow CH_3OH(l) + H_2O(l)$	0.016
$CO_2(g) + 8e^- + 8H^+ \rightarrow CH_4(g) + 2H_2O(l)$	0.169
$2CO_2(g) + 8e^- + 8H^+ \rightarrow CH_3COOH(l) + 2H_2O(l)$	0.11
$2CO_2(g) + 10e^- + 10H^+ \rightarrow CH_3CHO(l) + 3H_2O(l)$	0.06
$2CO_2(g) + 12e^- + 12H^+ \rightarrow C_2H_4(g) + 4H_2O(l)$	0.064
$2CO_2(g) + 12e^- + 12H^+ \rightarrow CH_3CH_2OH\ (l) + 3H_2O(l)$	0.084
$2H^+ + 2e^- \rightarrow H_2$	0

1.2.2.1 Intermediates for CO and $HCOO^-$ Formation

The theoretical investigations shows that the intrinsic catalytic performance of catalysts relies on their binding energy for intermediate species. Therefore, in order to achieve a high activity and selectivity to produce CO and HCOOH in CO_2 RR, understanding the binding energy of key intermediates is critical. The key intermediates during CO and formic acid (or formate in basic solution) production have been defined by Nørskov group.[33] They suggested that adsorbed COOH* intermediates is for producing CO,[34] whereas HCOOH is produced via the OCHO* intermediate.[35] In addition, with respect to the theoretical results, Jaramillo's group experimentally

showed a volcano relationships between intrinsic binding energies of key intermediate and CO_2 RR activities for various metals,[36, 37] as shown in **Figure 1.4**. This relationship revealed that the product selectivity strongly depends on the binding energies of the intermediates on the catalysts' surfaces. The moderate binding energy to the surface of catalysts (such as, Ag and Au) towards both COOH* and CO* will result in a high efficiency for CO production. Otherwise, the reaction will move forward to convert to hydrocarbon or oxygenates. For example, C-C coupling and further CHO* protonation become the key steps toward ethylene and methane, respectively. Therefore, CO* has been identified as a critical intermediate in the formation of hydrocarbons and alcohols. Similarly, when a metal shows the highest reactivity towards HCOOH production as it has a moderate binding energy for OCHO*, which is a key intermediate for HCOOH production, such as Sn.

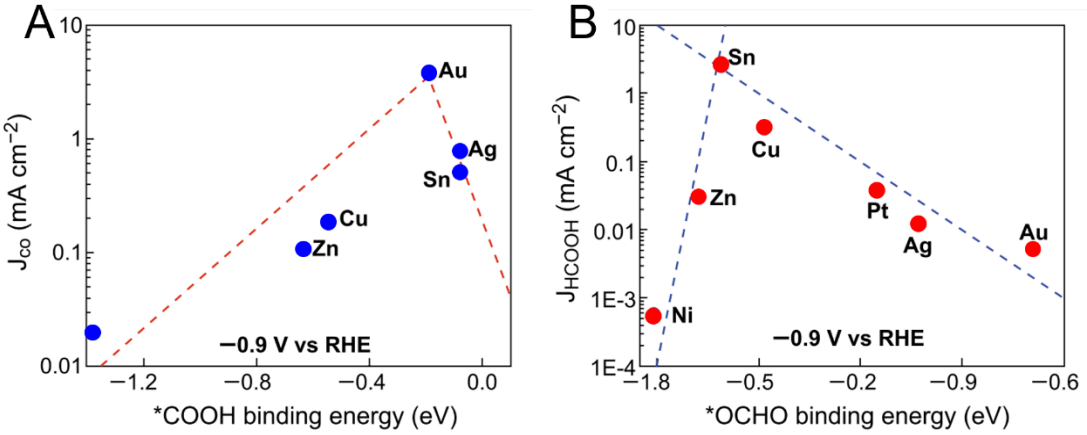

Figure 1.4 (A) Volcano plot using *COOH binding energy as a descriptor for CO partial current density at −0.9 V (vs. RHE). (B) Volcano plot using *OCHO binding energy as a descriptor for $HCOO^-$ partial current density at −0.9 V (vs. RHE). Adapted from ref[37]

1.2.2.2 Simple Reaction Pathway for CO and $HCOO^-$ Formation

Although the reaction mechanisms are quite complex under both theoretically and experimentally, simplified reaction steps for formation of CO and $HCOO^-$ has been proposed (**Figure 1.5**). CO_2 reduction to both CO and HCOOH can start with a one proton/electron transfer to a CO_2 molecule and followed by the stabilization of COOH* and OCHO* intermediates. Subsequently, for CO generation, COOH* transfers to CO* through a dehydration reaction, then, the CO* desorbs from the catalysts' surfaces,

forming the final CO product. The overall conversion process is proposed to occur in three steps: (i) $CO_2(g) + e^- + H^+ \rightarrow *COOH$; (ii) $*COOH + e^- + H^+ \rightarrow *CO + H_2O$; (iii) $*CO \rightarrow CO + *$ (* represents that the molecule is adsorbed on the surface of the catalysts). For HCOOH generation, the OCHO* intermediates desorb from the metal surface to form HCOOH. However, the proposed reaction mechanisms merely represent the reaction pathway for a specific catalyst and condition, yet, theoretical investigations generally proceed with assumptions such as the proton-coupled electron transfer model, which differ from actual reaction conditions.

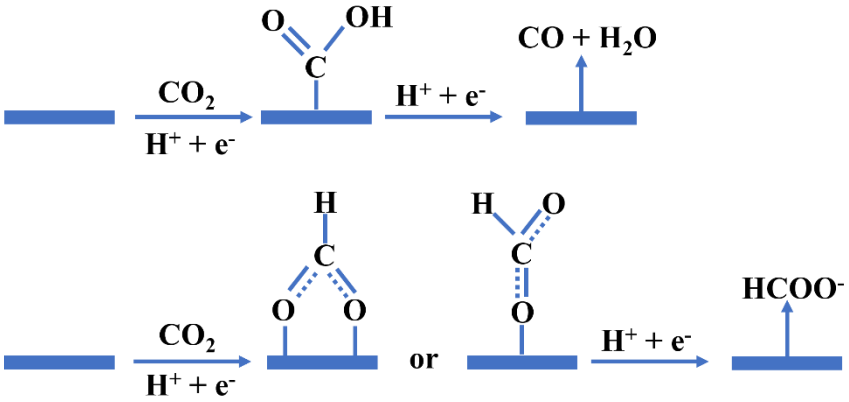

Figure 1.5 Possible reaction pathways for CO (top) and $HCOO^-$ (bottom). Adapted from ref[21, 38]

1.2.2.3 Tafel Slope for CO and $HCOO^-$ Formation

In order to rationally design high-performing catalytic systems, understanding the reaction pathways and mechanisms for CO_2 RR is critical. In some cases, Tafel analysis as an important parameter to reveal the reaction mechanisms during a reaction, in which the quantitative dependence of the partial current density toward a specific product (the electrochemical reaction rate) on the applied potential (Tafel slope) is determined.[39, 40] Through assuming the symmetry factor and other reaction conditions, the Tafel slopes of different reaction mechanism for CO and HCOOH are shown in **Table 1.2**. By matching theoretically calculated Tafel slopes and experimentally obtained Tafel slopes, the rate determining step of a reaction and the number of electrons involved in the rate-determine step (RDS) can be possible proposed.[41] Two types of RDSs are revealed for catalysts towards CO generation. For example, polycrystalline Au and Ag

catalysts with a Tafel slope of 118 mV/dec (zeroth reaction order) demonstrate that the formation of the CO_2^- anion is considered as the RDS. While the Tafel slope of 59 mV/dec with the first reaction order shows the RDS is COOH* formation.

However, Tafel analysis has its significant limitations. Firstly, the Tafel analysis is conducted in a low current region, a so-called Tafel region, so that the electrocatalytic reaction is not limited by the mass transport of reactants. For an electrochemical reaction of the form given in equation (1), the full Butler-Volmer equation is shown in equation (2), then the equation (2) can be simplified as Tafel equation (3) at Tafel region (only if the overpotential is sufficiently high so that the rate of the reverse reaction is negligible comparing to that of the forward reaction, that is $\exp(\frac{\eta\beta F}{RT}) << \exp(\frac{\eta(\beta-1)F}{RT})$).

$$O + ne^- \leftrightarrow R \quad (1)$$

$$j = nFk^0[a_R \exp(\frac{\eta\beta F}{RT}) - a_O \exp(\frac{\eta(\beta-1)F}{RT})] \quad (2)$$

$$j = -nFk^0[a_o \exp(\frac{\eta(\beta-1)F}{RT})] \quad (3)$$

Therefore, Tafel analysis is only appropriate within a specific overpotential range. Secondly, it cannot differentiate two mechanisms with the same Tafel slope. Furthermore, as informative as Tafel analysis is, independent experimental and theoretical techniques are necessary to support a proposed mechanism of multielectron electrocatalytic reactions (as it is the case for the CO_2 reduction).

Table 1.2 Tafel slopes and reaction orders derived under the assumption of well-known rate-determining steps (RDSs) for CO and $HCOO^-$ generation. In the derivation, the intermediate surface coverage is assumed to be zero. The reaction orders are denoted with superscripts. ref[42]

Product	RDS	Tafel slope (mV/dec) at T= 298 K and β = 0.5	$(\frac{\partial \log j}{\partial \log [HCO3-]})$
CO	$CO_2(aq) + e^- + * \rightarrow CO_2^{\cdot -*}$	118	0
	$CO_2^{\cdot -*} + HCO_3^- \rightarrow COOH* + CO_3^{2-}$	59	1
	$COOH* + e^- + HCO_3^- \rightarrow CO* + H_2O + CO_3^{2-}$	39	0^a
	$CO* \rightarrow CO + *$	30	-2^a

$HCOO^-$	$CO_2\,(aq) + e^- + * \rightarrow CO_2^{\cdot -*}$	118	0
	$CO_2^{\cdot -*} + HCO_3^- \rightarrow OCHO* + CO_3^{2-}$	59	1
	$OCHO* + e^- \rightarrow HCOO^{-*}$	39	-1[a]
	$CO_2^{\cdot -*} + e^- + HCO_3^- \rightarrow HCOO^{-*} + CO_3^{2-}$	39	1
	$HCOO^{-*} \rightarrow HCOO^- + *$	30	-1[a]

1.2.2.4 Competition of Hydrogen Evolution Reaction (HER)

The reaction complexity of CO_2 RR is not only to produce different products, in most cases, CO_2 RR must also compete with the relatively facile hydrogen evolution reaction (HER).[25, 43] As shown in **Table 1.1**, HER is a major side reaction that accompanies CO_2 reduction, because HER occurs at more positive potential than CO_2 RR, resulting in a significant decrease of the FE for CO_2 RR. Therefore, future strategies should take advantage of the excellent catalyst developments to optimize the adsorption of *H with *CO and other CO_2 RR intermediates for suppressing HER.

1.3 Important Factors Affecting CO_2 Electrochemical Reduction

As discussed above, the desired products in CO_2 RR are very complex for practical applications because of the different reaction pathways or combinations of different pathways. However, the kind of pathways and numbers of pathways are highly related to the experimental conditions, such as the catalysts materials, applied potentials, electrolyte solution, CO_2 concentration, as well as pressure and temperature.

1.3.1 Electrocatalysts

CO_2 is a linear molecule, as shown in **Figure 1.6**. In this molecule, carbon (C) and oxygen (O) atoms are held together through bonds formed by sharing electrons, and these bonds possess strong electrical affinities. Meanwhile, the bond energy of C=O in CO_2 is about 750 $kJmol^{-1}$, which is higher than that of O-H in H_2O molecules.[44, 45] Therefore, the high symmetry, low polarity and high bond energy of the CO_2 molecule

lead to a high stability.

During the electrochemical conversion, we need to provide an overpotential that is relatively high to activate C=O bonds. Using a proper catalyst, the overpotential will be significantly reduced, thus, the research on efficient and robust electrocatalysts is crucial to promote this kinetically slow reduction reaction.

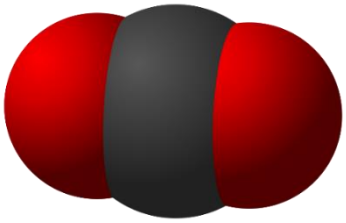

Figure 1.6 Structure of CO_2 molecule with space filling model (the red balls are for O atoms and the black one is for C).

1.3.1.1 Single Metal Catalysts

CO_2 RR are mostly catalyzed by metal-based materials in aqueous solutions. However, the selectivity observed on monometallic catalyst is different and summarized in **Figure 1.7**.[2, 46, 47] Considering reaction products, the electrocatalysts can be divided into different groups: 1) Ag, Au and Zn, which exhibit excellent activity for producing CO; 2) Pd, In and Sn, which show good selectivity for generating HCOOH; 3) Ni, Fe, Pt *et al.* which produce H_2 as the major product. These differences in selectivity on different single metal groups can be explained by the principle, when the key reaction intermediates such as *CO binds bonded on metal surfaces weakly will prohibit the reduction reaction to continue, therefore, the CO generates. For example, Cu takes an interesting place because of its special capacity of showing significant selectivity for hydrocarbon and alcohol evolution. The fact is that the key reaction intermediates with the optimal bonds (neither too weak nor too strong) on Cu surfaces could lead to further reaction to produce hydrocarbon and alcohol products.[48]

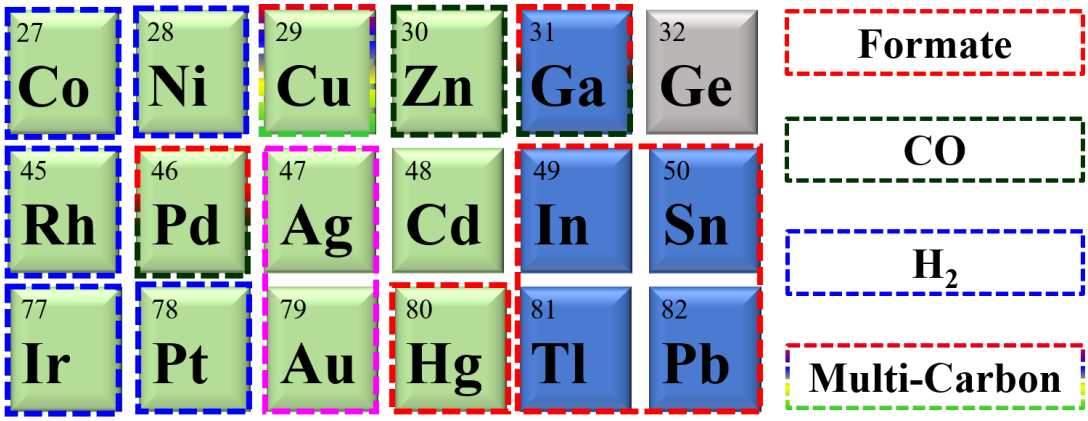

Figure 1.7 Selectivity differences observed on single monometallic catalyst during CO_2 RR.

1.3.1.2 Alloy Catalysts

While single metal catalysts showed their insufficient activity towards CO_2 RR, a second metal modification method has been proposed to influence the product distribution and efficiency obtained over single metal catalysts.[25] On one hand, the synergistic effects of bimetallic electrocatalysts can lead to change both the geometric and electronic modification of the active sites, further altering the binding strengths of intermediates and the activation barriers of the elementary steps tuning the activity and selectivity accordingly.[24] On the other hand, synergistic effects of bimetallic electrocatalysts could influence the adsorption and desorption process of key intermediates. Therefore, metal-alloys with tunable activity and selectivity through a combination of electronic and geometric effects have been widely prepared and used in CO_2 RR. For example, PdCu, PdAu, PdPt, PdSn, PdRu, PdTe, and PdIn have been identified to show improved activity and selectivity of CO_2 RR compared to the pure Pd. Therefore, designing bimetallic-based catalysts provides a strategy to weaken the binding affinity intermediate species on the pure metal surface.

1.3.1.3 Molecular Catalysts

A useful method to improve the catalytic activity and selectivity of metal catalysts is tuning the catalytic properties via surface modification. Molecular electrocatalysis thus is an excellent option because these factors can be optimized by chemical tuning of the metal centers through appropriate ligand design.[49-51] The first report of

homogeneous electrochemical CO_2 RR catalyzed by molecular catalysts appeared in the 1970s and 1980s, which offer the advantage of synthetic control over the steric and electronic properties in the vicinity of the active sites.[52] By application of appropriate organic ligands, some metals, including the second and third d-block series (such as Ru, Pd, and Re) and earth-abundant 3d transition metals (e.g. Mn, Fe, Co, and Ni), are widely used to prepare the molecular electrocatalysts, showing a high selectivity for target products, mainly CO and HCOOH. These molecular electrocatalysts are typically divided into five classes due to their different ligand architectures: 1) porphyrins; 2) cyclams; 3) bipyridyls; 4) polypyridyls and 5) phosphines.[53] Although most of molecular catalysts possess high selectivity towards CO_2 RR, in contrast to many heterogeneous catalysts, they generally show a low stability, and their poor recyclability deserves attention as well. In addition, most of molecular catalysts are mainly beneficial to two electron transfer processes for generation of CO and HCOOH, the efficient generation of the four-, six-, and eight-electron reduction products can be only achieved on a few molecular electrocatalysts. More importantly, they seldom used in the aqueous conditions because of low CO_2 concentration and competing HER. Therefore, the current methodologies should focus on immobilizing ligands or complexes within solids or at the surface of electrodes, hybrid systems composing of a simple molecular catalyst associated with a conductive support in order to boost the stability and conductivity of molecular catalyst.

1.3.1.4 Metal-Nitrogen-Carbon Catalysts

As discussed, homogeneous catalysts usually exhibit low current density due to their low solubility in aqueous electrolytes. As consequence, combing the advantages of homogeneous and heterogeneous catalysts is a good way to keep the high FE and good stability, simultaneously. The simple method to bridge homogeneous and heterogeneous catalysts is through directly creating atomically-defined active sites similar to those of homogeneous catalysts on the surface of heterogeneous catalysts. Therefore, as a frontier of material science, single-atom catalysts (SACs) are recently emerging because it mimics the role of the first coordination shell in molecular catalysis

through immobilizing the isolated metal atoms with three- or four-fold anchoring sites (C or N atoms), thus, showing an overwhelming performance towards CO_2 RR compared to majority of the reported catalysts. Despite the major benefits of SACs revealing high selectivity with maximal metal atom utilization, four challenges still exist: 1) Based on the experimental and theoretical results, for SACs, the activity, selectivity and overpotential during CO_2 RR strongly affected by the nature of the metal center and the structural features of the coordinative environment. Therefore, systematically rationalizing the configuration and local environment on the activity and selectivity is needed. 2) The aggregation phenomenon should be avoided in the SACs preparation because SACs tend to aggregate into clusters or NPs during synthesis process. 3) Future design and the investigation of SACs significantly influenced by the advanced characterization techniques, such as, electron microscopy, X-ray absorption spectroscopy (XAS), Fourier-transform infrared (FTIR) spectroscopy or scanning tunneling microscopy (STM). Especially, the aberration corrected TEM and high-angle annular dark-field STEM (HAADF STEM) are common techniques for directly determining the size and distribution as well as extract the local structural information. 4) As similar as molecular catalyst, most of SACs are mainly beneficial to CO generation.[54, 55]

1.3.1.5 Metal-Free Catalysts

As the main carbon-based catalysts, carbon fibers, CNTs, graphene, nano-porous carbon, and graphene dots doped with heteroatoms (e.g. N, B, S and F) have been widely considered as promising metal-free electrocatalysts for CO_2 RR because of their low cost, large surface area, high conductivity, remarkable activity, and long durability.[56-58] Among them, most of the carbon-based catalysts are beneficial to generate CO and formate through a two-electron transfer process. While the multi-electron reduction products such as CH_4, C_2H_4 and C_2H_6O are only obtained on a few carbon-based catalysts with specific composition, phase or morphology.

1.3.1.6 Limitations of the Current Electrocatalysts

Despite recent progress that has been reported in the literature, the current electrocatalysts towards CO_2 RR still suffer from many limitations.

- Most of current electrocatalysts are beneficial for generating CO and HCOOH instead of multi-carbon products.
- For the Cu catalysts that can produce multi-carbon products, however, they can produce many different reaction products during the CO_2 reduction, which leads to a difficult separation of the different products and a relatively low FE for target product.
- In addition, the low current density obtained on most of the current electrocatalysts hinders the future large-scale application.
- For the SACs catalysts with an atomic distribution, the nature of the active sites remains a puzzle, which makes rational design impossible for advanced catalysts with a high density of active sites for the CO_2 RR.
- Significant insight into the mechanisms of CO_2 RR still need to be established despite many challenges.

Although a variety of electrocatalysts have been prepared to boost the efficiency of CO_2 RR, the performance of an electrocatalyst is determined not only by its kind of metal sites, and the modified second metals or organic ligands. More importantly, the properties of the catalyst surface (surface adsorbates, facets, defects, structure, and morphology also significantly affect the thermodynamic adsorption energies of the key intermediates and kinetic barriers of the reactions, leading to different products. All in all, to overcome these technical boundaries, the catalyst material is one of the most essential building blocks to selectively and efficiently convert CO_2 into the desired products on a large scale.

1.3.2 Electrolyte

Chemically, an electrolyte is an ionic conductor consisting of ionic species in a specific solvent, providing ionic conductivity and thus facilitating charge compensation

on each electrode in the cell. Once an electrode immersed into an electrolyte, an electric double layer is constructed at the electrode/electrolyte interface, where covalently bonded species and reaction intermediates are present in the inner Helmholtz plane (IHP), and hydrated ions are situated in the outer Helmholtz plane (OHP), held by electrostatic forces (**Figure 1.8**).[17] Meanwhile, a series of dynamic equilibria for CO_2 and H_2O could potentially influence the local ion distribution and pH at the interface. As a result, during CO_2 RR, the electrolyte is the other important component that can control the CO_2 RR activity and selectivity. When CO_2 RR occurs at a specific potential, the electrode is negatively polarized, resulting in the attraction of the hydrated cations to the electrode because of Coulomb interactions, subsequently, the increase in the population of cations at the OHP. The cations at the OHP could not only enhance the local electrode potential, changing the charge transfer kinetics, but also generate a local electric field, improving the stability of the covalently adsorbed intermediates at the IHP. Meanwhile, the change of hydrated cations will determine the local pH, then influencing the reaction mechanism. In addition, specifically adsorbed ions at the IHP can alter the electronic structure of the surface catalyst atoms, block the active sites, and interact with the intermediates via van der Waals forces. Therefore, the local environment provided by the electrolyte, such as pH, and the presence of certain cations or anions could influence the reaction intermediates and the reaction pathways.[59-61]

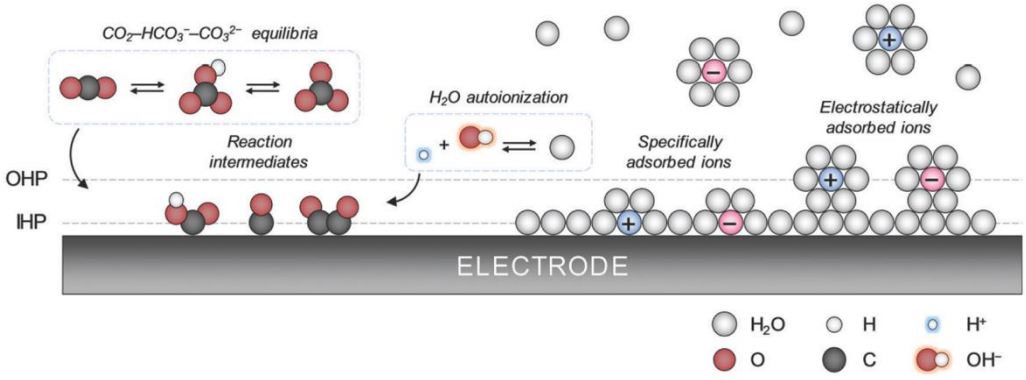

Figure 1.8 Simplified schematic illustration of the electric double layer composed of the inner Helmholtz plane (IHP) and outer Helmholtz plane (OHP) with chemical equilibria involved.[17]

1.3.2.1 Impact of pH

Most of the CO_2 RR catalyst studies have been mostly performed in H-cell electrolyzers, where CO_2 gas is bubbled into the electrolyte. In the electrolyte, dissolved CO_2 contains equilibriums: 1) $CO_2 + H_2O \leftrightarrow HCO_3^- + H^+$; 2) $HCO_3^- \leftrightarrow CO_3^{2-} + H^+$, as shown in **Table 1.3**.[17] $CO_{2(aq)}$ reacts with electrolytes to form carbonates, which causes a change in the local pH value and decreases the $CO_{2(aq)}$ concentration, thus, affecting the proton donation step as well as the mechanism change. For example, the equilibria of the acid-base reactions shift toward (bi)carbonates at a high local pH, reducing the concentration of CO_2 near the surface, which could decrease selectivity toward CO_2 RR and favoring the HER. The current studies have revealed a volcano-type dependence on pH for CO_2 RR selectivity and proposed an optimal local pH range of 9-10.[62] Therefore, understanding the impacts of pH is a major area for studying the dynamic reaction environment at the electrode surface.

Table 1.3 Acid-dissociation and kinetic rate constants for the formation of bicarbonate and carbonate anions.

Reaction	p*Ka*	k (s^{-1})
$CO_2 + H_2O \leftrightarrow HCO_3^- + H^+$	6.37	0.0371
$HCO_3^- \leftrightarrow CO_3^{2-} + H^+$	10.25	59.44

1.3.2.2 Cation/Anion Effects

Bicarbonate is a general electrolyte for CO_2 RR; however, the corresponding alkali metal cations could have a significant effect on the activity and selectivity towards CO_2 RR, due to the relatively high population of the cations at the OHP. Early experiments showed that the selectivity of CO_2 RR is affected by the choice of the alkaline cation in the electrolyte solution, where larger cations tend to shift the selectivity toward multi-carbon products on Cu catalysts.[63] In a previous work, Hori et al. revealed that the large cations are specifically adsorbed more easily than the small ones owing to the

relatively small hydration numbers.[63] The specifically adsorbed cations could increase the potential at the OHP and decrease the local proton concentration, thus, hindering the HER. In addition, electrolyte anions also influence the activity, selectivity and the product distributions of CO_2 RR. For example, the Cu-based electrodes in an electrolyte with non-buffering anions, such as SO_4^{2-}, the C2/C1 ratio increased. In addition, recent Raman spectroscopy experiments found that co-adsorbed halide ions (Cl^-, Br^-, I^-) also could enhance the amount of CO* adsorbed on Cu-based catalyst, consistent with earlier theoretical predictions.[64-66]

Although the importance of the electrolyte during the electrocatalytic process, its contribution has been less understood compared to the impact of heterogeneous catalysts, mainly because the characterization of electrolytes at the catalyst surface is not well-established yet. Therefore, optimal CO_2 RR systems require the conjunction of a catalyst with suitable adsorption properties and an electrolyte with beneficial effects on the catalytic activity and selectivity, which could be useful for understanding the CO_2 RR mechanism.

1.3.3 Applied Potential

In addition to the local pH in electrolytes, the different pathways can also be affected by the different ranges of the applied potentials. At the high overpotentials, the coupling of *CO-COH is dominant, while at low overpotentials, the *CO-CO dimerization pathway is found to be energetically favorable. As a consequence, the CO_2 RR enables a myriad of carbon-based chemicals and fuels to be synthesized at different applied potential.

1.4 Important Parameters for Evaluating Electrocatalysts

As different kinds of electrocatalysts have been widely used in CO_2 RR, finding some brief parameters for comparing and designing electrocatalysts CO_2 RR is important. Several key parameters are frequently used to evaluate the performance of electrocatalysts in this process, such as:

1.4.1 Catalysts Cost

The most effective catalysts rely on expensive metals, such as, Au, Ag, Pd, among others, the cheaper catalysts tend to have problems, i.e. low efficiency and insufficient stability, for commercial applications. Therefore, designing cost-friendly catalysts with high efficiency and activity will have a strong impact for future applications.

1.4.2 Faradaic Efficiency (FE)

CO_2 RR can lead to several products with competitive reactions (such as, HER). Therefore, producing a specific product with high FE is highly needed during CO_2 RR. The FE describes the amount of product produced per number of electrons transferred to facilitate the electrochemical reaction. It is calculated from the number of electrons consumed in the electroreduction process by using the formula:

$$FE = \frac{n(mol) \times X}{\frac{Q(C)}{F(C/mol)}} \times 100\ \%$$

where moles of formed product (n) multiplied by the required number of electrons (X) for CO_2 conversion into a particular product divided by the charge (Q, current density) to Faraday's constant (F, 96485C/mol). Finally, it will be multiplied by 100 to obtain the output in an easier form such as a percentage. Moles of formed products (n) can be obtained from analytic techniques such as GC.

1.4.3 Overpotential

The activation barrier associated with CO_2 RR is high, because bonds are broken and geometries changed along the reaction pathway, which brings challenges for the CO_2 RR at an electrode due to the necessity of applying a high overpotential.[28, 67] As an evaluating parameter, the overpotential presents the additional potential applied beyond the thermodynamically determined potential (E^0) required for the electrochemical reaction to transpire.[43] The high operating overpotential not only leads to a high level of energy waste, but also causes the H_2 produce, resulting in unsatisfactory selectivity. Therefore, the calculation of the overpotential is not trivial

but enables the comparison of electrocatalysts under different reaction conditions. As the result, the key element in improving the CO_2 RR activity is to achieve high faradaic efficiency at a small overpotential.

1.4.4 Current Density

The current density features the rate constant of the overall electrochemical reaction, consequently, the current density does not necessarily represent CO_2 reduction. However, some catalysts show an insufficient current density, which limits their practical implementation in CO_2 RR.[68]

1.4.5 Stability

Electrocatalysts with robust stability are necessary for catalysis in industrial applications.[69] Stability can be checked via chronoamperometry measurements such "I vs. t" plots; if current density decreases with time, consequently, the electrode is not stable. However, in the practical application, maintaining good stability under a long-term CO_2 RR stability still remains a big issue, because the overpotentials for obtaining CO_2 RR products, especially for multi-carbon products, are extremely high, which not only easily destroy the catalyst's structure and morphology, but also lead to large energy loss.

To summarize, there is a trade-off between product selectivity, energy efficiency, and current density that makes only certain products economically viable. Therefore, although there are many new materials developed in order to solve these challenges, one has to consider that the catalyst design should achieve an industrially large-scale CO_2 RR as the ultimate goal.

1.5 Limitations of CO_2 Electrochemical Reduction

Practically, there are still some challenges remaining in order to improve the CO_2 RR process:

1) The slow kinetics of CO_2 electroreduction, even when electrocatalysts and

high electrode reduction potential are applied;

2) The low energy efficiency of the process, due to the parasitic or decomposition reaction of the solvent at high reduction potential;

3) The high energy consumption. Researchers have recognized that the biggest challenge in CO_2 electroreduction is low performance of the electrocatalysts (i.e., low catalytic activity and insufficient stability);

4) Investigations on reaction mechanism.

Therefore, we still need to consider some parameters in CO_2 RR to realize the large-scale industrial applications.

1.5.1 Catalysts Design

The electrocatalyst is one of the most important components of a CO_2 electrolyzer because it determines both the product selectivity and energy efficiency of the CO_2 RR. Low-cost and high-efficient CO_2 RR electrochemical catalysts should be designed to reduce the energy barrier, promote product selectivity at a low overpotential. The search for a new catalyst that can simultaneously increase energy efficiency and product selectivity is complicated by various factors which can impact the catalyst activity, including intermediate binding energy, active sites, structure and geometry of catalyst, kinetic mechanism, desorption of products, and adsorbate-adsorbate interactions.[25, 70-72]

1.5.2 Selectivity and Activity

The reaction complexity of CO_2 RR is different from many other reactions. On one hand, for the products beyond 2 electron/proton transfer, the reaction complexity increases significantly, with many more proton-electron transfers. On the other hand, separation of products is difficult. Therefore, obtaining a high selectivity for specific product in the catalytic process is advantageous. Because single product generated during this process could reduce the cost of further product separation. Thus, we still need to focus on preparing high-efficient catalysts with a high selectivity towards single

product. In addition, although the higher FE has been obtained for CO and HCOOH, a method should be developed to produce the multi-carbon products with an extraordinarily high FE. Meanwhile, the selectivity is closely related to the reduction mechanism, thus, studying the reaction mechanism is needed for achieving the high selectivity.

1.5.3 Mechanism Research

Mechanistic investigations are the key to understanding catalytic cycles and effects of catalyst modifications. Density functional theory (DFT) is a powerful tool for understanding the intermediates and active species in the reaction.[73] Although the underpinning mechanisms of many catalysts have been studied extensively, the underlying fundamental processes are still not well understood at the molecular level. Meanwhile, with the increasing complexity of catalyst components, the identification of actual catalytic active sites will become more difficult. A combination of in situ, ex situ, and operando studies on the model catalysts with computational strategies is an effective means to find insight into the electrochemical reaction mechanisms involved at the molecular level.[74-76] Therefore, the highest priority should be focused on searching proper electrocatalysts in CO_2 RR to improve both reaction activity and selectivity in combination with DFT calculations and advanced characterizations. These new improvements are further used in predicting and preparing specific catalysts towards CO_2 RR.

1.5.4 Reactor Design

Research in the CO_2 RR field has largely focused experimentally on the H-cell. However, most investigations in H-cell for CO_2 RR are restricted by insufficient current density ($\leq$100 mA/cm^2) because of the mass transfer limitations and low CO_2 solubility.[77] One must consider that the excellent commercial CO_2 RR is contingent on achieving higher current density, high CO_2 RR FE at a relatively low applied potential as well as long stability. These requirements demand major advances not only in electrocatalyst materials design, but also in membrane as well as electrolyzer stack

engineering. Therefore, rational design of electrochemical reactors provides another method to improve the higher activity and selectivity during CO_2 RR that affect the industrial viability of CO_2.[61, 77]

1.6 Overview: Backgrounds of Metal-Organic Frameworks (MOFs)

First defined by Yaghi and co-workers in 1995, as a kind of interesting and novel materials, metal-organic frameworks (MOFs) built by metal ions and different organic ligands have emerged as a materials science frontier (**Figure 2.1**).[69, 78-80] Most of MOFs materials, synthesized by hydro-/solvothermal methods under gentle conditions,[81-83] possess many chemical and physical advantages, such as the high degree of order, crystalline structures, enormous flexibility in pore size, shape and structure, offering a plenty of opportunities for their functionalization, grafting and encapsulation.[84-87] Because of the above merits, during the last decades, a large number of research have been focusing on the functional MOFs materials in order to endow a desirable property for many fields, such as, gas storage and separation, luminescence, sensors, drug delivery, and especially in electrocatalysis.[84, 88-91]

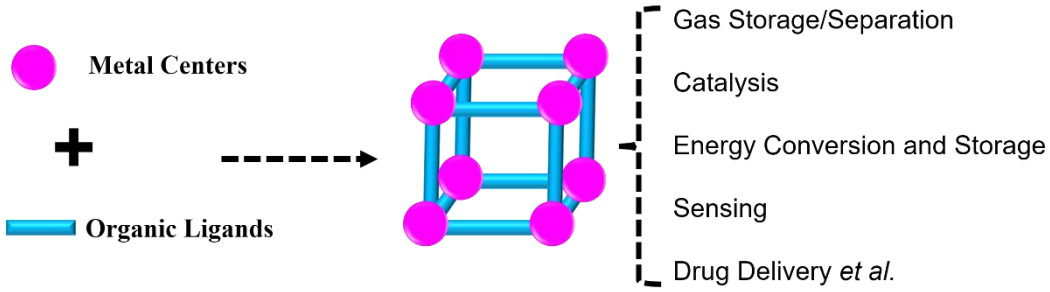

Figure 1.9 Schematic illustration of MOFs materials and their common applications.

1.7 MOFs as Electrocatalysts

The increasing interest in the development of electrocatalysis makes MOF chemistry as one of the fastest growing fields. The current applications of MOF as electrocatalysts have been established in the field of HER, oxygen evolution reaction (OER), oxygen reduction reaction (ORR), CO_2 RR, nitrogen reduction reaction (NRR),

methanol/ethanol oxidation reaction (M/EOR), and electrochemical sensing and energy storage (**Figure 2.2**). In particular, MOF electrocatalysts are better-suited for CO_2 reduction than other reactions mentioned before for several reasons. Firstly, MOFs can be functionalized to allow for better CO_2 capture. Secondly, the various catalytic sites in MOFs, including metal ions and organic ligands, could improve the catalytic efficiency.[78, 92]

Generally, MOFs as the electrocatalysts can be categorized in: 1) pristine MOF as an electrocatalyst; 2) MOFs as a support, and 3) MOFs as a precursor to produce electrocatalysts.[93-96] Although there are already many achievements about MOFs as electrocatalysts, for an electrocatalytic process, the active sites in MOFs-based materials, where reactants and intermediates adsorbed on and products desorbed from, are still intricate because of their complex compositions. Therefore, comprehensive understanding of active sites in MOFs and MOFs-derived materials is crucial for exploiting their future electrochemical applications.

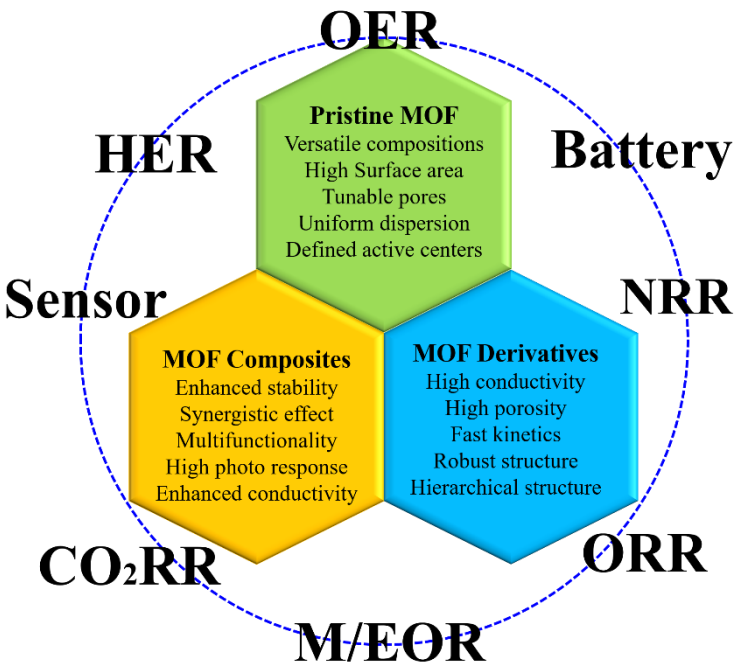

Figure 1.10 Different electrochemical applications of MOFs-based materials.

1.7.1 Active Sites of Pristine MOFs

MOFs materials are becoming an in-vogue issue for the electrocatalytic CO_2

reduction processes. Generally, the catalytic efficiencies towards CO_2 RR of MOFs materials are attributed to the following factors: 1) MOF materials can increase the local CO_2 concentration around materials' catalytically active sites by CO_2 pre-adsorption.[78] In this context, MOF pores serve as ''microreactors'', providing favorable environments for reactions between CO_2 and active sites; 2) some functional groups in MOFs enhance their CO_2 uptake and activate CO_2 molecules and/or other reactants, further improving MOFs' catalytic efficiencies.

1.7.1.1 Metal Centers as Active Sites

In this case, some MOFs materials can be certainly used directly as an electrocatalyst, since they already contain the necessary active sites, i.e., metal nodes (Fe,[97] Ni,[98] Co,[99] Cu[100], etc) or clusters. One example is the HKUST-1 with Cu-O clusters as the active sites, which showed catalytic properties towards CO_2 RR to produce C_2H_4 with 45 % selectivity.[100] In addition, it is worth noting that after introducing a new metal ion into the MOFs to form the uniform dispersed bi-/tri-metal active sites, MOFs can be functionalized with the unexpected catalytic performances through interactional metal nodes, providing a versatile platform for developing new catalytic properties.[101, 102]

1.7.1.2 Organic Linker as Active Sites

Apparently, in some cases, the electrocatalytic active sites in MOFs are not always a metal center, instead of the organic ligands. Experimental and theoretical results showed that the active sites can be located on the ligand next to the metal centers, thus, the diverse organic ligands in MOFs are the active sites. For example, a series of Zn-based MOFs, such as ZIF-7, ZIF-8, ZIF-108, and SIM-1, have been examined on their CO_2 RR activity and demonstrated that imidazolate was the optimal active site.[103] Furthermore, metal active sites in MOFs could be modified by coordinated ligands, which modulate the electronic configuration of metal centers, effectively tuning the catalytic activity of MOFs. For example, introducing an additional functional ligand with electron-rich group into MOFs could induce electron delocalization of the metal

active sites, which triggered charge transfer and change of the local environment around the metal centers, further enhancing the CO_2 RR performance of MOFs.[104]

1.7.1.3 Defects

Defects in MOFs arise from the removal of either a linker, a cluster, or a coordinated solvent (e.g., water) molecule, leading to a nonstoichiometric metal to linker ratio. Missing the organic linkers often make it possible to act as accessible active sites during the electrocatalysis.[105, 106] Because the coordinatively unsaturated metal sites are more easily oxidized to high valence, which is beneficial for some electrochemical reactions, such as CO_2 RR. On the other hand, active sites for electrocatalysis can be formed by partial replacement of the bridging linkers without the loss of crystallinity and porosity properties. Therefore, considering that the catalytic processes usually occur on the surfaces of electrocatalysts, the higher catalytic activity could be achieved by exposing surface atoms or active sites as much as possible in MOFs.[69] Although many breakthrough results have been achieved on pure MOFs as the electrocatalysts, the activity is still far from the practical requirements. Therefore, improving the catalytic performance of pure MOFs is the in-vogue issue in order to use them in practical applications.

1.7.2 Improve the Catalytic Performance of Pure MOFs

1.7.2.1 Lowering the Dimension of MOFs

As mentioned above, the metal ions or clusters in MOFs act as catalytic active sites, however, the catalytic processes only occur on the catalysts' surfaces. Therefore, the more exposed active sites in the surfaces of MOFs, the higher catalytic activity would achieve. Therefore, fabricating the low-dimensional MOFs with more exposed active sites could be a promising strategy to increase the number of electrocatalytic active sites in MOFs, resulting in an enhanced electrocatalytic performance because of the following advantages:[107-109] 1) the atomic thickness and two-dimensional structures are beneficial for rapid mass transport and fast electron transfer, 2) highly exposed catalytic active surfaces could enable high catalytic activity.

1.7.2.2 Coordinatively Unsaturated Sites Engineering

In most of MOF materials, the high coordination number (CN) of the metal nodes will limit the reaction between the metal active sites and the reactants, resulting in the sluggish kinetics for the electrocatalytic reactions. Therefore, the MOFs that can be directly used as electrocatalysts represent only a tiny proportion of the whole family of MOFs.[106, 110] Thus, to enhance the catalytic activity of MOFs in electrocatalysis, creating a plenty of coordinatively unsaturated sites (CUSs) is another rational method to increase the number of active sites. Although the obtained number of CUSs is usually not massive, removing the coordinated solvent molecules or portion of ligands to form CUSs (also called open metal sites) in MOFs could make metal active sites more accessible during the electrocatalysis.

1.7.2.3 Multi-Metal Center and Ligand Tuning

Introducing the multi-metal centers or other organic ligands is an effective strategy to modulate the local environment of active sites in MOFs, thus, optimizing their intrinsic activities on such modified MOFs.[69] For example, the integration of the different metal centers in MOFs will provide a synergistic effect to achieve a higher activity towards different electrocatalytic reactions, such as OER and CO_2 RR.

1.7.3 The Limitation of MOFs as Electrocatalysts

1.7.3.1 Conductivity

Although many efforts have been focused on increasing the active sites to boost the catalytic performance of pure MOFs, electron transfer is another essential process for electrocatalytic reactions, and thus, the electrical conductivity is of great importance for MOFs as the electrocatalysts.[110, 111] The MOFs are built by metal nodes and organic ligands. Such combination in MOFs usually cannot provide a good conjugation pathway for charge transport, nor any free charge carriers, leading to a poor conductive for MOFs. Therefore, designing the MOFs electrocatalysts with good conductivity is the main goal in the future research.

1.7.3.2 Stability

As the CO_2 RR field moves toward the industrial application phase, the reproducibility of the catalytic activities and a long-term stability of MOF catalysts is a determinant issue to be evaluated more thoroughly in practical applications. However, poor stability of most MOFs limits their further development in practical applications. Because the coordinate bonds between metal and ligands in a large portion of MOFs will be destroyed under high electrochemical potentials. Worse still, most of MOFs are unstable under an acid or base electrolyte, because a phase transformation and decomposition of the frameworks formed when these solutions attacked the metal centers in the MOFs. It is pointed out that the bond strength between the metal cation and the organic ligands is one of the main criteria that can influence the stability of MOFs. Therefore, the MOFs with high stability should be prepared by the proper fabrications.

1.7.4 MOFs Composites as Electrocatalysts

In order to overcome the intrinsic deficiencies of conventional pristine MOFs as discussed above like their insufficient numbers of active sites and poor conductivity, many MOFs composites have been prepared to solve these problems and meet the requirements for practical applications.[112, 113] Recent efforts have demonstrated that combination of MOFs with other functional materials to form MOF composites can overcome the above deficiencies that the pristine MOFs possessed while maintaining their original advantages. Generally, the introduced functional materials are combined with MOFs in two ways: (1) The functional materials are encapsulated inside MOF crystals as the active sites to overcome the insufficient active sites of pristine MOFs.[114, 115] (2) The functional materials serve as substrates to support MOFs for enhancing the limited conductivity of pristine MOFs.[86]

1.7.4.1 MOFs as the Templates

To enhance the catalytic activity of pristine MOFs in electrocatalysis, hybridizing MOFs with other active materials is considered as one of the promising methods.

Because the high porosity, as the obvious characteristic of MOFs, is beneficial to guest settlement. In such case, MOFs can act as the templates for supporting functional materials and make the active materials (i.e. nanoparticles) highly dispersive to avoid the active materials aggregations, which can not only realize a porous structure inherited from MOFs but also keep the high-efficient active sites. As a result, introducing the functional materials on the surface or inside the MOFs generally showed an improved electrically conductive performance, thus, effectively improving the catalytic performance of such MOF compositions.[116] Taking a zirconium MOF (NU-1000) as an example, Cu nanoparticles embedded into NU-1000 used as CO_2 RR and showed a faradaic efficiency of 31 % with formate as the major CO_2 reduction product.[117] Therefore, uniform distribution of the guest functional materials inside the MOF crystals could greatly enhance the overall electrocatalytic performance.

1.7.4.2 MOFs as Active Sites

Apart from the roles as the supports, MOFs can also act as the catalytic sites in MOFs composites. When MOFs supported on other functional substrates, MOFs generally function as the main active species and the functional substrates usually assist to disperse and stabilize the MOFs as well as enhance their conductivity to improve the catalytic performance of the overall materials. For example, conductive carbon-based materials (such as, graphene, N-doped carbon nanotubes and porous carbon materials) can not only make the MOFs strongly dispersed without the aggregations, but also improve the mechanical stability and conductivity of MOFs because of their strongly surficial immobilization ability and high conductivity.[85] In addition, these substrate materials generally possess the fast mass transport, desirable structural robustness, and good recyclability compared to the MOFs composites. Thus, the designing of a MOFs composite could ensure to obtain both the catalytic activity and the structure stability on one material.

1.7.5 MOFs Derivates as Electrocatalysts

Although extensive efforts have been devoted to prepare various pure MOFs or

their composites, we still face too many problems during electrochemical processes: 1) most of MOFs are unstable in aqueous acidic and basic solutions because of their weak coordination bonds, which are not beneficial for many catalytic reactions, such as, HER, OER. 2) The high oxidizing potential at the strong electrochemical reaction conditions will oxidize the non-redox active ligands and the metal nodes, leading to the structural collapse and phase conversion of MOFs into other materials (metal oxide/hydroxide).[85, 118, 119] Therefore, the MOFs that can be directly used as electrocatalysts represent only a tiny proportion of the whole family of MOFs. In order to solve these problems, generally, the most common method used is based on using MOFs as a significant precursor to generate diverse electrocatalysts or a sacrificial template. Because the effect of MOF during the formation of these advanced materials is irreplaceable in controlling the composition and morphology of the obtained materials. After a pyrolysis the confined metal or metal oxide in the resulting carbon-based materials can provide the high conductivity needed. During the pyrolysis processes, MOF structures are destroyed. Then, the carbon, metal/carbon, oxide/carbon, or other composites could be derived from MOF precursors.[119] A variety of active sites in these materials derived from MOFs show the excellent catalytic abilities. There are two main methods to prepare MOF-derived materials, as shown in **Figure 1.11**: (1) by direct pyrolysis of a MOF compound, (2) by heat-treatment of a MOFs composite based on other active materials. These MOF-derived materials can not only inherit the advantages of MOFs like high porosity and high surface area but also offer a new opportunity to control and design the multi-functional compositional/structural features by controlled fabricated process.[118]

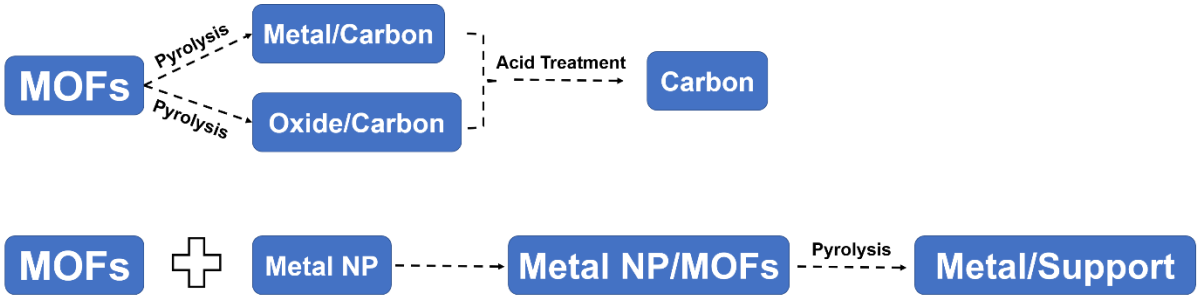

Figure 1.11 The synthetic routes for different MOFs-derived materials.

1.7.5.1 MOFs-Derived Materials without Metals

Due to the presence of carbon-containing organic linkers in MOFs crystals, nanocarbon-based materials are easily prepared by carbonization of MOFs precursors and then removal of metal species. Thus far, several Zn-based MOFs, such as ZIF-8, MOF-5, and MOF-74 have been demonstrated to be the most promising self-sacrificial precursors to produce metal-free nanocarbon composites due to the excellent boiling point (907 ℃) of Zn nodes. These MOF-derived materials can inherit the advantages of their MOFs precursors, especially their high surface area and tailorable porosity.[120] Meanwhile, these nanocarbon-based materials show the excellent conductivity compared to their MOFs parents. In addition, many heteroatoms-doped nanocarbon materials with the high conductivity and affinity for some adsorption of intermediates could also be designed from MOFs precursors, because some organic ligands are also composed of various heteroatoms (N, P, S, etc.) other than carbon.[121] For example, through tuning the calcination temperature and time, N-doped carbon materials derived from Zn-MOF-74 showed a superior CO_2 RR activity with a high FE of 98.4% to produce CO at −0.55 V vs. RHE.[122] Moreover, releasing the produced gas during pyrolysis of the ligands in MOFs templates can help to form hierarchically porous structures because the released gas could generate force to expand pores and induce the structure evolution, which is beneficial to facilitate the kinetics of electrochemical applications.[123]

1.7.5.2 MOFs-Derived Materials with Metals

MOFs are consisted of metal ions and corresponding coordinated organic ligands to form one-, two- or three-dimensional structures. Based on such advantages, MOFs can be used to prepare many metal-decorated carbon-based materials (e.g. metal/carbon materials, metal compound/carbon) by pyrolysis treatment at a wide range of temperatures.[124, 125] Generally, during the pyrolysis process, the aggregations formation is inevitable, and thus, hindering the catalytic performance of these nanoparticles derived from MOFs. To realize the higher catalytic behaviors and maximize the utilization efficiency of metals, downsizing the metal nanoparticles into

atomically dispersed metal sites (single atom catalysts, SACs) have recently emerged and have attracted extensive research attentions to greatly boost the electrocatalytic performances because of a high exposure of the active sites.[126] Based on this, various approaches have been employed to create dispersed metal sites derived from/based on MOFs. For the first option, single metal sites could be intrinsically created at the metal nodes within host frameworks before and during MOF syntheses. In the case of the metal nodes, much abundant single metal sites have been discovered in pristine and defective MOFs (also called open metal sites, OMSs). The second option is that immobilizing single metal sites into the host frameworks could enable inactive MOFs to exhibit into high-efficient electrocatalysts, including 1) utilization of unsaturated metal nodes that offer coordination sites to stabilize single metal atoms; 2) utilization of organic ligands that provide chelating sites to graft single metal atoms; 3) utilization of pore space that settle single metal atoms.[127] [128] These great potentials of the functionalization in metal nodes, organic linkers, and pore spaces actually make MOFs to become an ideal support for the SACs formation.

Over the years, SACs have emerged as one of the promising electrocatalysts for reduction of CO_2 to CO with superior FE. Although other composition, structure, and morphology of the carbon matrix are the same, the selectivity and activity for CO formation observed along the series of SACs is attributed to the nature of the transition metal in MN_x moieties.[128, 129] Regarding selectivity, Fe-N-C, Ni-N-C and Mn-N-C had FE for CO >80 %. While for the activity, Fe-N-C and Co-N-C catalysts showed a relatively low overpotential. Therefore, we still need to focus on the structure-performance relationship in SACs catalysts for CO_2 RR from both theoretical and experimental aspects.

An ideal MOF-based electrocatalyst should have high activity, selectivity, conductivity, and structural stability to ensure the application in the industrial energy conversion devices. Only if all the above parameters could be successfully integrated into MOF-based materials, the practical application of such materials in electrochemical devices could be realized. Thus, the design of MOFs with excellent

electrocatalytic activity is still a great challenge in broader areas.

1.8 Brief Introduction of Various Characterization Techniques for CO_2 RR Research

As shown in this chapter, although CO_2 RR is one of the most effective methods to solve environmental problems, many limitations caused by its inherent properties lead to the difficulties to understand its deep mechanism. On one hand, CO_2 RR is a multi-path reaction, in which the reaction intermediates are complex and diverse as well as at a low concentration, making it hard to identify them precisely. On the other hand, during the CO_2 RR, catalysts play an important role to reduce the kinetic energy barrier, however, most catalysts would undergo a structural or phase reconstruction during the reduction processes accompanied by an increase or decrease of the catalytic performance.[74, 130] Thus, it is necessary to use some specific characterization methodologies to capture the reaction intermediates and study the dynamic evolution of the catalysts. Generally, conventional characterization techniques have been used before and after the electrocatalysis process to deduce the possible active species, however, these conventional characterization techniques cannot be used for detecting the existence of the short-lived intermediates. Therefore, nowadays, some in situ measurements are drawing increasing attentions in CO_2 RR for precisely revealing the active sites and capturing the intermediate states change. Through these real-time detections, the catalysts and reaction intermediates could be clearly revealed, which is helpful to comprehensively understand CO_2 RR for further designing the elaborate CO_2 catalytic system. Therefore, the main detection targets, advantages and limitations of various in situ characterization techniques are shown in **Table 1.4**.

Table 1.4 Representative in Situ Techniques with main detection targets, advantages and limitations. ref[74]

Technique (in situ)	Advantages	Limitations
Ultraviolet-Visible Spectroscopy	1. Identify the organic species or reactive radical; 2. Investigate catalytic processes and catalytic products 3. work well on homogeneous and heterogeneous catalysis.	1. Perturbation errors caused by light source; 2. Low accuracy; 3. The test process usually takes more than a few minutes
Raman Spectroscopy	1. Works in aqueous solutions; 2. Suitable for detecting microscopic catalysts with a relatively high spatial resolution; 3. identify the materials present and uncover their intrinsic properties; 4. conduct to assess the valence-bond changes of the catalysts	1. It's not suitable for specific catalytic systems, such as pure metals
Fourier Transform Infrared Spectroscopy	1. High sensitivity; 2. Fast characterization speed.	1. Highly clean atmosphere; 2. Small signal-to-noise ratios in aqueous-phase experiments.
X-ray Diffraction Analysis	1. Detect the crystal phase of catalysts in real time; 2. Analyze the stability and phase transition of the	1. Only catalysts with good crystallinity. 2. Low spatial resolution, which makes it

	catalysts.	impossible to detect the local sites or components.
X-ray Photoelectron Spectroscopy	1. Element types can be qualitatively identified by analyzing the XPS spectrum; 2. Chemical shift for a feature peak will appear due to a change in the local chemical environment.	1. Only detects the elements near the surface; 2. The degree of vacuum needs to be strictly limited.
X-ray Absorption Spectroscopy	1. Monitor the changes in the catalysts; 2. Infer the intermediates in the catalytic process, and then analyze the reaction mechanism.	1. It is difficult to use for component analysis of complex systems.
Transmission Electron Microscopy	1. Can characterize the morphology changes of the catalyst during the reactions in real time; 2. Atomic scale; 3. Dynamic observation of chemical reactions could be also realized by combining TEM with electron diffraction and electron energy loss spectroscopy (EELS).	1. Initial stages for CO_2 RR; 2. Energy of the electron excitation source in TEM experiments is too strong for some structure-sensitive samples; 3. Operating environment and the sample preparation for in situ TEM experiments are relatively stringent, especially for high-resolution measurements.

Although in situ techniques play more and more important roles in the field of CO_2 RR to develop new electrocatalysts, only a single in situ technique cannot reveal the all information during the electrocatalysis. In addition, changes in phase, morphology, oxidation/spin states, as well as electronic/geometrical structures should also be

systematically taken into consideration during the catalytic process. Meanwhile, for the in-situ techniques, there are still many challenges and opportunities as follows: 1) **Active sites observation at atomic scale**. 2) **Reaction intermediates formation process**. 3) **In-depth understanding of mechanism.** To solve these problems, the advanced microscopy should be considered. For instance, recently, ultrafast four-dimensional electron microscopy (4D EM) has been applied for imaging the morphological dynamics of a single nanoparticle in real time and space. In situ environmental transmission electron microscopy (ETEM) can detect the intermediate evolutions down to the atomic level. The real-time monitoring of reaction intermediates will help reveal the catalytic mechanism under experimental conditions. By properly designing the in-situ reaction cells of the ETEM, it is quite possible to achieve dynamic observation and imaging of reaction intermediates during the CO_2 reduction process under more realistic conditions. Therefore, in situ studies cooperated with other techniques will play more and more important roles in the field of CO_2 RR in the future, which is helpful to precisely understand the catalytic mechanism and design efficient CO_2 catalytic systems.

References

[1] M. Aresta, A. Dibenedetto, A. Angelini, Chem. Rev., 114 (2014) 1709-1742.

[2] Z. Yin, G.T.R. Palmore, S. Sun, Trends in Chem., 1 (2019) 739-750.

[3] Y. Chen, H. Wu, D. Lv, W. Yang, Z. Qiao, Z. Li, Q. Xia, Energy & Fuels, 32 (2018) 8676-8682.

[4] G. Singh, J. Lee, A. Karakoti, R. Bahadur, J. Yi, D. Zhao, K. AlBahily, A. Vinu, Chem. Soc. Rev., 49 (2020) 4360-4404.

[5] W. Gao, S. Liang, R. Wang, Q. Jiang, Y. Zhang, Q. Zheng, B. Xie, C.Y. Toe, X. Zhu, J. Wang, L. Huang, Y. Gao, Z. Wang, C. Jo, Q. Wang, L. Wang, Y. Liu, B. Louis, J. Scott, A.-C. Roger, R. Amal, H. He, S.-E. Park, Chem. Soc. Rev., 49 (2020) 8584-8686.

[6] R. Sharifian, R.M. Wagterveld, I.A. Digdaya, C. Xiang, D.A. Vermaas, Energy Environ. Sci., (2021).

[7] M. Ding, R.W. Flaig, H.-L. Jiang, O.M. Yaghi, Chem. Soc. Rev., 48 (2019) 2783-2828.

[8] P. Zhang, J. Tong, K. Huang, Electrochemical CO_2 Capture and Conversion, Materials and Processes for CO_2 Capture, Conversion, and Sequestration 2018, pp. 213-266.

[9] R. Snoeckx, A. Bogaerts, Chem. Soc. Rev., 46 (2017) 5805-5863.

[10] S.C. Shit, I. Shown, R. Paul, K.-H. Chen, J. Mondal, L.-C. Chen, Nanoscale, 12 (2020) 23301-23332.

[11] Z. Yuan, M.R. Eden, R. Gani, Industrial Engineering Chem. Res., 55 (2016) 3383-3419.

[12] J.-P. Jones, G.K.S. Prakash, G.A. Olah, Israel J. Chem., 54 (2014) 1451-1466.

[13] J. Liu, C. Guo, A. Vasileff, S. Qiao, Small Methods, 1 (2017) 1600006.

[14] Y. Wu, S. Cao, J. Hou, Z. Li, B. Zhang, P. Zhai, Y. Zhang, L. Sun, Adv. Energy Mater., 10 (2020) 2000588.

[15] M. Goldman, E.W. Lees, P.L. Prieto, B.A.W. Mowbray, D.M. Weekes, A. Reyes, T. Li, D.A. Salvatore, W.A. Smith, C.P. Berlinguette, Chapter 10 Electrochemical Reactors, Carbon Dioxide Electrochemistry: Homogeneous and Heterogeneous Catalysis, The Royal Society of Chemistry 2021, pp. 408-432.

[16] F. Cai, D. Gao, H. Zhou, G. Wang, T. He, H. Gong, S. Miao, F. Yang, J. Wang, X. Bao, Chem. Sci., 8 (2017) 2569-2573.

[17] Y.J. Sa, C.W. Lee, S.Y. Lee, J. Na, U. Lee, Y.J. Hwang, Chem. Soc. Rev., 49 (2020) 6632-6665.

[18] D. Weekes, D.A. Salvatore, A. Reyes, A. Huang, C. Berlinguette, Acc. chem. research, 51 4 (2018) 910-918.

[19] T. Zheng, K. Jiang, N. Ta, Y. Hu, J. Zeng, J. Liu, H. Wang, Joule, 3 (2019) 265-278.

[20] F. Urbain, P. Tang, N.M. Carretero, T. Andreu, L.G. Gerling, C. Voz, J. Arbiol, J.R. Morante, Energy Environ. Sci., 10 (2017) 2256-2266.

[21] S. Zhao, S. Li, T. Guo, S. Zhang, J. Wang, Y. Wu, Y. Chen, Nano-Micro Lett., 11 (2019) 62.

[22] Y. Zheng, A. Vasileff, X. Zhou, Y. Jiao, M. Jaroniec, S.-Z. Qiao, J. Am. Chem. Soc., 141 (2019) 7646-7659.

[23] D.-H. Nam, O. Shekhah, G. Lee, A. Mallick, H. Jiang, F. Li, B. Chen, J. Wicks, M. Eddaoudi, E.H. Sargent, J. Am. Chem. Soc., 142 (2020) 21513-21521.

[24] D. Gao, H. Zhou, F. Cai, J. Wang, G. Wang, X. Bao, ACS Catal., 8 (2018) 1510-1519.

[25] C. Yang, Y. Wang, L. Qian, A.M. Al-Enizi, L. Zhang, G. Zheng, ACS Appl. Energy Mater., (2021).

[26] W. Wang, S. Wang, X. Ma, J. Gong, Chem. Soc. Rev., 40 (2011) 3703-3727.

[27] K. Fan, Y. Jia, Y. Ji, P. Kuang, B. Zhu, X. Liu, J. Yu, ACS Catal., 10 (2020) 358-364.

[28] C. Ding, A. Li, S.-M. Lu, H. Zhang, C. Li, ACS Catal., 6 (2016) 6438-6443.
[29] O.S. Bushuyev, P. De Luna, C.T. Dinh, L. Tao, G. Saur, J. van de Lagemaat, S.O. Kelley, E.H. Sargent, Joule, 2 (2018) 825-832.
[30] F. Li, Y.C. Li, Z. Wang, J. Li, D.-H. Nam, Y. Lum, M. Luo, X. Wang, A. Ozden, S.-F. Hung, B. Chen, Y. Wang, J. Wicks, Y. Xu, Y. Li, C.M. Gabardo, C.-T. Dinh, Y. Wang, T.-T. Zhuang, D. Sinton, E.H. Sargent, Nature Catal., 3 (2020) 75-82.
[31] T.-T. Zhuang, Z.-Q. Liang, A. Seifitokaldani, Y. Li, P. De Luna, T. Burdyny, F. Che, F. Meng, Y. Min, R. Quintero-Bermudez, C.T. Dinh, Y. Pang, M. Zhong, B. Zhang, J. Li, P.-N. Chen, X.-L. Zheng, H. Liang, W.-N. Ge, B.-J. Ye, D. Sinton, S.-H. Yu, E.H. Sargent, Nature Catal., 1 (2018) 421-428.
[32] S. Das, J. Pérez-Ramírez, J. Gong, N. Dewangan, K. Hidajat, B.C. Gates, S. Kawi, Chem. Soc. Rev., 49 (2020) 2937-3004.
[33] A.A. Peterson, F. Abild-Pedersen, F. Studt, J. Rossmeisl, J.K. Nørskov, Energy Environ. Sci., 3 (2010) 1311-1315.
[34] C.W. Lee, N.H. Cho, S.W. Im, M.S. Jee, Y.J. Hwang, B.K. Min, K.T. Nam, J. Mater. Chem. A, 6 (2018) 14043-14057.
[35] J.S. Yoo, R. Christensen, T. Vegge, J.K. Nørskov, F. Studt, ChemSusChem, 9 (2016) 358-363.
[36] K.P. Kuhl, T. Hatsukade, E.R. Cave, D.N. Abram, J. Kibsgaard, T.F. Jaramillo, J. Am. Chem. Soc., 136 (2014) 14107-14113.
[37] J.T. Feaster, C. Shi, E.R. Cave, T. Hatsukade, D.N. Abram, K.P. Kuhl, C. Hahn, J.K. Nørskov, T.F. Jaramillo, ACS Catal., 7 (2017) 4822-4827.
[38] R. Kortlever, J. Shen, K.J.P. Schouten, F. Calle-Vallejo, M.T.M. Koper, J. Phys. Chem. Lett., 6 (2015) 4073-4082.
[39] C.W. Lee, N.H. Cho, K.D. Yang, K.T. Nam, ChemElectroChem, 4 (2017) 2130-2136.
[40] S. Fletcher, J. Solid State Electrochem., 13 (2009) 537-549.
[41] Y. Chen, C.W. Li, M.W. Kanan, J. Am. Chem. Soc., 134 (2012) 19969-19972.
[42] M. Dunwell, W. Luc, Y. Yan, F. Jiao, B. Xu, ACS Catal., 8 (2018) 8121-8129.
[43] W. Ni, Y. Xue, X. Zang, C. Li, H. Wang, Z. Yang, Y.-M. Yan, ACS Nano, 14 (2020) 2014-2023.
[44] L. Wang, W. Chen, D. Zhang, Y. Du, R. Amal, S. Qiao, J. Wu, Z. Yin, Chem. Soc. Rev., 48 (2019) 5310-5349.
[45] S. Samanta, R. Srivastava, Mater. Adv., 1 (2020) 1506-1545.
[46] V.C. Hoang, V.G. Gomes, N. Kornienko, Nano Energy, 78 (2020) 105311.
[47] F. Zhang, H. Zhang, Z. Liu, Current Opinion in Green and Sustainable Chem., 16 (2019) 77-84.
[48] H. Xie, T. Wang, J. Liang, Q. Li, S. Sun, Nano Today, 21 (2018) 41-54.
[49] J. Bonin, A. Maurin, M. Robert, Coordination Chem. Rev., 334 (2017) 184-198.
[50] D.-C. Liu, D.-C. Zhong, T.-B. Lu, EnergyChem, 2 (2020) 100034.
[51] S. Zhang, Q. Fan, R. Xia, T.J. Meyer, Acc. Chem. Research, 53 (2020) 255-264.
[52] C. Costentin, K. Daasbjerg, M. Robert, Chapter 2 Homogeneous Electrochemical Reduction of CO_2. From Homogeneous to Supported Systems, Carbon Dioxide Electrochemistry: Homogeneous and Heterogeneous Catalysis, The Royal Society of Chemistry 2021, pp. 67-97.
[53] F. Franco, C. Rettenmaier, H.S. Jeon, B. Roldan Cuenya, Chem. Soc. Rev., 49 (2020) 6884-6946.
[54] A.S. Varela, W. Ju, A. Bagger, P. Franco, J. Rossmeisl, P. Strasser, ACS Catal., 9 (2019) 7270-

7284.
[55] H.-Y. Jeong, M. Balamurugan, C.H. Choi, K.T. Nam, Chapter 6 Bridging Homogeneous and Heterogeneous Systems: Atomically Dispersed Metal Atoms in Carbon Matrices for Electrocatalytic CO_2 Reduction, Carbon Dioxide Electrochemistry: Homogeneous and Heterogeneous Catalysis, The Royal Society of Chemistry 2021, pp. 226-286.
[56] A.G.A. Mohamed, Y. Huang, J. Xie, R.A. Borse, G. Parameswaram, Y. Wang, Nano Today, 33 (2020) 100891.
[57] S. Liu, H. Yang, X. Su, J. Ding, Q. Mao, Y. Huang, T. Zhang, B. Liu, J. Energy Chem., 36 (2019) 95-105.
[58] K. Zhao, X. Quan, ACS Catal., (2021) 2076-2097.
[59] H. Hashiba, L.-C. Weng, Y. Chen, H.K. Sato, S. Yotsuhashi, C. Xiang, A.Z. Weber, J. Phys. Chem. C, 122 (2018) 3719-3726.
[60] J. Albo, M. Alvarez-Guerra, P. Castaño, A. Irabien, Green Chem., 17 (2015) 2304-2324.
[61] A. Mustafa, B.G. Lougou, Y. Shuai, Z. Wang, S. Razzaq, J. Zhao, H. Tan, Sustainable Energy Fuels, 4 (2020) 4352-4369.
[62] S. Nitopi, E. Bertheussen, S.B. Scott, X. Liu, A.K. Engstfeld, S. Horch, B. Seger, I.E.L. Stephens, K. Chan, C. Hahn, J.K. Nørskov, T.F. Jaramillo, I. Chorkendorff, Chem. Rev., 119 (2019) 7610-7672.
[63] M. Akira, H. Yoshio, Bulletin. Chem. Soc. Japan, 64 (1991) 123-127.
[64] A.S. Varela, W. Ju, T. Reier, P. Strasser, ACS Catal., 6 (2016) 2136-2144.
[65] D. Gao, F. Scholten, B. Roldan Cuenya, ACS Catal., 7 (2017) 5112-5120.
[66] Y. Huang, C.W. Ong, B.S. Yeo, ChemSusChem, 11 (2018) 3299-3306.
[67] W. Lv, J. Bei, R. Zhang, W. Wang, F. Kong, L. Wang, W. Wang, ACS Omega, 2 (2017) 2561-2567.
[68] Z. Chen, X. Zhang, W. Liu, M. Jiao, K. Mou, X. Zhang, L. Liu, Energy Environ. Sci., (2021).
[69] S. Dou, X. Li, X. Wang, ACS Mater. Lett., 2 (2020) 1251-1267.
[70] J. Huang, R. Buonsanti, Chem. Mater., 31 (2019) 13-25.
[71] Y. Wang, P. Han, X. Lv, L. Zhang, G. Zheng, Joule, 2 (2018) 2551-2582.
[72] Z. Sun, T. Ma, H. Tao, Q. Fan, B. Han, Chem, 3 (2017) 560-587.
[73] S. Xu, E.A. Carter, Chem. Rev., 119 (2019) 6631-6669.
[74] X. Li, S. Wang, L. Li, Y. Sun, Y. Xie, J. Am. Chem. Soc., 142 (2020) 9567-9581.
[75] Y. Zhang, S.-X. Guo, X. Zhang, A.M. Bond, J. Zhang, Nano Today, 31 (2020) 100835.
[76] B. Petrovic, M. Gorbounov, S. Masoudi Soltani, Microporous and Mesoporous Mater., 312 (2021) 110751.
[77] S. Liang, N. Altaf, L. Huang, Y. Gao, Q. Wang, J. CO_2 Utilization, 35 (2020) 90-105.
[78] C.S. Diercks, Y. Liu, K.E. Cordova, O.M. Yaghi, Nature Mater., 17 (2018) 301-307.
[79] C. Wang, D. Liu, W. Lin, J. Am. Chem. Soc., 135 (2013) 13222-13234.
[80] X. Li, Q.-L. Zhu, EnergyChem, 2 (2020) 100033.
[81] D. Bradshaw, A. Garai, J. Huo, Chem. Soc. Rev., 41 (2012) 2344-2381.
[82] J. Hwang, A. Ejsmont, R. Freund, J. Goscianska, B.V.K.J. Schmidt, S. Wuttke, Chem. Soc. Rev., 49 (2020) 3348-3422.
[83] N. Stock, S. Biswas, Chem. Rev., 112 (2012) 933-969.
[84] A.M. Rice, G.A. Leith, O.A. Ejegbavwo, E.A. Dolgopolova, N.B. Shustova, ACS Energy Lett., 4 (2019) 1938-1946.

[85] T. Qiu, Z. Liang, W. Guo, H. Tabassum, S. Gao, R. Zou, ACS Energy Lett., 5 (2020) 520-532.
[86] F. Zheng, Z. Zhang, C. Zhang, W. Chen, ACS Omega, 5 (2020) 2495-2502.
[87] L. Oar-Arteta, T. Wezendonk, X. Sun, F. Kapteijn, J. Gascon, Mater. Chem. Frontiers, 1 (2017) 1709-1745.
[88] L. Yang, S. Qian, X. Wang, X. Cui, B. Chen, H. Xing, Chem. Soc. Rev., 49 (2020) 5359-5406.
[89] L.J. Murray, M. Dincă, J.R. Long, Chem. Soc. Rev., 38 (2009) 1294-1314.
[90] W.P. Lustig, S. Mukherjee, N.D. Rudd, A.V. Desai, J. Li, S.K. Ghosh, Chem. Soc. Rev., 46 (2017) 3242-3285.
[91] A.H. Chughtai, N. Ahmad, H.A. Younus, A. Laypkov, F. Verpoort, Chem. Soc. Rev., 44 (2015) 6804-6849.
[92] C.A. Trickett, A. Helal, B.A. Al-Maythalony, Z.H. Yamani, K.E. Cordova, O.M. Yaghi, Nature Rev. Mater., 2 (2017) 17045.
[93] Q. Wang, D. Astruc, Chem. Rev., 120 (2020) 1438-1511.
[94] L. Cao, C. Wang, ACS Central Sci., 6 (2020) 2149-2158.
[95] A. Bavykina, N. Kolobov, I.S. Khan, J.A. Bau, A. Ramirez, J. Gascon, Chem. Rev., 120 (2020) 8468-8535.
[96] T. Wang, X. Cao, L. Jiao, Small, DOI: 10.1002/smll.202004398.
[97] I. Hod, M.D. Sampson, P. Deria, C.P. Kubiak, O.K. Farha, J.T. Hupp, ACS Catal., 5 (2015) 6302-6309.
[98] W. Lu, X. Wu, New J. Chem., 42 (2018) 3180-3183.
[99] J. Gao, J. Cong, Y. Wu, L. Sun, J. Yao, B. Chen, ACS Appl. Energy Mater., 1 (2018) 5140-5144.
[100] D.-H. Nam, O.S. Bushuyev, J. Li, P. De Luna, A. Seifitokaldani, C.-T. Dinh, F.P. García de Arquer, Y. Wang, Z. Liang, A.H. Proppe, C.S. Tan, P. Todorović, O. Shekhah, C.M. Gabardo, J.W. Jo, J. Choi, M.-J. Choi, S.-W. Baek, J. Kim, D. Sinton, S.O. Kelley, M. Eddaoudi, E.H. Sargent, J. Am. Chem. Soc., 140 (2018) 11378-11386.
[101] X. Wang, H. Xiao, A. Li, Z. Li, S. Liu, Q. Zhang, Y. Gong, L. Zheng, Y. Zhu, C. Chen, D. Wang, Q. Peng, L. Gu, X. Han, J. Li, Y. Li, J. Am. Chem. Soc., 140 (2018) 15336-15341.
[102] X. Zhao, B. Pattengale, D. Fan, Z. Zou, Y. Zhao, J. Du, J. Huang, C. Xu, ACS Energy Lett., 3 (2018) 2520-2526.
[103] X. Jiang, H. Li, J. Xiao, D. Gao, R. Si, F. Yang, Y. Li, G. Wang, X. Bao, Nano Energy, 52 (2018) 345-350.
[104] S. Dou, J. Song, S. Xi, Y. Du, J. Wang, Z.-F. Huang, Z.J. Xu, X. Wang, Angew. Chem. Int. Ed., 58 (2019) 4041-4045.
[105] D. Yang, M. Babucci, W.H. Casey, B.C. Gates, ACS Central Sci., 6 (2020) 1523-1533.
[106] Ü. Kökçam-Demir, A. Goldman, L. Esrafili, M. Gharib, A. Morsali, O. Weingart, C. Janiak, Chem. Soc. Rev., 49 (2020) 2751-2798.
[107] K.A.S. Usman, J.W. Maina, S. Seyedin, M.T. Conato, L.M. Payawan, L.F. Dumée, J.M. Razal, NPG Asia Mater., 12 (2020) 58.
[108] M.A. Tekalgne, H.H. Do, A. Hasani, Q. Van Le, H.W. Jang, S.H. Ahn, S.Y. Kim, Mater. Today Adv., 5 (2020) 100038.
[109] P. Chen, Y. Tong, C. Wu, Y. Xie, Acc. Chem. Research, 51 (2018) 2857-2866.
[110] S.M.J. Rogge, A. Bavykina, J. Hajek, H. Garcia, A.I. Olivos-Suarez, A. Sepúlveda-Escribano, A. Vimont, G. Clet, P. Bazin, F. Kapteijn, M. Daturi, E.V. Ramos-Fernandez, F.X. Llabrés i Xamena, V. Van Speybroeck, J. Gascon, Chem. Soc. Rev., 46 (2017) 3134-3184.

[111] W.-H. Li, K. Ding, H.-R. Tian, M.-S. Yao, B. Nath, W.-H. Deng, Y. Wang, G. Xu, Adv. Funct. Mater., 27 (2017) 1702067.
[112] S. Kempahanumakkagari, K. Vellingiri, A. Deep, E.E. Kwon, N. Bolan, K.-H. Kim, Coordination Chem. Rev., 357 (2018) 105-129.
[113] X.F. Lu, B.Y. Xia, S.-Q. Zang, X.W. Lou, Angew. Chem. Int. Ed., 59 (2020) 4634-4650.
[114] Y. Xue, S. Zheng, H. Xue, H. Pang, J. Mater. Chem. A, 7 (2019) 7301-7327.
[115] J. Yu, C. Mu, B. Yan, X. Qin, C. Shen, H. Xue, H. Pang, Mater. Horizons, 4 (2017) 557-569.
[116] Q.-L. Zhu, Q. Xu, Chem. Soc. Rev., 43 (2014) 5468-5512.
[117] C.-W. Kung, C.O. Audu, A.W. Peters, H. Noh, O.K. Farha, J.T. Hupp, ACS Energy Lett., 2 (2017) 2394-2401.
[118] H.-F. Wang, L. Chen, H. Pang, S. Kaskel, Q. Xu, Chem. Soc. Rev., 49 (2020) 1414-1448.
[119] X. Cao, C. Tan, M. Sindoro, H. Zhang, Chem. Soc. Rev., 46 (2017) 2660-2677.
[120] B. Liu, H. Shioyama, H. Jiang, X. Zhang, Q. Xu, Carbon, 48 (2010) 456-463.
[121] H. Zhang, J. Nai, L. Yu, X.W. Lou, Joule, 1 (2017) 77-107.
[122] L. Ye, Y. Ying, D. Sun, Z. Zhang, L. Fei, Z. Wen, J. Qiao, H. Huang, Angew. Chem. Int. Ed., 59 (2020) 3244-3251.
[123] X. Liu, L. Zhang, J. Wang, J. Materiomics, 7 (2021) 440-459.
[124] J. Meng, X. Liu, C. Niu, Q. Pang, J. Li, F. Liu, Z. Liu, L. Mai, Chem. Soc. Rev., 49 (2020) 3142-3186.
[125] X.F. Lu, Y. Fang, D. Luan, X.W.D. Lou, Nano Lett., 21 (2021) 1555-1565.
[126] Y. Yang, Y. Yang, Z. Pei, K.-H. Wu, C. Tan, H. Wang, L. Wei, A. Mahmood, C. Yan, J. Dong, S. Zhao, Y. Chen, Matter, 3 (2020) 1442-1476.
[127] C.-C. Hou, H.-F. Wang, C. Li, Q. Xu, Energy Environ. Sci., 13 (2020) 1658-1693.
[128] Y.-S. Wei, M. Zhang, R. Zou, Q. Xu, Chem. Rev., 120 (2020) 12089-12174.
[129] J. Li, P. Pršlja, T. Shinagawa, A.J. Martín Fernández, F. Krumeich, K. Artyushkova, P. Atanassov, A. Zitolo, Y. Zhou, R. García-Muelas, N. López, J. Pérez-Ramírez, F. Jaouen, ACS Catal., 9 (2019) 10426-10439.
[130] Y. Zhu, J. Wang, H. Chu, Y.-C. Chu, H.M. Chen, ACS Energy Lett., 5 (2020) 1281-1291.

Chapter 2

Improvement of Carbon Dioxide Electroreduction by Crystal Surface Modification of ZIF-8

2.1 Introduction

Electrochemical reduction of carbon dioxide (CO_2 RR) to fuels and chemical feedstocks has been considered as a promising option to mitigate the excessive emissions of CO_2 and balance the global carbon cycle.[1-3] Among the various CO_2 RR products, carbon monoxide (CO) is one of the most promising and economically valuable candidates because it can be directly utilized as a feedstock for value-added chemicals and complex multi-carbon products via the well-known Fischer-Tropsch synthesis.[4-6] Recently, metal-organic frameworks (MOFs) materials have sparked a considerable interest as new-fashioned catalysts in the field of CO_2 RR to produce CO, as both metal ions and organic ligands could influence the catalytic performance.[7-11] More importantly, the inherent porous confinement properties of MOFs are expected to induce a local CO_2 concentration enhancement, thus, facilitating CO_2 RR catalysis.[12, 13] Despite these advantages, the current density for CO, when using pure MOF catalysts in the CO_2 RR, is still limited (usually lower than 3.4 mA cm^{-2}), [9] hindering the wide utilization of MOFs in electrocatalytic reactions.[11] Therefore, there is still a grand challenge to achieve MOFs based catalysts presenting high current densities while maintaining a high Faradaic efficiency (FE), being both properties essentially required for practical applications.

Two key aspects should be primarily considered to achieve high CO_2 RR performance for a catalyst: 1) increase the number of the exposed active sites and 2) promote the mass transport of CO_2 or relevant species during the catalytic reaction.[11, 14] To achieve these two goals, surface regulation of catalysts is reported as a promising method to simultaneously increase the number of exposed active sites and improve reactants mass transport.[15-17] For example, amounts of active sites have been increased by surface nitrogen-decoration strategy, leading to a high formation rate of formate on surface decorated Sn.[18] Moreover, due to promoted mass diffusion and transport, an enhanced FE of CO can be achieved on F-doped cage-like porous carbon through engineering the pore size distributions at the surface of F-doped carbon shell.[14] Therefore, a rationally chemical modification of the catalyst's surface could

be an effective strategy to obtain high CO_2 RR performance, which would not largely change the crystal structure of the original bulk phase.[18] However, there are few reports on enhancing CO_2 RR through regulating the surface of MOFs catalysts. Specifically, experimental and computational insights into such surface modification-performance relationship of MOFs catalysts are still rare.

Here, we demonstrate that a surface modification strategy to treat ZIF-8 crystals with a polyphenolic acid such as 2,5-dihidroxyterephthalic acid (DOBDC) could bring a high-efficient CO_2 RR performance. As an efficient etching and doping agent for MOFs, on one hand, this acid can etch the surface of ZIF-8 crystals to create high surface areas and proportion of mesopores, potentially offering large amount of surface active sites for CO_2 RR and allowing the facile diffusion of CO_2 RR-relevant species to the active sites.[19-21] On the other hand, DOBDC can be adsorbed on the ZIF-8 surface, and then progressively replace partial original organic linkers in ZIF-8 due to its ability to coordinate with metals,[22] thus, influencing local environment of active sites to facilitate COOH* generation (the key intermediate for CO production).[10] Both experimental and theoretical results in this work reveal that this synergistic effect could promote the CO_2 RR performance on surface modified ZIF-8, realizing a dual improvement of selectivity and activity. In detail, through precisely controlling the DOBDC addition, when DOBDC is used in a concentration of 5 % in weight with respect to ZIF-8 (hereafter denoted as ZIF-8-5 %), ZIF-8-5 % achieves a remarkable increase of the FE of CO up to 79 % at −1.20 V vs. RHE, which is higher than that of parent ZIF-8 (56 %). More importantly, it also shows a 2.5 times higher CO current density, from −4 mA cm^{-2} on the pure ZIF-8 to −10 mA cm^{-2} on the ZIF-8-5 %. Moreover, the selectivity can be retained over 60 % in a range of working potentials from −1.0 to −1.2 V vs. RHE, proving that CO is the main product on ZIF-8-5 % at high overpotentials. The theoretical analyses further demonstrate that ZIF-8-5 % could reduce the reaction energy for COOH* intermediates formation during the CO_2 RR process, thus enhancing the production efficiency of CO. We believe that this post-synthetic treatment could open a new way for boosting the catalytic performances on

MOFs catalysts with controllable surface modification.

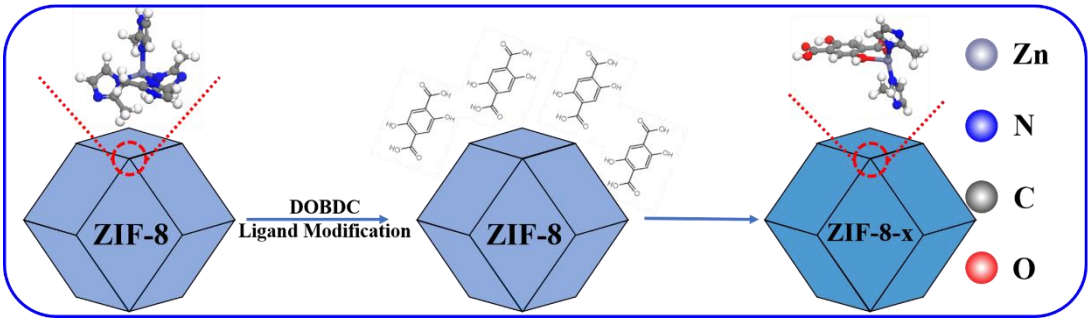

Schematic 2.1 Schematic illustration of the formation of ZIF-8-x samples.

A schematic illustration of the synthesis route followed to obtain the ZIF-8 and the corresponding functionalized samples is shown in **Figure 2.1**. ZIF-8 was initially synthesized based on previous literature.[10] In a second step, the corresponding ZIF-8-x (where x represents the weight percentage of DOBDC with respect to ZIF-8) were prepared by incubating a dispersion of the parent ZIF-8 crystals and different amounts of DOBDC in a mixture of DMF, ethanol and water for 7 days. Following this synthetic protocol, five different samples denoted as ZIF-8-1.7 %, ZIF-8-5 %, ZIF-8-10 %, ZIF-8-17 % and ZIF-8-33 % were prepared. The detailed synthesis information is shown in **Section 2.2**.

2.2 Experimental Section

2.2.1 Materials and Methods

Materials: If not specified, all chemical reagents were purchased from Sigma-Aldrich. Zinc nitrate hexahydrate ($Zn(NO_3)_2 \cdot 6H_2O$), 2-methylimidazole (2-mim), methanol, 2, 5-dihydroxyterephthalic acid (DOBDC), N,N-dimethylformamide (DMF), ethanol and sodium bicarbonate ($NaHCO_3$) were all of analytical grade and used as received without further purification. Meanwhile, all solutions were prepared with Milli-Q water (DI-H_2O, Ricca Chemical, ASTM Type I). The Nafion (N-117 membrane, 0.18 mm thick) was purchased from Alfa Aesar and kept in 0.5 M NaOH solution. The carbon paper was also purchased from Alfa Aesar.

Characterization: X-ray diffraction patterns (XRD) were obtained through a Bruker D4 X-ray powder diffractometer using Cu Kα radiation (1.54184 Å). Field emission scanning electron microscopy (FE-SEM) images were collected on a FEI

Magellan 400 L scanning electron microscope. Transmission electron microscopy (TEM) and high angle annular dark field scanning TEM (HAADF-STEM) images were obtained in a Tecnai F20 field emission gun microscope with a 0.19 nm point-to-point resolution at 200 kV equipped with an embedded Quantum Gatan Image Filter for EELS analyses. Images have been analyzed by means of Gatan Digital Micrograph software. X-ray photoelectron spectroscopy (XPS) was performed on a Phoibos 150 analyser (SPECS GmbH, Berlin, Germany) in ultra-high vacuum conditions (base pressure 4×10^{-10} mbar) with a monochromatic aluminium Kα X-ray source. Binding energies (BE) were determined using the C 1s peak at 284.5 eV as a charge reference. Raman spectra were obtained using Senterra. Bruker. Brunauer-Emmett-Teller (BET) surface areas were measured using nitrogen adsorption at 77 K (TriStar II 3020-Micromeritics). Proton nuclear magnetic resonance (^{1}H-NMR) was conducted in a Bruker Advance III 400 MHz.

2.2.2 Synthesis Methods

2.2.2.1 Preparation of ZIF-8

The fabrication of ZIF-8 is similar to the one reported elsewhere.[10] Typically, 1.115 g $Zn(NO_3)_2\cdot6H_2O$ were dissolved in 50 ml methanol under magnetic stirring at room temperature to form a homogeneous solution. Then, 50 ml methanolic solution containing 1.232 g 2-mim were added into the above mixture under ultrasonic until the formation of clear solution. The obtained homogeneous solution reacted at room temperature for 24 h without stirring. Then, the white powder was collected by centrifugation, washed with methanol several times to remove organic residual. The final products were then dried in vacuum at 60 ºC overnight.

2.2.2.2 Preparation of Zn-MOF-74

Zn-MOF-74 sample was synthesized according to previous published protocols with minor modification.[23, 24] First, 60 mg $Zn(NO_3)_2\cdot6H_2O$ and 20 mg DOBDC were dissolved in 15 ml mixed DMF/H_2O/ethanol solution (v/v/v=1:1:1) under ultrasonication to form the homogeneous solution. Then, the obtained solution was transferred into Teflon reactor and heated at 120 °C for 24 h, in turn cooled to room

temperature, produced brown needle-shaped crystals were obtained by centrifugation, washed with methanol several times to remove organic residual. Finally, the final products were dried in vacuum at 60 ºC overnight.

2.2.2.3 Preparation of Modified ZIF-8-x with the Second Organic Ligand Modification

In this procedure, 300 mg as-prepared ZIF-8 powder was dispersed in the 45 ml mixture solution consisting in 15 ml DMF, 15ml ethanol and 15 ml water under ultrasound for 20 min at room temperature. After forming a homogeneous solution, DOBDC with different quantities (5 mg, 15 mg, 30 mg, 50 mg and 100 mg) was added into the above solution under ultrasound for 5 min at room temperature. The previous DOBDC added weights correspond to a 1.7 %, 5 %, 10 %, 17 % and 33 % vs. the ZIF-8 weight, respectively. Next, the mixed solution was left in the oven at 60 ºC for 7 days. After reacting, the flavescent powders were collected by centrifugation, washed with ethanol and DMF several times to remove the organic residuals and dried in vacuum at 60 ℃ overnight. The samples have been labelled depending on the percentage of the added DOBDC: ZIF-8-1.7 %, ZIF-8-5 %, ZIF-8-10 %, ZIF-8-17 % and ZIF-8-33 %, respectively.

2.2.2.4 Preparation of Physical Mixture ZIF-8-5 % (Labelled as ZIF-8-5 %-P)

For the preparation of the ZIF-8-5 %-P sample, 15 mg of DOBDC powder were directly added into 300 mg of ZIF-8 powder. The powder was then mixed with a spoon.

2.2.3 Preparation of working electrodes

10 mg of the different synthesized samples and 50 µl 5 wt % Nafion solutions were dissolved in ethanol (1 mL) and ultrasonicated for 1 h to form evenly suspensions for the further electrochemical experiments. To prepare the working electrode, 500 µL of the above as-prepared inks were dropped onto the two sides of the carbon paper electrode with 1×1 cm^2 and then dried at room temperature for few minutes, giving a catalyst total loading mass of ~5 mg/cm^2 (using both sides of the carbon paper).

2.2.4 Electrochemical Measurement

The electrocatalytic performance of different catalysts was measured at room

temperature by using a gas-tight H-cell with two-compartments separated by a cation exchange membrane (Nafion N-117 membrane) with a continuously Ar or CO_2 gas injection. Each compartment contained 70 ml electrolyte (0.5 M $NaHCO_3$ made from deionized water). In a typical experiment, a standard three electrode setup in 0.5 M $NaHCO_3$ solution was assembled: an Ag/AgCl electrode was used as reference electrode, a Pt wire as auxiliary electrode and the carbon paper modified with the different samples as working electrode (with a total surface area = 1 cm^2). The potentials were measured versus Ag/AgCl and converted to the reversible hydrogen electrode (RHE) according to the following equation: $E_{RHE} = E^0_{Ag/AgCl} + E_{Ag/AgCl} + 0.059 \times pH$, pH=7.[25, 26] All the electrochemical results were showed without iR-compensation by using a computer-controlled BioLogic VMP3 electrochemical workstation. Meanwhile, the linear sweep voltammetry (LSV) measurements were performed to reach a stable state at a scan rate of 10 mV/s from −0.5 V to −2.0 V vs. Ag/AgCl in Ar-saturated 0.5 M $NaHCO_3$ (pH=8.5) and CO_2-saturated 0.5 M $NaHCO_3$ (pH=7) as supporting electrolyte.

Before the electrochemical CO_2 reduction experiments, an average rate of 20 ml min^{-1} Ar was injected into the cathodic electrolyte in order to form an Ar-saturated solution. During electrochemical CO_2 reduction experiments, the CO_2 gas was delivered at an average rate of 20 ml min^{-1} at room temperature and ambient pressure, measured downstream by a volumetric digital flowmeter. The gas phase composition was analyzed by gas chromatography (GC) during potentiostatic measurements every 20 min using a 490 Micro GC (Agilent Technologies). The calibration of peak area vs. gas concentration was used for the molar quantification of each gaseous effluent. The Faradaic efficiency was calculated by determining the number of coulombs needed for each product and then dividing by the total charge passed during the time of the GC sampling according to the flow rate. The liquid products were analyzed afterwards by quantitative ^{1}H-NMR using water as the deuterated solvent. The MOF sample was digested by HF solution overnight to completely destroy the structure. The ^{1}H-NMR of the sample was conducted using MeOD as solvent.

2.2.5 Calculation Method

Details concerning the calculation are shown below.

The partial current density for a given gas product was calculated as below:[27]

$$j_i = x_i \times V \times \frac{n_i F P_0}{RT} \times (electrode\ area)^{-1}$$

Where x_i is the volume fraction of certain product determined by online GC referenced to calibration curves from three standard gas samples, V is the flow rate, n_i is the number of electrons involved, P_0= 101.3 kPa, F is the Faraday constant, T is temperature and R is the gas constant. The corresponding FE at each potential is calculated by

$$FE = \frac{j_i}{j} \times 100\%$$

2.2.6 DFT Calculations

DFT calculations were performed using the Vienna Ab initio Simulation Package (VASP) code[28] with projector augmented wave (PAW) method.[29-32] Generalized gradient approximation (GGA) with Perdew-Burke-Ermzerhof (PBE) exchange-correlation function was employed to set the plane wave basis.[33, 34] The energy cutoff was 500 eV and all structures were allowed to relax. The force convergence criteria on each configuration were below 0.05 eV/Å. In order to avoid interactions between molecules in the periodic structures, we placed the model in a 20 Å×20 Å×20 Å cell. 1×1×1 k-point grids with Monkhorst-Pack scheme were used for all systems. DFT-D3 method with Becke-Jonson damping was employed to include van der Waals interactions between molecules.[35, 36]

Molecular orbital (MO) analyses were performed with the PBE function and dgdzvp2 basis sets in Gaussian 09 program.[37, 38] The ZIF-8 model was generated with four 2-mim ligands coordinating with the central Zn^{2+} to form a tetrahedral configuration, which is following the approach reported previously.[10] The ZIF-8-5 % structure was built with one DOBDC replacing two 2-mim of ZIF-8. The reaction free energy of each elementary step was estimated using the computational hydrogen electrode model,[39] and the following elementary steps were considered for

electrochemical CO_2 RR to CO:

$CO_2(g) + * + H^+(aq) + e^- \leftrightarrow COOH*$ Equation S.1

$COOH* + H^+(aq) + e^- \leftrightarrow CO* + H_2O(l)$ Equation S.2

$CO* \leftrightarrow CO(g) + *$ Equation S.3

where *, COOH* and CO* represent the free site, adsorption state of COOH and CO, respectively. The reaction free energies were calculated according to the following formula:

$$G = E_{DFT} + E_{ZPE} - TS + E_{sol}$$ Equation S.4

where E_{DFT} is the DFT calculated total energy, E_{ZPE} represents the zero-point energy, S is the entropy. E_{sol} is solvation correction and the values used for CO* was −0.1 eV and COOH* by −0.25 eV.[40]

2.3 Results and Discussion

2.3.1 Characterization of Prepared Samples

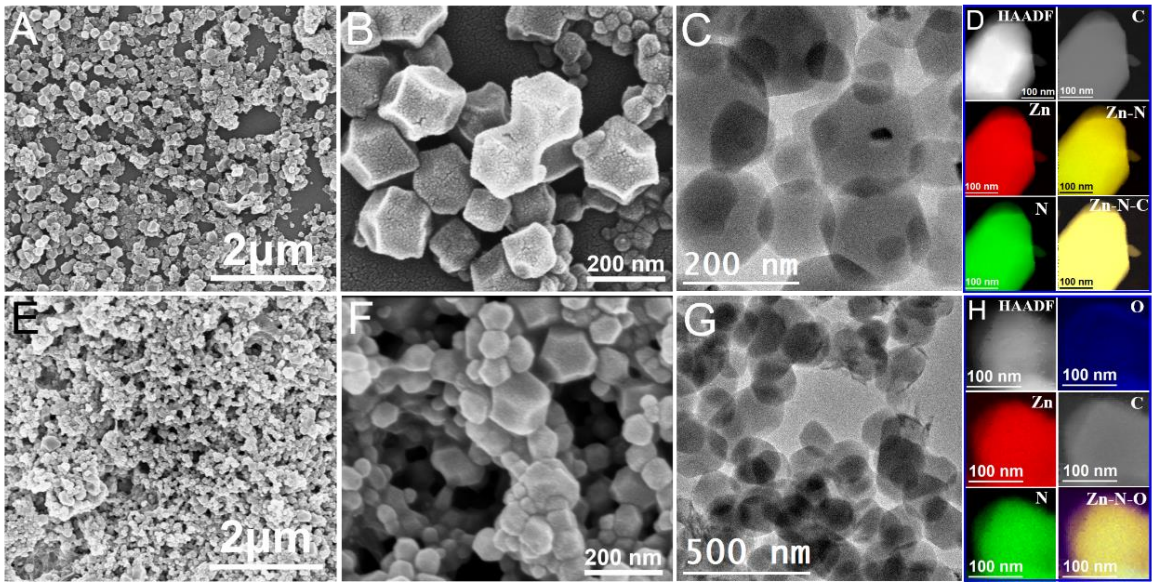

Figure 2.2 (A and B) FESEM images, (C) BF TEM and (D) HAADF STEM and EELS chemical composition maps of ZIF-8. (E and F) FESEM images, (G) BF TEM and (H) HAADF STEM and EELS chemical composition maps of ZIF-8-5 %. Individual Zn $L_{2,3}$-edges at 1020 eV (red), N K-edges at 401 eV (green), O K-edges at 532 eV (blue) and C K-edges at 285 eV (grey) as well as composites.

The surface morphology and elementary composition of the ZIF-8 and ZIF-8-5 % samples are revealed by field emission scanning electron microscopy (FE-SEM) and transmission electron microscopy (TEM). As revealed by FE-SEM (**Figures 2.2A** and **B**), the prepared ZIF-8 shows homogeneous crystals with the characteristic rhombic dodecahedral morphology. In addition, TEM analyses show that the ZIF-8 crystals have a size in the range of 80 − 200 nm (**Figure 2.2C**). After DOBDC functionalization, various morphologies of ZIF-8-5 % samples are shown in **Figures 2.2E-G**. As shown in **Figures 2.2 E** and **F**, the as-synthesized ZIF-8-5 % sample still inherits the overall rhombic dodecahedral morphology, which is similar to the one shown by the unmodified ZIF-8 structures, suggesting that there is not an apparent morphology change of these crystals after exposing them with a small proportion of DOBDC. Moreover, the chemical composition of ZIF-8 and ZIF-8-5 % crystals are investigated by high angle annular dark field scanning transmission electron microscopy (HAADF-STEM) and electron energy loss spectroscopy (EELS) elemental maps. STEM EELS

compositional maps show the homogeneous distribution of Zn, N and C in ZIF-8 and ZIF-8-5 % crystals (**Figure 2.2D** and **H**). It is interesting to point out the presence of O in the ZIF-8-5 % crystal, which is not found in the native ZIF-8.

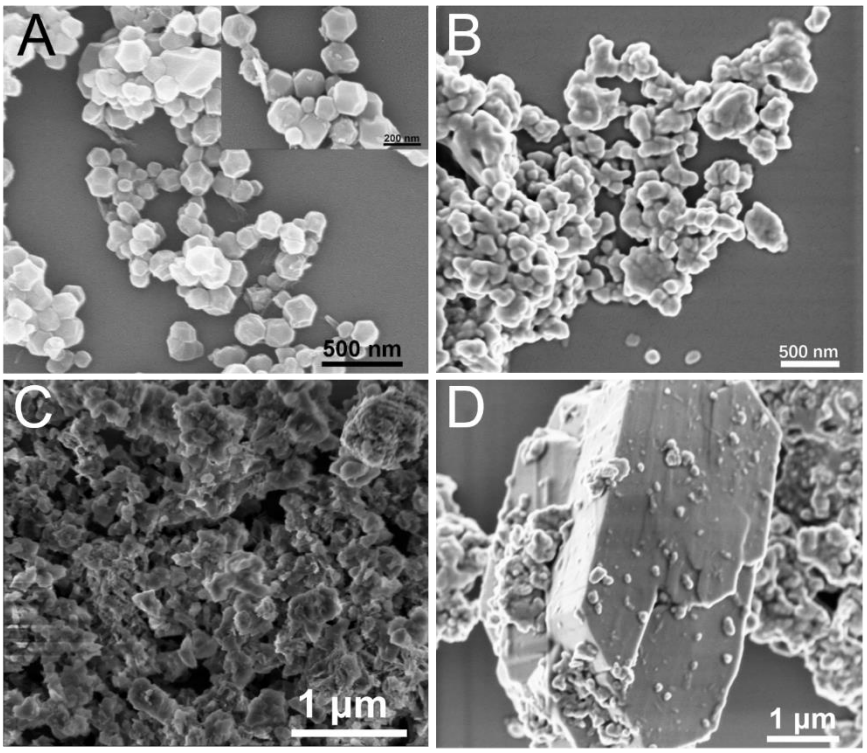

Figure 2.3 FE-SEM images of (A) ZIF-8-1.7 % (B) ZIF-8-10 %, (C) ZIF-8-17 % and (D) ZIF-8-33 %.

Likewise, the morphology of other ZIF-8-x samples was also studied by SEM. As shown in Figure **2.3A**, the as-synthesized ZIF-8-1.7 % sample also keeps the structure of ZIF-8. However, with increased ratio of DOBDC, ZIF-8-10 % samples display an irregular spherical shape (**Figure 2.3B**), while ZIF-8-17 % and ZIF-8-33 % samples are composed by some larger bulks and small spherical particles. We attribute the formation of this bulky structures to the large concentration of DOBDC used, which it can further etch the ZIF-8 crystals and liberate 2-mim and Zn(II) ions, together with DOBDC, forming other crystalline species.

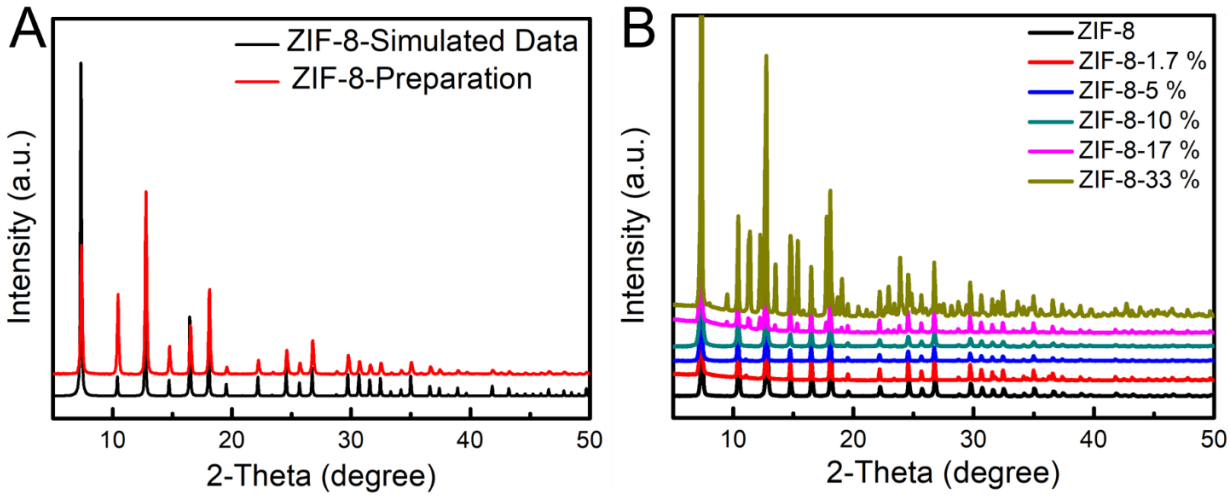

Figure 2.4 (A) Simulated data from crystal structure and experimental XRPD patterns of ZIF-8 and (B) ZIF-8-x with different DOBDC modification ratios.

The ZIF-8-x samples were further characterized by X-ray powder diffraction (XRD) (**Figure 2.4**). Indeed, XRD spectra obtained on of ZIF-8-1.7 %, ZIF-8-5 % and ZIF-8-10 % indicate that they retain the core crystallinity of the parent ZIF-8, revealing that the addition of a low concentration (up to 10 %) of DOBDC does not affect the crystal structure of ZIF-8.[10] However, XRD spectra of ZIF-8-17 % and ZIF-8-33 % show some additional diffraction peaks, indicating that a high DOBDC introduction can change the crystal structure of ZIF-8, which are accordance with the results of SEM.

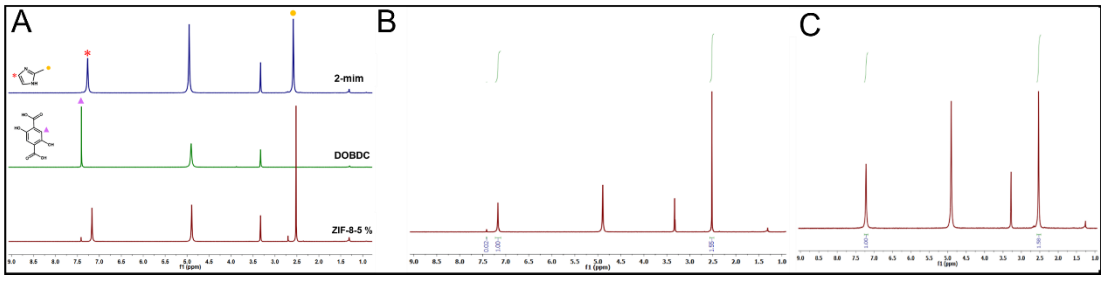

Figure 2.5 (A and B) ^{1}H-NMR spectra of ZIF-8-5 % and (C) ^{1}H-NMR spectra of ZIF-8-1.7 %.

Based on the above results, in order to further confirm the successful introduction of DOBDC into ZIF-8-5% crystals surface, we digested ZIF-8-5 % samples and

analysed the resulting solutions by ^{1}H-NMR. As shown in **Figure 2.5A**, ZIF-8-5 % sample shows a small peak at 7.41 ppm attributed to the DOBDC functional group, thus corroborating its successful introduction to promote a surface modification in the MOF. We then calculated the DOBDC:2-mim ratio for ZIF-8-5 % by comparison of the peak integration at 7.41 ppm corresponding to DOBDC and the peak at 7.17 ppm corresponding to 2-mim **(Figure S3B)**, indicating a DOBDC:2-mim ratio of 0.02. On the contrary, no signal attributed to DOBDC could be observed in ZIF-8-1.7 % sample, suggesting a negligible DOBDC surface modification of this sample (**Figure 2.5C**).

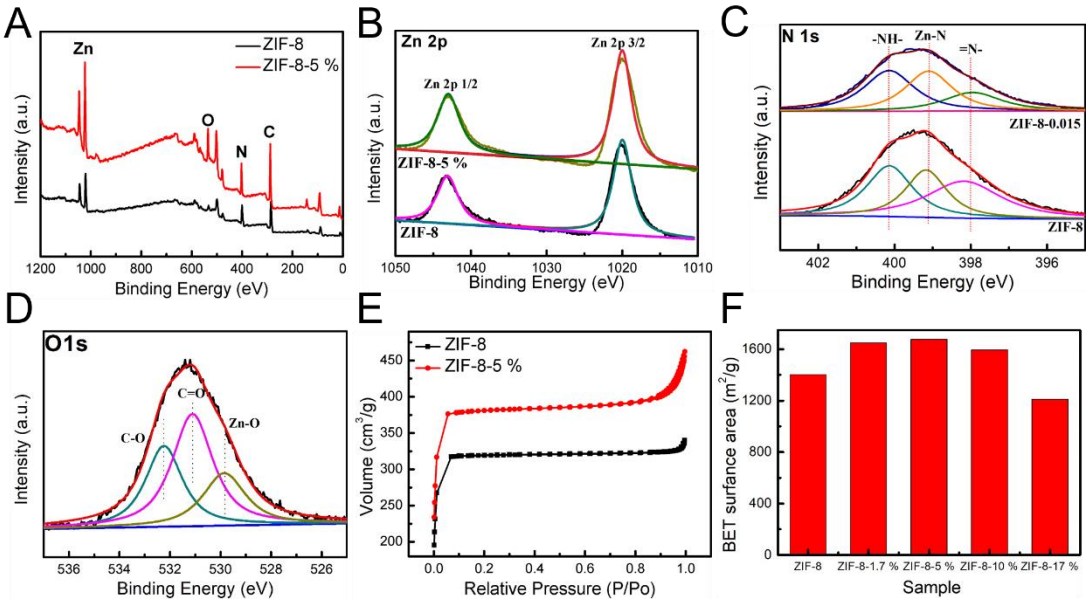

Figure 2.6 (A) XPS survey spectra, (B) High resolution XPS spectra of Zn 2p, and (C) N 1s of ZIF-8 and ZIF-8-5 %. (D) High resolution XPS spectra of O 1s of ZIF-8-5 %. (E) N_2 adsorption-desorption isotherms of ZIF-8 and ZIF-8-5 %. (F) The BET surface area of different samples.

Furthermore, the chemical valence state and surface composition of the ZIF-8 and ZIF-8-5 % samples have been proved by X-ray photoelectron spectroscopy (XPS). The full survey scan XPS spectrum shown in **Figure 2.6A** indicates the presence of C, N, O and Zn in both ZIF-8 and ZIF-8-5 % samples. The high-resolution XPS spectra obtained on the Zn 2p shows two main peaks in all the samples at around 1020 eV and 1044 eV (**Figure 2.5B**), corresponding to Zn $2p_{3/2}$ and Zn $2p_{1/2}$, respectively, which indicates the presence of Zn^{2+} in both samples.[41] The N 1s spectra for ZIF-8 and ZIF-

8-5 % are shown in **Figure 2.5C**, which clearly displays that both samples mainly show three major peaks corresponding to −NH−, Zn−N and −N= at 398.0 eV, 399.2 eV and 400.3 eV, respectively.[10] Remarkably, the O signal in ZIF-8-5 % is significantly larger than in ZIF-8, further supporting the successful introduction of DOBDC into ZIF-8-5 %. The O 1s XPS core level spectra for ZIF-8-5 % can be deconvoluted into three peaks at around at 532.8, 531.7 and 530.1 eV that would be related to C−O, C=O and Zn−O, respectively (**Figure 2.5D**).[42] Moreover, the surface area and porosity at the as-prepared samples are investigated by N_2 adsorption-desorption measurements. The ZIF-8 and ZIF-8-5 % show a typical type I adsorption/desorption isotherm curve in **Figure 2.5E**, indicating that both samples have numerous micropores.[43, 44] The adsorption of ZIF-8-5 % increases obviously at the relative pressures $P/P_0 < 0.1$ and $P/P_0 > 0.9$, which could be assigned to the micropores generation caused by DOBDC surface functionalization.[45] As shown in **Figure 2.5F**, the measured surface area (1403 m^2/g) of ZIF-8 is fully consistent with our previously reported values for ZIF-8.[46] However, an increased specific surface area is observed on ZIF-8-5 % sample, which should potentially offer large amount of surface active sites for CO_2 RR.[47] In addition, compared to the parent ZIF-8, ZIF-8-1.7 % sample also shows an increased surface area. However, combine the ^{1}H-NMR results, the enhanced surface area of ZIF-8-1.7 % could be attributed to the fact that etch process only occurred on the ZIF-8-1.7 % surface, while there is a negligible ligand modification process because of deficient DOBDC content.

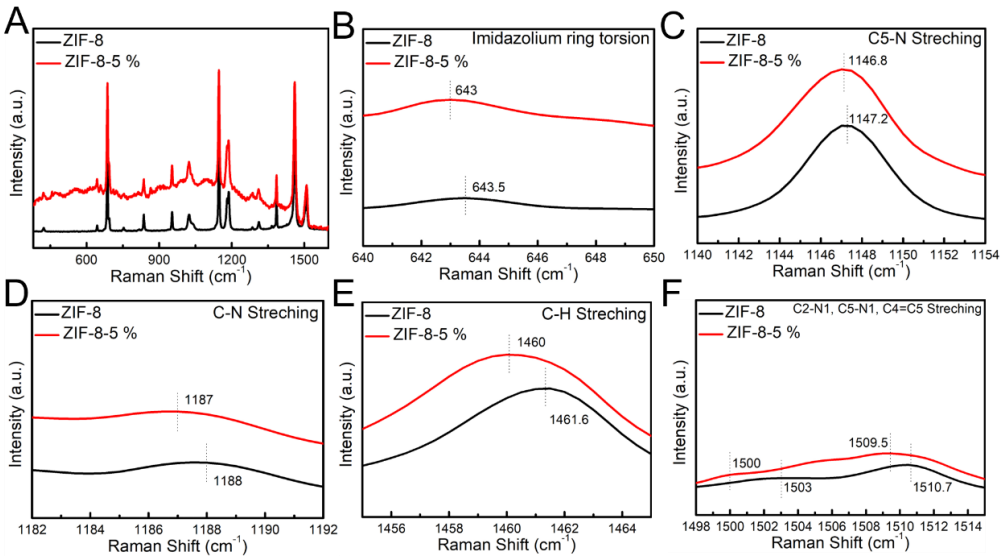

Figure 2.7 Raman spectra of the ZIF-8 and ZIF-8-5 %.

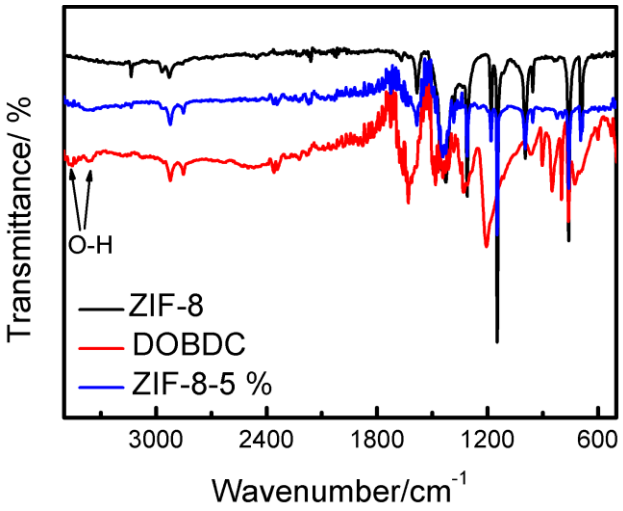

Figure 2.8 FTIR spectra of the ZIF-8, DOBDC and ZIF-8-5 %.

In addition, as shown in **Figure 2.7**, red-shifts at ca. 643.5, 1147.2, 1188, 1461.5, 1503 and 1510.7 cm^{-1}, are observed in the high-resolution Raman spectrum obtained on the ZIF-8 after DOBDC surface modification. These shifts are attributed to the tiny torsion and stretching of the different bonds, clearly indicating that the coordinated environment of ZIF-8 is influenced by the introduced DOBDC ligand.[48] Meanwhile, Fourier transform infrared spectrophotometry (FT-IR) of ZIF-8-5 %, as shown in **Figure 2.8**, proves the formation of Zn-DOBDC coordination by the negligible peak from characteristic O-H vibration peaks in ZIF-8-5 % compared to DOBDC. [22] These results indicate that the ZIF-8-5 % have been successfully prepared with surface functionalization.

2.3.2 Electrochemical Performance

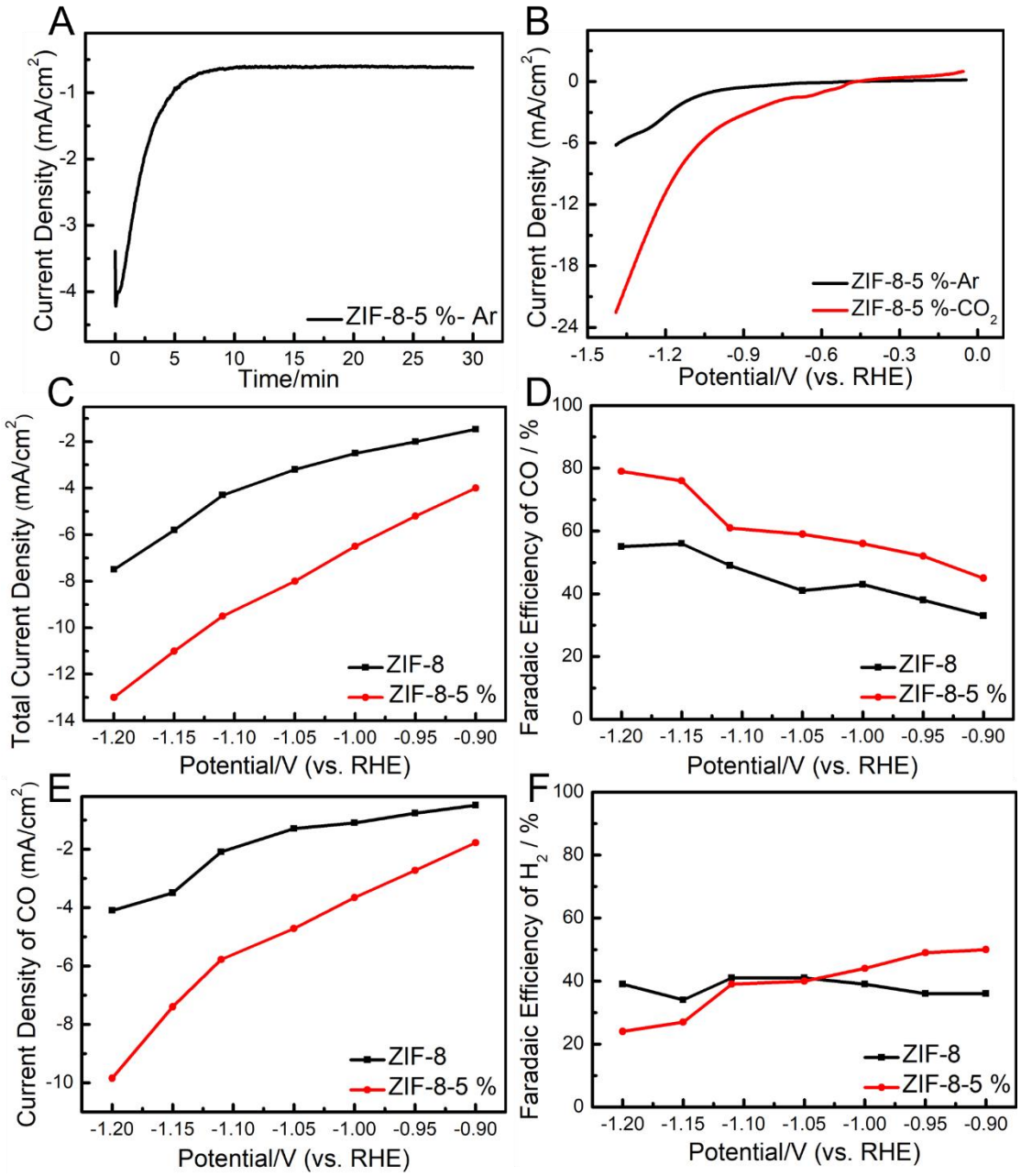

Figure 2.9 (A) Electrode current recorded during reduction of ZIF-8-5 % at −0.90 V vs. RHE in 0.5 M $NaHCO_3$ purged with Ar gas; (B) LSV curves of ZIF-8-5 % in N_2- and CO_2-saturated 0.5 M $NaHCO_3$ solution. (C) Total current densities for the different samples coated on carbon paper in CO_2-saturated 0.5 M $NaHCO_3$ solution at different applied potentials. (D) Corresponding FE for CO. (E) Partial current densities of CO. (F) Corresponding FE for H_2.

The electrocatalytic activity of ZIF-8 and ZIF-8-5 % coated on carbon paper with the same mass loading of 5 mg cm^{-2} are studied in Ar or CO_2-saturated 0.5 M $NaHCO_3$ solution as electrolyte using a three-electrode H-cell separated by an anion exchange membrane. During the CO_2 RR, the cathodic compartment was continuously purged

with CO_2 (20 ml min^{-1}). The periodic quantification of the gas-phase products was obtained by gas chromatography (GC). Online GC results showed that CO and H_2 were the main products obtained for all the catalysts, while the corresponding liquid products were detected by ^{1}H-NMR after the electrochemical CO_2 reduction processes.

Before the CO_2 RR electrochemical tests, the prepared electrodes were pretreated at a constant potential of −0.90 V vs. RHE for 30 min until a stable current reached (**Figure 2.9A**). To roughly evaluate the electroreduction ability of ZIF-8-5 % sample, linear sweep voltammetry (LSV) curves under Ar- and CO_2-saturated atmosphere were performed (**Figure 2.9B**). Under CO_2 purging, an enhanced current density could be observed on ZIF-8-5 %, which was higher than that observed in an Ar-saturated solution, delivering a higher activity toward CO_2 RR. **Figure 2.9C** shows the total current density plotted against the applied potential of different samples. The current density of the ZIF-8-5 % sample increases to −13 mA cm^{-2} as the applied potential shifted negatively, however, a lower current density is observed at all applied potentials in the case of ZIF-8 sample. The high current density achieved by ZIF-8-5 % in comparison to the pristine ZIF-8 structure could be attributed to the increased active-site density caused by DOBDC surface modification.[47, 49] As shown in **Figure 2.9D**, the parent ZIF-8 exhibits lower FE(CO) values similar to previous reports.[8] However, the FE(CO) for the ZIF-8-5 % sample at each applied potential is higher than that of the ZIF-8, with a highest FE(CO) of 79 % at −1.20 V vs. RHE. In addition, according to **Figure 2.9E**, the corresponding partial current densities of CO obtained on the ZIF-8-5 % sample at all applied potentials are higher than those of the ZIF-8, which reveals its higher reaction rate during CO_2 RR.[6] The FE(H_2) obtained on both samples are shown in **Figure 2.9F**.

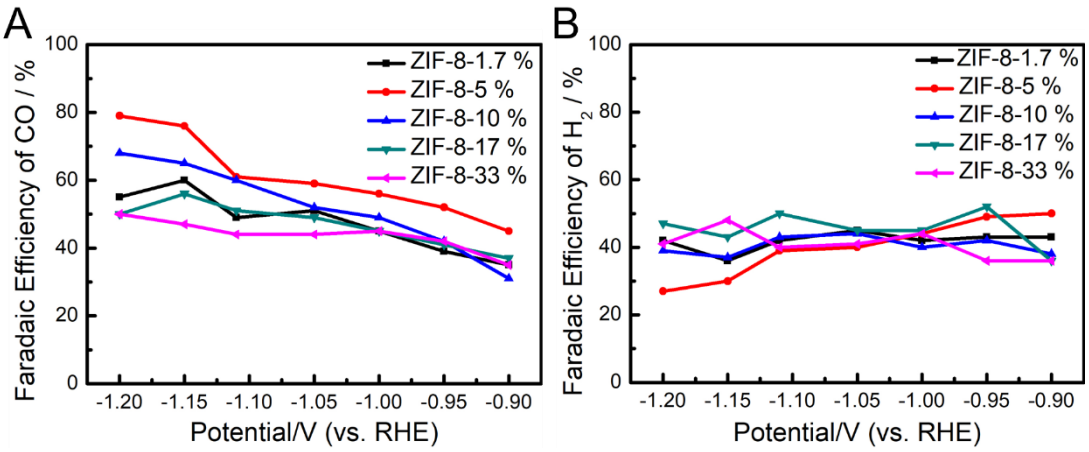

Figure 2.10 Corresponding FE of (A) CO and (B) H_2 on ZIF-8-x samples with different modifying ratio.

The FE for CO and H_2 on different ZIF-8-x samples are shown in **Figure 2.10** for comparison. Apparently, the other samples show lower FE(CO) than that of ZIF-8-5 %. Such a decreased selectivity was attributed to the introduction concentration of DOBDC. The FE (CO and H_2) values of ZIF-8-1.7 % at applied potentials were similar to that of ZIF-8, although this sample shows an increased surface area compared to ZIF-8. In order to reveal this phenomenon, we also digested the ZIF-8-1.7 % and analysed the resulting solutions by ^{1}H-NMR. There is no signal from the functional group of DOBDC observed in ZIF-8-1.7 % sample. Therefore, its FE(CO) is limited by a deficient DOBDC content, leading to an etching process that only occurred on the ZIF-8-1.7 % surface, while there is a negligible Zn-DOBDC coordination formation because of deficient DOBDC content. However, for ratios above 17 %, the significantly decrease in their catalytic activities is due to the formed new crystalline species that tend to cover up the active sites and even further change the active sites of catalysts, as found in our SEM and XRD results.

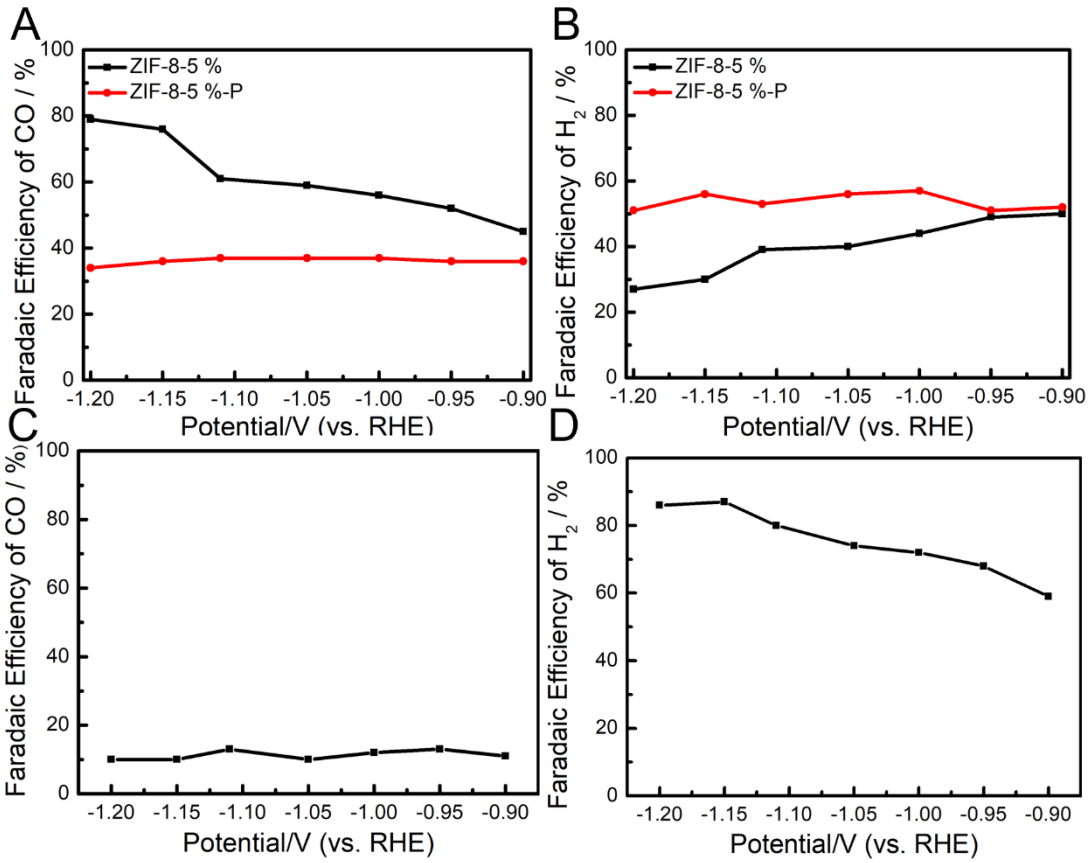

Figure 2.11 FE of (A) CO and (B) H_2 on ZIF-8-5 % and ZIF-8-5 %-P electrodes. (C) Corresponding FE for CO and (D) FE for H_2 for Zn-MOF-74.

In order to understand the role of the chemical modification, we further compared the FE(CO) of a ZIF-8-5 % sample prepared by physical mixture (ZIF-8-5 %-P) with the ZIF-8-5 % fabricated by our chemical linker modification route. As observed in **Figure 2.11A**, the ZIF-8-5 %-P shows a poorer CO selectivity, lower than 40 % FE(CO) at all applied potentials. As we can see, the increase of catalytic activity comes from the second organic ligand modification instead of formation of new tiny crystals of Zn-MOF-74 crystallized from the rests of DOBDC on the surface of our ZIF-8 crystals, pure Zn-MOF-74 sample was prepared by using DOBDC and Zn^{2+}. Then we used this Zn-MOF-74 for CO_2 RR and found that it exhibits a poor performance for generating CO (below 20 %) at each applied potential (**Figures 2.11C** and **D**). Therefore, the inert catalytic ability of Zn-MOF-74 further proved that the increase of FE(CO) on our champion sample ZIF-8-5 % comes from the second organic ligand modification. All these results suggest that the incorporation of a second ligand to form surface

functionalized ZIF-8 through the chemical synthesis route proposed here, gives an improved catalytic performance towards CO_2 RR.

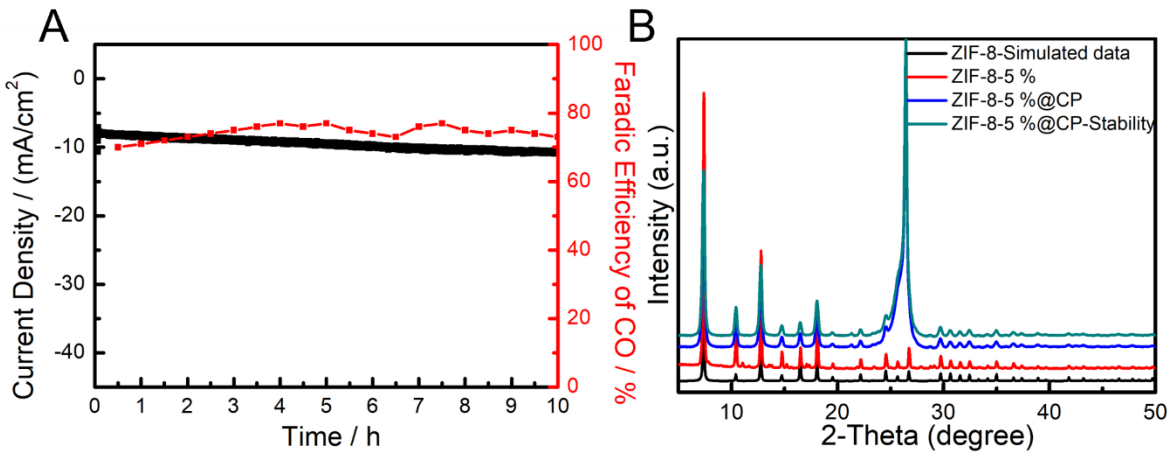

Figure 3.12. (A) Current density vs. time (I-t) curve for ZIF-8-5 % modified carbon paper at −1.2 V vs. RHE and (B) XRD pattern of ZIF-8-5 % coated on the carbon paper before and after the stability test.

The operating stability of a catalyst is a significant parameter for its practical applications. In this way, as displayed in **Figure 2.12A**, the I-t curve for ZIF-8-5 % was obtained, showing a negligible decay of the current density (from −9.7 to −10 mA cm^{-2}) and the FE(CO) (from 79 to 73 %) during continuous electrolysis under a CO_2-sturated solution at −1.2 V vs. RHE for 10 h, indicating a good long-term stability of the prepared ZIF-8-5 %. The good stability of the electrode was further confirmed by XRD before and after the I-t test (**Figure 2.12B**), no appreciable difference in the crystal structure was observed after 10 h stability test in 0.5 M $NaHCO_3$, proving that the main structure of ZIF-8-5 % was retained. These results show that ZIF-8-5 % possesses a good stability. Meanwhile, ^{1}H-NMR analyses were used to detect the presence of any liquid sub-products after the stability measurement, revealing there is no liquid sub-product produced during the CO_2 RR process (**Figure 2.13A**). Finally, a control experiment was performed verifying that the obtained CO came from the reduction of CO_2 on ZIF-8-5 %, instead of ligand decomposition, as shown in **Figure 2.13B**.

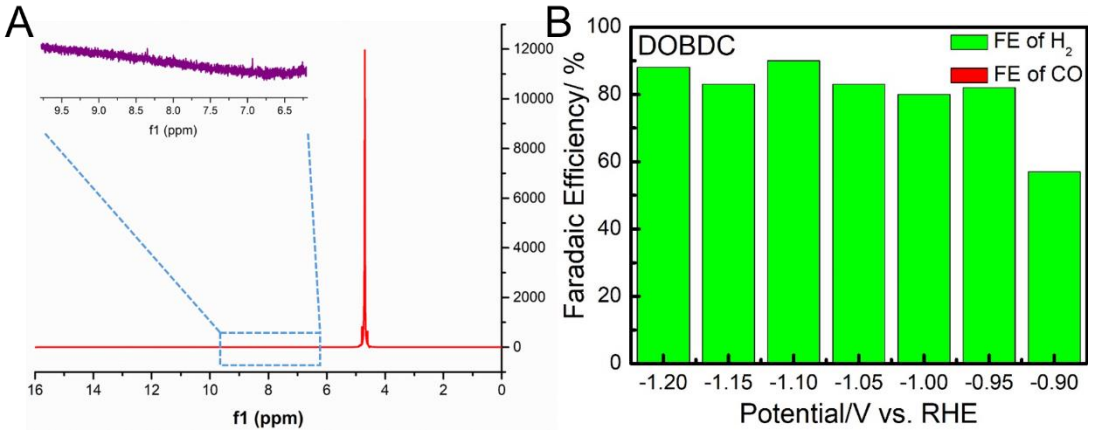

Figure 2.13 The representative NMR spectra of the electrolyte after electrolysis of −1.2 V for ZIF-8-5 % in CO_2-saturated 0.5 M $NaHCO_3$ electrolyte for 10 h. (B) FE of CO and H_2 on DOBDC ligand.

2.3.3 DFT Calculation

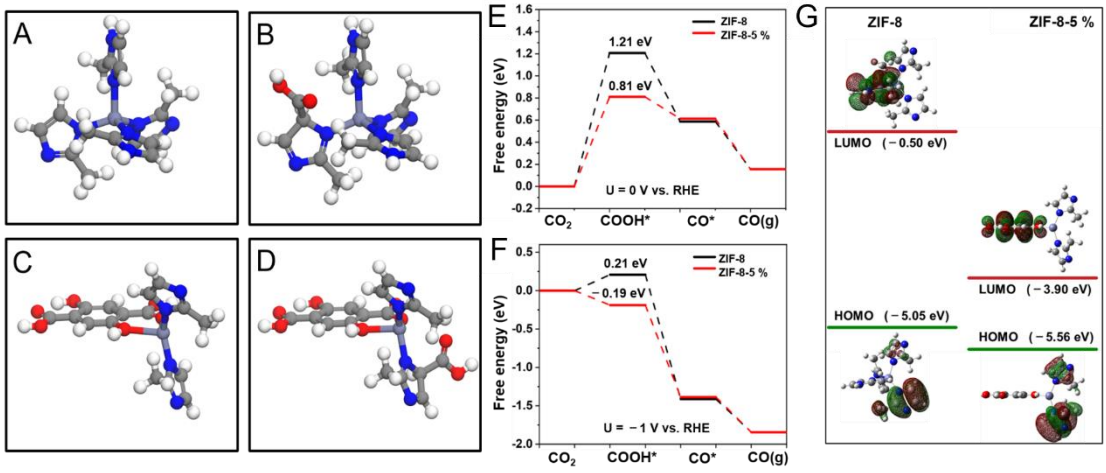

Figure 2.14 The clean surface and optimized adsorption configuration on (A, B) ZIF-8 and (C, D) ZIF-8-5 % surface model (Zn, C, N, O atoms are represented in purple, grey, blue, and red, respectively). (E, F) Free energy profiles for CO_2 RR over ZIF-8 and ZIF-8-5 % at 0 V and −1 V vs. RHE; (G) The HOMO and LUMO energy level of ZIF-8 and ZIF-8-5 % models (Zn, C, N, O atoms are represented in purple, grey, blue, and red, respectively).

DFT calculations are performed to further reveal the origin of the excellent activity upon dopant decoration. The catalyst models of ZIF-8 and ZIF-8-5 % used in the simulations are shown in **Figures 2.14A-D**. The Gibbs free energy profiles of CO_2 reduction to CO at 0 V and −1.0 V vs. RHE are shown in **Figures 2.14E** and **F**, CO_2 activation to form COOH* is endergonic at 0 V vs. RHE on the two catalysts studied, whilst the following steps of CO formation and desorption are exergonic. Therefore, one can see that the first step of COOH* formation is potential-limiting in the

electrocatalytic reduction of CO_2. In addition, the reaction Gibbs energy of COOH* formation on ZIF-8 is 0.4 eV more positive than that on ZIF-8-5 % at both 0 V and −1.0 V vs. RHE, strongly suggesting that ZIF-8-5 % is much more active than ZIF-8 towards electrocatalytic reduction of CO_2 to CO, which is in good agreement with the experimental results reported in the current work.

Further molecular orbital (MO) analysis were performed to elucidate the origin of distinct behaviors of ZIF-8 and ZIF-8-5 % for the formation of COOH*. The HOMO and LUMO energy level of ZIF-8 and ZIF-8-5 % are shown in **Figure 2.14G**. Interestingly, ZIF-8 and ZIF-8-5% exhibit a similar value of HOMO energy. In contrast, ZIF-8-5 % shows a much lower LUMO energy (−3.90 eV) than that of ZIF-8 (−0.50 eV), and thus, forming a narrower HOMO-LUMO energy gap, which is beneficial for charge transfer, making electrocatalytic CO_2 RR more efficient.[50]

2.4 Summary

In summary, we systematically explored the surface modification strategy of ZIF-8 with the DOBDC and found that it indeed influences the activity and selectivity towards CO production. In the case of the optimized ZIF-8-5 % sample, an increase of selectivity towards the CO_2 RR is observed. The product selectivity to CO raised to 79 %, which is higher than that of the pristine ZIF-8 (56 %). In addition, ZIF-8-5 % also exhibited an enhanced CO partial current density of −10 mA cm^{-2} at −1.20 V vs. RHE, leading to a boosted CO production rate. The DFT calculations suggest that DOBDC modification not only maintain the active sites of ZIF-8 but also promote the formation of COOH* during CO_2 RR in the newly synthesized ZIF-8-5 %. The promoted activity and performance of ZIF-8-5 % can be attributed to a decrease of the energy gap between the HOMO and LUMO. These results offer an efficient strategy to synthesize improved MOF-based materials towards CO_2 electroreduction by surface modification.

References

[1] Y.J. Sa, C.W. Lee, S.Y. Lee, J. Na, U. Lee, Y.J. Hwang, Chem. Soc. Rev., 49 (2020) 6632-6665.
[2] W. Shan, R. Liu, H. Zhao, Z. He, Y. Lai, S. Li, G. He, J. Liu, ACS Nano, 14 (2020) 11363-11372.
[3] A. Ozden, Y. Wang, F. Li, M. Luo, J. Sisler, A. Thevenon, A. Rosas-Hernández, T. Burdyny, Y. Lum, H. Yadegari, T. Agapie, J.C. Peters, E.H. Sargent, D. Sinton, Joule, (2021).
[4] D.M. Koshy, S. Chen, D.U. Lee, M.B. Stevens, A.M. Abdellah, S.M. Dull, G. Chen, D. Nordlund, A. Gallo, C. Hahn, D.C. Higgins, Z. Bao, T.F. Jaramillo, Angew. Chem. Int. Ed., 59 (2020) 4043-4050.
[5] Q. He, D. Liu, J.H. Lee, Y. Liu, Z. Xie, S. Hwang, S. Kattel, L. Song, J.G. Chen, Angew. Chem. Int. Ed., 59 (2020) 3033-3037.
[6] O.S. Bushuyev, P. De Luna, C.T. Dinh, L. Tao, G. Saur, J. van de Lagemaat, S.O. Kelley, E.H. Sargent, Joule, 2 (2018) 825-832.
[7] W. Geng, W. Chen, G. Li, X. Dong, Y. Song, W. Wei, Y. Sun, ChemSusChem, 13 (2020) 4035-4040.
[8] Y. Wang, P. Hou, Z. Wang, P. Kang, ChemPhysChem, 18 (2017) 3142-3147.
[9] X. Jiang, H. Li, J. Xiao, D. Gao, R. Si, F. Yang, Y. Li, G. Wang, X. Bao, Nano Energy, 52 (2018) 345-350.
[10] S. Dou, J. Song, S. Xi, Y. Du, J. Wang, Z.-F. Huang, Z.J. Xu, X. Wang, Angew. Chem. Int. Ed., 58 (2019) 4041-4045.
[11] S. Dou, X. Li, X. Wang, ACS Mater. Lett., 2 (2020) 1251-1267.
[12] D.-H. Nam, P. De Luna, A. Rosas-Hernández, A. Thevenon, F. Li, T. Agapie, J.C. Peters, O. Shekhah, M. Eddaoudi, E.H. Sargent, Nature Mater., 19 (2020) 266-276.
[13] C.S. Diercks, Y. Liu, K.E. Cordova, O.M. Yaghi, Nature Mater., 17 (2018) 301-307.
[14] W. Ni, Y. Xue, X. Zang, C. Li, H. Wang, Z. Yang, Y.-M. Yan, ACS Nano, 14 (2020) 2014-2023.
[15] P. Chen, Y. Tong, C. Wu, Y. Xie, Acc. Chem. Res., 51 (2018) 2857-2866.
[16] L. Cao, C. Wang, ACS Central Sci., 6 (2020) 2149-2158.
[17] L. Jiao, J. Wang, H.-L. Jiang, Acc. Mater. Res., (2021).
[18] H. Cheng, S. Liu, J. Zhang, T. Zhou, N. Zhang, X.-s. Zheng, W. Chu, Z. Hu, C. Wu, Y. Xie, Nano Lett., 20 (2020) 6097-6103.
[19] X. Song, Z. Ou, X. Hu, X. Zhang, M. Lin, L. Wen, M. Li, ACS Mater. Lett., 3 (2021) 171-178.
[20] M. Hu, Y. Ju, K. Liang, T. Suma, J. Cui, F. Caruso, Adv. Funct. Mater., 26 (2016) 5827-5834.
[21] Y. Liu, Z. Liu, N. Lu, E. Preiss, S. Poyraz, M.J. Kim, X. Zhang, Chem. Commun., 48 (2012) 2621-2623.
[22] H. Wang, W. Zhu, Y. Ping, C. Wang, N. Gao, X. Yin, C. Gu, D. Ding, C.J. Brinker, G. Li, ACS Appl. Mater. Interfaces, 9 (2017) 14258-14264.
[23] X. Wang, H. Xiao, A. Li, Z. Li, S. Liu, Q. Zhang, Y. Gong, L. Zheng, Y. Zhu, C. Chen, D. Wang, Q. Peng, L. Gu, X. Han, J. Li, Y. Li, J. Am. Chem. Soc., 140 (2018) 15336-15341.
[24] H.Q. Wu, L. Huang, J.Q. Li, A.M. Zheng, Y. Tao, L.X. Yang, W.H. Yin, F. Luo, Inorg. Chem., 57 (2018) 12444-12447.
[25] T. Zhang, J. Du, P. Xi, C. Xu, ACS Appl. Mater. Interfaces, 9 (2017) 362-370.
[26] J. Yin, Q. Fan, Y. Li, F. Cheng, P. Zhou, P. Xi, S. Sun, J. Am. Chem. Soc., 138 (2016) 14546-14549.
[27] T. Zheng, K. Jiang, N. Ta, Y. Hu, J. Zeng, J. Liu, H. Wang, Joule, 3 (2019) 265-278.

[28] J. Hafner, J. Comput. Chem., 29 (2008) 2044.
[29] P.E. Blöchl, Phys. Rev. B, 50 (1994) 17953-17979.
[30] G. Kresse, J. Furthmüller, Phys. Rev. B, 54 (1996) 11169-11186.
[31] G. Kresse, J. Furthmüller, Comput. Mater. Sci., 6 (1996) 15-50.
[32] G. Kresse, D. Joubert, Phys. Rev. B, 59 (1999) 1758-1775.
[33] J.P. Perdew, K. Burke, M. Ernzerhof, Phys. Rev. Lett., 77 (1996) 3865-3868.
[34] J.P. Perdew, K. Burke, M. Ernzerhof, Phys. Rev. Lett., 78 (1997) 1396-1396.
[35] G. Stefan, J. chem. phys., 15 (2010).
[36] G. Stefan, J. comput. chem., 7 (2011).
[37] G.W.T. M. J. Frisch, H. B. Schlegel, G. E. Scuseria, M. A. Robb, J. R. Cheeseman, G. Scalmani, V. Barone, B. Mennucci, G. A. Petersson, H. Nakatsuji, M. Caricato, X. Li, H. P. Hratchian, A. F. Izmaylov, J. Bloino, G. Zheng, J. L. Sonnenberg, M. Hada, M. Ehara, K. Toyota, R. Fukuda, J. asegawa, M. Ishida, T. Nakajima, Y. Honda, O. Kitao, H. Nakai, T. Vreven, J. A. Montgomery, Jr., J. E. Peralta, F. Ogliaro, M. Bearpark, J. J. Heyd, E. Brothers, K. N. Kudin, V. N. Staroverov, T. Keith, R. Kobayashi, J. Normand, K. Raghavachari, A. Rendell, J. C. Burant, S. S. Iyengar, J. Tomasi, M. Cossi, N. Rega, J. M. Millam, M. Klene, J. E. Knox, J. B. Cross, V. Bakken, C. Adamo, J. Jaramillo, R. Gomperts, R. E. Stratmann, O. Yazyev, A. J. Austin, R. Cammi, C. Pomelli, J. W. Ochterski, R. L. Martin, K. Morokuma, V. G. Zakrzewski, G. A. Voth, P. Salvador, J. J. Dannenberg, S. Dapprich, A. D. Daniels, O. Farkas, J. B. Foresman, J. V. Ortiz, J. Cioslowski, and D. J. Fox, (2013).
[38] N. Godbout, D.R. Salahub, J. Andzelm, E. Wimmer, Canadian J. Chem., 70 (1992) 560-571.
[39] J.K. Nørskov, J. Rossmeisl, A. Logadottir, L. Lindqvist, J.R. Kitchin, T. Bligaard, H. Jónsson, J. Phys. Chem. B, 108 (2004) 17886-17892.
[40] A.A. Peterson, F. Abild-Pedersen, F. Studt, J. Rossmeisl, J.K. Nørskov, Energy Environ. Sci., 3 (2010) 1311-1315.
[41] K. Liu, J. Wang, M. Shi, J. Yan, Q. Jiang, Adv. Energy Mater., 9 (2019) 1900276.
[42] Z. Liu, Z. Zhao, Y. Wang, S. Dou, D. Yan, D. Liu, Z. Xia, S. Wang, Adv. Mater., 29 (2017) 1606207.
[43] C. Wang, Q. Lai, P. Xu, D. Zheng, X. Li, H. Zhang, Advanced Materials, 29 (2017) 1605815.
[44] C. Chen, H. Huang, Y. Yu, J. Shi, C. He, R. Albilali, H. Pan, Chem. Engineering J., 353 (2018) 584-594.
[45] L. Qi, X. Tang, Z. Wang, X. Peng, Int. J. Mining Sci. Technology, 27 (2017) 371-377.
[46] J.K. Zaręba, M. Nyk, M. Samoć, Crystal Growth Design, 16 (2016) 6419-6425.
[47] C.-W. Kung, C.O. Audu, A.W. Peters, H. Noh, O.K. Farha, J.T. Hupp, ACS Energy Lett., 2 (2017) 2394-2401.
[48] S. Tanaka, K. Fujita, Y. Miyake, M. Miyamoto, Y. Hasegawa, T. Makino, S. Van der Perre, J. Cousin Saint Remi, T. Van Assche, G.V. Baron, J.F.M. Denayer, J. Phys. Chem. C, 119 (2015) 28430-28439.
[49] N. Kornienko, Y. Zhao, C.S. Kley, C. Zhu, D. Kim, S. Lin, C.J. Chang, O.M. Yaghi, P. Yang, J. Am. Chem. Soc., 137 (2015) 14129-14135.
[50] Y. Zhang, J. Liu, Z. Wei, Q. Liu, C. Wang, J. Ma, J. Energy Chem., 33 (2019) 22-30.

Chapter 3

Engineering the FeN_4 Sites of Fe-N-C Catalysts via Bonded Oxygen for High-Efficient Electroreduction of Carbon Dioxide

3.1 Introduction

Environmental problems caused by excessive emissions of carbon dioxide (CO_2) triggered the development of electrochemical CO_2 reduction reaction (CO_2 RR), which has been considered as a potential route to reduce the CO_2 concentration in atmosphere.[1, 2] Among all reduction products, carbon oxide (CO) is one of the most appealing candidates in CO_2 RR, because CO can be used as the feedstock to prepare high-value fuels via the downstream Fischer-Tropsch process.[3, 4] Meanwhile, producing CO is more achievable as it only requires a simple two-electron/proton transfer pathway during CO_2 RR process ($CO_2 + 2H^+ + 2e^- \rightarrow CO + H_2O$).[5, 6] Hence, numerous efforts have been devoted to the study of the CO_2 to CO electroreduction process.[7, 8]

In the past few decades, the electrocatalysts for the CO_2-to-CO conversion have been categorized into two types: 1) metal-based catalysts with strong COOH* binding but weak CO* binding [9] (typical examples are Au[10] and Ag[11]); 2) molecular catalysts with a well-defined metal coordination, including transition-metal phthalocyanines and porphyrins.[12-15] However, their high price, inadequate stability and the scarce conductivity associated to these catalysts hinder them from practical applications.[16] At this point, as promising alternatives, transition metal-nitrogen-carbon (M-N-C) materials with atomically dispersed metal cations (such as, Fe, Ni and Co) come into being due to their low-cost, earth abundancy, stability, good conductivity, and theoretical high activity and selectivity.[17-19] Previous works have revealed that the distinct activity and selectivity of M-N-C materials are highly influenced by the kind of the transition metal in the MN_x moieties.[20] On one side, FeN_x and CoN_x are excellent CO_2 RR catalysts because they can produce CO at a low applied potential. On the other side, FeN_x and NiN_x have generally shown a high selectivity because of their Faradaic efficiency (FE) for CO >80 %.[21]

Considering both activity and selectivity, FeN_x has been regarded as the most promising M-N-C based catalyst. Nevertheless, the activity and selectivity of FeN_x catalysts are still lagging far behind the noble-metal benchmarks. In light of this, improvement of the FeN_x catalysts is drawing increasing attention to obtain activity and selectivity closer to the noble-metal based electrocatalysts.

It is well established that the activity of catalysts could be affected by the oxygen-containing subgroups presented on the active sites based on previous experimental and theoretical investigations.[20, 22-24] Such kind of materials are initially developed to boost the catalysis of the oxygen reduction reaction (ORR).[22] Inspired by this, oxygen containing species are used as strong hydrogen-bonding donors in photocatalytic CO_2 RR to stabilize the initial Co-CO_2 adduct. Meanwhile, the μ-OH^- acts as the local proton source to facilitate the C-O bond breaking.[23] Moreover, the oxygen-containing groups can also improve the catalytic performance of metal-free catalysts as the main active components towards electrochemical CO_2 RR.[25] Therefore, rationally engineering the coordination environment via oxygen-containing subgroups is considered as a promising method to prepare FeN_x based catalysts for a high-efficient electroreduction of CO_2.

Until now, most materials with FeN_x sites have been mainly prepared via pyrolyzing mixtures of iron salts, nitrogen-containing species and high-surface-area carbon precursors. The regulation of oxygen-containing subgroup structure and coordinated environment is still highly challenging via such method.[26, 27] To tackle these challenges, in this work, we have developed a facile IRMOF-3-assisted strategy to generate a highly dispersed Fe-N-C based structure (denoted as D-Fe-N-C) with the introduced axial bonded -OH subgroups, obtaining high-efficient CO_2 RR to produce CO. The Zn-based IRMOF-3, assembled from Zn^{2+} nodes and 2-aminoterephthalic acid ligands, caters for the fabrication requirements, not only allowing the stabilization of foreign Fe ions as a self-sacrificial platform, but also providing nitrogen/oxygen-rich sources from

organic ligands, replacing simple N-containing precursors. On one hand, the oxygen-rich ligands are beneficial to form Fe-O coordinated bonds during the thermal pyrolysis to form the HO-FeN_4 active sites. On the other hand, such oxygen-rich organic ligands could facilitate the formation of D-Fe-N-C materials with large pore sizes, which are favorable for the CO_2 RR.[28] As a result, after a thermal pyrolysis, we successfully obtain the D-Fe-N-C catalyst with a complete integration of the single active HO-FeN_4 moieties and a modicum of Fe nanoparticles, according to transmission electron microscopy (TEM) and X-ray absorption spectroscopy (XAS) results. Benefiting from the above advantages, D-Fe-N-C catalysts show a remarkable CO_2 RR activity in 0.5 M $NaHCO_3$ solution, accompanied by an excellent selectivity with Faradaic efficiency of CO (95 %) at −0.50 V vs. RHE, as well as a robust stability, which are superior to those of the previously reported Fe-N-C-based materials derived from MOFs. Moreover, the selectivity could be retained over 80 % in a range of working potentials from −0.40 to −0.60 V vs. RHE. Density functional theory (DFT) calculations revealed that the axial -OH coordination on the FeN_4 sites not only facilitates product desorption during the CO_2 RR process, but also limits undesired HER, leading to a higher activity towards CO_2 RR. Furthermore, we demonstrate the generalization of the synthesis process by obtaining highly disperse Co-N-C (D-Co-N-C) and Ni-N-C (D-Ni-N-C) catalysts via the same IRMOF-3 assisted-method. Both D-Co-N-C and D-Ni-N-C show good CO_2 RR activity as well. All these results not only demonstrate that the D-Fe-N-C with oxygen-containing subgroups is a promising electrocatalyst for CO_2 RR, but also probe a universal success of the nitrogen and oxygen-rich IRMOF-3-assistant synthetic strategy for the rational design and development of highly disperse M-N-C catalysts with a fundamental understanding of the higher active sites.

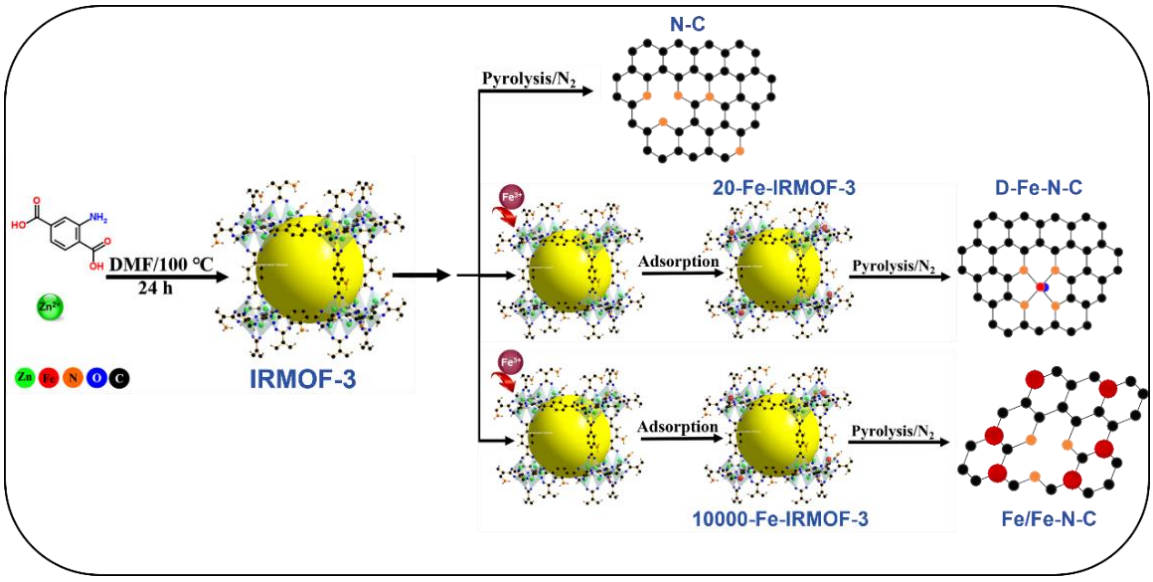

Figure 3.1 Schematic illustration of the formation of different samples.

The synthesis steps for N-C, D-Fe-N-C and Fe/Fe-N-C are schematically displayed in **Figure 3.1**, the detailed synthesis procedures are included in the supporting information. By precisely controlling the fabrication process, such as the content of Fe, different obtained samples are labelled as IRMOF-3, 20-Fe-IRMOF-3 and 10000-Fe-IRMOF-3, respectively. These three representative samples have been subjected to pyrolysis treatments; the obtained samples after pyrolysis are labelled as N-C, D-Fe-N-C and Fe/Fe-N-C, respectively. The detailed synthesis procedures are included in the following Section.

3.2 Experimental Section

3.2.1 Materials and Characterizations

3.2.1.1 Materials

If not specified, all chemical reagents were purchased from Sigma-Aldrich. Zinc nitrate hexahydrate ($Zn(NO_3)_2 \cdot 6H_2O$), 2-Aminoterphthalic acid, iron chloride hexahydrate ($FeCl_3 \cdot 6H_2O$), 2-methylimidazole (2-mim), sodium thiocyanate (NaSCN), cobaltous nitrate hexahydrate ($Co(NO_3)_2 \cdot 6H_2O$), nickel chloride hexahydrate

($NiCl_2 \cdot 6H_2O$), N,N-dimethylformamide (DMF), ethanol and sodium bicarbonate ($NaHCO_3$) were all of analytical grade and used as received without further purification. Meanwhile, all solutions were prepared with Milli-Q water (DI-H_2O, Ricca Chemical, ASTM Type I). The Nafion (N-117 membrane, 0.18 mm thick) was purchased from Alfa Aesar and kept in 0.5 M NaOH solution. The carbon paper was also purchased from Alfa Aesar.

3.2.1.2 Characterizations

The X-ray diffraction patterns (XRD) were obtained through a Bruker D4 X-ray powder diffractometer using Cu Kα radiation (1.54184 Å). Field emission scanning electron microscopy (FESEM) images were collected on a FEI Magellan 400 L scanning electron microscope. The transmission electron microscopy (TEM) and high angle annular dark field scanning TEM (HAADF-STEM) images were obtained in a Tecnai F20 field emission gun microscope with a 0.19 nm point-to-point resolution at 200 kV equipped with an embedded Quantum Gatan Image Filter for EELS analyses. Images have been analyzed by means of Gatan Digital Micrograph software. Parts of HAADF-STEM images and elemental mapping were obtained in a spherical aberration-corrected transmission electron microscope FEI Titan G2 80-200 Chemi-STEM with four EDX detectors and operated at 200 kV. X-ray photoelectron spectroscopy (XPS) was performed on a Phoibos 150 analyser (SPECS GmbH, Berlin, Germany) in ultra-high vacuum conditions (base pressure 4×10^{-10} mbar) with a monochromatic aluminum Kα X-ray source (1486.74 eV). Binding energies (BE) were determined using the C 1s peak at 284.5 eV as a charge reference. Inductively coupled plasma-mass spectrometry (ICP-MS) measurements were carried out to determine the concentration of Fe. Brunauer-Emmett-Teller (BET) surface areas were measured using nitrogen adsorption at 77 K. For BET measurement, samples were outgassed at 473 K during 12 h. Raman spectra were obtained using Senterra. Fourier transformed infrared (FTIR) spectroscopy data were recorded on an Alpha Bruker spectrometer. Thermogravimetric Analysis were measured by Pyris 1 TGA, Perkin Elmer.

3.2.1.3 XAFS Measurements

The X-ray absorption find structure spectra (Fe K-edge) were collected at 1W1B station in Beijing Synchrotron Radiation Facility (BSRF). The storage rings of BSRF were operated at 2.5 GeV with an average current of 250 mA. Using Si (111) double-crystal monochromator, the data collection was carried out in transmission/fluorescence mode using ionization chamber. All spectra were collected in ambient conditions.

3.2.1.4 XAFS Analysis and Results

The acquired EXAFS data were processed according to the standard procedures using the ATHENA module implemented in the IFEFFIT software packages. The k^3-weighted EXAFS spectra were obtained by subtracting the post-edge background from the overall absorption and then normalizing with respect to the edge-jump step. Subsequently, k^3-weighted $\chi(k)$ data of Fe K-edge were Fourier transformed to real (R) space using a hanning windows (dk=1.0 $Å^{-1}$) to separate the EXAFS contributions from different coordination shells. To obtain the quantitative structural parameters around central atoms, least-squares curve parameter fitting was performed using the ARTEMIS module of IFEFFIT software packages.[29-31]

3.2.2 Synthesis Methods

3.2.2.1 Preparation of IRMOF-3

The fabrication process of IRMOF-3 is according to previous report with minor modification.[32] Typically, 932 mg $Zn(NO_3)_2 \cdot 6H_2O$ was dissolved in 100 ml DMF under magnetic stirring at room temperature to form a homogeneous solution. Then, 181 mg 2-aminoterphthalic acid were added into the above mixture under ultrasonic until the formation of clear solution. The obtained homogeneous solution was transferred into the Teflon-lined stainless-steel autoclave and reacted at 100 ºC for 24 h. After cooling to room temperature, the powder was collected by centrifugation, washed with ethanol and DMF several times to remove organic residual. The final products were then dried in vacuum at 65 ºC for 4 h.

3.2.2.2 Preparation of ZIF-8

The fabrication of ZIF-8 is similar to the published report in [33]. Typically, 1.115 g $Zn(NO_3)_2 \cdot 6H_2O$ was dissolved in 50 ml methanol under magnetic stirring at room temperature to form a homogeneous solution. Then, 50 ml methanolic solution containing 1.232 g 2-mim were added into the above mixture under ultrasonic until the formation of clear solution. The obtained homogeneous solution reacted at room temperature for 24 h without stirring. Then, the white powder was collected by centrifugation, washed with methanol several times to remove organic residual. The final products were then dried in vacuum at 60 ºC for overnight.

3.2.2.3 Preparation of 20-Fe-IRMOF-3, 10000-Fe-IRMOF-3, 20-Co-IRMOF-3, 20-Ni-IRMOF-3 and 20-Fe-ZIF-8

In this procedure, 100 mg IRMOF-3 powder was dispersed in 10 ml DMF under ultrasound for 10 min at room temperature. After forming a homogeneous solution, $FeCl_3 \cdot 6H_2O$ aqueous solution (10 mg/ml, 20 μL) was dropwise injected into the above solution under ultrasound for 5 min at room temperature. Next, the mixed solution was under magnetic stirring at room temperature for 3 h. After reacting, the powder was collected by centrifugation, washed with ethanol and DMF several times to remove organic residual and dried in vacuum at 65 ℃ for 6 h. Then, we obtained the 20-Fe-IRMOF-3. Similarly, the 10000-Fe-IRMOF-3 with higher Fe content were harvested by adding 10 ml $FeCl_3 \cdot 6H_2O$ aqueous solution (10 mg/ml). For 20-Co-IRMOF-3 and 20-Ni-IRMOF-3, similar procedures with adding 20 μL $Co(NO_3)_2 \cdot 6H_2O$ (10 mg/ml) or $NiCl_2 \cdot 6H_2O$ (10 mg/ml) were employed. 20-Fe-ZIF-8 was prepared by replacing IRMOF-3 with ZIF-8.

3.2.2.4 Preparation of Disperse Fe-N-C (denoted as D-Fe-N-C and Z-Fe-N-C)

As-prepared 20-Fe-IRMOF-3 (or IRMOF-3, 20-Co-IRMOF-3 or 20-Ni-IRMOF-3 or 10000-Fe-IRMOF-3) powders were put at the porcelain boat. Subsequently, the samples were placed in a tube furnace and heated at 950 °C for 2 h with heating rate of 5 °C/min under an Ar atmosphere to yield disperse D-Fe-N-C (N-C, D-Co-N-C, D-Ni-N-C and Fe/Fe-N-C). Meanwhile, the D-Fe-N-C-850 and D-Fe-N-C-1050 were

obtained by changing the temperature to 850 °C or 1050 °C, respectively. For Z-Fe-N-C, a similar procedure was used by replacing 20-Fe-IRMOF-3 with 20-Fe-ZIF-8.

3.2.3 Ink Preparation

2 mg synthesized different samples and 50 μl 5 wt% Nafion solutions were dissolved in ethanol (1 ml) and ultrasonicated for 30 min to form evenly suspension for the further electrochemical experiments. To prepare the working electrode, 500 μL above as-prepared inks were dropped onto the two sides of the carbon paper electrode with 1×1 cm^2 and then dried at room temperature for a few minutes, giving a catalyst loading mass of ~1 mg/cm^2.

3.2.4 Electrochemical Measurement

The electrocatalytic performance of different catalysts was measured at room temperature by using a gas-tight H-cell with two-compartments separated by a cation exchange membrane (Nafion N-117 membrane) with a continuously Ar or CO_2 gas injection. Each compartment contained 70 ml electrolyte (0.5 M $NaHCO_3$ made from de-ionized water). In a typical experiment, a standard three electrode setup in 0.5 M $NaHCO_3$ solution was assembled: an Ag/AgCl electrode as reference electrode, a Pt wire as auxiliary electrode and a carbon paper coated with the different samples as working electrode (surface area = 1 cm^2). The potentials were measured versus Ag/AgCl and converted to the reversible hydrogen electrode (RHE) according to the following equation: $E_{RHE} = E^0_{Ag/AgCl} + E_{Ag/AgCl} + 0.059 \times pH$, pH=7.[34] All electrochemical results were showed without iR-compensation by using a computer-controlled BioLogic VMP3 electrochemical workstation. Meanwhile, the linear sweep voltammetry (LSV) was performed to reach a stable state at a scan rate of 20 mV/s from 0 V to −1.0 V vs. RHE in Ar-saturated 0.5 M $NaHCO_3$ (pH=8.5) and CO_2-saturated 0.5 M $NaHCO_3$ (pH=7) as supporting electrolyte. The cyclic voltammetry (CV) curves were performed at a scan rate of 20 mV/s. Moreover, electrochemical impedance spectroscopy (EIS) of different samples was carried out in a frequency range from 100 kHz to 100 mHz.

Before the electrochemical CO_2 reduction experiments, an average rate of 20 ml/min Ar was injected into the cathodic electrolyte in order to form an Ar-saturated solution. During electrochemical CO_2 reduction experiments, the CO_2 gas was delivered at an average rate of 20 ml/min at room temperature and ambient pressure, measured downstream by a volumetric digital flowmeter. The gas phase composition was analyzed by gas chromatography (GC) during potentiostatic measurements every 20 min. The calibration of peak area vs. gas concentration was used for the molar quantification of each gaseous effluent. The Faradaic efficiency was calculated by determining the number of coulombs needed for each product and then dividing by the total charge passed during the time of the GC sampling according to the flow rate. Liquid products were analyzed afterwards by quantitative ^{1}H-NMR using water as the deuterated solvent.

3.2.5 Calculation Method

Details concerning the calculation of mass activity, Faradaic Efficiency (FE) is shown below.[34-36]

The mass activity (A/g) is calculated from the mass loading density (m) of catalyst (1.0 mg cm^{-2}) and the measured partial current density j (mA/cm^2) at −0.50 V vs. RHE.

$$\text{mass activity} = j_{CO}/m$$

The partial current density for a given gas product was calculated as below:

$$j_i = x_i \times V \times \frac{n_i F P_0}{RT} \times (electrode\ area)^{-1}$$

Where x_i is the volume fraction of certain product determined by online GC referenced to calibration curves from three standard gas samples, v is the flow rate, n_i is the number of electrons involved, P_0= 101.3 kPa, F is the Faraday constant, and R is the gas constant. The corresponding FE at each potential is calculated by

$$FE = \frac{j_i}{j} \times 100\ \%$$

3.2.6 DFT Calculations

The spin-polarized DFT calculations with projector augmented wave (PAW) method [37-40] were performed using the Vienna Ab initio Simulation Package (VASP) code.[41] The Bayesian error estimation functional with van der Waals correlation (BEEF-vdW) was employed to set the plane wave basis.[42] The convergence criteria was 0.05 eV/ Å in force and 1×10^{-4} eV in energy and the plane wave cutoff was 500 eV. The Monkhorst–Pack mesh k-point grids was 2×2×1 for all models. All the vacuum thicknesses were higher than 15 Å. With the BEEF-vdW function, the energy of the gas phase molecules gave a systematic correction by +0.41 and +0.09 eV for gaseous CO_2 and H_2, respectively.[43-45] For the electroreduction of CO_2 to CO, the following elementary steps were considered:

$CO_2(g) + * + H^+(aq) + e^- \leftrightarrow COOH*$ (Equation 3.1)

$COOH* + H^+(aq) + e^- \leftrightarrow CO* + H_2O(l)$ (Equation 3.2)

$CO* \leftrightarrow CO(g) + *$ ((Equation 3.3)

where (g), (aq) represent the gaseous phase and aqueous phase, respectively. The *, COOH* and CO* represent free site, adsorption state of COOH and CO, respectively. The reaction free energies of each steps were calculated by following formula:

$$G = E_{\mathrm{DFT}} + E_{\mathrm{ZPE}} + \int C_p \mathrm{d}T - TS + E_{\mathrm{sol}} \quad \text{(Equation 3.4)}$$

Where E_{DFT} is the DFT calculated energy, E_{ZPE} is the zero-point energy, C_p is the constant pressure heat capacity, T is temperture, S is the entropy and E_{sol} is solvation correction and for CO* was stabilized by 0.1 eV and COOH* by 0.25 eV.[46] The temperature of the reaction is 298.15 K. The free energy corrections for each species are shown in **Table 3.1**.[47]

Table 3.1 Parameters used for the free energy corrections. T = 298.15 K.

Species	ZPE (eV)	$\int C_p \, dT$ (eV)	$-TS$ (eV)
H_2	0.28	0.09	-0.40
CO_2	0.31	0.11	-0.66
CO	0.13	0.09	-0.61
H_2O	0.58	0.10	-0.67
H*	0.19	0.01	-0.01
CO*	0.22	0.08	-0.16
COOH*	0.62	0.10	-0.19

3.3 Results and Discussion

3.3.1 Characterization of Prepared x-Fe-IRMOF-3

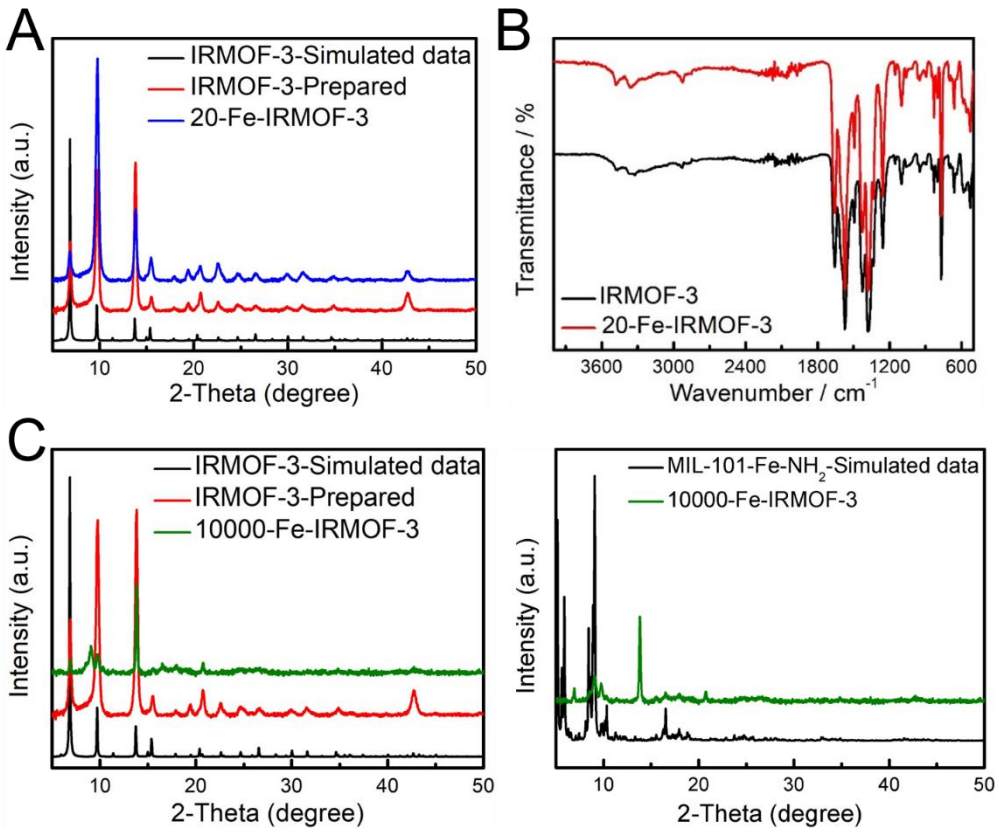

Figure 3.2 (A) XRD patterns, (B) FTIR spectrum of IRMOF-3 and 20-Fe-IRMOF-3 and (C) XRD patterns of 10000-Fe-IRMOF-3.

The high crystallinity of the as-prepared IRMOF-3 and the corresponding Fe-doped IRMOF-3 are confirmed by powder X-ray diffraction (XRD) measurements. As shown in **Figure 3.2A**, the presence of a modicum Fe amount in the IRMOF-3 does not affect the crystal structure of the parent IRMOF-3. Both IRMOF-3 and 20-Fe-IRMOF-3 samples exhibit similar crystal patterns, as expected for the standard IRMOF-3 structure.[48] The FTIR spectra obtained on the IRMOF-3 and 20-Fe-IRMOF-3 samples are shown in **Figure 3.2B**. Different characteristic bands ascribed to chemical groups are found in 20-Fe-IRMOF-3, which are similar to those of IRMOF-3, further suggesting that slightly Fe doping into the IRMOF-3 does not induce any structural change. However, after the incorporation of high Fe content into the IRMOF-3, a new diffraction peak at around 9.1° appears in the XRD pattern (e.g., in sample 10000-Fe-IRMOF-3), indicating that further addition of Fe content changes the crystal structure of parent IRMOF-3 (**Figure 3.2C**).

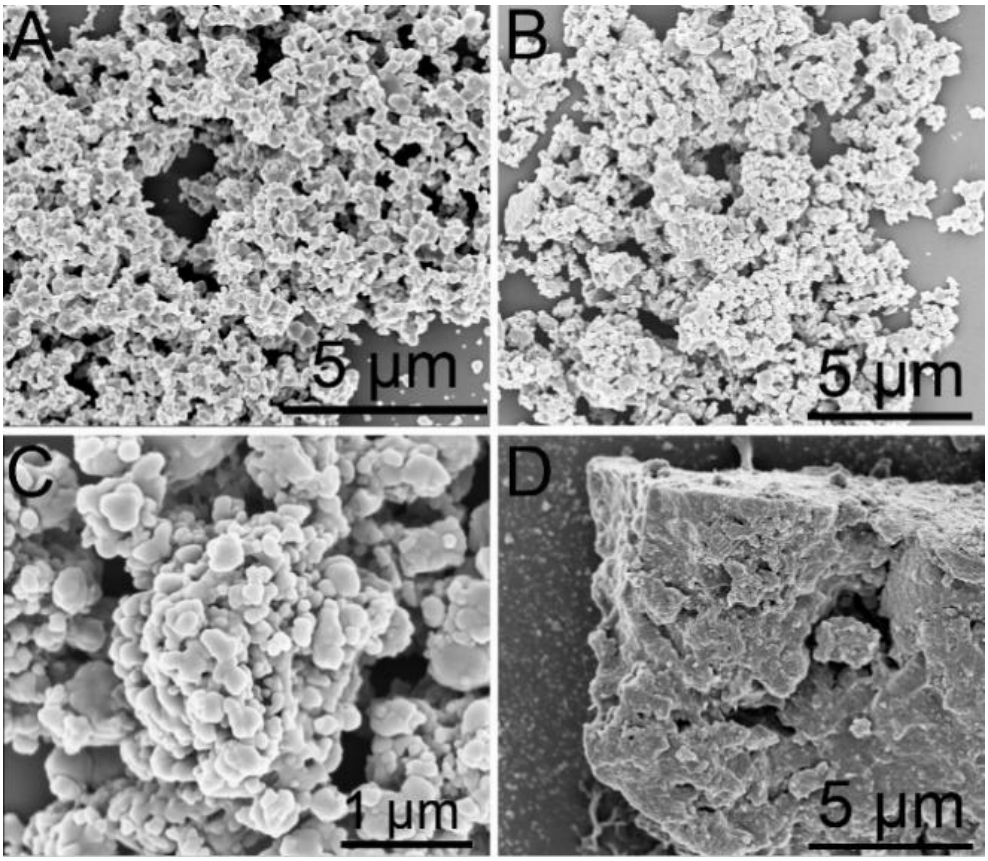

Figure 3.3 SEM images of (A) IRMOF-3, (B, C) 20-Fe-IRMOF-3 and (D) 10000-Fe-IRMOF-3.

To examine the surface morphology of the as-prepared samples, field emission scanning electron microscopy (FE-SEM) was performed (**Figure 3.3**). FE-SEM images show that 20-Fe-IRMOF-3 sample is composed of spheroidal 3D nanostructures with an irregular size, which are similar to the structures observed for the IRMOF-3 sample, indicating that a small amount of Fe doping does not change the morphology of IRMOF-3 (**Figure 3.3A-C**). However, the addition of higher amount of Fe salts, in the case of 10000-Fe-IRMOF-3 sample, induces the formation of inhomogeneous nanostructures and agglomerates (**Figure 3.3D**).

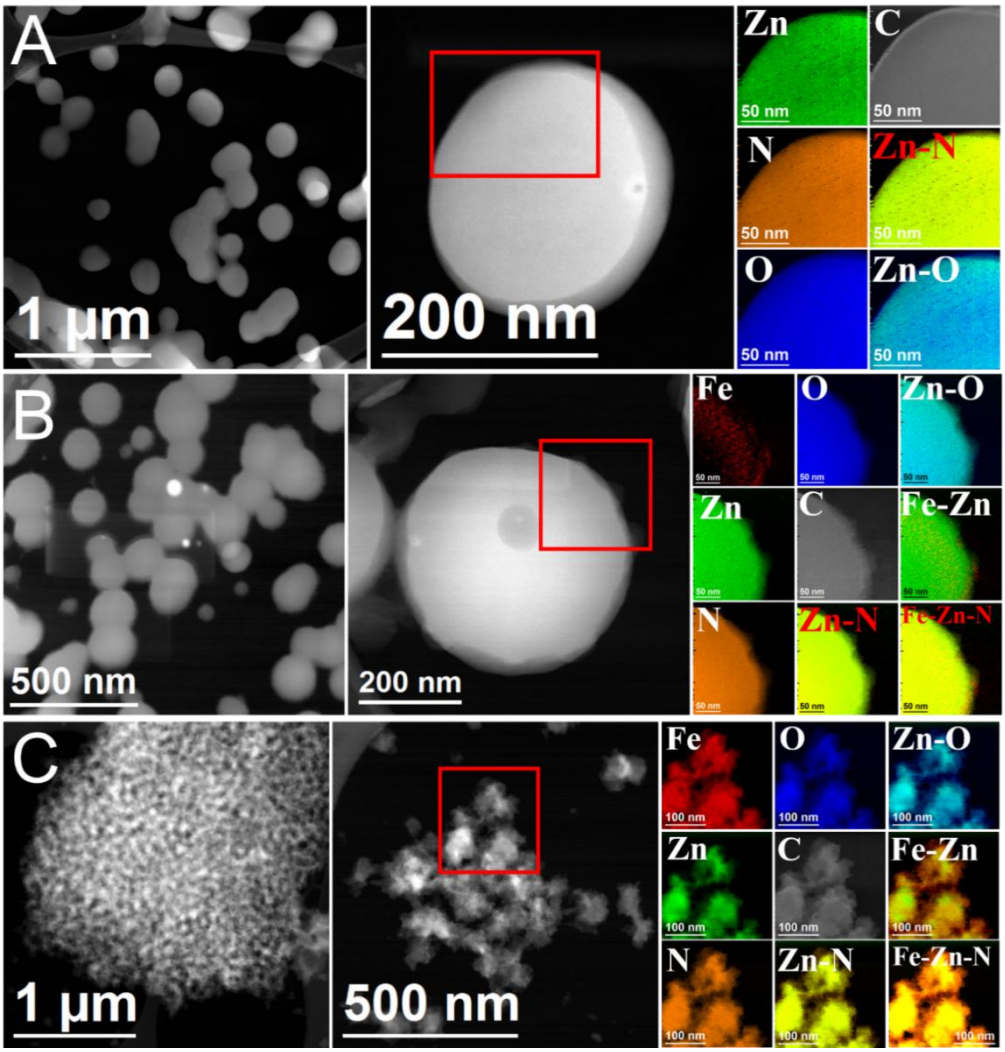

Figure 3.4 HAADF-STEM image of (A) IRMOF-3, (B) 20-Fe-IRMOF-3 and (C) 10000-FeIRMOF-3 as well as representative EELS chemical composition maps obtained from the red squared area of the STEM micrograph. Individual Fe $L_{2,3}$-edges at 708 eV (red), Zn $L_{2,3}$-edges at 1020 eV (green), N K-edges at 401 eV (orange), O K-edges at 532 eV (blue) and C K-edges at 285 eV (grey) as well as composites of their compositions.

High-angle annular dark-field scanning TEM (HAADF-STEM) further confirms the above SEM results that the introduction of a modicum Fe amount does not change the sample morphology (**Figures 3.4**). Elemental composition maps are obtained by means of electron energy loss spectroscopy (EELS) in STEM mode, showing a homogeneous distribution of Zn, N, O and C in IRMOF-3, 20-IRMOF-3 and 10000-IRMOF-3 samples. Fe is only maintained at the trace scale in 20-IRMOF-3 sample, whereas, it is abundant in 10000-IRMOF-3 sample, further indicating the successful introduction of Fe into the IRMOF-3 with different concentrations.

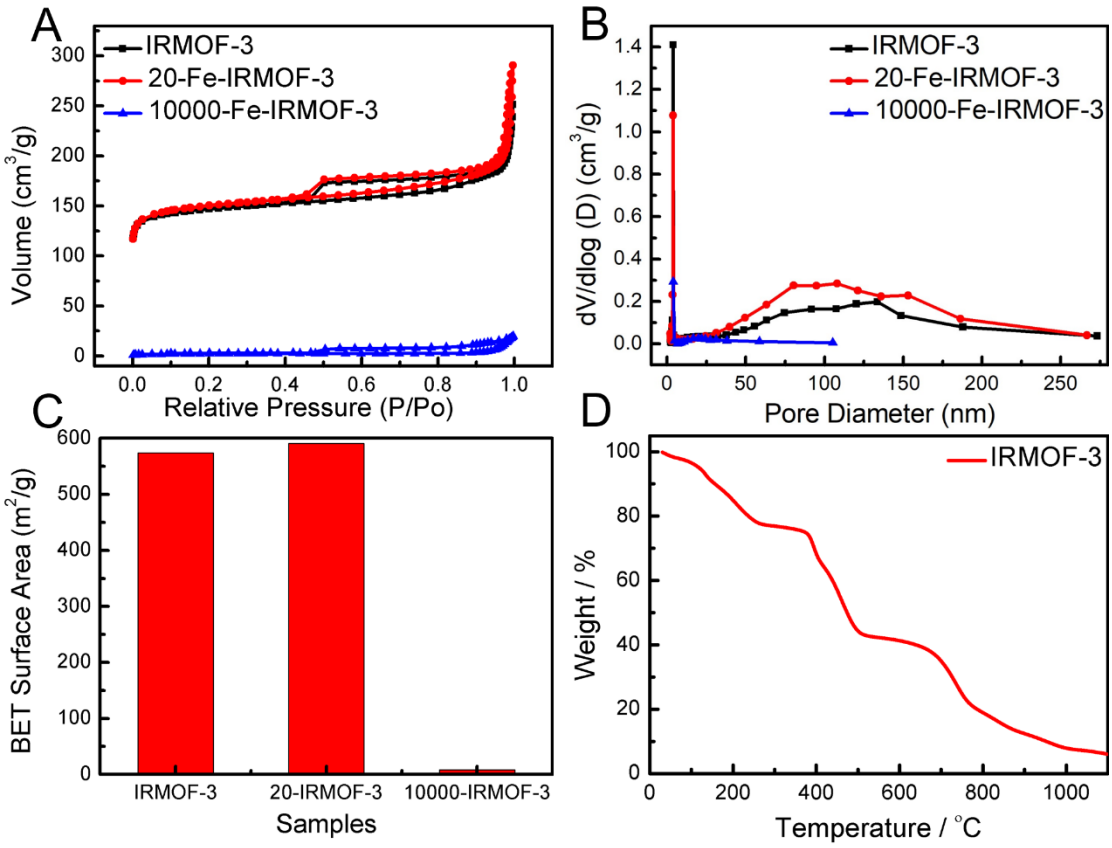

Figure 3.5 (A) N_2 adsorption and desorption isotherm for IRMOF-3, 20-Fe-IRMOF-3, 10000-Fe-IRMOF-3. (B) Pore size distribution from BJH calculation based on the desorption branch of the corresponding isotherm. (C) The BET surface area of IRMOF-3, 20-Fe-IRMOF-3, 10000-Fe-IRMOF-3 samples. (D) TGA patterns of IRMOF-3.

In addition, as verified by Brunauer-Emmett-Teller (BET) measurements (**Figure 3.5A-C**), the sample 20-Fe-IRMOF-3 inherits the high surface area and abundant porosity of IRMOF-3. By contrast, sample 10000-Fe-IRMOF-3 possesses a sharp

decrease of surface areas and pore diameters (ca. 23 nm), showing that the abundant presence of Fe covered the cavities of IRMOF-3 and formed new structures, leading to a lower surface area and porosity. The pyrolysis process carried out on the IRMOF-3 sample is carefully tracked by thermogravimetric analysis (TGA) (**Figure 3.5D**). The weight loss observed before 800 °C could be attributed to the carbonization and decomposition of the organic linker in IRMOF-3 at a continuous high temperature, which gives N, O and C sources for the growth of the targeted samples. When the temperature continued increasing to over 900 °C, the weight loss mainly results from the release of Zn species because of the low boiling point of Zn nodes (907 °C).[49] After pyrolysis, the inductively coupled plasma atomic emission spectroscopy (ICP-AES) is performed to determine the Fe molar ratio in samples N-C, D-Fe-N-C and Fe/Fe-N-C (**Table 3.2**).

Table 3.2 Fe Ratio of different samples.

Samples	Feeding (Fe)	Final product ICP ratio (Fe)
N-C	0	0 %
D-Fe-N-C	20 l	0.74 %
Fe/Fe-N-C	10 ml	43.7 %

3.3.2 Characterization of Samples after Pyrolysis

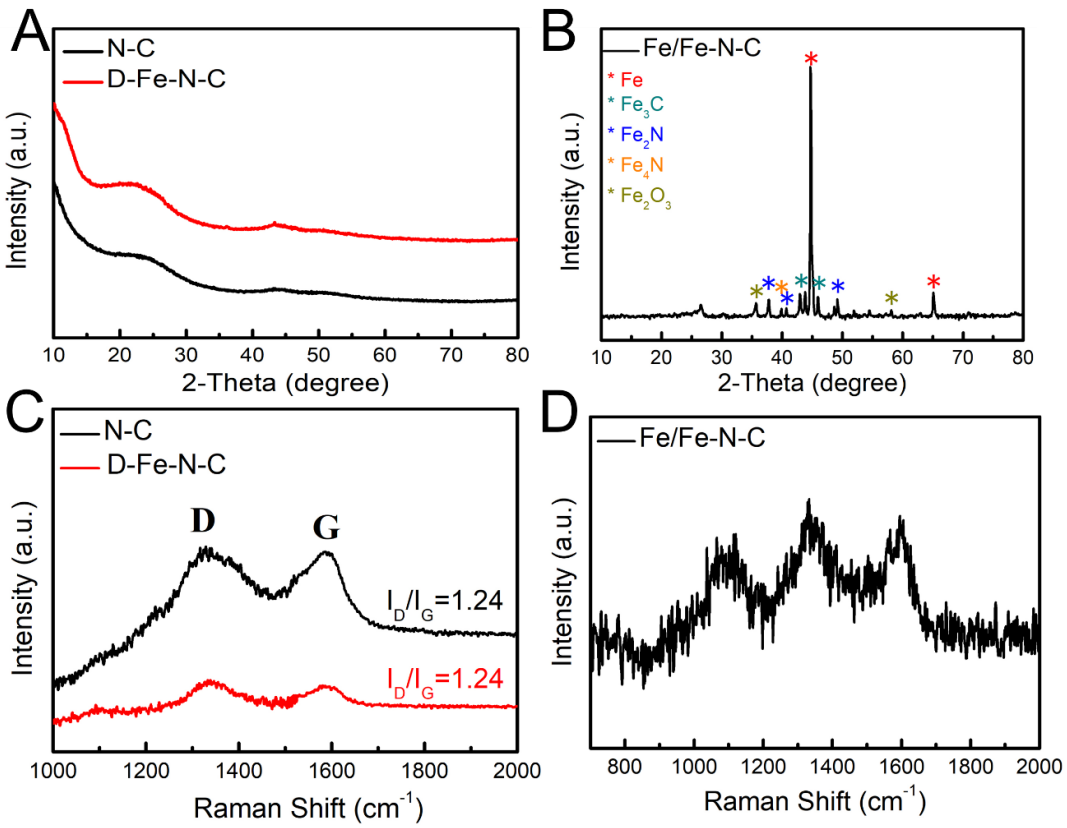

Figure 3.6 (A) XRD patterns and (B) Raman spectra of the N-C and D-Fe-N-C samples. (C) XRD pattern and (D) Raman spectra of Fe/Fe-N-C.

After pyrolysis, as observed in the XRD patterns shown in **Figure 3.6A**, the sharp peaks observed in IRMOF-3 and 20-Fe-IRMOF-3 samples are replaced by two broad peaks. These peaks at around 25° and 43°, belong to the (002) and (100) planes of graphitic carbon, indicating the successful conversion of MOFs into carbon-based materials without the metal, metal oxide or metal carbide impurity structures.[28, 50] As a counterpart, in the case of the as-prepared Fe/Fe-N-C sample, clear peaks of typical mixed crystals corresponding to iron, iron carbide, iron oxides and iron nitride crystal structures are present in its XRD pattern, as shown in **Figure 3.6B**. The Raman spectra of N-C and D-Fe-N-C samples exhibits two distinct features at around 1365 and 1590 cm^{-1}, which are attributed to the D (defective) band and G (graphite) band, respectively (**Figure 3.6C**).[51, 52] By comparing the value of I_D/I_G, the presence of

defects in the above samples are investigated. The value of I_D/I_G (1.24 in both samples) suggests that N-C and D-Fe-N-C samples have the same degree of defects.[52] In addition, as shown in **Figure 3.6D**, Fe/Fe-N-C sample shows three main peaks in the Raman spectrum at around 1100, 1365 and 1590 cm^{-1}. The additional peak observed at ca. 1100 cm^{-1} could be attributed to iron hybrids.[53] These outcomes further highlight the importance of Fe amount introduced into IRMOF-3 because a large amount of Fe promotes its aggregation and the further formation of iron hybrids.

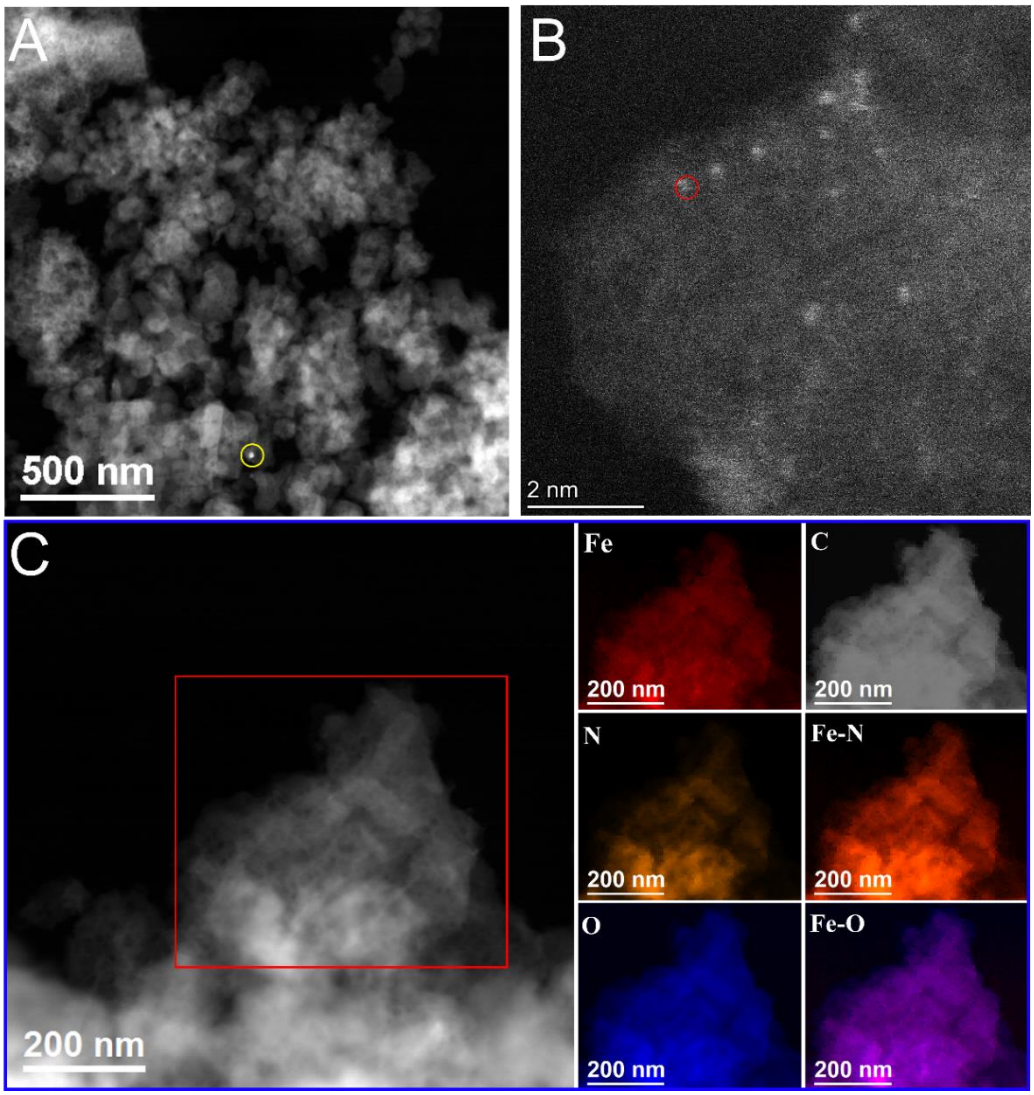

Figure 3.7 (A-B) HAADF-STEM images of the D-Fe-N-C sample. Iron clusters are circled in yellow and single iron atoms are circled in red. (C) HAADF-STEM image of D-Fe-N-C and representative EELS chemical composition maps obtained from the red squared area of the STEM micrograph. Individual Fe $L_{2,3}$-edges at 708 eV (red), N K-edges at 401 eV (orange), O K-edges at 532 eV (blue) and C K-edges at 285 eV (grey) as well as composites of Fe-N and Fe-O.

The D-Fe-N-C sample is further characterized by TEM, as shown in **Figure 3.7**. It is worth noting that D-Fe-N-C does not retain the spherical morphology of the MOFs precursor. Instead, all the spheres are broken during the pyrolysis process, which is ascribed to the destruction of the MOFs frameworks (**Figure 3.7A**). Multiple areas of the D-Fe-N-C sample are examined and only few Fe nanoparticles (precipitates) could be observed, as shown in **Figure 3.7A**, which is consistent with the XRD results (lack of Fe diffraction peaks). Furthermore, aberration-corrected high-angle annular dark-field scanning transmission electron microscopy (HAADF-STEM) is employed for directly detecting Fe single atoms thanks to the different Z contrast among Fe, N, O and C elements. The representative HAADF-STEM images in **Figure 3.7B** show isolated starry spots densely planted in the oxygen/nitrogen-doped carbon matrix, that can be assigned to the Fe single atom sites. Thus, it is confirmed that Fe is atomically dispersed in the D-Fe-N-C sample, which plays a dominant impact on the activation of CO_2. EELS elemental maps analyses reveal that Fe, N, O and C elements are homogeneously dispersed on the D-Fe-N-C sample (**Figure 3.7C**). Moreover, the absence of Zn in all the samples demonstrates the successful vaporization of Zn at 950 °C upon heat treatment, which simultaneously creates multiple micropores at the atomic size. STEM, EDX and EELS analyses indicate that the metals are mainly atomically dispersed in the oxygen/nitrogen-doped carbon matrix in the case of D-Fe-N-C sample.

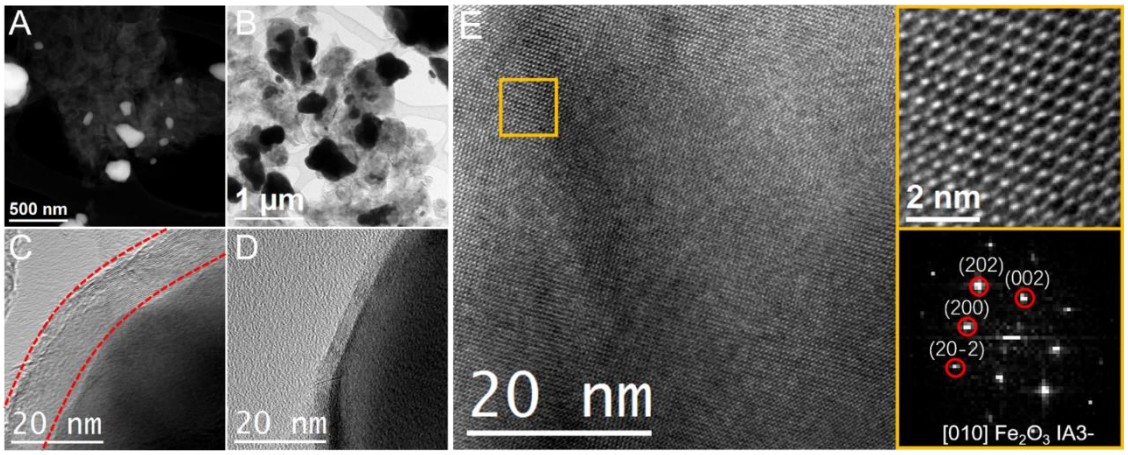

Figure 3.8 Different (A) HAADF-STEM, (B) BF TEM and (C-E) HRTEM micrographs and detail of the orange squared region and its corresponding power spectrum of Fe/Fe-N-C sample.

Compared to D-Fe-N-C, bulk Fe particles are observed in the Fe/Fe-N-C sample (**Figure 3.8**), indicating that the introduction of larger amounts of Fe leads to the formation of Fe aggregation (**Figure 3.8A** and **Figure 3.8B**). It is worth mentioning that some Fe nanoparticles in Fe/Fe-N-C are also covered by a few layers of graphitic-like carbon, as shown in **Figure 3.8C** and **Figure 3.8D**. Moreover, **Figure 3.8E** shows a HRTEM micrograph of a nanoparticle. Detail of the orange squared region and its corresponding power spectrum which reveals that this nanoparticle has a crystal phase that is in agreement with the Fe_2O_3 cubic phase (space group =IA3-) with a=b=c= 9.3930 Å. From the crystalline domain in **Figure 3.8E**, the Fe_2O_3 lattice fringe distances were measured to be 0.335 nm, 0.475 nm, 0.338 nm and 0.517 nm, at 41.19º, 86.31º and 135.17º which could be interpreted as the cubic Fe_2O_3 phase, visualized along its [010] zone axis. It is worth noting that only a few area could obtain the HRTEM of Fe_2O_3.

Table 3.3 Comparison between the experimental and the theoretical bulk plane spacing distances and angles between planes.

Spot	Experimental (nm)	Fe_2O_3 (IA3-) [010]
1	0.335	0.332 (20-2)
2	0.475 (41.19º vs Spot 1)	0.470 (45.00º) (200)
3	0.338 (86.31º vs Spot 1)	0.332 (90.00º) (202)
4	0.517 (135.17º vs Spot 1)	0.470 (135.00º) (002)

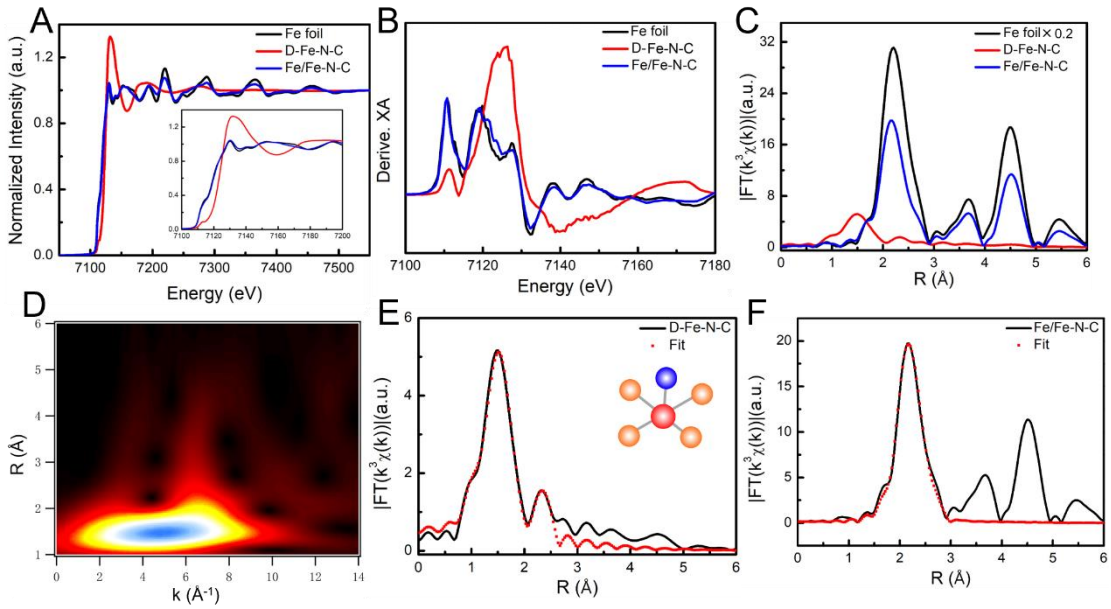

Figure 3.9 (A) Fe K-edge XANES spectra, (B) the first derivative spectra, (C) Fourier transformation of the EXAFS spectra at R space of D-Fe-N-C and Fe/Fe-N-C. (D) WT-EXAFS of D-Fe-N-C. Corresponding EXAFS fitting curves for (E) D-Fe-N-C and (F) Fe/Fe-N-C (Fe, O, N, atoms are represented in red, blue and orange, respectively).

The detailed local structure and electronic states of the Fe atoms in the catalysts have been further disclosed via XAS analyses. As shown in **Figure 3.9A**, Fe K-edge X-ray absorption near edge structure (XANES) spectra of D-Fe-N-C sample shift towards higher binding energy compared to that of a standard Fe foil, suggesting a positive charge state of Fe atoms in the D-Fe-N-C catalyst.[54, 55] On the contrary, the Fe K-edge XANES spectra of the as-prepared Fe/Fe-N-C exhibit the same energy absorption threshold of a standard Fe foil, proving the main presence of Fe^0 in Fe/Fe-N-C. To more clearly compare the differences of the XANES features, the first derivative XANES of the three samples are exhibited in **Figure 3.9B** to compare the average oxidation state of iron between the different samples. A shift to higher energy is observed in D-Fe-N-C at the Fe K-edge, which indicates a larger number of a higher valence state in the Fe ions present in the D-Fe-N-C sample in comparison to those of the Fe/Fe-N-C and the standard Fe foil.[56] Furthermore, the intrinsic structure of the reactive sites is further corroborated with the Fourier transformed (FT) k3-weighted χ(k)-function of the Fe K-edge EXAFS in R space (**Figure 3.9C**). A dominant peak

centered around 1.5 Å for D-Fe-N-C sample is shown in **Figure 3.9C**, attributed to the light backscattering induced by light atoms (N, O or C) situated in the first coordination shell of the absorbing metal. The slight presence of a peak at ~2.27 Å, which corresponds to the Fe-Fe bond, further confirms that there is a co-existence of the atomically isolated Fe dispersion with a modicum presence of Fe nanoparticles, in accordance with HAADF-STEM results.[21, 51] By contrast, the Fe/Fe-N-C sample presents a high peak at ca. 2.2 Å (attributed to the Fe-Fe scattering path),[22] which reveals a high signature of Fe-Fe bonds due to the presence of a high content of Fe nanoparticles (as previously observed in XRD patterns). To more clearly indicate the presence of Fe atomic dispersion throughout the samples, a wavelet transform (WT) of the Fe K-edge EXAFS oscillations was carried out thanks to its powerful resolutions in both k and r spaces. WT contour plots were obtained on the D-Fe-N-C sample (**Figure 3.9D**). The intensity maxima at 5 $Å^{-1}$ observed at the WT contour plots was associated with the Fe-N (O, C) contributions, respectively.[57] Therefore, according to FT- and WT-EXAFS analyses, it could be concluded that most of the Fe atoms are atomically dispersed in sample D-Fe-N-C. The Fe K-edge EXAFS spectra were then fitted with the model structures depicted in the insets of **Figure 3.9E**. The structural parameters obtained from the fittings are shown in **Table 3.4**, including the coordination number (CN) and different bond distances. The optimized fit results for D-Fe-N-C show a CN-value of 5 and a mean bond length of 2.02 Å. However, EXAFS alone cannot distinguish between N, O, and C atoms. Experimentally and theoretically, metal-nitrogen bonds are more likely than metal-carbon or metal-oxygen ones to form in-plane FeN_4 sites in the first coordination sphere. While under further hypotheses, the higher average CN-value of 5 for Fe-N-C strongly suggests that one axial O atom is adsorbed on top of the FeN_4 moieties, resulting in coordinatively saturated iron cations, in line with the high oxophilicity of Fe.[20, 22, 57] In summary, the spectra obtained on the D-Fe-N-C sample are fitted assuming the presence of four in-plane nitrogen and one oxygen atom as an axial ligand, as FeN_x moieties are in an oxygen-rich atmosphere.

Table 3.4 EXAFS fitting parameters at the Fe K-edge for various samples

Sample	Shell	N [a]	R (Å) [b]	σ^2 (Å$^2\cdot10^{-3}$) [c]	ΔE0 (eV) [d]	*R* factor (%)
D-Fe-N-C	Fe-N	5.1	2.02	9.8	0.2	0.8
	Fe-Fe	0.4	2.54	4.9	0.6	
Fe/Fe-N-C	Fe-Fe	5.1	2.47	6.1	2.1	0.6
	Fe-Fe	3.6	2.83	8.3		

[a] *N*: coordination numbers; [b] *R*: bond distance; [c] σ^2: Debye-Waller factors; [d] ΔE_0: the inner potential correction. *R* factor: goodness of fit. *S*02 were set as 0.85/0.90 for Fe-N/Fe-Fe, which were obtained from the experimental EXAFS fit of reference FePc/Fefoil by fixing CN as the known crystallographic value and was fixed to all the samples.

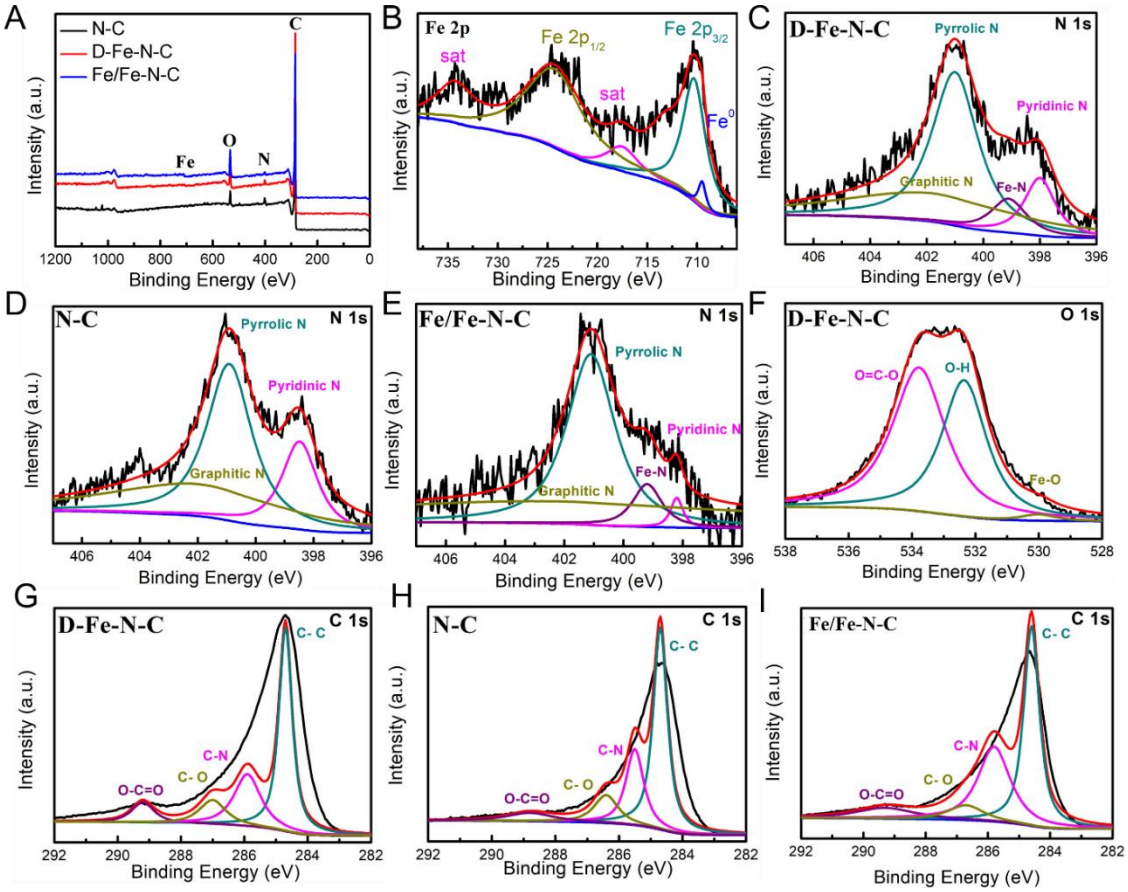

Figure 3.10 XPS spectra for the (A) survey scan. (B) High-resolution XPS Fe 2p spectrum of Fe/Fe-N-C. High-resolution XPS N 1s spectrum of (C) D-Fe-N-C, (D) N-C and (E) Fe/Fe-N-C. (F) high-resolution XPS O 1s spectrum of D-Fe-N-C. High-resolution XPS C 1s spectrum of (G) D-Fe-N-C, (H) N-C and (I) Fe/Fe-N-C.

In addition, the surface composition and bonding configuration of the different catalysts are characterized by X-ray photoelectron spectroscopy (XPS). The full survey scan XPS spectra shown in **Figure 3.10A** exhibit the presence of C, N and O in all the samples. A higher proportion of Fe is only detected in the Fe/Fe-N-C sample (**Figure 3.10B**). The high-resolution N 1s spectra obtained on the D-Fe-N-C sample shown in Fig. 3c demonstrates the presence of pyridinic (398.6 eV), pyrrolic (401 eV), graphitic (402 eV), and Fe-NX (399.4 eV) species.[50] Notably, other than the bare N-C material, the D-Fe-N-C and Fe/Fe-N-C samples show porphyrin-like moieties at 399.4 eV which correspond to the iron-nitrogen (Fe-N) coordination, indicating that the Fe is substantially coordinated with N (**Figures 3.10C-E**). The core-level XPS of O 1s spectra obtained in D-Fe-N-C sample are shown in **Figure 3.10F** and deconvoluted into three types at around 530.0, 532.6 and 533.8 eV, being assigned to the oxygen configuration in Fe-O, -OH group and O=C-O, respectively.[22] The results provided here imply the retains of Fe-O chelation after calcination. The analyses of the high-resolution C 1s XPS spectrum of D-Fe-N-C show the presence of C-C (284.5 eV), C-N (285.9 eV), C-O (286.8 eV) and O-C=O (289.0 eV) bonds (**Figure 3.10G**). Similarly, the N-C and Fe/Fe-N-C samples also exhibit the C-C (284.5 eV), C-N (285.9 eV), C-O (286.8 eV) and O-C=O (289.0 eV) bonds in C 1s XPS spectrum (**Figure 3.10H** and **Figure 3.10I**), indicating that these samples are derived from the same MOFs precursor.[25]

3.3.3 Electrochemical Performance

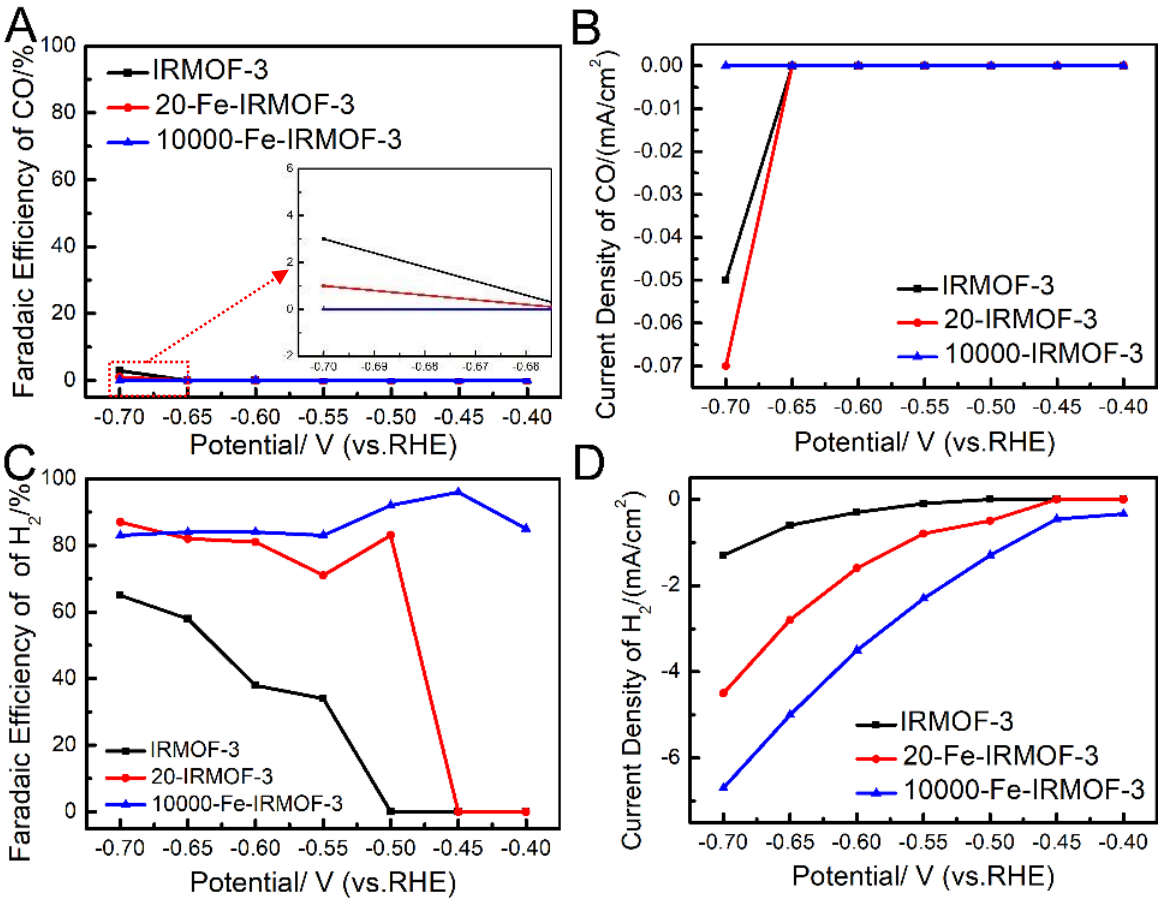

Figure 3.11 (A) FE of CO at various potentials, (B) Current density for CO production, (C) FE of H_2 at various potentials and (D) Current density for H_2 production on IRMOF-3, 20-Fe-IRMOF-3 and 10000-Fe-IRMOF-3.

The electrocatalytic activity of the different samples towards CO_2 RR were investigated in a CO_2-saturated 0.5 M $NaHCO_3$ solution as electrolyte using a three-electrode H-cell separated by an anion exchange membrane to prevent the further oxidation of as-generated products. The cathodic compartment was continuously purged with CO_2 (20 ml min^{-1}). The periodic quantification of the gas-phase products were detected by gas chromatography (GC). Online GC results show that CO and H_2 were the main gas products obtained for all the catalysts, and no liquid product was detected by ^1H nuclear magnetic resonance (^1H-NMR) spectroscopy after the electrochemical CO_2 reduction processes.

The samples were previously coated on carbon paper (1 cm×1 cm) with a mass loading of ~1.0 mg cm^{-2}. Firstly, the Faradaic efficiency and partial current density of the prepared MOFs precursors were obtained, as shown in **Figure 3.11**. It is interesting to point out that all the precursors showed an excellent HER ability while they present a scarcely catalytic performance toward CO_2 RR.

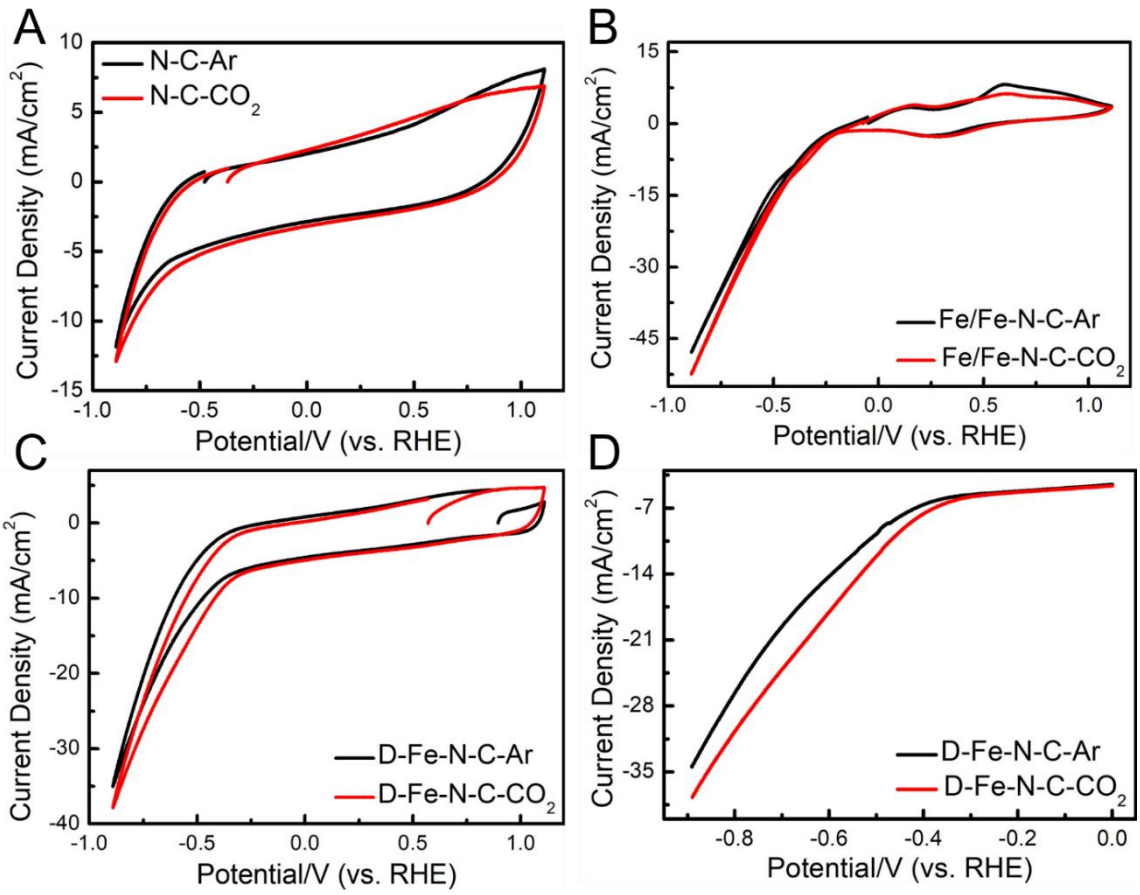

Figure 3.12 Cyclic voltammograms curves vs. RHE of (A) N-C, (B) D-Fe/Fe-N-C and (C) Fe-N-C obtained in Ar or CO_2-saturated 0.5 M $NaHCO_3$ solution. (D) is the LSV comparison for D-Fe-N-C in Ar-and CO_2-saturated 0.5 M $NaHCO_3$ solution.

After pyrolysis, cyclic voltammetry (CV) curves were carried out to evaluate the electrocatalytic CO_2 RR performance, roughly. As shown in **Figure 3.12**, the D-Fe-N-C sample presented a current reduction under Ar atmosphere, typically attributed to the HER. Upon saturating the solution with CO_2, the current reduction increased. The same

phenomenon was observed on N-C and Fe/Fe-N-C samples, although the current increase in the case of Fe/Fe-N-C was less significant.

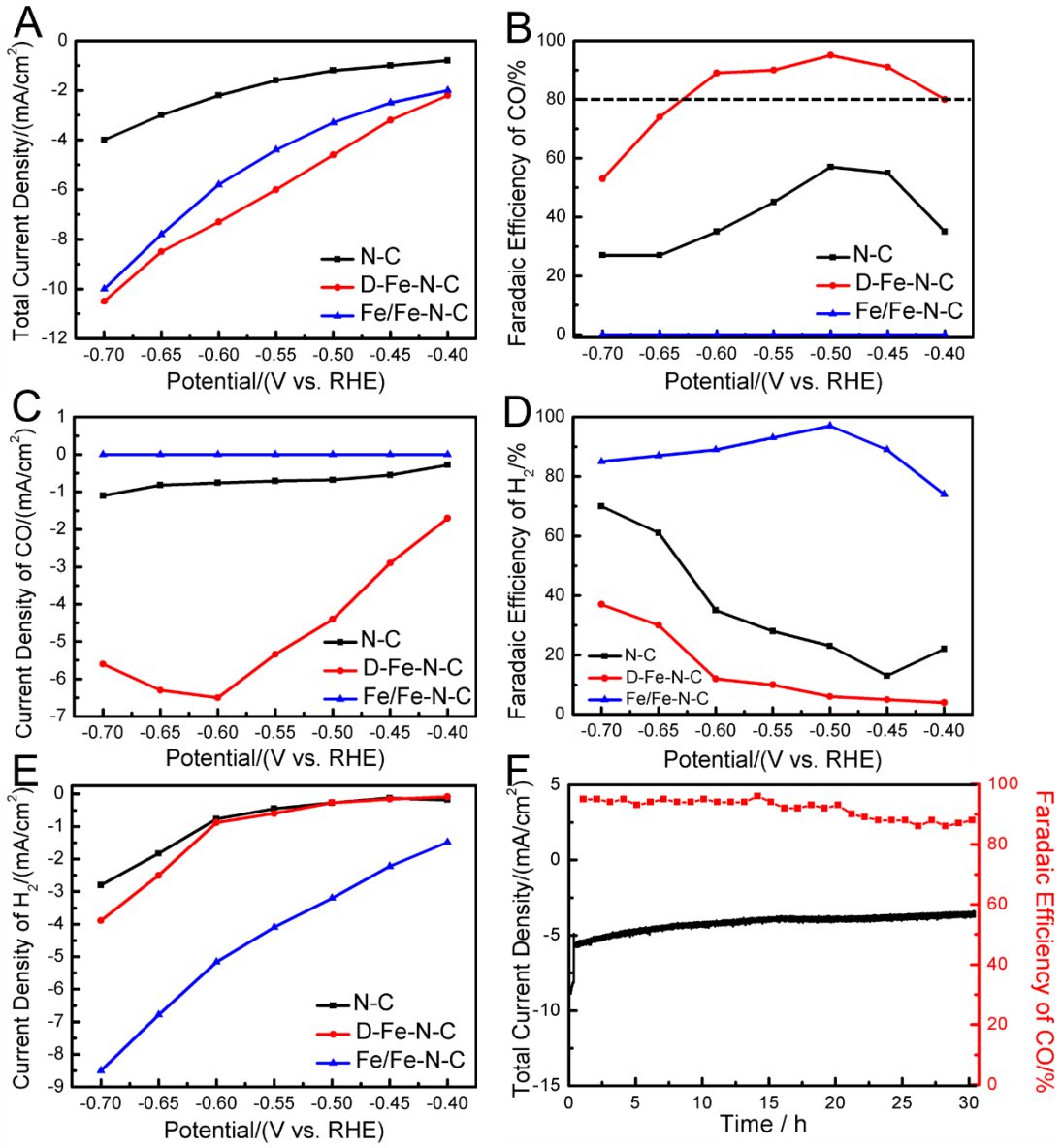

Figure 3.13 (A) Total current density (B) FE of CO at various potentials. (C) Current density for CO production. (D) FE of H_2 at various potentials. (E) Current density for H_2 production on N-C, D-Fe-N-C and Fe/Fe-N-C. (F) Stability test of D-Fe-N-C at −0.50 V vs. RHE.

Then, the catalytic activities for CO_2 RR were further investigated by the chronoamperometry method. The total current densities of the N-C, D-Fe-N-C and Fe/Fe-N-C samples were plotted against potential, as presented in **Figure 3.13A**.

Compared to N-C, after introducing Fe, the total current densities of D-Fe-N-C and Fe/Fe-N-C increased significantly at different applied potential, indicating the faster rate of reaction obtained on D-Fe-N-C and Fe/Fe-N-C samples.[58] **Figure 3.13B** shows the Faradaic efficiencies (FE) of CO formed during CO_2 RR at a cathode potential from −0.40 to −0.70 V vs. RHE. The FE (CO) obtained on the N-C and D-Fe-N-C samples changes with the applied potentials. For D-Fe-N-C, reduction of CO_2 to CO could start at a potential as low as −0.40 V vs. RHE with a FE (CO) of 80 %, reaching the maximum FE (CO) of 95 % at −0.50 V vs. RHE, that percentage is above those obtained on N-C and Fe/Fe-N-C samples. In **Figure 3.13C**, we show the potential-dependent CO partial current densities calculated based on the total current densities and the corresponding FE (CO), demonstrating that the D-Fe-N-C exhibits a higher current density of CO than the other electrodes in the whole applied potentials, with a partial current density of −4.4 mA cm^{-2} at −0.50 V vs. RHE. The decreasing trend of FE (CO) for N-C and D-Fe-N-C observed as the potential shifted to more negative values mainly stems from the dominance of the H_2 evolution over the CO_2 RR, which can be evidenced directly according to the FE (H_2) shown in **Figure 3.13D**. The potential-dependent H_2 current densities for the different catalysts are shown in **Figure 3.13E**. In order to evaluate the long-term stability of the D-Fe-N-C electrocatalyst, we performed a 30 hr durability test at a constant −0.50 V vs. RHE cathode potential. The outlet gases were analyzed every 30 min by GC, while calculating the corresponding FE of CO. The current density of D-Fe-N-C maintain a steady value of approximately −4.5 mA cm^{-2} with no significant decay (**Figure 3.13F**) during the 30h test, while the corresponding Faradaic efficiency of CO only decreases slightly to 88 % after the 30h stability test.

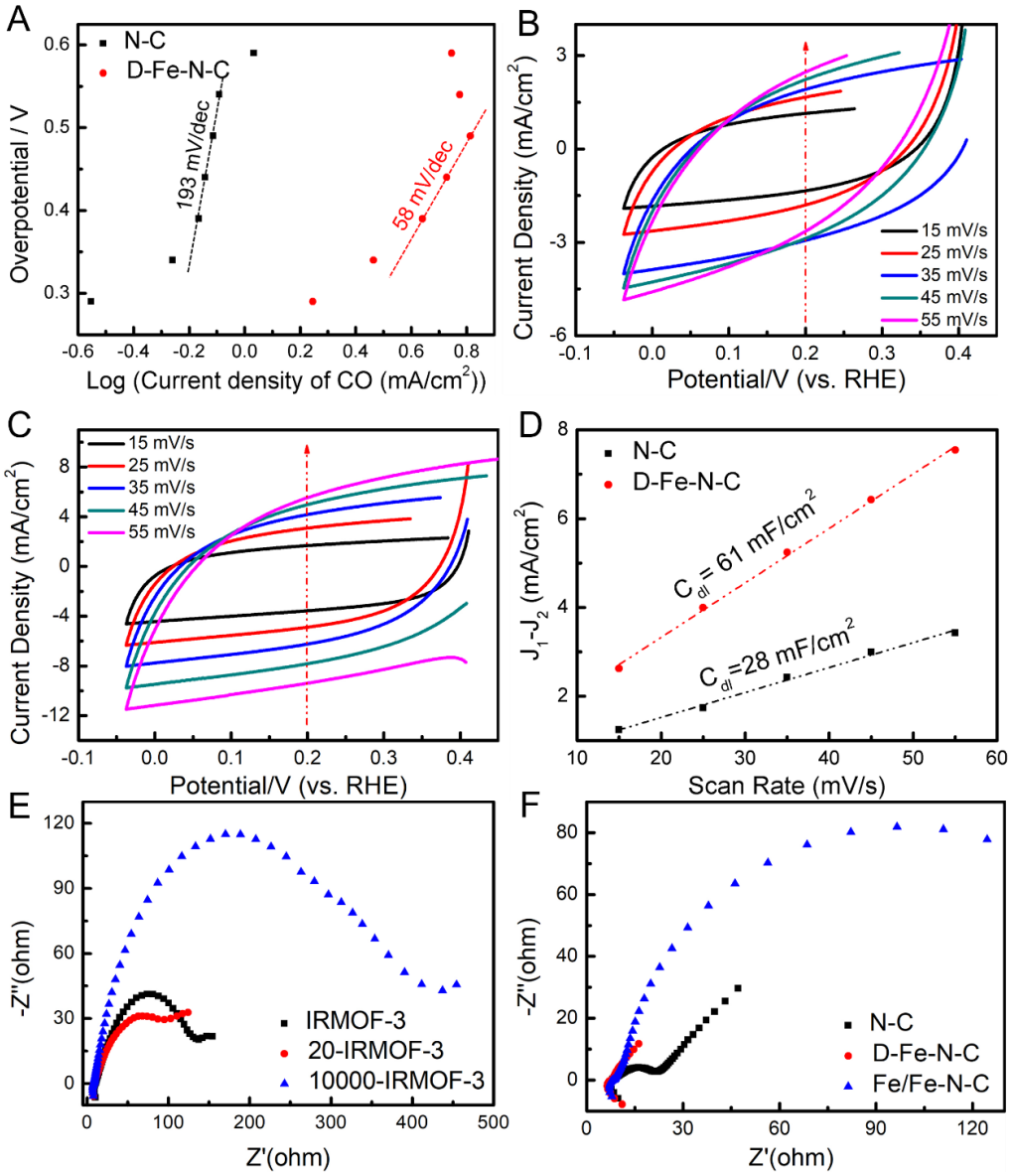

Figure 3.14 (A) Tafel Slope of N-C and D-Fe-N-C. Cyclic voltammograms curves between −0.05 and 0.40 V vs. RHE for (B) N-C and (C) D-Fe-N-C. (D) Plots of the current density vs. scan rate for N-C and D-Fe-N-C electrodes. (E) Electrochemical impedance spectroscopy (EIS) of IRMOF-3, 20-Fe-IRMOF-3, 10000-Fe-IRMOF-3 (F) N-C, D-Fe-N-C and Fe/Fe-N-C after the activated process.

The intrinsic activity of the catalysts was further disclosed by the mass activities of N-C and D-Fe-N-C at −0.50 V vs. RHE. Mass activity of D-Fe-N-C was found to be 4.4 A/g in 0.5 M $NaHCO_3$, which is much higher than that of N-C (0.68 A/g), showing that the D-Fe-N-C possesses an excellent catalytic performance toward CO_2 RR. As revealed in **Figure 3.14A**, the Tafel slope of D-Fe-N-C is 58 mV dec^{-1}, much smaller

than that of N-C (193 mV dec^{-1}), indicating more favorable kinetics for the formation of CO.[59, 60] Moreover, it is well known that an increase of the electrochemical active surface area (ECSA) often leads to the enhancement of the catalytic activity.[34] In order to further explain the high efficiency of the D-Fe-N-C compared to the N-C sample, the ECSA was calculated by electrochemical double-layer capacitance (C_{dl}) of the active materials. As shown in **Figure 3.14B-D**, the C_{dl} of the N-C and D-Fe-N-C samples was obtained by CV (**Figure S33B** and **Figure S33C**). By plotting the $\Delta J= J_a- J_c$ at 0.20 V vs. RHE against the scan rate, the slope which is twice of C_{dl} could be obtained. As shown in **Figure S33D**, the C_{dl} of N-C and D-Fe-N-C samples is 28 mF cm^{-2} and 61 mF cm^{-2}, respectively, confirming that the higher intrinsic catalytic activity of the D-Fe-N-C is due to an increase of the electroactive sites during the CO_2 RR.[61] In addition, the surface roughness factor (R_f) was calculated by taking the estimated ECSA and dividing by the geometric area of the electrode (1 cm^2). Generally, a constant capacitance was used in the same solution, therefore, R_f is linear with C_{dl}. The higher R_f obtained on the D-Fe-N-C sample could significantly reduce the adhesion force between the electrode surface and gas bubbles, which favors the CO_2 RR.[52] Nyquist plots reveals that D-Fe-N-C have a lower interfacial charge-transfer resistance (R_{CT}) than N-C sample, hence ensuring faster electron transfer during CO_2 RR process, which is favorable for the formation of intermediate (**Figure 3.14F**).[50, 52, 62]

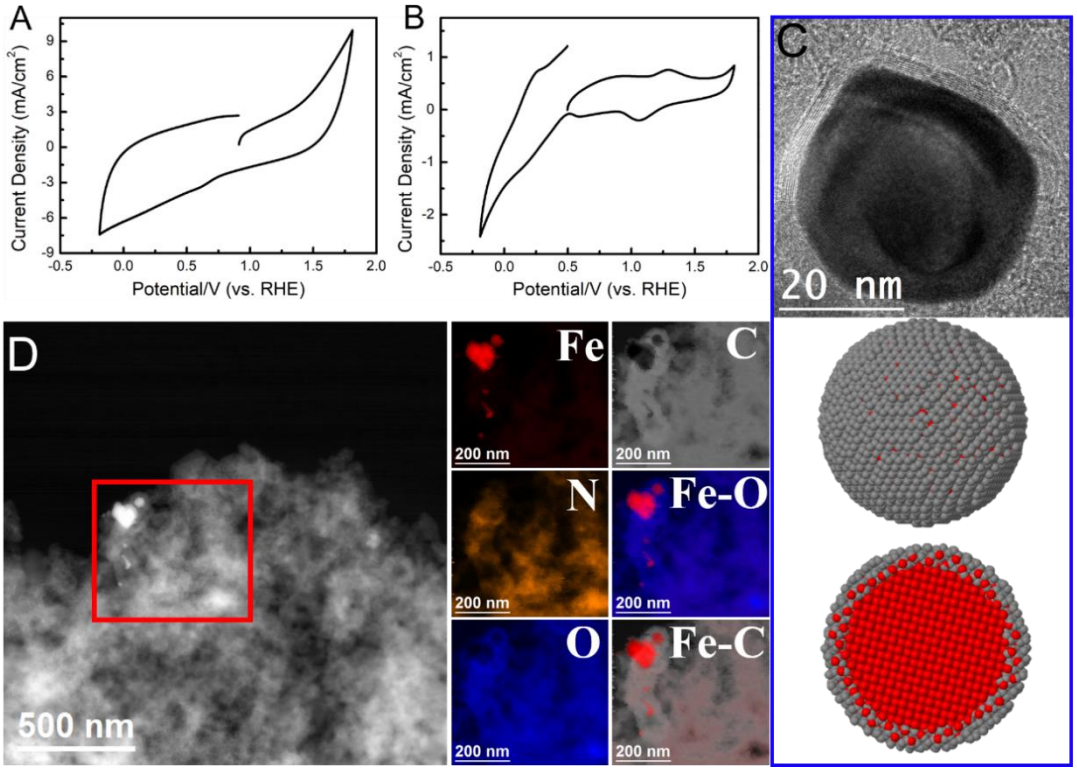

Figure 3.15 CV curves of (A) D-Fe-N-C and (B) Fe/Fe-N-C in 0.5 M Ar-saturated $NaHCO_3$ electrolyte. (C) HRTEM micrographs of D-Fe-N-C sample as well as atomic supercell model illustration of the Fe nanoparticle with carbon shell (Fe and C are represented in red and grey, respectively) (D) HAADF-STEM image of D-Fe-N-C and representative EELS chemical composition maps obtained from the red squared area of the STEM micrograph.

In order to prove that the excellent CO_2 RR performance of the D-Fe-N-C catalyst is attributed to the highly dispersed single active sites rather than Fe nanoparticles or agglomerates, CV curves measurements were employed, as shown in **Figure 3.15A** and **Figure 3.15B**. Based on the CV curves, we observed that Fe reduction/oxidation redox peaks disappeared for the D-Fe-N-C sample. According to the HAADF STEM, EELS and HRTEM results, it could be corroborated that the Fe clusters are rigorously encapsulated by a few layers of carbon, which would encumber the interaction between the Fe nanoparticles and the electrolyte, resulting in an inactive performance of these Fe nanoparticles (**Figure 3.15C** and **Figure 3.15D**).

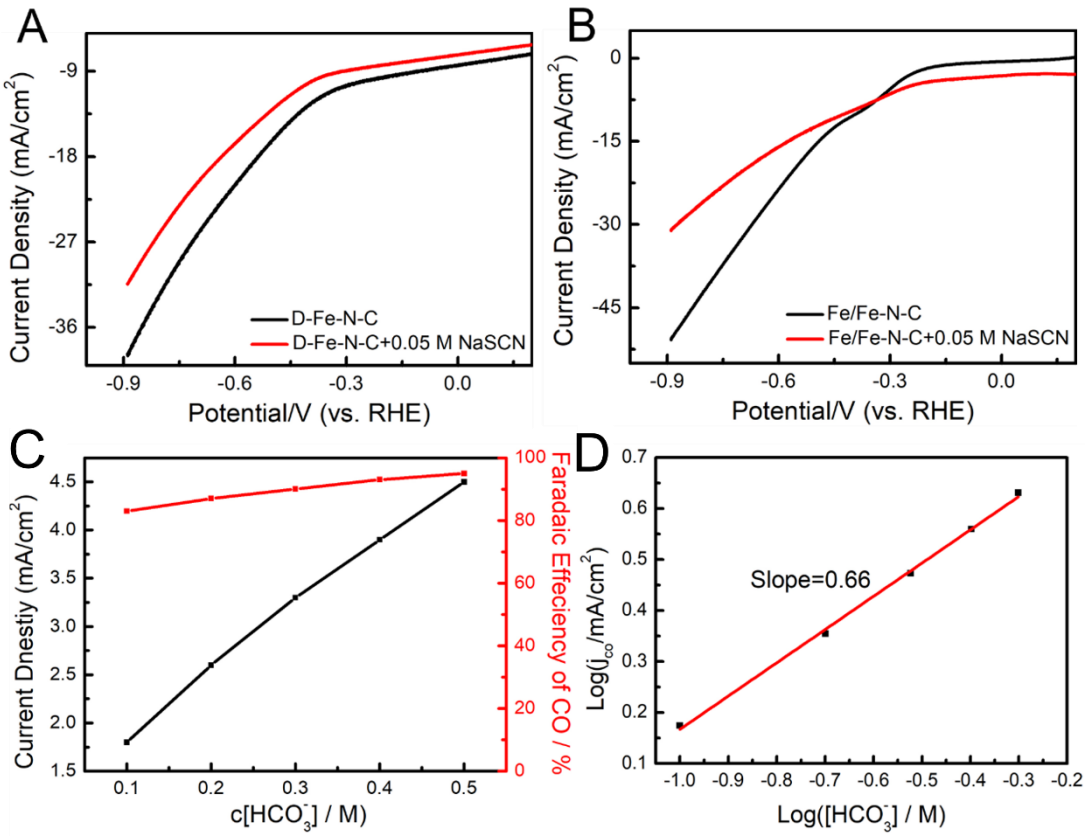

Figure 3.16 Linear sweep voltammetry curves of (A) D-Fe-N-C and (B) Fe/Fe-N-C with and without 0.05 M NaSCN. (C) Current density and FE of D-Fe-N-C at different $NaHCO_3$ concentration at a constant potential (−0.5 V vs. RHE). (D) Partial CO current density of D-Fe-N-C vs. $NaHCO_3$ concentration at −0.50 V vs. RHE.

Meanwhile, it has been documented that the SCN^- ion has a high affinity to Fe ions and thus can poison the isolated Fe single-atom sites.[52] As shown in **Figure 3.16A** and **Figure 3.16B**, a significant depression of the catalytic activity for D-Fe-N-C and Fe/Fe-N-C is observed, which could be attributed to the blocking effect of SCN^- on single Fe sites. Hence, it is reasonable to attribute the dominant impact on the high activity and selectivity to the exposed isolated Fe sites. To further probe the role of HCO_3^- within the reaction, different HCO_3^- concentrations were studied at a constant applied potential of −0.50 V vs. RHE. As revealed in **Figure 3.16C** and **Figure 3.16D**, a plot of log (j_{CO}) versus log ([HCO_3^-]) show a slope of 0.66, demonstrating that the concentration effect of HCO_3^- plays a considerable role, influencing the efficiency of the conversion reaction of CO_2 to CO.[52, 59] In addition, since the pKa value of

HCO_3^- (10.33) is smaller than that of H_2O (15.7), the HCO_3^- could also act as a proton donor in the reaction.[63] Therefore, the HCO_3^- not only simply acts as a pH buffer and proton donor in this reaction, but also increase the concentration of CO_2 near the electrode surface.[52, 59, 63]

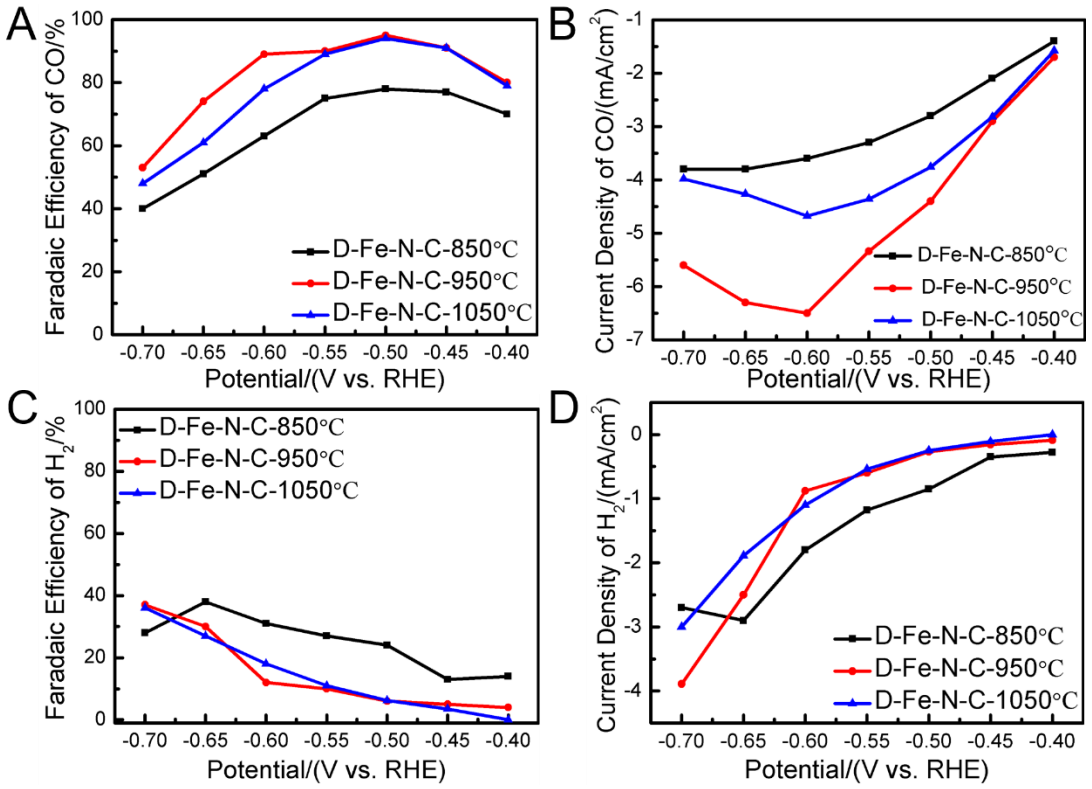

Figure 3.17 (A) FE of CO at various potentials, (B) Current density for CO production, (C) FE of H_2 at various potentials, (D) Current density for H_2 production on D-Fe-N-C-850, D-Fe-N-C-950 and D-Fe-N-C-1050.

The FE for CO and H_2 on different samples obtained at different pyrolysis temperatures are shown in **Figure 3.17** for comparison. Apparently, D-Fe-N-C-850 sample shows lower FE(CO) than that of D-Fe-N-C-950 and D-Fe-N-C-1050. Such a decreased selectivity can be attributed to the resident Zn at low pyrolysis temperature. While the FE (CO and H_2) values of D-Fe-N-C-1050 at applied potentials are similar to those of D-Fe-N-C-950. Therefore, we can conclude that the CO_2 RR activity could be influenced by the pyrolysis because at the low temperature could not remove the Zn completely from the MOFs precures, hence, hindering the CO_2 RR activity.

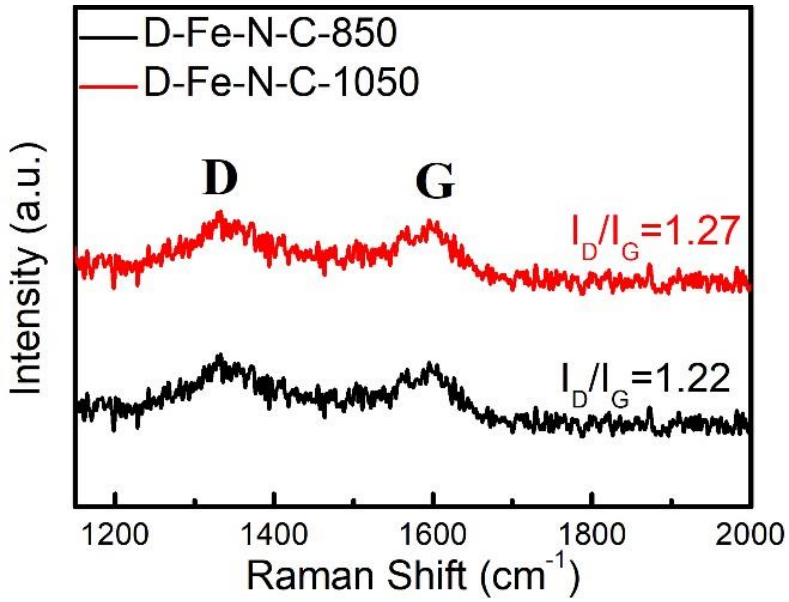

Figure 3.18 Raman spectra for D-Fe-N-C-850 ℃ and D-Fe-N-C-1050 ℃.

In order to understand the role of the pyrolysis temperature, we further investigated the Raman spectra of different samples. As observed in **Figure 3.18**, an increased ratio of D band (at 1365 cm^{-1}) to G band (at 1590 cm^{-1}) from 1.22 to 1.27 with the increasing pyrolytic temperature was observed in the Raman spectra, showing that the graphitization degree of carbon materials increased with the increasing temperature, and more structural defects were generated on the surface carbon matrix. Meanwhile, compared to D-Fe-N-C-850, the FE (CO) of D-Fe-N-C promotes accompanied with the enhanced value of I_D/I_G, suggesting that the graphitic degree of carbon had an effect on the catalytic efficiency. However, the graphitic degree of carbon is not the sole limiting factor, this is further evidenced by the increasing value of I_D/I_G for D-Fe-N-C-1050 without leading to enhanced FE (CO) of D-Fe-N-C-1050 sample (**Figure 3.18**).

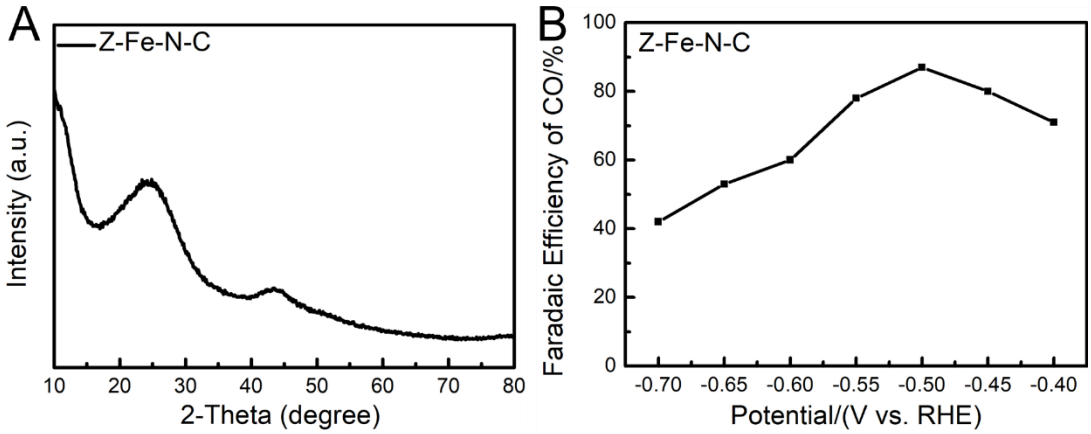

Figure 3.19 (A) XRD patterns and (B) FE of CO at various potentials on Z-Fe-N-C.

In addition, we used the ZIF-8 with a non-oxygen ligand as the precursor to prepare the Fe single atom catalyst, we found a slight decrease of FE of CO, further providing the advantages of rich-oxygen organic ligand we used.

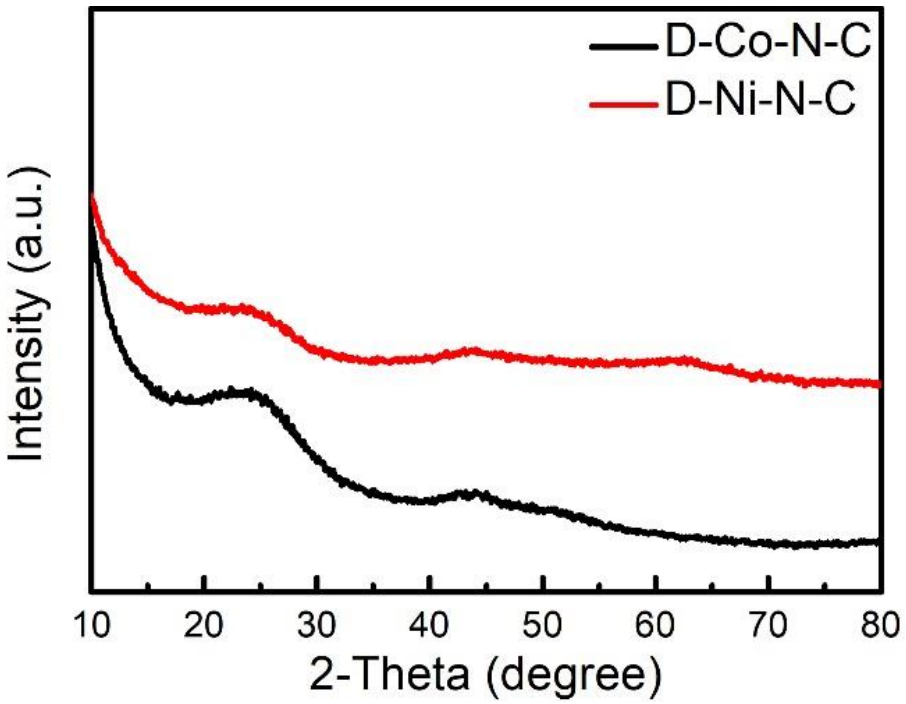

Figure 3.20 XRD patterns of D-Co-N-C and D-Ni-N-C.

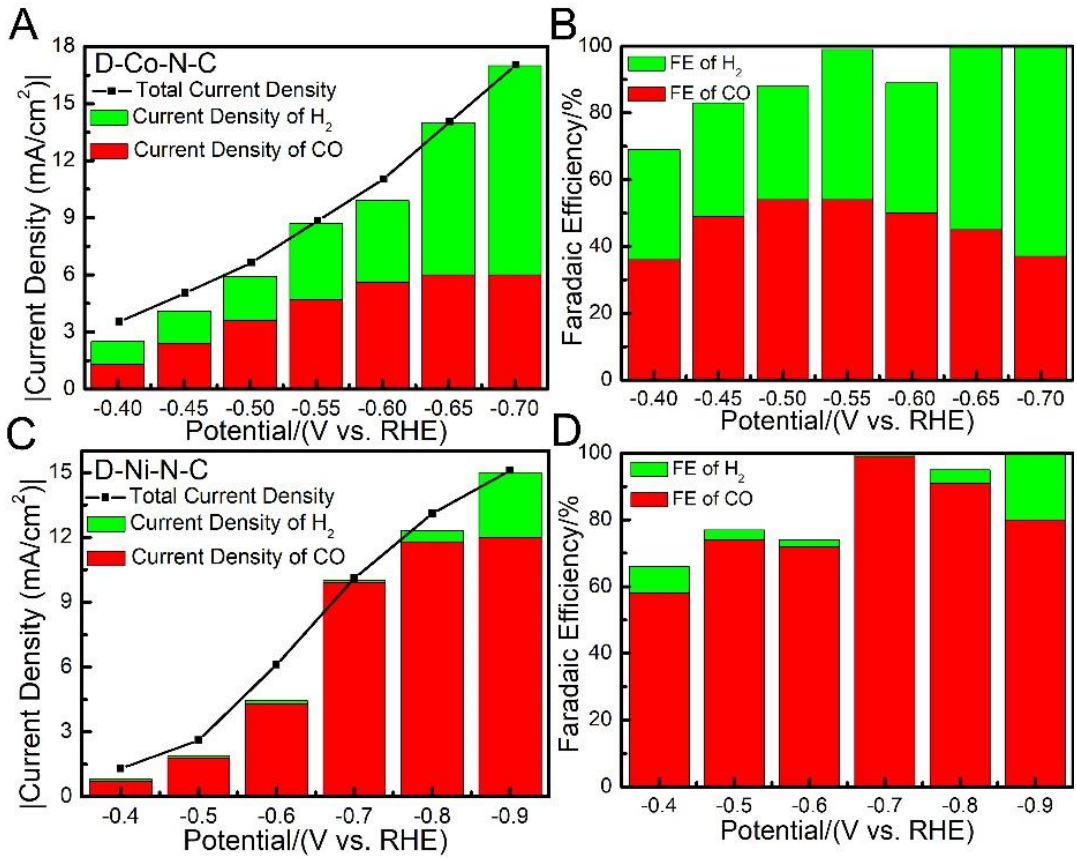

Figure 3.21 (A and C) Current density and partial current density on D-Co-N-C and D-Ni-N-C. (B and D) FE of CO and FE of H_2 at various potentials on D-Co-N-C and D-Ni-N-C

Meanwhile, we prepared highly disperse Co-N-C (D-Co-N-C) and Ni-N-C (D-Ni-N-C) catalysts through the same synthesis process using the IRMOF-3 assisted-method. The D-Ni-N-C showed an excellent FE(CO) towards CO_2 RR, demonstrating that the nitrogen and oxygen-rich IRMOF-3-assistant strategy is rational for design and development of highly disperse M-N-C.

3.3.4 DFT Calculations

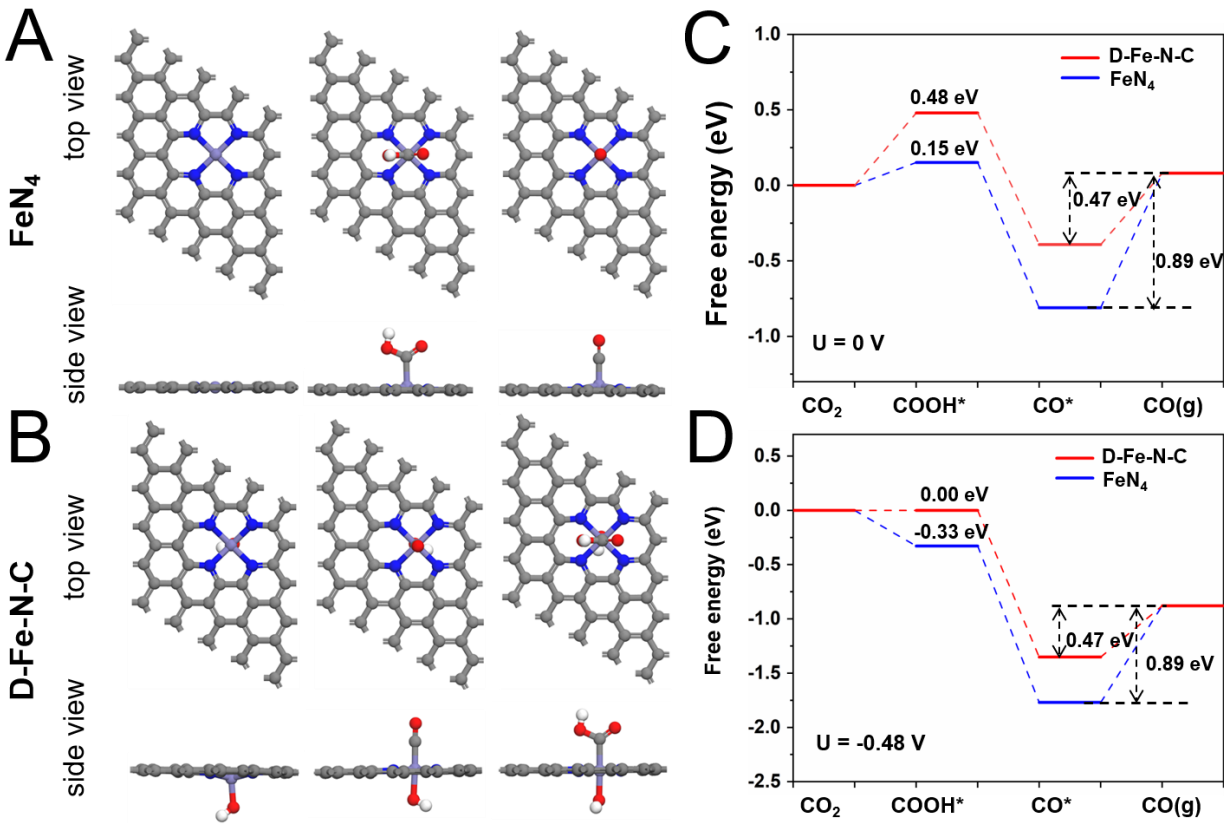

Figure 3.22 (A and B) The top view and side view of optimized adsorption configuration on simulated FeN_4 and D-Fe-N-C (Fe, O, N and C atoms are represented in purple, red, blue and grey, respectively). Free energy profiles for the CO_2 RR to CO at (C) 0 V (vs. RHE) (D) −0.48 V (vs. RHE) on simulated FeN_4 and D-Fe-N-C.

To further understand the intrinsic activity of the D-Fe-N-C catalyst in CO_2 RR, DFT calculations were performed to calculate the free energies of possible intermediates in the reaction pathways from CO_2 to CO by using the computational hydrogen electrode model and parameters reported in literature.[64-66] As the counterpart, we created a simulation model with a tetra-nitrogen atom coordinated Fe atom by replacing six C atoms in a graphene surface to represent the reported normal FeN_4 catalysts.[67] For the D-Fe-N-C catalyst, an axial -OH ligand was added to coordinate with the Fe single atom in the simulated FeN_4 catalyst model. The optimized structures and the optimal adsorption configurations of reaction intermediates were

shown in **Figure 3.22A** and **Figure 3.22B**. There are three elementary steps and two important intermediates (COOH* and CO*) in the CO_2 RR process. The free energy profiles at a potential of 0 V vs. RHE are shown in **Figure 3.22C**. From **Figure 3.22C**, we can find that the ΔG for the formation of COOH* over D-Fe-N-C and normal FeN_4 is 0.48 eV and 0.15 eV, respectively. The ΔG for the dissociation of COOH* assisted by proton-electron transfer to produce CO* and H_2O is downhill on both catalyst models. As for the final step of CO desorption, the ΔG over D-Fe-N-C and normal FeN_4 are 0.47 eV and 0.89 eV, respectively. It is obvious that the potential determining step (PDS) is COOH* formation (ΔG = 0.48 eV) on D-Fe-N-C, while for normal FeN_4, the CO desorption step is more difficult (ΔG = 0.89 eV). The free energy profiles at −0.48 V (vs. RHE) are shown in **Figure 3.22D**. As the potential becomes more negative, the ΔG for the formation of COOH* would decrease, whilst the ΔG for the non-electrochemical step of CO desorption would remain unchanged. Consequently, CO desorption becomes the most difficult step on both catalysts' surfaces at −0.48 V vs. RHE, while this step is much easier over the D-Fe-N-C catalyst than the normal FeN_4, thus, the performance of CO_2 RR on D-Fe-N-C catalyst is better.

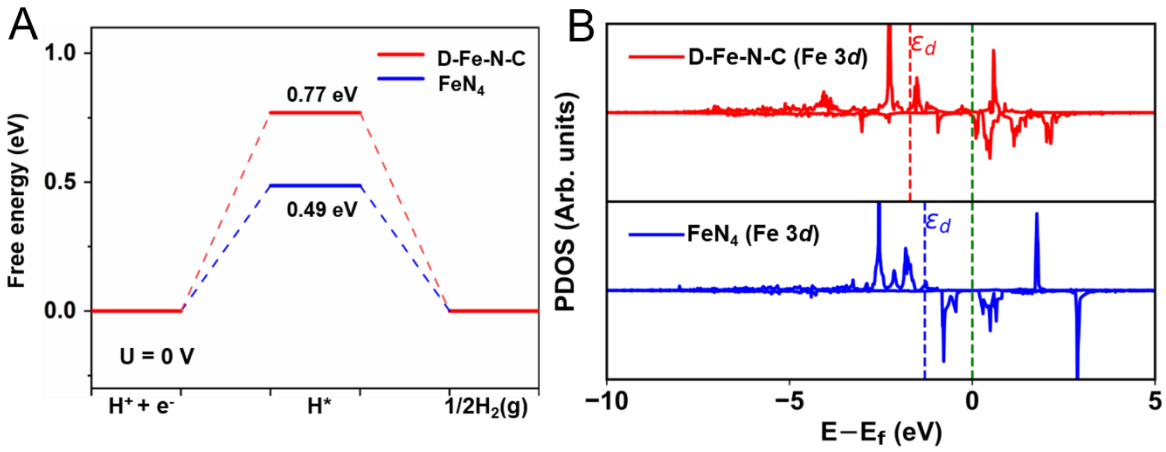

Figure 3.23 (A) Free energy profile for the HER at 0 V (vs. RHE) on D-Fe-N-C and FeN_4. (B) Projected d-density of states (PDOS) of D-Fe-N-C and FeN_4 surfaces.

In addition, HER as an important side reaction was also considered. The free energy profiles are shown in **Figure 3.23A**. It can be concluded that the HER is less active on D-Fe-N-C than on normal FeN_4. The projected density of states (PDOS) of D-Fe-N-C and normal FeN_4 surfaces were calculated to investigate the origin of the difference between adsorption of the reaction intermediates over these two catalysts (results are shown in **Figure 3.23B)**. We found that the d-band center of Fe over D-Fe-N-C downshifts to a more negative value than over normal FeN_4, leading to weaker CO adsorption over the former catalyst, thus improving the performance of the catalyst.[68]

3.4 Summary

In conclusion, we propose that the introduction of oxygen-containing subgroups into FeN_4 active sites can highly influence the electrochemical reduction of CO_2. In this way, via using a simple self-sacrificing oxygen and nitrogen-rich IRMOF-3, a robust Fe-based electrocatalyst consisting of atomically dispersed Fe-N sites with an axial -OH group and a little trace of Fe nanoparticles towards a high-efficient electrochemical CO_2 RR has been prepared. The detailed structures of prepared samples were systematically characterized and investigated via XRD, Raman, TGA, SEM, XPS, XAS and TEM etc. The proposed D-Fe-N-C catalyst with an axial -OH group was experimentally and theoretically proved to be more active than the previously reported normal FeN_4 based catalysts, showing an excellent catalytic behavior for CO conversion (FE (CO) of 95 %) at a low applied potential of −0.50 V vs. RHE. Meanwhile, DFT simulations suggested that the -OH subgroup could weaken the bonding energy of CO_2 RR intermediates, thus, shifting the CO_2 RR activity. Overall, we have been able to engineer the coordination environment of the active sites via axial -OH group to achieve high-efficient CO_2 RR and demonstrated that a universal synthesis approach involving a self-sacrificial MOFs with nitrogen and oxygen-rich ligands. The strategy presented here is a promising route to facilitate the rational design of efficient M-N-C catalysts with highly active dispersed MN_x moieties.

References

[1] H.B. Yang, S.-F. Hung, S. Liu, K. Yuan, S. Miao, L. Zhang, X. Huang, H.-Y. Wang, W. Cai, R. Chen, J. Gao, X. Yang, W. Chen, Y. Huang, H.M. Chen, C.M. Li, T. Zhang, B. Liu, Nature Energy, 3 (2018) 140-147.
[2] D.U. Nielsen, X.-M. Hu, K. Daasbjerg, T. Skrydstrup, Nature Catal., 1 (2018) 244-254.
[3] Q. Cheng, K. Mao, L. Ma, L. Yang, L. Zou, Z. Zou, Z. Hu, H. Yang, ACS Energy Lett., 3 (2018) 1205-1211.
[4] J. Huang, R. Buonsanti, Chem. Mater., 31 (2019) 13-25.
[5] T.N. Huan, N. Ranjbar, G. Rousse, M. Sougrati, A. Zitolo, V. Mougel, F. Jaouen, M. Fontecave, ACS Catal., 7 (2017) 1520-1525.
[6] W. Sheng, S. Kattel, S. Yao, B. Yan, Z. Liang, C.J. Hawxhurst, Q. Wu, J.G. Chen, Energy Environmental Science, 10 (2017) 1180-1185.
[7] T. Möller, W. Ju, A. Bagger, X. Wang, F. Luo, T. Ngo Thanh, A.S. Varela, J. Rossmeisl, P. Strasser, Energy & Environmental Science, 12 (2019) 640-647.
[8] Y. Wang, Y. Liu, W. Liu, J. Wu, Q. Li, Q. Feng, Z. Chen, X. Xiong, D. Wang, Y. Lei, Energy Environ. Sci., 13 (2020) 4609-4624.
[9] W. Choi, D.H. Won, Y.J. Hwang, J. Mater. Chem. A, (2020).
[10] N.T. Nesbitt, M. Ma, B.J. Trześniewski, S. Jaszewski, F. Tafti, M.J. Burns, W.A. Smith, M.J. Naughton, J. Phys. Chem. C, 122 (2018) 10006-10016.
[11] Y.S. Ham, S. Choe, M.J. Kim, T. Lim, S.-K. Kim, J.J. Kim, Appl. Catal. B: Environ., 208 (2017) 35-43.
[12] S. Zhang, Q. Fan, R. Xia, T.J. Meyer, Acc. Chem. Res., 53 (2020) 255-264.
[13] Y. Wu, G. Hu, C.L. Rooney, G.W. Brudvig, H. Wang, ChemSusChem, 13 (2020) 6296-6299.
[14] Y.-R. Wang, Q. Huang, C.-T. He, Y. Chen, J. Liu, F.-C. Shen, Y.-Q. Lan, Nature Commun., 9 (2018) 4466.
[15] S. Lin, C.S. Diercks, Y.-B. Zhang, N. Kornienko, E.M. Nichols, Y. Zhao, A.R. Paris, D. Kim, P. Yang, O.M. Yaghi, C.J. Chang, Science, 349 (2015) 1208-1213.
[16] H. Zhang, J. Li, S. Xi, Y. Du, X. Hai, J. Wang, H. Xu, G. Wu, J. Zhang, J. Lu, J. Wang, Angew. Chem. Int. Ed., 58 (2019) 14871-14876.
[17] A.S. Varela, W. Ju, A. Bagger, P. Franco, J. Rossmeisl, P. Strasser, ACS Catal., 9 (2019) 7270-7284.
[18] M. Li, H. Wang, W. Luo, P.C. Sherrell, J. Chen, J. Yang, Adv. Mater., 32 (2020) 2001848.
[19] G. Zhang, Y. Jia, C. Zhang, X. Xiong, K. Sun, R. Chen, W. Chen, Y. Kuang, L. Zheng, H. Tang, W. Liu, J. Liu, X. Sun, W.-F. Lin, H. Dai, Energy Environ. Sci., 12 (2019) 1317-1325.
[20] J. Li, P. Pršlja, T. Shinagawa, A.J. Martín Fernández, F. Krumeich, K. Artyushkova, P. Atanassov, A. Zitolo, Y. Zhou, R. García-Muelas, N. López, J. Pérez-Ramírez, F. Jaouen, ACS Catal., 9 (2019) 10426-10439.
[21] X.-M. Hu, H.H. Hval, E.T. Bjerglund, K.J. Dalgaard, M.R. Madsen, M.-M. Pohl, E. Welter, P. Lamagni, K.B. Buhl, M. Bremholm, M. Beller, S.U. Pedersen, T. Skrydstrup, K. Daasbjerg, ACS Catal., 8 (2018) 6255-6264.
[22] L. Gong, H. Zhang, Y. Wang, E. Luo, K. Li, L. Gao, Y. Wang, Z. Wu, Z. Jin, J. Ge, Z. Jiang, C. Liu, W. Xing, Angew. Chem. Int. Ed., 59 (2020) 13923-13928.

[23] Y. Wang, N.-Y. Huang, J.-Q. Shen, P.-Q. Liao, X.-M. Chen, J.-P. Zhang, J. Am. Chem. Soc., 140 (2018) 38-41.
[24] D. Wang, R. Huang, W. Liu, D. Sun, Z. Li, ACS Catal., 4 (2014) 4254-4260.
[25] F. Yang, X. Ma, W.-B. Cai, P. Song, W. Xu, J. Am. Chem. Soc., 141 (2019) 20451-20459.
[26] J. Liu, ACS Catalysis, 7 (2017) 34-59.
[27] B. Lu, Q. Liu, S. Chen, ACS Catal., 10 (2020) 7584-7618.
[28] L. Ye, Y. Ying, D. Sun, Z. Zhang, L. Fei, Z. Wen, J. Qiao, H. Huang, Angew. Chem. Int. Ed., 59 (2020) 3244-3251.
[29] B. Ravel, M. Newville, J. Synchrotron Rad., 12 (2005) 537-541.
[30] H. Baumgartel, Nachrichten aus Chemie, Technik und Laboratorium, 36 (1988) 650-650.
[31] J.J. Rehr, R.C. Albers, Rev. Modern Phys., 72 (2000) 621-654.
[32] S.J. Lyle, R.W. Flaig, K.E. Cordova, O.M. Yaghi, J. Chem. Education, 95 (2018) 1512-1519.
[33] S. Dou, J. Song, S. Xi, Y. Du, J. Wang, Z.-F. Huang, Z.J. Xu, X. Wang, Angew. Chem. Int. Ed., 58 (2019) 4041-4045.
[34] T. Zhang, J. Du, P. Xi, C. Xu, ACS Appl. Mater. Interfaces, 9 (2017) 362-370.
[35] T. Zheng, K. Jiang, N. Ta, Y. Hu, J. Zeng, J. Liu, H. Wang, Joule, 3 (2019) 265-278.
[36] C. Zhao, X. Dai, T. Yao, W. Chen, X. Wang, J. Wang, J. Yang, S. Wei, Y. Wu, Y. Li, J. Am. Chem. Soc., 139 (2017) 8078-8081.
[37] P.E. Blöchl, Phys. Rev. B, 50 (1994) 17953-17979.
[38] G. Kresse, J. Furthmüller, Phys. Rev. B, 54 (1996) 11169-11186.
[39] G. Kresse, J. Furthmüller, Computational Mater. Sci., 6 (1996) 15-50.
[40] G. Kresse, D. Joubert, Phys. Rev. B, 59 (1999) 1758-1775.
[41] J. Hafner, J. Comput. Chem., 29 (2008) 2044.
[42] J. Wellendorff, K.T. Lundgaard, A. Møgelhøj, V. Petzold, D.D. Landis, J.K. Nørskov, T. Bligaard, K.W. Jacobsen, Phys. Rev. B, 85 (2012) 235149.
[43] F. Studt, M. Behrens, E.L. Kunkes, N. Thomas, S. Zander, A. Tarasov, J. Schumann, E. Frei, J.B. Varley, F. Abild-Pedersen, J.K. Nørskov, R. Schlögl, ChemCatChem, 7 (2015) 1105-1111.
[44] F. Studt, F. Abild-Pedersen, J.B. Varley, J.K. Nørskov, Catal. Lett., 143 (2013) 71-73.
[45] R. Christensen, H.A. Hansen, T. Vegge, Catal. Sci. Technol., 5 (2015) 4946-4949.
[46] A.A. Peterson, F. Abild-Pedersen, F. Studt, J. Rossmeisl, J.K. Norskov, Energy Environ. Sci., 3 (2010) 1311-1315.
[47] K. Chan, C. Tsai, H.A. Hansen, J.K. Nørskov, ChemCatChem, 6 (2014) 1899-1905.
[48] Y. Luan, Y. Qi, H. Gao, R.S. Andriamitantsoa, N. Zheng, G. Wang, J. Mater. Chem. A, 3 (2015) 17320-17331.
[49] H. Zhang, S. Hwang, M. Wang, Z. Feng, S. Karakalos, L. Luo, Z. Qiao, X. Xie, C. Wang, D. Su, Y. Shao, G. Wu, J. Am. Chem. Soc., 139 (2017) 14143-14149.
[50] W. Ren, X. Tan, W. Yang, C. Jia, S. Xu, K. Wang, S.C. Smith, C. Zhao, Angew. Chem. Int. Ed., 58 (2019) 6972-6976.
[51] X. Ao, W. Zhang, Z. Li, J.-G. Li, L. Soule, X. Huang, W.-H. Chiang, H.M. Chen, C. Wang, M. Liu, X.C. Zeng, ACS Nano, 13 (2019) 11853-11862.
[52] C. Zhao, Y. Wang, Z. Li, W. Chen, Q. Xu, D. He, D. Xi, Q. Zhang, T. Yuan, Y. Qu, J. Yang, F. Zhou, Z. Yang, X. Wang, J. Wang, J. Luo, Y. Li, H. Duan, Y. Wu, Y. Li, Joule, 3 (2019) 584-594.

[53] H. Tan, Y. Li, J. Kim, T. Takei, Z. Wang, X. Xu, J. Wang, Y. Bando, Y.-M. Kang, J. Tang, Y. Yamauchi, Adv. Sci., 5 (2018) 1800120.
[54] Y. Lou, J. Liu, M. Liu, F. Wang, ACS Catal., 10 (2020) 2443-2451.
[55] J. Wang, R. You, C. Zhao, W. Zhang, W. Liu, X.-P. Fu, Y. Li, F. Zhou, X. Zheng, Q. Xu, T. Yao, C.-J. Jia, Y.-G. Wang, W. Huang, Y. Wu, ACS Catal., 10 (2020) 2754-2761.
[56] V. Harnchana, S. Chaiyachad, S. Pimanpang, C. Saiyasombat, P. Srepusharawoot, V. Amornkitbamrung, Sci. Rep., 9 (2019) 1494.
[57] Y. Chen, S. Ji, Y. Wang, J. Dong, W. Chen, Z. Li, R. Shen, L. Zheng, Z. Zhuang, D. Wang, Y. Li, Angew. Chem. Int. Ed., 56 (2017) 6937-6941.
[58] O.S. Bushuyev, P. De Luna, C.T. Dinh, L. Tao, G. Saur, J. van de Lagemaat, S.O. Kelley, E.H. Sargent, Joule, 2 (2018) 825-832.
[59] J. Gu, C.-S. Hsu, L. Bai, H.M. Chen, X. Hu, Science, 364 (2019) 1091-1094.
[60] C.W. Li, M.W. Kanan, J. Am. Chem. Soc., 134 (2012) 7231-7234.
[61] C.-W. Kung, C.O. Audu, A.W. Peters, H. Noh, O.K. Farha, J.T. Hupp, ACS Energy Lett., 2 (2017) 2394-2401.
[62] C.F. Wen, F. Mao, Y. Liu, X.Y. Zhang, H.Q. Fu, L.R. Zheng, P.F. Liu, H.G. Yang, ACS Catal., 10 (2020) 1086-1093.
[63] T. Li, C. Yang, J.-L. Luo, G. Zheng, ACS Catal., 9 (2019) 10440-10447.
[64] J.K. Nørskov, J. Rossmeisl, A. Logadottir, L. Lindqvist, J.R. Kitchin, T. Bligaard, H. Jónsson, J. Phys. Chem. B, 108 (2004) 17886-17892.
[65] H. Liu, J. Liu, B. Yang, Phys. Chem. Chem. Phys., 21 (2019) 9876-9882.
[66] H. Liu, J. Liu, B. Yang, Phys. Chem. Chem. Phys., 22 (2020) 9600-9606.
[67] J. Li, J. Liu, B. Yang, J. Energy Chem., 53 (2021) 20-25.
[68] X. Liu, H. Liu, C. Chen, L. Zou, Y. Li, Q. Zhang, B. Yang, Z. Zou, H. Yang, Nano Res., 12 (2019) 1651-1657.

Chapter 4

Quasi-Double-Star Nickel and Iron Active Sites for High-Efficient Carbon Dioxide Electroreduction

4.1 Introduction

Severe environmental problems have triggered the development of the electrochemical CO_2 reduction reaction (CO_2 RR) in order to mitigate the high atmospheric CO_2 concentration at ambient conditions and allow the production of useful and added value chemicals (e.g. CO, HCOOH, CH_4, CH_3CH_2OH).[1, 2] However, the efficiency of CO_2 RR is far from satisfactory due to the inherent inertness of CO_2 molecules and the parallel presence of the competitive hydrogen evolution reaction (HER) during the electrocatalytic processes.[3-5] Therefore, many research works have been devoted to design cost-friendly electrocatalysts for achieving a high CO_2 conversion efficiency.

As a frontier in materials science, single-atom catalysts (SACs) with a higher density of exposed catalytic sites at an atomic level, have recently emerged, showing a great potential in the field of CO_2 RR, due to their high selectivity and suppression of the competing HER.[6-10] Typically, Ni-based SACs have been the focus of interest for the CO generation because of their high Faradaic efficiencies (FEs).[11-15] For example, Wen et al. reported that Ni-N-C catalysts exhibited an excellent CO_2 RR performance with a FE for CO over 99 % at −0.80 V vs. RHE.[16] A Ni single-atom catalyst loaded in a hollow mesoporous carbon sphere was fabricated by Xiong et al., delivering a high CO_2 RR selectivity (FE(CO) of 95 %) at −0.90 vs. RHE.[17] It is then well established that most of the Ni-N-C catalysts possess a high selectivity. However, as a counterpart, they usually show a high overpotential (generally > 600 mV vs. RHE), which is derived from their sluggish kinetics on Ni-N sites during the first proton-coupled electron transfer ($CO_2 + H^+ + e^- \rightarrow COOH^*$).[18, 19] These high overpotentials necessitate more energy to drive the CO_2 RR than that thermodynamically needed.[20, 21] In light of this, researchers spared no effort in optimizing the Ni-N-C catalysts to achieve a high FE(CO) at a low overpotential, thus, meeting the requirements of practical applications.[22-24]

In order to improve the catalytic activity on Ni-N-C catalysts, one direct method is to optimize the first reaction step to obtain a high performance in the overall CO_2-to-CO conversion process. In this way, 'tandem catalysis' is considered as one of the most inspiring strategies to break the linear scaling relations of the adsorption and desorption of reaction intermediates on the different active sites, thus, leading to an unprecedented catalytic ability.[10, 25-27] Moreover, the electronic interactions and configuration environment between two active sites would be regulated and hence influence their synergistic catalytic performance.[28-31] For instance, in comparison to metal single-atom sites, the formed double-metal active sites with their configuration structures can not only facilitate the O_2 adsorption, but also weak the O=O bonds, thus, boosting the efficiency of the oxygen reduction reaction (ORR).[30, 32, 33] With this in mind, we propose that a bimetallic catalyst should hold the potential for high efficiency CO_2 RR, although such double metal-atom catalysts are still in their infancy towards CO_2 RR.[10] In the present work, we have combined the advantages of both Ni-N-C and Fe-N based catalysts. Herein, we have prepared a Ni/Fe based catalyst with a quasi-double-star local structure (see **Figure 4.1**), aiming to achieve a high selectivity at a low overpotential during CO_2 RR. On one hand, Ni-N-C catalysts possess a rapid desorption of *CO ($CO^* \rightarrow CO + *$) due to weak bonding of CO, whereas Fe-N active sites generally show a low overpotential for CO_2 RR because of the fast first proton-coupled electron transfer.[19] The cooperation of closely positioned Fe and Ni active sites in a catalyst might act as a nano-reactor, and significantly, affect different reaction steps on the two separated active sites, enhancing the CO_2 RR activity and selectivity. In addition, the presence of Fe adjacent to the Ni sites in a specific environment could influence the electron density and configuration environment between both active sites, and thus facilitate the adsorption and desorption of intermediates in the CO_2 reduction process.[33] Specifically, via a one-pot solvothermal synthesis, instead of a slower and less efficient multi-step doping process, we have prepared ternary metal-organic frameworks (MOFs) by rationally controlling Ni and Fe additive amounts in Zn-based IRMOF-3. hen, the adjacent Ni and Fe double active sites were formed via a simple

pyrolysis. As a result, the optimized Ni_7/Fe_3-N-C sample shows an excellent selectivity to CO evolution (FE_{CO} is 98 %) at a low overpotential (390 mV vs. RHE), which are superior to both single metal counterparts (Ni-N-C and Fe-N-C catalysts) and other state-of-the-art single/double atom catalysts. Meanwhile, DFT results reveal that compared to Ni-N-C catalysts, this bimetallic catalyst with neighboring Ni and Fe sites could facilitate the formation of COOH*. Moreover, the Ni/Fe-N-C catalyst not only could boost the desorption of CO*, but also limit the undesired HER in comparison to Fe-N-C, thus, leading to a win-win activity towards CO_2 RR. Consequently, the excellent catalytic activity is attributed to the synergistic effect between the adjacent Ni and Fe active sites, which plays an important role in regulating the binding energy of different intermediates during the adsorption and desorption processes, influencing different reaction steps towards CO_2 RR. This work not only demonstrates that the catalysts with adjacent double-metal single atoms are promising electrocatalysts for CO_2 RR, but also proves that such double metal sites can perfectly work as a nano-reactor, influencing different reaction steps on different active sites.

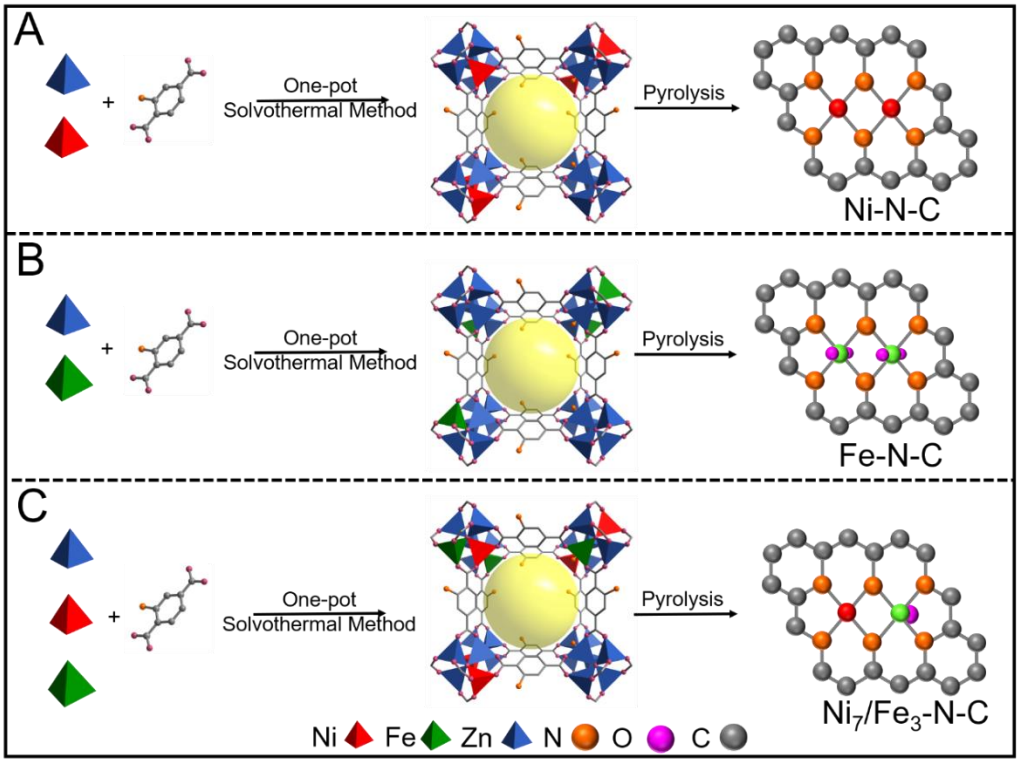

Figure 4.1 Schematic illustration of the preparation process of (A) Ni-N-C, (B) Fe-N-C and (C) Ni_7/Fe_3-N-C samples together with the schematics of the quasi double-star structure.

The Ni/Fe-N-C sample was synthesized using a two-step procedure, as shown in **Figure 4.1C**. First, a Ni and Fe co-doped Zn-IRMOF-3 was prepared by a simple one-pot solvothermal method. For comparison, single metal (Fe or Ni) doped-Zn-IRMOF-3 was also synthesized through the same method only containing Fe or Ni salt solutions (**Figure 4.1A** and **Figure 4.1B**). Afterwards, the Ni-N-C, Fe-N-C and Ni/Fe-N-C catalysts were obtained by a simple pyrolysis under Ar atmosphere. The detailed synthesis procedures are included in **4.2 experimental section**.

4.2 Experimental Section

4.2.1 Materials and Characterizations

4.2.1.1 Materials

If not specified, all chemical reagents were purchased from Sigma-Aldrich. Zinc nitrate hexahydrate ($Zn(NO_3)_2 \cdot 6H_2O$), 2-Aminoterphthalic acid, iron chloride hexahydrate ($FeCl_3 \cdot 6H_2O$), cobaltous nitrate hexahydrate ($Co(NO_3)_2 \cdot 6H_2O$), nickel chloride hexahydrate ($NiCl_2 \cdot 6H_2O$), N,N-dimethylformamide (DMF), sodium thiocyanate (NaSCN), ethanol and sodium bicarbonate ($NaHCO_3$) were all of analytical grade and used as received without further purification. Meanwhile, all solutions were prepared with Milli-Q water (DI-H_2O, Ricca Chemical, ASTM Type I). The carbon paper was purchased from Alfa Aesar. The Nafion (N-117 membrane, 0.18 mm thick) was also purchased from Alfa Aesar and kept in 0.5 M NaOH solution.

4.2.1.2 Characterization

The X-ray diffraction patterns (XRD) were obtained through a Bruker D4 X-ray powder diffractometer using Cu Kα radiation (1.54184 Å). Field emission scanning electron microscopy (FESEM) images were collected on a FEI Magellan 400 L scanning electron microscope. The transmission electron microscopy (TEM) and high angle annular dark field scanning TEM (HAADF STEM) images were obtained in a Tecnai F20 field emission gun microscope with a 0.19 nm point-to-point resolution at 200 kV equipped with an embedded Quantum Gatan Image Filter for EELS analyses.

Images have been analyzed by means of Gatan Digital Micrograph software. Parts of HAADF-STEM images and elemental mapping (EDX) were obtained in a spherical aberration-corrected (AC) transmission electron microscope FEI Themis Z and operated at 200 kV. X-ray photoelectron spectroscopy (XPS) was performed on a Phoibos 150 analyser (SPECS GmbH, Berlin, Germany) in ultra-high vacuum conditions (base pressure 4×10^{-10} mbar) with a monochromatic aluminum Kα X-ray source (1486.74 eV). Binding energies (BE) were determined using the C 1s peak at 284.5 eV as a charge reference. Inductively coupled plasma-mass spectrometry (ICP-MS) measurements were carried out to determine the concentration of Fe. Brunauer-Emmett-Teller (BET) surface areas were measured using nitrogen adsorption at 77 K. Raman spectra were obtained using Senterra. Fourier transformed infrared (FTIR) spectroscopy data were recorded on an Alpha Bruker spectrometer. Thermogravimetric Analysis was measured by Pyris 1 TGA, Perkin Elmer.

4.2.1.3 XAFS Measurements

The X-ray absorption fine structure spectra (Fe K-edge) were collected at 1W1B station in Beijing Synchrotron Radiation Facility (BSRF). The storage rings of BSRF were operated at 2.5 GeV with an average current of 250 mA. Using Si(111) double-crystal monochromator, the data collection were carried out in transmission/fluorescence mode using ionization chamber. All spectra were collected in ambient conditions.

4.2.1.4 XAFS Analysis and Results

The acquired EXAFS data were processed according to the standard procedures using the ATHENA module implemented in the IFEFFIT software packages. The k^3-weighted EXAFS spectra were obtained by subtracting the post-edge background from the overall absorption and then normalizing with respect to the edge-jump step. Subsequently, k^3-weighted $\chi(k)$ data of Fe K-edge were Fourier transformed to real (R) space using a hanning windows (dk=1.0 $Å^{-1}$) to separate the EXAFS contributions from different coordination shells. To obtain the quantitative structural parameters around

central atoms, least-squares curve parameter fitting was performed using the ARTEMIS module of IFEFFIT software packages.[34-36]

4.2.2 Synthesis Methods

4.2.2.1 Preparation of Ni-IRMOF-3, Fe-IRMOF-3, Ni_x/Fe_y-IRMOF-3

In this procedure, the fabrication process of M-IRMOF-3 is similar to the reported in literature with minor modification.[37] In detail, 932 mg $Zn(NO_3)_2 \cdot 6H_2O$ were dissolved in 100 ml DMF under magnetic stirring at room temperature to form a homogeneous solution. 181 mg 2-aminoterphthalic acid was added into the above mixture under ultrasonic for 5 min at room temperature. Then, 70 µl $Ni(NO_3)_2 \cdot 6H_2O$ or $FeCl_3 \cdot 6H_2O$ solution (10 mg ml^{-1}, DMF) were dropwise injected into the above solution under ultrasonic stirring until the formation of a clear solution. The obtained homogeneous solution was transferred into the Teflon-lined stainless-steel autoclave and reacted at 100 °C for 24 h. After cooling to room temperature, the powder was collected by centrifugation, washed with ethanol and DMF several times to remove organic residual. The final products denoted as Ni-IRMOF-3 or Fe-IRMOF-3 were then dried in vacuum at 65 °C overnight. Similarly, the Ni_x/Fe_y-IRMOF-3 were harvested by adding $Ni(NO_3)_2 \cdot 6H_2O$ (63 µl, 56 µl, 49 µl, 42 µl, 35 µl) and $FeCl_3 \cdot 6H_2O$ (7 µl, 14 µl, 21 µl, 28 µl, 35 µl) solution with different quantities. We denoted the resulting sample as Ni_x/Fe_y-IRMOF-3.

4.2.2.2 Preparation of 2-Ni_7/Fe_3-IRMOF-3

The 100 mg IRMOF-3 powder was dispersed in 10 ml DMF under ultrasound for 10 min at room temperature. After forming a homogeneous solution, $FeCl_3 \cdot 6H_2O$ (10 mg ml^{-1}, 9 µl) and $Ni(NO_3)_2 \cdot 6H_2O$ (10 mg ml^{-1}, 21 µl) solution were dropwise injected into the above solution under ultrasonic stirring for 5 min at room temperature. Next, the mixed solution was left under magnetic stirring at room temperature for 3 h. After reacting, the powder was collected by centrifugation, washed with ethanol and DMF

several times to remove organic residual and dried in vacuum at 65 °C overnight. Then, we obtained the 2-Ni_7/Fe_3-IRMOF-3 sample.

4.2.2.3 Preparation of Ni-N-C, Fe-N-C, Ni_x/Fe_y-N-C and 2-Ni_7/Fe_3-N-C

As-prepared Ni-IRMOF-3 (or Fe-IRMOF-3, Ni_x/Fe_y-N-C and 2-Ni_7/Fe_3-N-C) powders were put in a porcelain boat. Subsequently, the samples were placed in a tube furnace and heated at 950 °C for 2 h with a heating rate of 5 °C min^{-1} under an Ar atmosphere to yield disperse Ni-N-C, Fe-N-C, Ni_x/Fe_y-N-C and 2-Ni_7/Fe_3-N-C.

4.2.2.4 Preparation of Physical Mixture Ni_7/Fe_3-N-C (Labelled as Ni_7/Fe_3-N-C-P)

For the preparation of the Ni_7/Fe_3-N-C-P sample, 3.5 mg of Ni-N-C powder were directly added into 1.5 mg of Fe-N-C powder. The powder was then mixed with a spoon.

4.2.3 Ink Preparation

2 mg synthesized different samples and 50 μl 5 wt% Nafion solutions were dissolved in ethanol (1 ml) and ultrasonicated for 1 h to form evenly suspension for the further electrochemical experiments. To prepare the working electrode, 500 μL above as-prepared inks were dropped onto the two sides of the carbon paper electrode with 1×1 cm^2 and then dried at room temperature for a few minutes, giving a catalyst loading mass of ~1 mg cm^{-2}.

4.2.4 Electrochemical Measurement

The electrocatalytic performance of different catalysts was measured at room temperature by using a gas-tight H-cell with two-compartments separated by a cation exchange membrane (Nafion N-117 membrane) with a continuously Ar or CO_2 gas injection. Each compartment contained 70 ml electrolyte (0.5 M $NaHCO_3$ made from de-ionized water). In a typical experiment, a standard three electrode setup in 0.5 M $NaHCO_3$ solution was assembled: an Ag/AgCl electrode as a reference electrode, a Pt plate as a counter electrode and a carbon paper coated with the different samples as a

working electrode (surface area = 1 cm^2). The potentials were measured versus Ag/AgCl and converted to the reversible hydrogen electrode (RHE) according to the following equation: $E_{RHE} = E^0_{Ag/AgCl} + E_{Ag/AgCl} + 0.059 \times pH$, pH=7.[38] All electrochemical results were showed without iR-compensation by using a computer-controlled BioLogic VMP3 electrochemical workstation. Meanwhile, the linear sweep voltammetry (LSV) was performed at a scan rate of 20 mV s^{-1} from 0 V to −1.5 V vs. Ag/AgCl in Ar-saturated 0.5 M $NaHCO_3$ (pH=8.5) and CO_2-saturated 0.5 M $NaHCO_3$ (pH=7) as supporting electrolyte. The cyclic voltammetry (CV) was performed at a scan rate of 20 mV s^{-1}. Moreover, electrochemical impedance spectroscopy (EIS) of different samples was carried out in a frequency range from 100 kHz to 100 mHz.

Before the electrochemical CO_2 reduction experiments, an average rate of 20 ml min^{-1} Ar was injected into cathodic electrolyte in order to form an Ar-saturated solution. During electrochemical CO_2 reduction experiments, the CO_2 gas was delivered at an average rate of 20 ml min^{-1} at room temperature and ambient pressure, measured downstream by a volumetric digital flowmeter. The gas phase composition was analyzed by gas chromatography (GC) during potentiostatic measurements every 20 min. The calibration of peak area vs. gas concentration was used for the molar quantification of each gaseous effluent. The Faradaic efficiency was calculated by determining the number of coulombs needed for each product and then dividing by the total charge passed during the time of the GC sampling according to the flow rate. Liquid products were analyzed afterwards by quantitative ^{1}H-NMR using water as the deuterated solvent.

4.2.5 Calculation Method

Details concerning the Faradaic Efficiency (FE) calculations are shown below.[11, 13, 38]

The partial current density for a given gas product was calculated as below:

$$j_i = x_i \times V \times \frac{n_i F P_0}{RT} \times (electrode\ area)^{-1}$$

Where x_i is the volume fraction of a certain product determined by online GC referenced to calibration curves from three standard gas samples, V is the flow rate, n_i is the number of electrons involved, P_0= 101.3 kPa, F is the Faraday constant, and R is the gas constant. The corresponding FE at each potential is calculated by

$$FE = \frac{j_i}{j} \times 100\%$$

4.2.6 DFT Calculations:

The spin-polarized DFT calculations with projector augmented wave (PAW) method[39-42] were performed using the Vienna ab initio Simulation Package (VASP) code.[43] The Bayesian error estimation functional with van der Waals correlation (BEEF-vdW) was employed to set the plane wave basis.[44] The convergence criteria were 0.05 eV/ Å in force and 1×10^{-4} eV in energy and the plane wave cutoff was 500 eV. The Monkhorst–Pack mesh k-point grids were 2×2×1 for all models. All the vacuum thicknesses were higher than 15 Å. With the BEEF-vdW function, the energy of the gas phase molecules gave a systematic correction by +0.41 and +0.09 eV for gaseous CO_2 and H_2, respectively.[45-47] For the electroreduction of CO_2 to CO, the following elementary steps were considered:

$CO_2(g) + * + H^+(aq) + e^- \leftrightarrow COOH*$ (Equation S.1)

$COOH* + H^+(aq) + e^- \leftrightarrow CO* + H_2O(l)$ (Equation S.2)

$CO* \leftrightarrow CO(g) + *$ (Equation S.3)

where (g), (aq) represent the gaseous phase and aqueous phase, respectively. The *, COOH* and CO* represent free site, adsorption state of COOH and CO, respectively. The reaction free energies of each step was calculated by the following formula:

$$G = E_{\mathrm{DFT}} + E_{\mathrm{ZPE}} + \int C_p \mathrm{d}T - TS + E_{\mathrm{sol}}$$ (Equation S.4)

the E_{DFT} is the DFT calculated energy, E_{ZPE} is the zero-point energy, C_p is the constant pressure heat capacity, T is temperture, S is the entropy. The E_{sol} is solvation

correction, which is -0.1 eV for CO* and -0.25 eV COOH*.[48] The temperature for the reaction is considered as 298.15 K here.

4.3 Results and Discussion

4.3.1 Characterization of Prepared MOFs Precursors

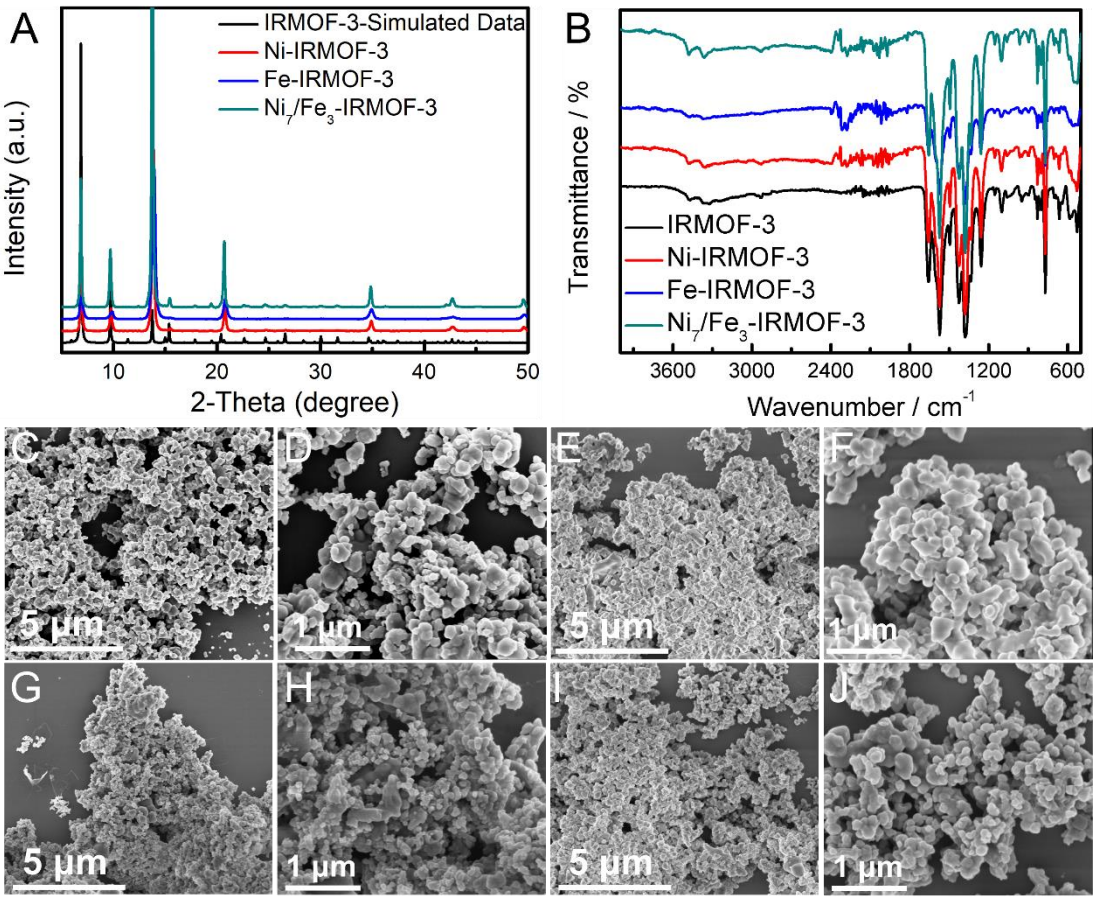

Figure 4.2 (A) XRD patterns and (B) FTIR spectra of Ni-IRMOF-3, Fe-IRMOF-3 and Ni_7/Fe_3-IRMOF-3. SEM images of (C and D) IRMOF-3, (E and F) Ni-IRMOF-3, (G and H) Fe-IRMOF-3, (I and J) Ni_7/Fe_3-IRMOF-3.

X-ray diffraction (XRD) analysis indicates that the Ni and/or Fe-doped MOF precursors and IRMOF-3 possessed a similar crystal structure, according to their XRD patterns (**Figure 4.2A**).[49] Meanwhile, as shown in the Fourier transform infrared (FTIR) spectra (**Figure 4.2B**), compared to the pure IRMOF-3, the absence of obvious differences on the characteristic peaks proved that introducing Ni and/or Fe did not change the functional groups of IRMOF-3. Furthermore, the structures, morphologies and element distributions of the different precursors were studied by field emission

scanning electron microscopy (FE-SEM). As revealed by FE-SEM (**Figure 4.2C-J**), the as-prepared Ni/Fe-IRMOF-3 and the corresponding single M-IRMOF-3 exhibited a similar morphology, maintaining the initial spherical shapes of IRMOF-3.

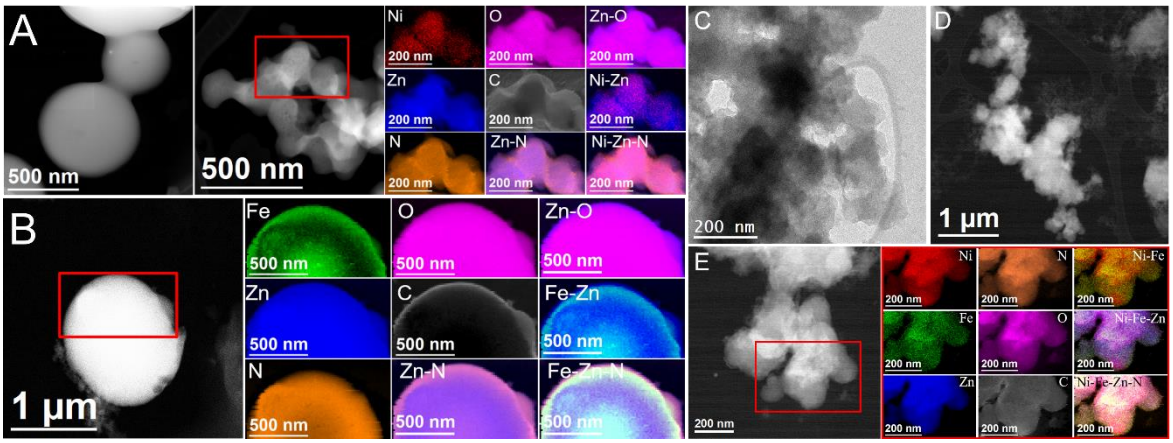

Figure 4.3 HAADF STEM image of (A) Ni-IRMOF-3, (B) Fe-IRMOF-3 and representative EELS chemical composition maps. (C) BF TEM, (D and E) HAADF STEM of Ni_7/Fe_3-IRMOF-3 as well as representative EELS chemical composition maps obtained from the red squared area.

In addition, transmission electron microscopy (TEM) was performed to observe the morphologies and element distributions for the different precursors, as shown in **Figure 4.3**. The representative high angle annular dark-field scanning transmission electron microscopy (HAADF STEM) images showed that the Fe-IRMOF-3, Ni-IRMOF-3 and Ni_7/Fe_3-IRMOF-3 catalysts exhibited spheroidal particle-shape structures. The elemental distribution of these materials was investigated by electron energy loss spectroscopy (EELS), demonstrating the uniform dispersions of C, N, O and Zn elements throughout all the samples. In addition, we also found a uniform distribution of Ni or/and Fe, when present, in the Ni-IRMOF-3, Fe-IRMOF-3 and Ni_7/Fe_3-IRMOF-3 samples.

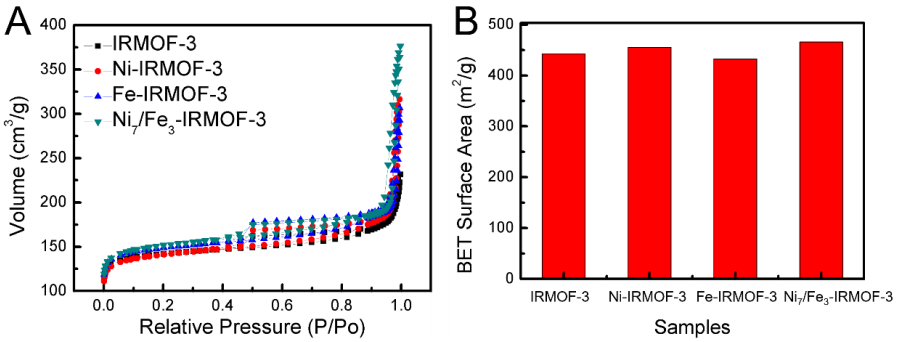

Figure 4.4 (A) N_2 adsorption and desorption isotherm and (B) BET surface areas for IRMOF-3, Ni-IRMOF-3, Fe-IRMOF-3 and Ni_7/Fe_3-IRMOF-3.

Figure 4.4A shows the typical nitrogen isothermal adsorption/desorption curves for the different samples. Significantly, the prepared precursors exhibited the typical type IV N2 adsorption isotherm. In addition, the surface area values calculated by Brunauer-Emmett-Teller (BET) analyses suggest that the porosity of the initial IRMOF-3 remained almost intact after the introduction of the Ni and/or Fe species, suggesting that the pores were not filled by metallic precipitates or clusters, during the one-pot synthesis process (**Figure 4.4B**).

4.3.2 Characterization of Samples after Pyrolysis

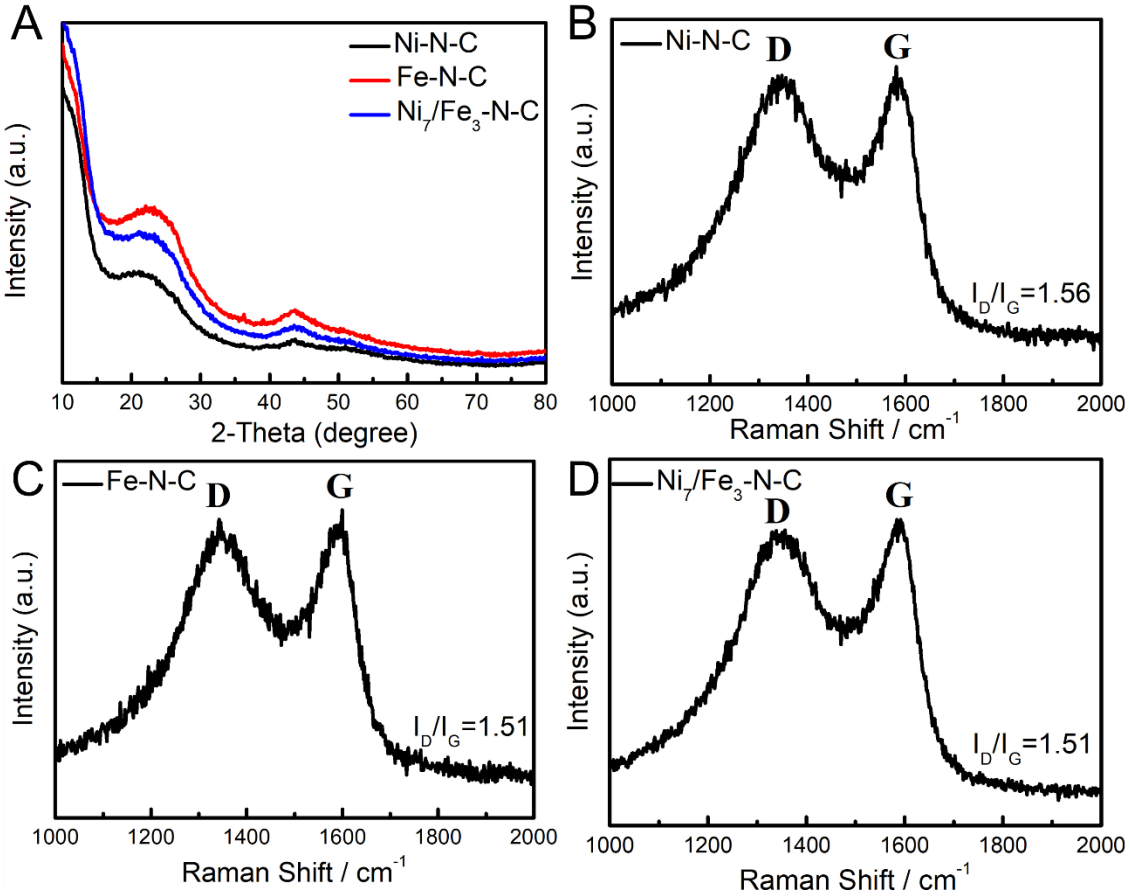

Figure 4.5 (A) XRD patterns (B-D) Raman spectra of Ni-N-C, Fe-N-C and Ni_7/Fe_3-N-C.

After pyrolysis, the crystal structure of Ni-N-C, Fe-N-C and Ni_7/Fe_3-N-C catalysts was also analysed by XRD in **Figure 4.5A**. Clearly, these three samples show similar diffraction patterns with two broad peaks at about 24° and 44°, representing the (002) and (100) diffraction planes for graphite carbon, which indicates the existence of a carbon matrix in these samples after pyrolysis.[50, 51] Moreover, the characteristic

peaks of metal hybrids are absent in the XRD patterns of the pyrolyzed products. The Raman spectra of Ni-N-C, Fe-N-C and Ni_7/Fe_3-N-C samples are shown in **Figure 4.5B-D**, presenting two main peaks at around 1365 and 1590 cm^{-1} corresponding to the typical D and G bands of graphitic carbon. Compared to the Raman spectra of the pure Ni-N-C sample, the I_d/I_g band intensity ratio of Fe-N-C and Ni_7/Fe_3-N-C samples was slightly lower, suggesting a smaller number of defects and a higher extent of graphitization in these two samples.[52, 53]

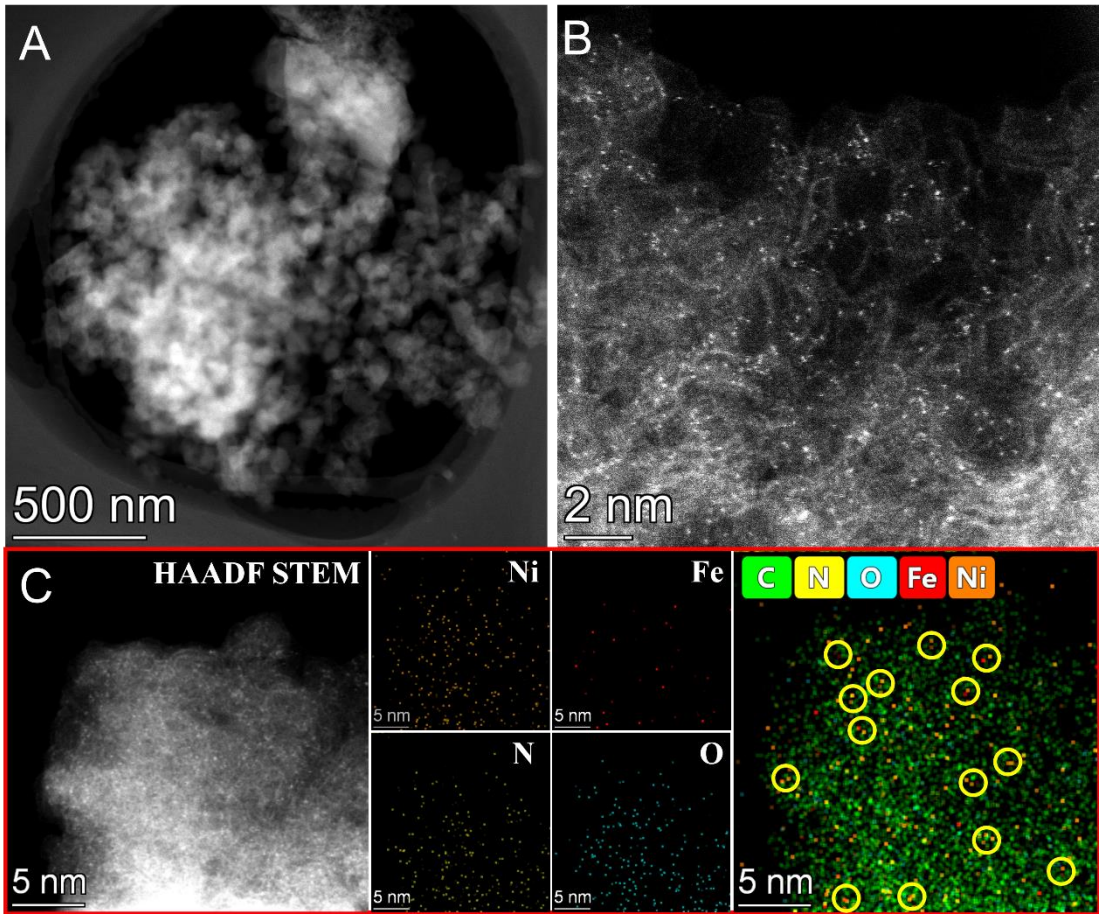

Figure 4.6 (A) Low magnification, and (B and C) High magnification aberration-corrected HAADF-STEM image, (D) HAADF-STEM and representative EDS chemical composition of Ni_7/Fe_3-N-C sample.

Aberration corrected (AC) HAADF STEM analyses was used to determine the morphology, structure and element distribution in the Ni_7/Fe_3-N-C sample, as displayed in **Figure 4.6**. **Figure 4.6A** shows that the as-prepared Ni_7/Fe_3-N-C is still composed of irregular shape nanoparticles, indicating that the pyrolysis process did not completely

destroyed the pristine structure of the MOF precursors. More importantly, we could not observe the presence of small bright clusters in low magnification HAADF STEM images, revealing that there are no metal nanoparticles or cluster formed during the Ni_7/Fe_3-N-C catalyst formation process, which is consistent with the XRD results (**Figure 4.5A**). AC HAADF STEM images (**Figure 4.6B-C**), validate the presence of homogeneously distributed high density of metal single-atoms, directly proving that the Ni and Fe have successfully been introduced as atomically dispersed sites in the Ni_7/Fe_3-N-C sample. In addition, the elemental distribution was elucidated by energy dispersive X-ray spectroscopy (EDS), which not only revealed the homogeneous distribution of Ni, Fe, O and N dispersed in the whole carbon matrix (**Figure 4.6D**), but also clearly identified the existence of many neighboring dual-dots marked by the yellow circles, suggesting the formation of adjacent Ni and Fe sites. These results indicate that neighboring Ni and Fe sites could be successfully prepared, although few Ni or Fe individual sites also exist.

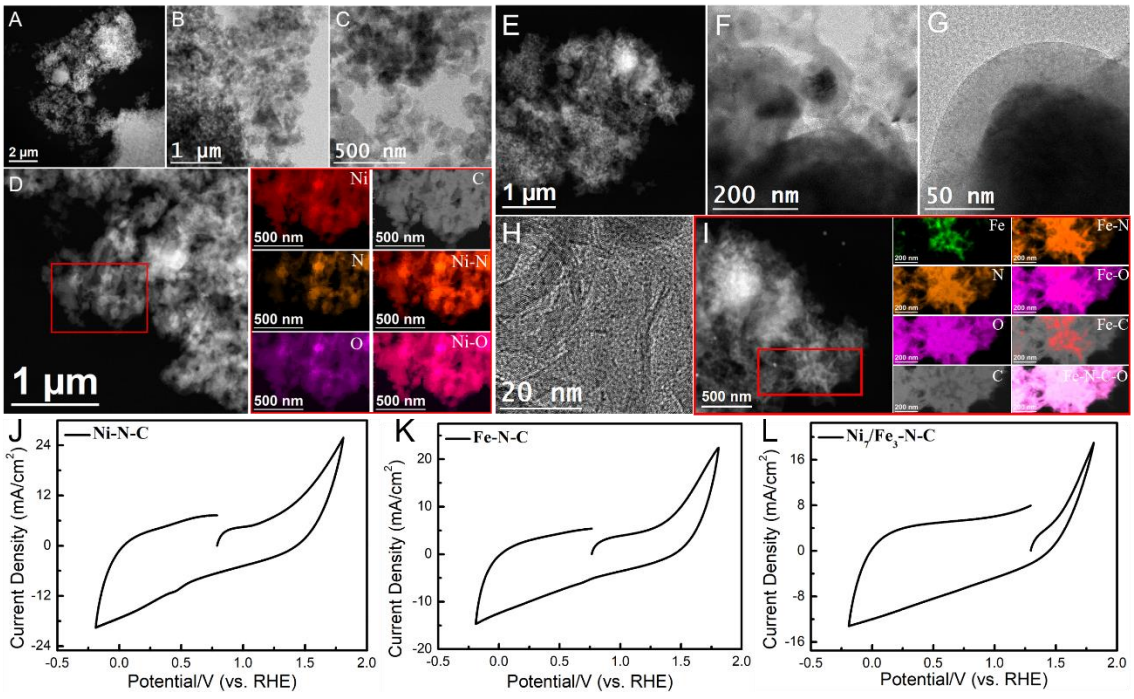

Figure 4.7 (A-D) HAADF STEM image of Ni-N-C and representative EELS chemical composition maps obtained from the red squared area of the STEM micrograph. Individual Ni $L_{2,3}$-edges at 855 eV (green), N K-edges at 401 eV (orange), O K-edges at 532 eV (pink) and C K-edges at 285 eV (grey) as well as composites of Ni-N and Ni-O. (E-I) HAADF STEM, BF TEM and HRTEM image of Fe-N-C as well as representative EELS chemical composition maps

obtained from the red squared area of the STEM micrograph. CV curves of (J) Ni-N-C, (K) Fe-N-C and (L) Ni_7/Fe_3-N-C in 0.5 M $NaHCO_3$ electrolyte.

In addition, the HAADF STEM images of Ni-N-C and Fe-N-C are shown in **Figure 4.7A-I**. Multiple areas of the Ni-N-C sample were examined and no presence of Ni nanoparticles (precipitates) could be observed, proving that Ni atoms were also atomically dispersed, in agreement with the XRD results. However, it is worth noting that some Fe nanoparticles could be observed in **Figure 4.7E-G**, indicating that a small partial Fe aggregation occurred in the Fe-N-C sample. Interestingly, the cyclic voltammetry (CV) curves in **Figure 4.7K**, did not show the typical Fe reduction/oxidation redox peaks in the Fe-N-C sample, which was similar to the result obtained for the Ni_7/Fe_3-N-C catalyst, suggesting that the Fe clusters could not directly contact the solution to react. This result is rationalized by the presence of a carbon shell over the Fe clusters as observed by HRTEM (**Figure 4.7G**), which could cut off the reaction between Fe particles and the solution.[54]

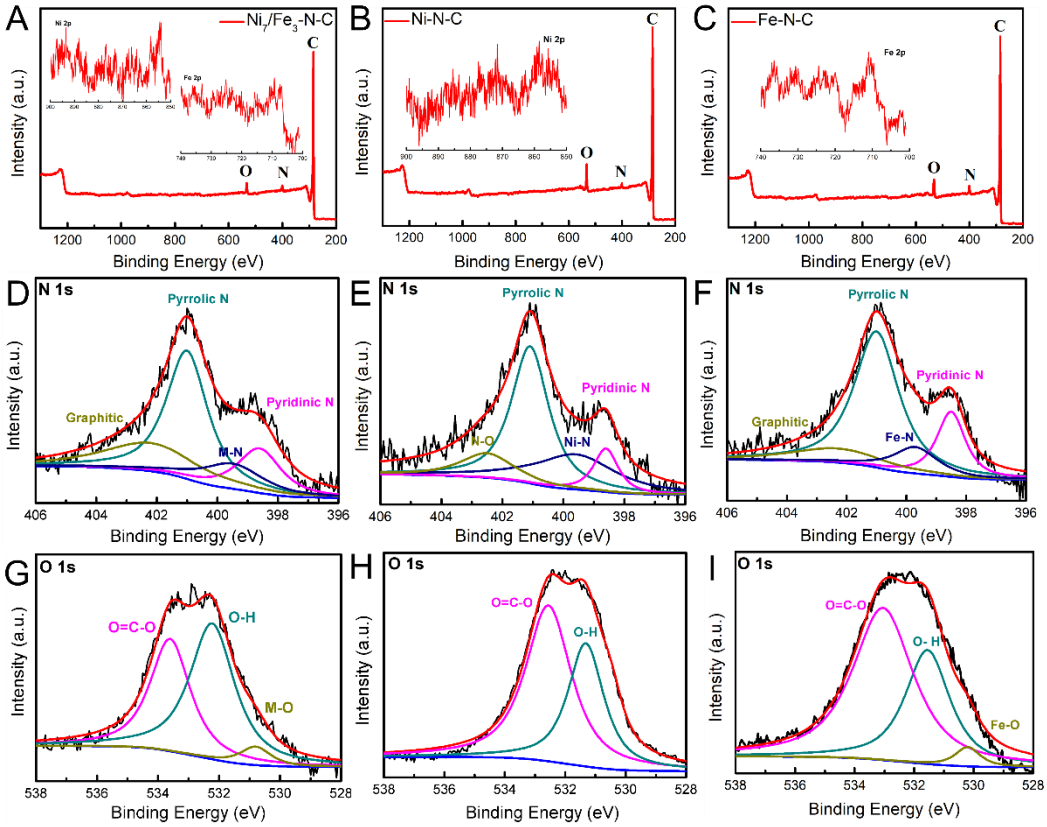

Figure 4.8 XPS spectra for the survey scan of (A) Ni_7/Fe_3-N-C, (inset) Ni 2p and Fe 2p, (B) Ni-N-C, (inset) Ni 2p, (C) Fe-N-C, (inset) Fe 2p. High-resolution XPS N 1s spectrum of (D) Ni_7/Fe_3-N-C, (E) Ni-N-C, (F) Fe-N-C, and O 1s spectrum of (G) Ni_7/Fe_3-N-C, (H) Ni-N-C, (I) Fe-N-C.

X-ray photoelectron spectroscopy (XPS) was used to characterize the catalysts' surfaces and compositions. The full survey scan XPS spectrum of Ni_7/Fe_3-N-C shown in **Figure 4.8A** indicates that only the elemental signals for C, N and O could be observed. Meanwhile, a similar phenomenon is observed in the full XPS spectrum survey scan for Ni-N-C and Fe-N-C catalysts, as shown in **Figure 4.8B-C**. The high-resolution N 1s spectrum (**Figure 4.8D-F**) of all samples can be de-convoluted into four components corresponding to pyridinic N (centred at 398.7 eV), pyrrolic N (401.0 eV), graphitic N (402.1 eV), and a porphyrin-like moiety at 399.5 eV corresponding to the metal-nitrogen (M-N) coordination.[19, 55] Notably, the high resolution O 1s spectroscopy deconvolution revealed the presence of the metal-O bond at 530 eV in Fe-N-C and Ni_7/Fe_3-N-C samples, potentially implying the retainment of M-O chelation after calcination because of the oxygen-rich IRMOF-3 precursors (**Figure 4.8G-I**).[56]

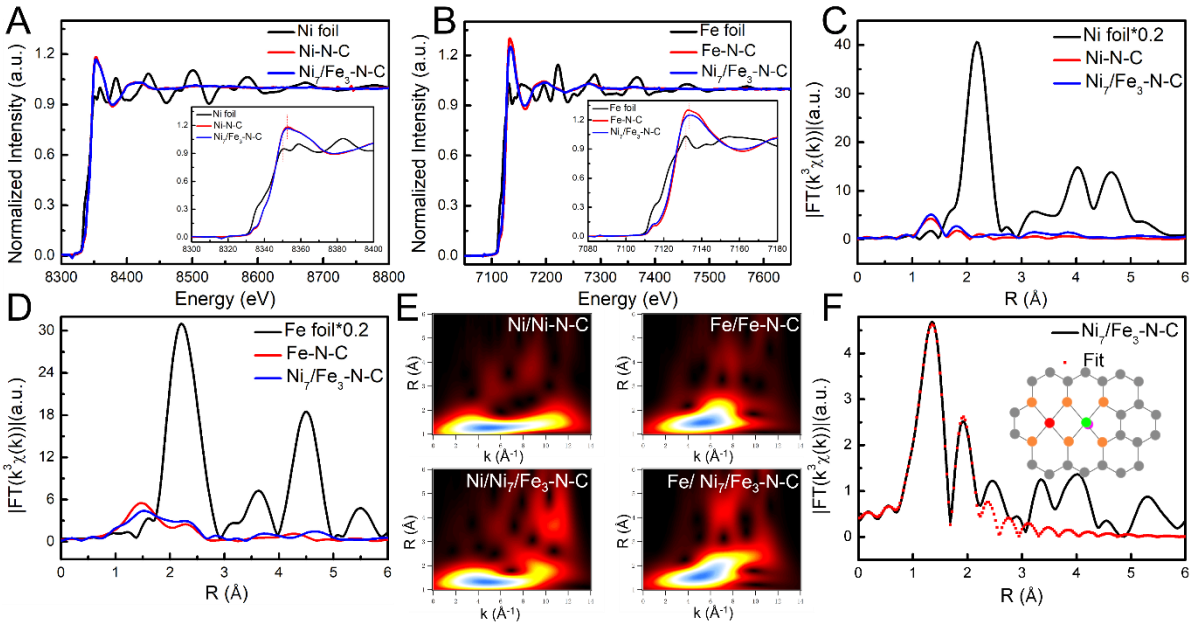

Figure 4.9 XANES spectra of the Ni-N-C, Fe-N-C and Ni_7/Fe_3-N-C at (A) Ni K-edge and (B) Fe K-edge. The insets are the magnified corresponding regions. EXAFS spectra at (C) Ni K-edge and (D) Fe K-edge. (E) WT-EXAFS of Ni-N-C, Fe-N-C and Ni_7/Fe_3-N-C. The corresponding Ni K-edge EXAFS fitting parameters for (F) Ni_7/Fe_3-N-C samples (Ni, Fe, O, N, C atoms are represented in red, green, pink, orange and grey, respectively).

To further uncover information on the local structure of the different samples, X-ray absorption spectroscopy (XAS) was performed at both Ni K-edge and Fe K-edge for Ni_7/Fe_3-N-C and the corresponding single M-N-C catalysts. The XANES K-edge characterization was used to explore the structure and valence of the metal in the active sites.[33] As shown in the Ni K-edge X-ray absorption near-edge structure (XANES) of a reference Ni foil, Ni-N-C and Ni_7/Fe_3-N-C (**Figure 4.9A**), the Ni K-edge spectra of both Ni-N-C and Ni_7/Fe_3-N-C shift towards higher binding energy compared to that of the Ni foil, suggesting a positive charge state of Ni atoms in the as-prepared catalysts (Ni-N-C and Ni_7/Fe_3-N-C).[11] The insets of Fig. 3d and Fig. S19a highlight the pre-edge features at approximately 8334 eV, corresponding to the signals of 3d and 4p orbital hybridization of the Ni central atoms.[18] Meanwhile, the increased peak intensity in Ni_7/Fe_3-N-C, compared to the Ni-N-C, is ascribed to the distorted D_{4h} symmetry.[18, 57] These results certify that Ni species in Ni-N-C and Ni_7/Fe_3-N-C exhibit a similar coordination path between metal centres and pyridinic/pyrrolic N, but the D_{4h} symmetry in Ni_7/Fe_3-N-C is distorted by another coordination path such as the

presence of a neighbouring Fe coordination, in good agreement with the dual bright dots observed in AC HAADF STEM and EDS images (**Figure 4.6D)**.[19] Similarly, **Figure 4.9B** present the Fe K-edge spectra for the Ni_7/Fe_3-N-C catalyst along with the Fe foil reference and the Fe-N-C sample for comparison. Here, XANES clearly reveals that the Fe K-edge energy absorption threshold of Ni_7/Fe_3-N-C and Fe-N-C are different from the Fe foil reference, which indicates that the valence of Fe in Ni_7/Fe_3-N-C and Fe-N-C catalysts is higher than Fe^0.[58] Moreover, as shown in **Figure 4.9B inset**, the presence of the pre-edge peak at around 7117 eV, which is the fingerprint of D_{4h} symmetry, can be attributed to the Fe-N square planar configuration and the existence of Fe-N (O, C) coordination in Ni_7/Fe_3-N-C and Fe-N-C catalysts.[59] Additional information is obtained from the Fourier transform (FT) k^2-weighted $\chi(k)$ function of the Ni K-edge EXAFS of Ni-N-C and Ni_7/Fe_3-N-C catalysts, as shown in **Figure 4.9C**. The Ni-N-C and Ni_7/Fe_3-N-C spectra show a main peak at 1.35 Å corresponding to the Ni-N scattering path, which is quite different from that observed at the standard Ni foil at 2.2 Å assigned to the metal-metal path.[16, 19] From the Fourier transform (FT) k^2-weighted $\chi(k)$ function spectra of the Fe K-edge EXAFS of Fe-N-C and Ni_7/Fe_3-N-C catalysts (**Figure 4.9D**), the main peaks at 1.5 Å stand for Fe-N(O, C) bonds, respectively.[21, 58] Meanwhile, there is no obvious metal-metal path for Ni_7/Fe_3-N-C, corroborating the absence of Ni-Fe, Ni-Ni or Fe-Fe coordination. Wavelet-transform (WT) plots (**Figure 4.9E**) were conducted to further verify the coordination information of the Ni_7/Fe_3-N-C catalyst. One intensity maximum is present at about 4.0 $Å^{-1}$ in the Ni WT contour plots of the Ni-N-C and Ni_7/Fe_3-N-C catalysts, which can be assigned to the Ni-N pair.[3] The analysis results of the Fe WT contour plots for all the samples are similar to the Ni plots. Therefore, both the FT- and WT-EXAFS analyses demonstrate that Ni and Fe atoms are mainly present in the Ni_7/Fe_3-N-C sample as atomic dispersions. To verify the detailed atomic structure of Ni_7/Fe_3-N-C, we obtained their corresponding EXAFS spectra, as shown in **Figure 4.9F**. According to the fitting results and the corresponding fitting parameters, the Ni-N coordination number for Ni_7/Fe_3-N-C and Ni-N-C catalysts are 4.5 and 3.9, with a corresponding bond length of

1.84 Å and 1.87 Å, respectively. These latest results suggest that most of the single Ni atoms are coordinated with four nitrogen atoms on the Ni_7/Fe_3-N-C and Ni-N-C samples. In addition, the optimized Fe K-edge EXAFS spectra fitting results for the Ni_7/Fe_3-N-C catalyst showed a CN-value of 4.8 and a mean bond length of 1.98 Å, suggesting that the Fe single atoms should coordinate with four N atoms and one O atom. Both experimentally and theoretically previous results show that metal-nitrogen bonds are more likely than the metal-carbon or metal-oxygen ones, suggesting to form in-plane FeN_4 sites in the first coordination sphere.[56, 60] However, the higher average CN-value in the Fe-N-C-based material strongly suggests that one axial O atom is adsorbed on top of the FeN_4 moieties, resulting in coordinatively saturated iron cations, in line with the high oxophilicity of Fe.[56, 60, 61] Meanwhile, the formed HO-FeN_4 active sites could induce a rapid CO* desorption and suppress the competitive HER, resulting in an improved catalytic performance in comparison to that of the FeN_4 sites without axial O ligand.[62] Therefore, in an atmosphere with the oxygen-rich ligand, the spectra obtained on the Ni_7/Fe_3-N-C sample are fitted as presenting adjacent NiN_4 and HO-FeN_4 sites.

4.3.3 Electrochemical Performance

The electrochemical CO_2 reduction activity of the as-prepared catalysts was assessed using a typical three-electrode H-cell separated by an anion exchange membrane in 0.5 M $NaHCO_3$ electrolyte. The gas products were regularly examined by online gas chromatography (GC), showing that CO and H_2 were the main gas products obtained for all the samples. In parallel, the liquid-phase products were analysed by using nuclear magnetic resonance (^{1}H-NMR) spectroscopy after the electrochemical CO_2 reduction processes, demonstrating there no liquid products were produced.

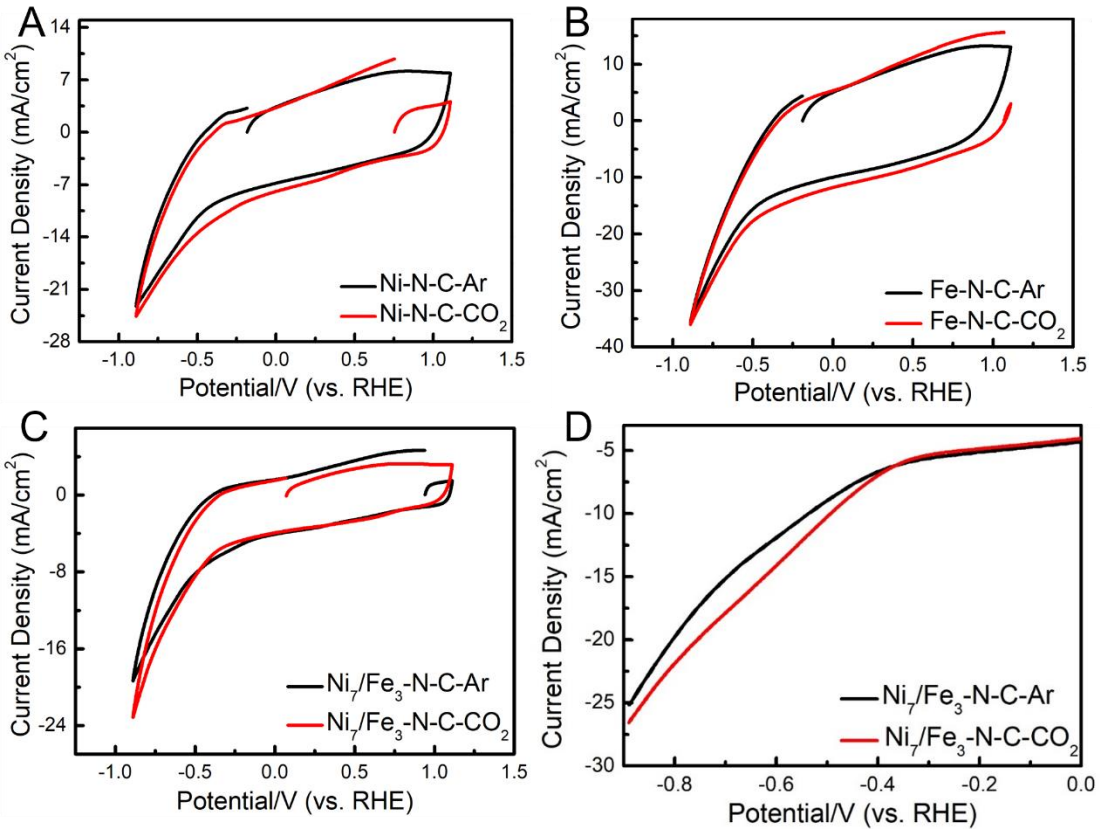

Figure 4.10 CV curves vs. RHE of (A) Ni-N-C, (B) Fe-N-C, (C) Ni_7/Fe_3-N-C and (D) LSV curves vs. RHE of Ni_7/Fe_3-N-C obtained in Ar- or CO_2-saturated 0.5 M $NaHCO_3$ solution.

In **Figure 4.10**, we firstly obtained CV curves to roughly assess the double/single M-N-C samples towards CO_2 RR. These samples exhibited an increase of current density in CO_2-saturated solution, compared to those obtained in the Ar-saturated electrolyte, which confirmed the efficient catalytic performance of Ni-N-C, Fe-N-C and Ni_7/Fe_3-N-C samples.[14]

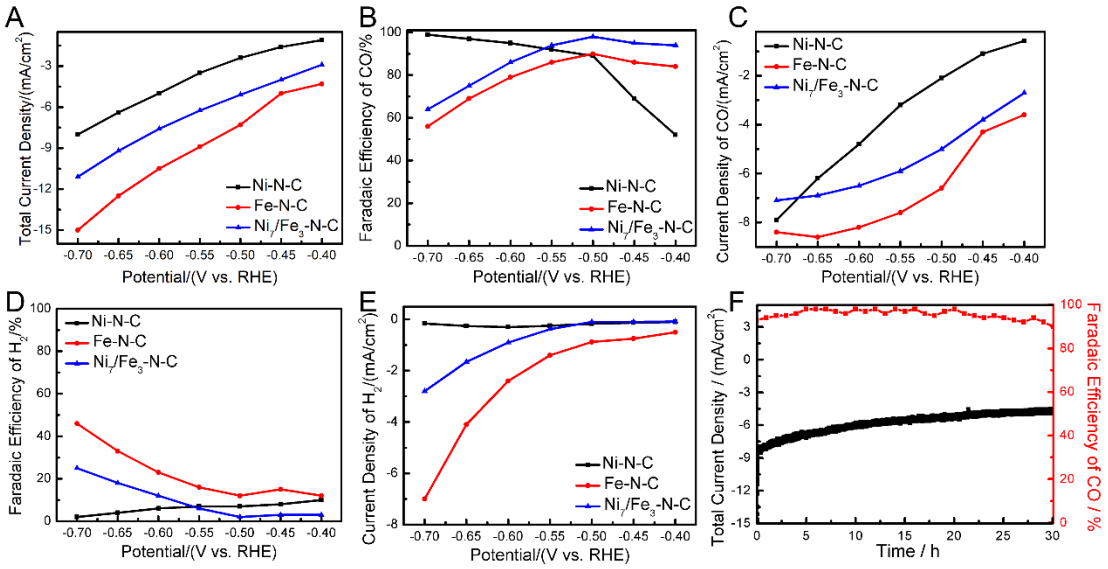

Figure 4.11 (A) Current density, (B) FE of CO at various potentials, (C) Current density for CO production, (D) FE of H_2 at various potentials, (E) Current density for H_2 production on Ni-N-C, Fe-N-C and Ni_7/Fe_3-N-C and (F) stability test of Ni_7/Fe_3-N-C at −0.50 V vs. RHE.

Then, the catalytic activities for CO_2 RR were further investigated by the chronoamperometry method in CO_2-saturated 0.5 M $NaHCO_3$ solution. **Figure 4.11A** summarizes the measured total current density for Ni-N-C, Fe-N-C and Ni_7/Fe_3-N-C samples. With the same mass loading of catalysts (ca. 1 mg cm^{-2}), the Ni-N-C delivers the smallest current density on each applied potential, which is lower than those obtained by the Fe-N-C and Ni_7/Fe_3-N-C samples. The result in **Figure 4.11A** reveals that Ni-N-C exhibits a relatively poor activity for generating a current density (*j*). The corresponding FE for CO production is measured in a potential range from −0.40 to −0.70 V (vs. RHE) for all the catalysts synthesized, as shown in **Figure 4.11B**. CO was the dominant gas product for these single/double M-N-C catalysts. Moreover, the FEs of the products varied with the electrode applied potentials. Specifically, the FE(CO) for the Fe-N-C and Ni_7/Fe_3-N-C catalysts typically exhibited an increase from ca. −0.40 to −0.50 V vs. RHE, reaching a maximum FE(CO) (90 % and 98 %, respectively) at −0.50 V vs. RHE. As the potential changed to more negative values (−0.6 to −0.7 V vs. RHE), the FEs(CO) for Fe-N-C and Ni_7/Fe_3-N-C gradually decreased since the competitive HER became the dominant reaction, as evidenced in the FE (H_2) shown in **Figure 4.11D**. However, the FE(CO) of Ni-N-C increased dramatically as the potentials

were getting more negative, until reaching the maximum FE (CO) (nearly 100 %) at −0.70 V vs. RHE. Accordingly, the obtained FEs of CO can be ranked in the following order: Ni_7/Fe_3-N-C > Fe-N-C > Ni-N-C in the potential range from −0.40 V to −0.50 V vs. RHE. Instead, when the potential is more negative than −0.60 V vs. RHE, the selectivity for CO follows the order: Ni-N-C > Ni_7/Fe_3-N-C > Fe-N-C. As discussed, the overpotential at the maximum FE for CO formation is crucial for catalysts in electrocatalysis, as it represents the energy that is required to drive the reaction beyond the one that is thermodynamically needed.[24] Among these catalysts, Ni_7/Fe_3-N-C exhibited the highest selectivity for CO production at −0.50 V (vs. RHE), corresponding to an overpotential of just 390 mV vs. RHE, which is lower than that of Ni-N-C as well as the majority of other reported Ni-N-C catalysts. Furthermore, Ni_7/Fe_3-N-C shows a partial current density for CO production of −5 mA cm^{-2} at −0.50 V (**Figure 4.11C**). Meanwhile, the partial current density for CO production obtained by Ni_7/Fe_3-N-C is also significantly higher compared to the one obtained by Fe-N-C and Ni-N-C catalysts at most of the applied potentials. The potential-dependent H_2 current densities for the different catalysts are shown in **Figure 4.11E**. To further investigate the stability of the Ni_7/Fe_3-N-C during the CO_2 RR, a 30-h durability measurement was conducted, as shown in **Figure 4.11F**. A CO_2 RR current density of around –5.6 mA cm^{-2} and a FE(CO) of over 90 % was maintained during the 30 h. Based on these results, it is shown that the bimetallic Ni_7/Fe_3-N-C produces a high-efficient CO_2 RR with a high selectivity and enhanced current densities at a low overpotential, results that are much better than those presented by the Ni-N-C sample.

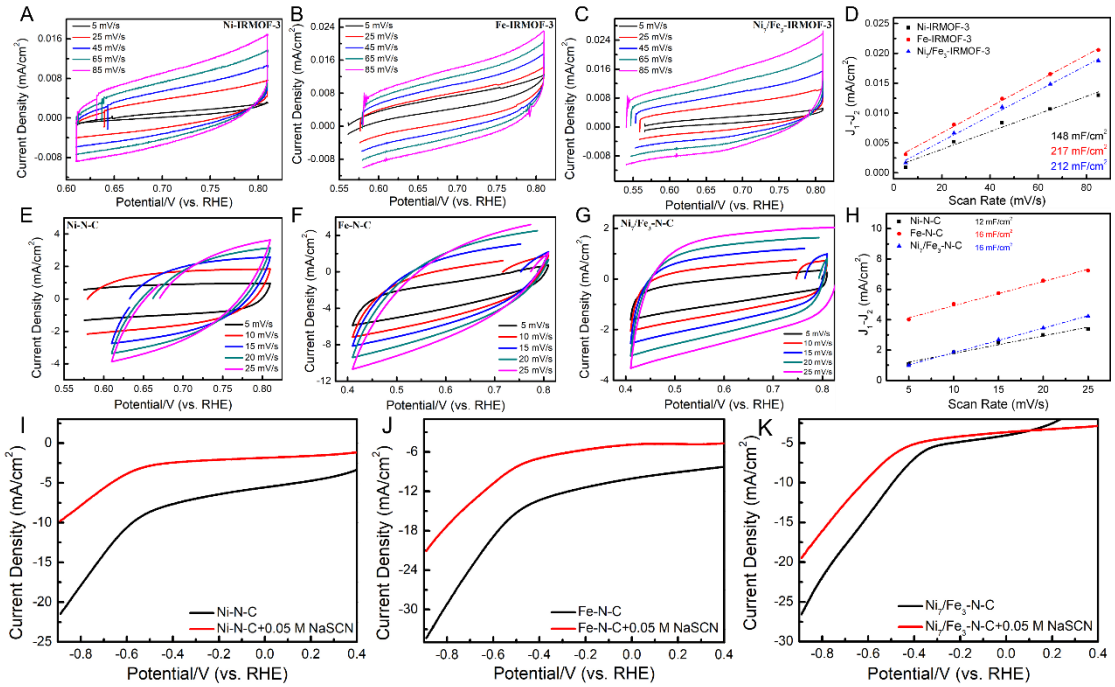

Figure 4.12 Cyclic voltammograms curves for (A) Ni-IRMOF-3, (B) Fe-IRMOF-3, (C) Ni_7/Fe_3-IRMOF-3, (E) Ni-N-C, (F) Fe-N-C and (G) Ni_7/Fe_3-N-C. (D) Plots of the current density vs. scan rate for Ni-IRMOF-3, Fe-IRMOF-3 and Ni_7/Fe_3-IRMOF-3 electrodes. (H) Plots of the current density vs. scan rate for Ni-Ni-N-C, Fe-N-C and Ni_7/Fe_3-N-C electrodes. Linear sweep voltammetry curves of (I) Ni-N-C, (J) Fe-N-C and (K) Ni_7/Fe_3-N-C with and without 0.05 M NaSCN.

In order to further probe the high efficiency of Ni_7/Fe_3-N-Csample, we estimated the electrochemical active surface areas (ECSA) of all samples and corresponding MOF precursors from the double-layer capacitance (C_{dl}) (**Figure 4.12A-H**). It is well established that higher ECSA often leads to higher catalytic activity.[38, 63] Compared to the MOF precursors, the samples after pyrolysis exhibited the smallest C_{dl}. This phenomenon suggests that the intrinsic catalytic activity of these M-N-C samples is not correlated to a higher ECSA. Instead, the improved CO_2 RR catalytic properties of these catalysts must be due to the presence of exposed isolated double or single metal active sites. The latest was further supported by the results obtained in a designed poisoning experiment with NaSCN solution. As shown in **Figure 4.12I-K**, the significant decrease of catalytic activity for Ni-N-C, Fe-N-C and Ni_7/Fe_3-N-C samples observed in $NaHCO_3$ solution containing NaSCN, could be attributed to the high affinity of SCN^- to metal ions poisoning the single/double active sites. Meanwhile, Ni-N-C, Fe-N-C and Ni_7/Fe_3-

N-C samples showed a similar C_{dl} (~16 mF cm^{-2}). The small difference in their ECSAs further proves that the adjacent Ni and Fe active sites in Ni_7/Fe_3-N-C significantly dominated the CO_2 RR process compared to the two single metal counterparts.[19]

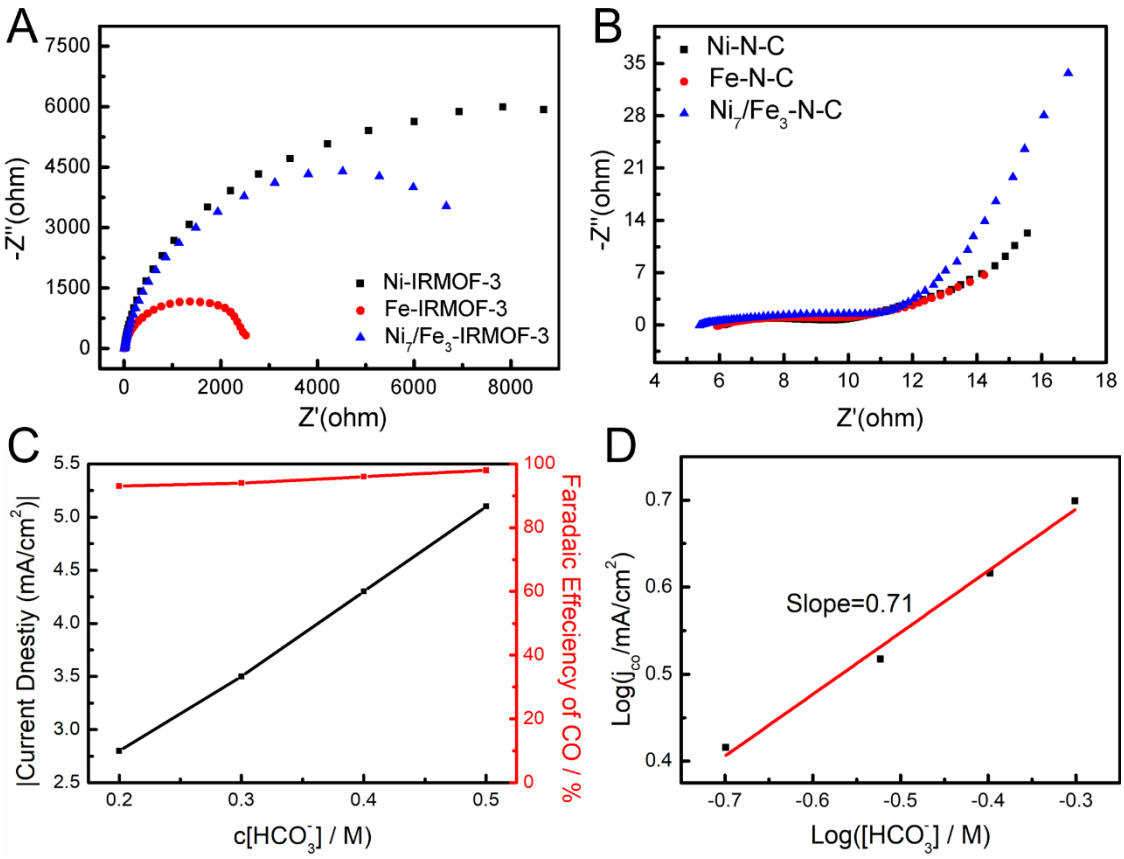

Figure 4.13 Electrochemical impedance spectroscopy (EIS) of (A) Ni-IRMOF-3, Fe-IRMOF-3 and Ni_7/Fe_3-IRMOF-3, as well as (B) Ni-N-C, Fe-N-C and Ni_7/Fe_3-N-C. (C) Current density and FE of Ni_7/Fe_3-N-C at different $NaHCO_3$ concentration at a constant potential (−0.5 V vs. RHE). (B) Partial CO current density of Ni_7/Fe_3-N-C vs. $NaHCO_3$ concentration at −0.50 V vs. RHE.

In addition, Nyquist plots revealed that the double/single M-N-C had a lower interfacial charge-transfer resistance (R_{CT}) compared to the MOF precursors, revealing faster electron transfer during CO_2 RR process, which is favourable for the formation of intermediates (**Figure 4.13A-B**).[16, 19, 54] Furthermore, the concentration effect of $NaHCO_3$ in the CO_2 RR on the Ni_7/Fe_3-N-C catalyst was also investigated (**Figure 4.13C-D**). The plot of log (j_{CO}) versus log ([HCO_3^-]) at the constant potential of −0.50 V vs. RHE showed a slope of 0.71, indicating that the concentration effect of HCO_3^- played a considerable role in promoting the conversion reaction of CO_2 to CO.[54, 64]

Therefore, the HCO_3^- not only acts as a pH buffer and proton donor in this reaction, but also increases the concentration of CO_2 near the electrode surface.[54, 64, 65]

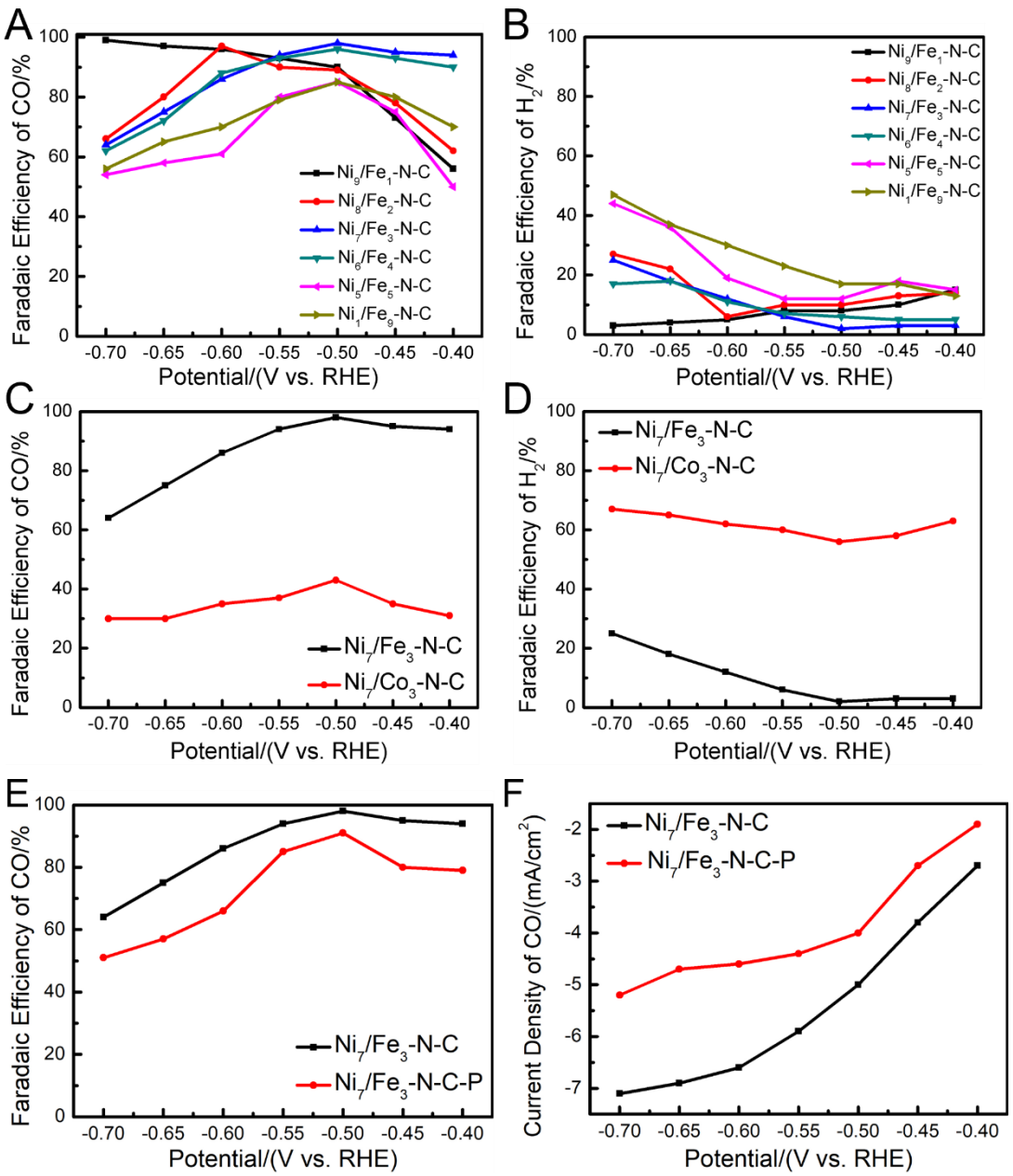

Figure 4.14 (A) FE of CO and (B) FE of H_2 at various potentials on Ni_x/Fe_y-N-C. (C) FE of CO and (D) FE of H_2 at various potentials on Ni_7/Fe_3-N-C and Ni_7/Co_3-N-C. (E) FE of CO at various potentials and (F) Current density for CO production on Ni_7/Fe_3-N-C and Ni_7/Fe_3-N-C-P.

In addition, by systematically controlling the ratio of Ni and Fe dopants, a series of Ni_x/Fe_y-N-C catalysts engaging both Ni and Fe sites were synthesized. We studied the electrochemical FEs on different Ni_x/Fe_y-N-C samples, as shown in **Figure 4.14A-**

B. Specifically, Ni_x/Fe_y-N-C with a higher Ni dose still kept the high selectivity, but at a larger overpotential; however, Ni_x/Fe_y-N-C with a higher Fe dose showed a similar selectivity at the same applied potential compared with the single Fe-N-C catalyst. These results demonstrate that the presence of a certain amount of Fe single atoms indeed influences the generation of CO at different applied potentials. Similarly, a Ni_7/Co_3-N-C sample was fabricated by following the same methodology. However, it exhibited higher catalytic performance towards H_2 generation, as shown in **Figure 4.14C-D**. This result further reveals the dependence of the electrocatalytic performance on the introduction of different metals that are adjacent to the Ni sites. Because the secondary metal introduction determines the adsorption properties and surface reactivity of the bimetallic catalysts through the tuning of the electron environment, thus, influencing the activity and selectivity. To further confirm the synergy effect between adjacent Ni and Fe active sites in the Ni_7/Fe_3-N-C bimetallic catalysts toward CO_2 RR, a Ni_7/Fe_3-N-C-P sample was prepared by physical mixture of Ni-N-C and Fe-N-C with the same Ni/Fe ratio. In comparison to the Ni_7/Fe_3-N-C, the Ni_7/Fe_3-N-C-P sample showed a decreased FE(CO) at all applied potentials, demonstrating the important impact of neighbouring Ni and Fe active sites prepared by the chemical process towards CO2 RR. (**Figure 4.14E-F**)

4.3.4 DFT Studies

Density Functional Theory (DFT) calculations were employed to further explore the origin of the improved CO_2 RR performance on the Ni_7/Fe_3-N-C sample. Based on the XAS results, a simulation model with neighbouring Ni and Fe sites embedded in N-doped graphene surface was created to represent the Ni_7/Fe_3-N-C catalyst. It is worth noting that there is an axial -OH ligand coordinated with the Fe atom. For comparison, the two single metal counterpart models for Ni-N-C and HO-Fe-N-C were also considered. We denote Ni sites in Ni-N-C catalyst as Ni-N-C-Ni, Fe sites in HO-Fe-N-C catalyst as HO-Fe-N-C-Fe, and Ni sites or Fe sites in Ni_7/Fe_3-N-C as Ni/Fe-N-C-Ni or Ni/Fe-N-C-Fe,

respectively. The optimized structures and the optimal adsorption configurations of the reaction intermediates are shown in **Figure 4.15**.

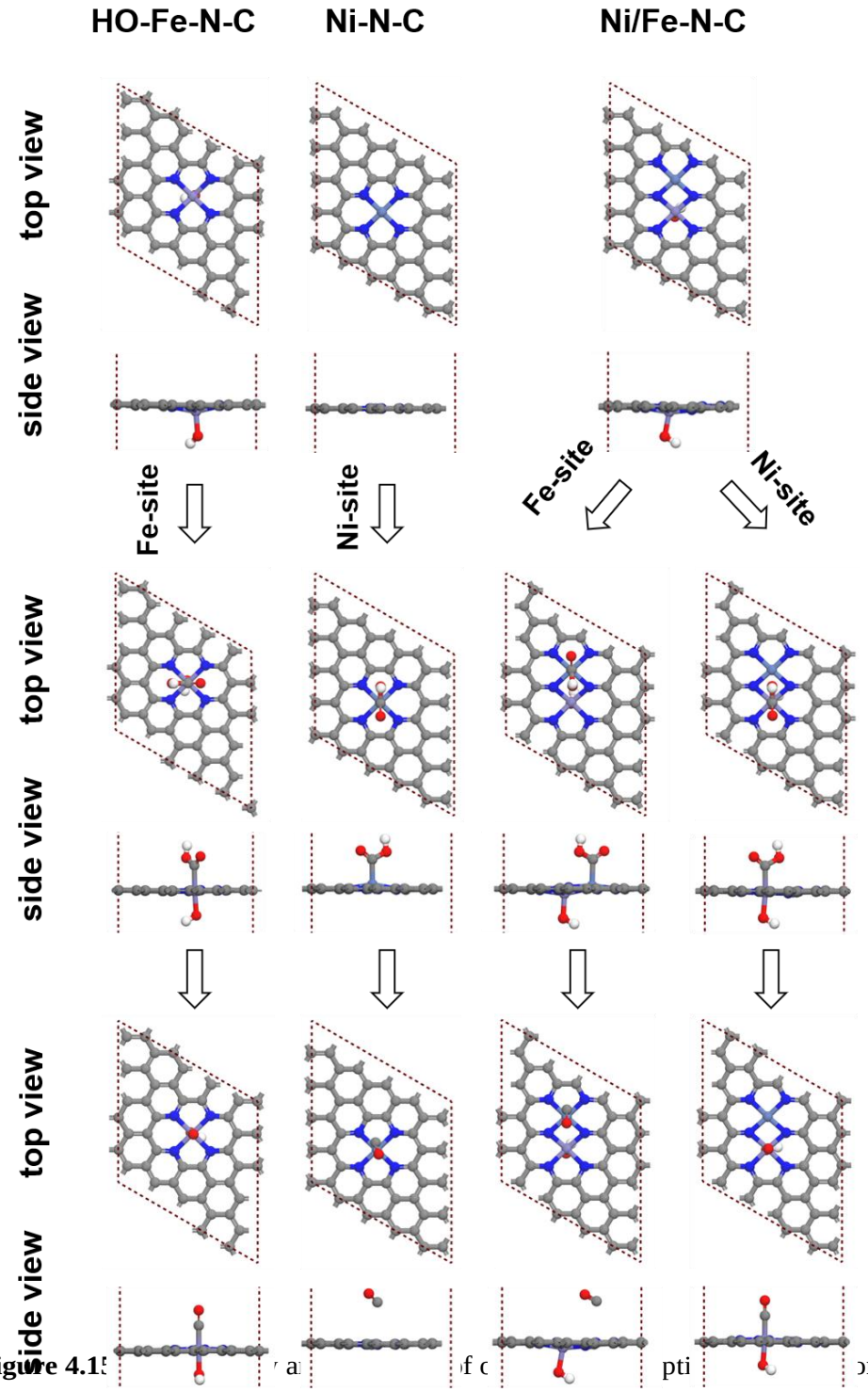

Figure 4.15 [illegible] of [illegible] optimized [illegible] on simulated models (Ni, Fe, O, N and C atoms are represented in purple, cyan, red, blue and grey, respectively).

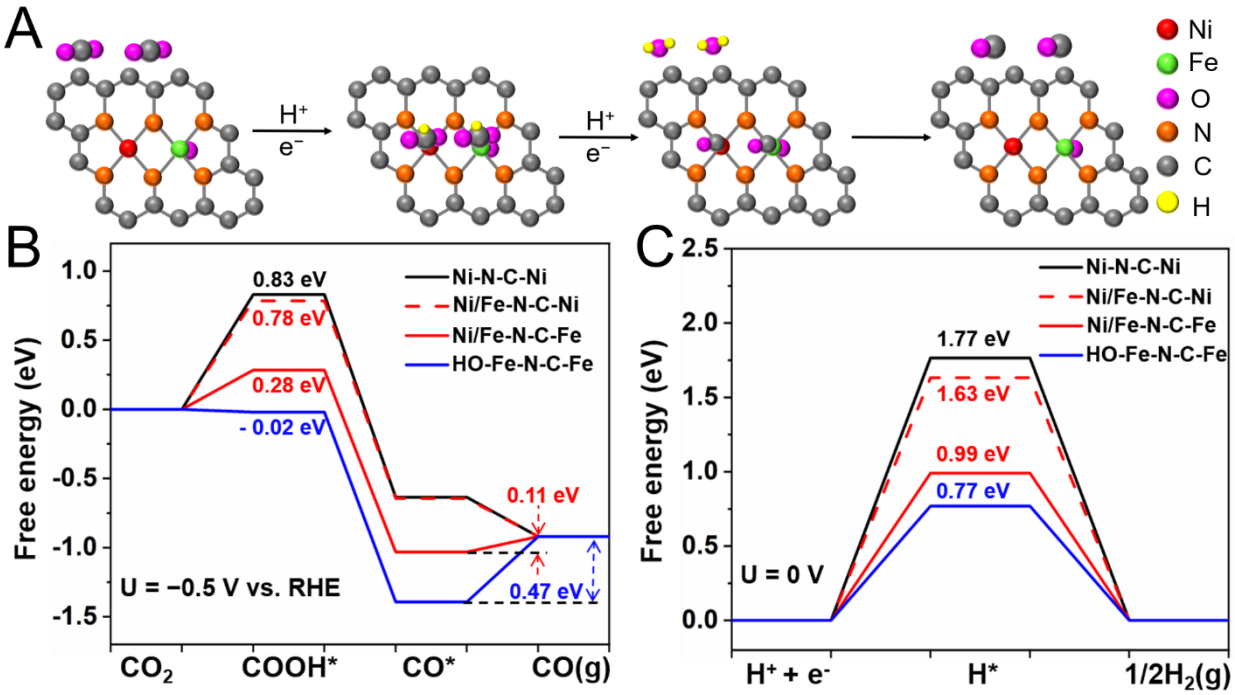

Figure 4.16. DFT Studies of CO_2 RR. (A) Supposed pathway of CO_2 reduction to CO in DFT calculations. Free energy profiles for the (B) CO_2 RR to CO at −0.5 V (vs. RHE) and (C) HER at 0 V (vs. RHE) on simulated models.

It is well established that there are three elementary steps during CO_2 RR, namely the formation of COOH*, conversion of COOH* to CO*, and the desorption of CO* from the active site, as shown in **Figure 4.16A**.[19, 66] The free energy profiles of CO_2 reduction to CO on different models at −0.5 V (vs. RHE) are illustrated in **Figure 4.16B**. We can see that the free energy of COOH* formation on the Ni-N-C-Ni model is 0.83 eV, which is much higher than that of HO-Fe-N-C-Fe (−0.02 eV), which reflects the sluggish formation of COOH* on Ni sites. Regarding the CO* desorption process, it is exergonic on Ni-N-C-Ni due to the weak binding of CO* at the Ni active site. In contrast, it requires to overcome 0.47 eV of desorption free energy on HO-Fe-N-C-Fe due to the strong binding of CO* at the Fe site. These results reveal that the catalytic performances of single metal atom catalysts for CO_2 RR are limited by either the difficult formation of *COOH (on Ni sites) or the slow desorption of CO* (on Fe sites). When Ni and Fe were embedded adjacently in one catalyst model, a decrease of COOH* adsorption free energy could be seen over Ni/Fe-N-C-Ni (0.78 eV)

compared to that over Ni-N-C-Ni (0.83 eV), while Ni/Fe-N-C-Fe (0.28 eV) exhibited a weaker COOH* adsorption free energy compared to HO-Fe-N-C-Fe (−0.02 eV). However, the presence of Ni sites could promote CO* desorption on Ni/Fe-N-C-Fe, and the desorption free energy is only 0.11 eV, which was much lower than that over HO-Fe-N-C-Fe (0.47 eV). Meanwhile, the desorption of *CO over Ni/Fe-N-C-Ni was still spontaneous, which was similar to that for Ni-N-C-Ni. When comparing the reaction free energy of the most difficult step in CO_2 RR on HO-Fe-N-C-Fe (CO* desorption, 0.47 eV) and Ni/Fe-N-C-Fe (COOH* formation, 0.28 eV), we could find that the presence of Ni would promote the activity of CO_2 RR at Fe sites. Therefore, we found that this bimetallic catalyst showed priority on CO_2 RR to CO due to its synergistic effect for *COOH formation and *CO desorption, leading to an excellent performance in CO_2 RR in comparison to the single metal counterparts. Taking into account all the above results, we suggest that Ni and Fe sites in this nano-reactor (Ni_7/Fe_3-N-C catalyst) could simultaneously adsorb COOH* and desorb CO*, but mainly influence different reaction steps, leading to an excellent performance in CO_2 RR.

Additionally, HER as a competing side reaction was also studied (see the free energy profiles obtained in **Figure 4.16C**). It can be found that Ni-N-C-Ni and Ni/Fe-N-C-Ni require relatively high free energies towards *H formation. In contrast, the adsorption free energies on HO-Fe-N-C-Fe and Ni/Fe-N-C-Fe are relatively lower (0.77 eV and 0.99 eV). These results suggest that HER occurs more easily on Fe sites than Ni sites, and that the existence of neighbouring Ni atoms can further hinder the HER on Fe atoms. Taking CO_2 RR and HER together into consideration, it can be concluded that the quasi-double-star Ni_7/Fe_3-N-C catalyst with adjacent Ni and Fe sites is superior for CO_2 RR, not only facilitating the formation of COOH* compared to the single Ni-N-C catalyst, and boosting the CO* desorption, but also limiting the undesired HER in comparison to the single Fe-N-C catalyst. These results are in good agreement

with the experimental observations that Ni_7/Fe_3-N-C exhibits enhanced activity and selectivity for CO_2 RR over individual Ni-N-C and Fe-N-C catalysts.

4.4 Summary

In summary, we have demonstrated that a quasi-double-star catalyst composed of adjacent Ni and Fe active sites can enhance the activity towards CO_2 RR, in comparison to the single atom moieties. In this way, an atomically dispersed bimetallic Ni/Fe-N-C sample has been successfully prepared through rationally controlling the Fe and Ni additive amounts into Zn-IRMOF-3, showing an excellent selectivity for generating CO (98 %) at a low overpotential (390 mV vs. RHE). These results are superior to those obtained in the single atom catalyst counterparts. Furthermore, the adjacent Ni and Fe active sites act as a nano-reactor, affecting different reaction steps in comparison to two separate active sites during CO_2 RR, thus, enhancing the overall activity. DFT simulations suggest that the adjacent Ni and Fe sites weaken the bonding energy of CO_2 RR intermediates as well as limit the competitive HER, and, thus, boost the CO_2 RR activity. Overall, this work provides a possibility for manipulating two active sites in a catalyst for improving both, selectivity and activity in CO_2 RR, simultaneously. The strategy employed here might be also adaptable for other electrocatalytic processes, such as, nitrogen reduction reaction (NRR), ORR and oxygen evolution reaction (OER).

References

[1] J. Shen, R. Kortlever, R. Kas, Y.Y. Birdja, O. Diaz-Morales, Y. Kwon, I. Ledezma-Yanez, K.J.P. Schouten, G. Mul, M.T.M. Koper, Nature Commun.s, 6 (2015) 8177.
[2] D. Gao, H. Zhou, F. Cai, J. Wang, G. Wang, X. Bao, ACS Catal., 8 (2018) 1510-1519.
[3] J. Pei, T. Wang, R. Sui, X. Zhang, D. Zhou, F. Qin, X. Zhao, Q. Liu, W. Yan, J. Dong, L. Zheng, A. Li, J. Mao, W. Zhu, W. Chen, Z. Zhuang, Energy Environ. Sci., (2021).
[4] S. Gao, Y. Lin, X. Jiao, Y. Sun, Q. Luo, W. Zhang, D. Li, J. Yang, Y. Xie, Nature, 529 (2016) 68-71.
[5] Z. Chen, X. Zhang, W. Liu, M. Jiao, K. Mou, X. Zhang, L. Liu, Energy Environ. Sci., (2021).
[6] M.B. Gawande, P. Fornasiero, R. Zbořil, ACS Catal., 10 (2020) 2231-2259.
[7] D. Zhao, Z. Zhuang, X. Cao, C. Zhang, Q. Peng, C. Chen, Y. Li, Chem. Soc. Rev., 49 (2020) 2215-2264.
[8] Y. Yang, Y. Yang, Z. Pei, K.-H. Wu, C. Tan, H. Wang, L. Wei, A. Mahmood, C. Yan, J. Dong, S. Zhao, Y. Chen, Matter, 3 (2020) 1442-1476.
[9] A. Wang, J. Li, T. Zhang, Nature Rev. Chem., 2 (2018) 65-81.
[10] D. Gao, T. Liu, G. Wang, X. Bao, ACS Energy Lett., 6 (2021) 713-727.
[11] C. Zhao, X. Dai, T. Yao, W. Chen, X. Wang, J. Wang, J. Yang, S. Wei, Y. Wu, Y. Li, J. Am. Chem. Soc., 139 (2017) 8078-8081.
[12] K. Jiang, S. Siahrostami, T. Zheng, Y. Hu, S. Hwang, E. Stavitski, Y. Peng, J. Dynes, M. Gangisetty, D. Su, K. Attenkofer, H. Wang, Energy Environ. Sci., 11 (2018) 893-903.
[13] T. Zheng, K. Jiang, N. Ta, Y. Hu, J. Zeng, J. Liu, H. Wang, Joule, 3 (2019) 265-278.
[14] S. Liu, H.B. Yang, S.-F. Hung, J. Ding, W. Cai, L. Liu, J. Gao, X. Li, X. Ren, Z. Kuang, Y. Huang, T. Zhang, B. Liu, Angew. Chem. Int. Ed., 59 (2020) 798-803.
[15] Y. Zhang, L. Jiao, W. Yang, C. Xie, H.-L. Jiang, Angew. Chem. Int. Ed., 60 (2021) 7607-7611.
[16] C.F. Wen, F. Mao, Y. Liu, X.Y. Zhang, H.Q. Fu, L.R. Zheng, P.F. Liu, H.G. Yang, ACS Catal., 10 (2020) 1086-1093.
[17] W. Xiong, H. Li, H. Wang, J. Yi, H. You, S. Zhang, Y. Hou, M. Cao, T. Zhang, R. Cao, Small, 16 (2020) 2003943.
[18] H.B. Yang, S.-F. Hung, S. Liu, K. Yuan, S. Miao, L. Zhang, X. Huang, H.-Y. Wang, W. Cai, R. Chen, J. Gao, X. Yang, W. Chen, Y. Huang, H.M. Chen, C.M. Li, T. Zhang, B. Liu, Nature Energy, 3 (2018) 140-147.
[19] W. Ren, X. Tan, W. Yang, C. Jia, S. Xu, K. Wang, S.C. Smith, C. Zhao, Angew. Chem. Int. Ed., 58 (2019) 6972-6976.
[20] A.S. Varela, W. Ju, A. Bagger, P. Franco, J. Rossmeisl, P. Strasser, ACS Catal., 9 (2019) 7270-7284.
[21] X.-M. Hu, H.H. Hval, E.T. Bjerglund, K.J. Dalgaard, M.R. Madsen, M.-M. Pohl, E. Welter, P. Lamagni, K.B. Buhl, M. Bremholm, M. Beller, S.U. Pedersen, T. Skrydstrup, K. Daasbjerg, ACS Catal., 8 (2018) 6255-6264.
[22] O.S. Bushuyev, P. De Luna, C.T. Dinh, L. Tao, G. Saur, J. van de Lagemaat, S.O. Kelley, E.H. Sargent, Joule, 2 (2018) 825-832.
[23] L. Cao, D. Raciti, C. Li, K.J.T. Livi, P.F. Rottmann, K.J. Hemker, T. Mueller, C. Wang, ACS Catal., 7 (2017) 8578-8587.
[24] C. Ding, A. Li, S.-M. Lu, H. Zhang, C. Li, ACS Catal., 6 (2016) 6438-6443.

[25] X. Wang, J.F. de Araújo, W. Ju, A. Bagger, H. Schmies, S. Kühl, J. Rossmeisl, P. Strasser, Nature Nanotechnology, 14 (2019) 1063-1070.
[26] L. Lin, T. Liu, J. Xiao, H. Li, P. Wei, D. Gao, B. Nan, R. Si, G. Wang, X. Bao, Angew. Chem. Int. Ed., 59 (2020) 22408-22413.
[27] D. Gao, R.M. Arán-Ais, H.S. Jeon, B. Roldan Cuenya, Nature Catal., 2 (2019) 198-210.
[28] L. Bai, C.-S. Hsu, D.T.L. Alexander, H.M. Chen, X. Hu, J. Am. Chem. Soc., 141 (2019) 14190-14199.
[29] Y. Cheng, S. He, J.-P. Veder, R. De Marco, S.-z. Yang, S. Ping Jiang, ChemElectroChem, 6 (2019) 3478-3487.
[30] S. Wang, L. Shi, X. Bai, Q. Li, C. Ling, J. Wang, ACS Central Sci., 6 (2020) 1762-1771.
[31] J. Wang, Z. Huang, W. Liu, C. Chang, H. Tang, Z. Li, W. Chen, C. Jia, T. Yao, S. Wei, Y. Wu, Y. Li, J. Am. Chem. Soc., 139 (2017) 17281-17284.
[32] S. Sarkar, A. Biswas, T. Purkait, M. Das, N. Kamboj, R.S. Dey, Inorg. Chem., 59 (2020) 5194-5205.
[33] Y. Zhou, W. Yang, W. Utetiwabo, Y.-m. Lian, X. Yin, L. Zhou, P. Yu, R. Chen, S. Sun, The J. Phys. Chem. Lett., 11 (2020) 1404-1410.
[34] B. Ravel, M. Newville, J. Synchrotron Rad., 12 (2005) 537-541.
[35] H. Baumgartel, Nachrichten aus Chemie, Technik und Laboratorium, 36 (1988) 650-650.
[36] J.J. Rehr, R.C. Albers, Rev. Modern Phys., 72 (2000) 621-654.
[37] S.J. Lyle, R.W. Flaig, K.E. Cordova, O.M. Yaghi, J. Chem. Education, 95 (2018) 1512-1519.
[38] T. Zhang, J. Du, P. Xi, C. Xu, ACS Appl. Mater. Interfaces, 9 (2017) 362-370.
[39] P.E. Blöchl, Phys. Rev. B, 50 (1994) 17953-17979.
[40] G. Kresse, J. Furthmüller, Phys. Rev. B, 54 (1996) 11169-11186.
[41] G. Kresse, J. Furthmüller, Comput. Mater. Sci., 6 (1996) 15-50.
[42] G. Kresse, D. Joubert, Phys. Rev. B, 59 (1999) 1758-1775.
[43] J. Hafner, J. Comput. Chem., 29 (2008) 2044.
[44] J. Wellendorff, K.T. Lundgaard, A. Møgelhøj, V. Petzold, D.D. Landis, J.K. Nørskov, T. Bligaard, K.W. Jacobsen, Phys. Rev. B, 85 (2012) 235149.
[45] F. Studt, M. Behrens, E.L. Kunkes, N. Thomas, S. Zander, A. Tarasov, J. Schumann, E. Frei, J.B. Varley, F. Abild-Pedersen, J.K. Nørskov, R. Schlögl, ChemCatChem, 7 (2015) 1105-1111.
[46] F. Studt, F. Abild-Pedersen, J.B. Varley, J.K. Nørskov, Catal. Lett., 143 (2013) 71-73.
[47] R. Christensen, H.A. Hansen, T. Vegge, Catal. Sci. Technol., 5 (2015) 4946-4949.
[48] A.A. Peterson, F. Abild-Pedersen, F. Studt, J. Rossmeisl, J.K. Nørskov, Energy Environ. Sci., 3 (2010) 1311-1315.
[49] Y. Luan, Y. Qi, H. Gao, R.S. Andriamitantsoa, N. Zheng, G. Wang, J. Mater. Chem. A, 3 (2015) 17320-17331.
[50] L. Ye, Y. Ying, D. Sun, Z. Zhang, L. Fei, Z. Wen, J. Qiao, H. Huang, Angew. Chem. Int. Ed., 59 (2020) 3244-3251.
[51] H. Yang, Y. Wu, G. Li, Q. Lin, Q. Hu, Q. Zhang, J. Liu, C. He, J. Am. Chem. Soc., 141 (2019) 12717-12723.
[52] Q. Zhang, H. Jiang, D. Niu, X. Zhang, S. Sun, S. Hu, ChemistrySelect, 4 (2019) 4398-4406.
[53] S. Liu, H. Yang, X. Huang, L. Liu, W. Cai, J. Gao, X. Li, T. Zhang, Y. Huang, B. Liu, Adv. Funct. Mater., 28 (2018) 1800499.

[54] C. Zhao, Y. Wang, Z. Li, W. Chen, Q. Xu, D. He, D. Xi, Q. Zhang, T. Yuan, Y. Qu, J. Yang, F. Zhou, Z. Yang, X. Wang, J. Wang, J. Luo, Y. Li, H. Duan, Y. Wu, Y. Li, Joule, 3 (2019) 584-594.
[55] D. Guo, R. Shibuya, C. Akiba, S. Saji, T. Kondo, J. Nakamura, Science, 351 (2016) 361-365.
[56] L. Gong, H. Zhang, Y. Wang, E. Luo, K. Li, L. Gao, Y. Wang, Z. Wu, Z. Jin, J. Ge, Z. Jiang, C. Liu, W. Xing, Angew. Chem. Int. Ed., 59 (2020) 13923-13928.
[57] T. Yamamoto, X-Ray Spectrometry, 37 (2008) 572-584.
[58] H. Zhang, J. Li, S. Xi, Y. Du, X. Hai, J. Wang, H. Xu, G. Wu, J. Zhang, J. Lu, J. Wang, Angew. Chem. Int. Ed., 58 (2019) 14871-14876.
[59] S. Zhao, L. Zhang, B. Johannessen, M. Saunders, C. Liu, S.-Z. Yang, S.P. Jiang, Adv. Mater. Interfaces, 8 (2021) 2001788.
[60] J. Li, P. Pršlja, T. Shinagawa, A.J. Martín Fernández, F. Krumeich, K. Artyushkova, P. Atanassov, A. Zitolo, Y. Zhou, R. García-Muelas, N. López, J. Pérez-Ramírez, F. Jaouen, ACS Catal., 9 (2019) 10426-10439.
[61] Y. Chen, S. Ji, Y. Wang, J. Dong, W. Chen, Z. Li, R. Shen, L. Zheng, Z. Zhuang, D. Wang, Y. Li, Angew. Chem. Int. Ed., 56 (2017) 6937-6941.
[62] Z. Chen, A. Huang, K. Yu, T. Cui, Z. Zhuang, S. Liu, J. Li, R. Tu, K. Sun, X. Tan, J. Zhang, D. Liu, Y. Zhang, P. Jiang, Y. Pan, C. Chen, Q. Peng, Y. Li, Energy Environ. Sci., (2021).
[63] L. Xia, H. Song, X. Li, X. Zhang, B. Gao, Y. Zheng, K. Huo, P.K. Chu, Front. Chem., 8 (2020).
[64] J. Gu, C.-S. Hsu, L. Bai, H.M. Chen, X. Hu, Science, 364 (2019) 1091-1094.
[65] T. Li, C. Yang, J.-L. Luo, G. Zheng, ACS Catal., 9 (2019) 10440-10447.
[66] W. Zhu, L. Zhang, S. Liu, A. Li, X. Yuan, C. Hu, G. Zhang, W. Deng, K. Zang, J. Luo, Y. Zhu, M. Gu, Z.-J. Zhao, J. Gong, Angew. Chem. Int. Ed., 59 (2020) 12664-12668.

Chapter 5

General Conclusions and Outlook

In this dissertation, we have designed and comprehensively investigated a series of Zn-based MOFs or derived materials for electrochemical CO_2 reduction applications in order to improve the conversion efficiency from selectivity, current density and overpotential aspects. Various Zn-based MOFs have been prepared through a simple solvothermal method and employed as self-sacrificed templates to design surface modified MOFs or (double) single atom(s) catalysts. The structural characterization of as-prepared samples was achieved by the utilization of XRD, XPS, XAS, Raman spectroscopy; SEM, EDS and specially (S)TEM advanced techniques, mainly aberration-corrected HAADF and EDS. More importantly, the DFT analyses combining different characterization and electrochemical methods allowed a better understanding of different structure-activity relationships in our materials. We could carefully engineer several types of Zn-based/derived materials, namely surface modified ZIF-8, Fe single atom catalysts with axial bonded O-containing groups and finally, Ni and Fe double atom catalysts, all of them for CO_2 RR. We started our study focusing on the design of surface modified ZIF-8 in order to boost the selectivity of pure ZIF-8. According to this first work, we found that the improvement of the efficiency of pure MOFs is still limited by their low exposure of the active atoms and insufficient stability. Then, we moved to prepare MOFs derived (double) single atom(s) catalysts to solve the above problems. In the following part, we present the main general conclusions achieved in this dissertation.

5.1 General Conclusions

Low selectivity and current density are the critical bottlenecks for metal organic coordination materials in the field of CO_2 RR. In **Chapter 2**, we have described a strategy to enhance the CO_2 RR activity on a ZIF-8 by introducing a very small proportion (5 % in weight) of DOBDC (ZIF-8-5 %), achieving a higher current density of CO and a boosted Faradaic efficiency. DFT calculations demonstrated that the excellent CO_2 RR performance of the ZIF-8-5 % sample could be attributed to the improved formation of *COOH intermediates stemming from the successful DOBDC surface modification. Therefore, we could draw the following conclusions:

• **Successful Modification:** Through the use of DOBDC as both etching and doping agent, a surface modified ZIF-8-5 % has been successfully synthesized and used in CO_2 RR. The optimized proportion of DOBDC could promote the formation of surface modification ZIF-8-0.5 without any morphology damage.

• **Enhanced Faradaic efficiency and current density:** ZIF-8-5 % exhibits an enhanced efficiency towards CO_2 RR in comparison to the parent ZIF-8, showing a 2.5 times higher partial current density (from −4 mA cm^{-2} to −10 mA cm^{-2}) and a boosted Faradaic efficiency, from 56 % to 79 %.

• **DFT calculations supports:** The DFT calculations proved that the enhanced activity is attributed to the favored formation of the *COOH intermediate on ZIF-8-5 %, which is induced by the narrowed HOMO-LUMO gap upon surface modification with DOBDC.

The results gained from **Chapter 2** showed that the catalytic performance of MOFs can be improved via their surface modification by using DOBDC. Despite the observed improvement, the FE(CO) obtained still cannot reach an industrial requirement, therefore, in the following chapter the main goal, we will be boosting the FE(CO).

Utilization of Fe-N-C based catalysts towards CO_2 RR is promising but hindered by their limited activity. In **Chapter 3**, we regulated neighboring groups of FeN_4 active sites to effectively enhance the catalytic performance of the obtained catalysts. Therefore, we report a facile route to introduce axial bonded O-containing groups to a Fe-N-C catalyst (denoted as D-Fe-N-C) through pyrolysis of Fe-doped Zn-based metal organic frameworks (IRMOF-3). This process is forming highly dispersed Fe single atoms with HO-FeN_4 active sites. Due to the local environment modulation induced by such -OH groups, the D-Fe-N-C catalyst exhibits an enhanced CO_2 RR activity. DFT calculations also reveal that the axial -OH ligand on the FeN_4 site acts as the main active site through not only reducing the binding energies of CO and facilitating product

desorption during the CO_2 RR process, but also preventing the undesired hydrogen evolution reaction (HER). Thanks to the detailed experimental and characterization techniques presented in this chapter, we could draw the following conclusions:

• **Successful preparation:** A facile strategy could be presented to regulate the active sites of Fe-N-C catalysts with an axial oxygen subgroup by using an oxygen and nitrogen-rich MOF, instead of simple N-containing precursors. The Zn-based IRMOF-3, assembled from Zn^{2+} nodes and 2-aminoterephthalic acid ligands, caters for the fabrication requirements, not only allowing the stabilization of foreign Fe ions as a self-sacrificial platform, but also providing nitrogen/oxygen-rich sources from organic ligands, replacing simple N-containing precursors. Therefore, the oxygen-rich ligands have been shown to be beneficial to form Fe-O coordinated bonds during the thermal pyrolysis and create the HO-FeN_4 active sites.

• **Detailed characterization:** The prepared D-Fe-N-C catalysts show a complete integration of the single active FeN_4-OH moieties and a modicum of Fe nanoparticles, as successfully proved by combining transmission electron microscopy (TEM) and X-ray absorption spectroscopy (XAS).

• **Enhanced FE of CO:** Benefiting from the above advantages, D-Fe-N-C catalysts show a remarkable CO_2 RR activity in 0.5 M $NaHCO_3$ solution, accompanied by an excellent selectivity with Faradaic efficiency of CO (95 %) at −0.50 V vs. RHE, as well as a robust stability, which are superior to those of the previously reported Fe-N-C-based materials derived from MOFs. Moreover, the selectivity could be retained over 80 % in a range of working potentials from −0.40 to −0.60 V vs. RHE.

• **DFT calculation supports:** The theoretical results further proved that rationally engineering the coordination environment of FeN_4 via oxygen-containing subgroups could effectively boost the CO_2 RR activity through reducing the binding energies of CO desorption and disfavoring the hydrogen evolution reaction (HER).

• **Universal synthesis strategy.** The facile synthesis strategy presented here can also be employed for synthesising other atomically dispersed Co-N-C and Ni-C-N

catalysts with good CO_2 reduction catalytic performances, indicating its universal nature.

According to the results obtained on **Chapter 3**, it is found that the general selectivity order for CO_2-to-CO conversion is found to be Ni > Fe ≫ Co, while the activity follows Ni, Fe ≫ Co. It is found that obtaining at the same time a high selectivity and activity on the single M-N-C is still a challenge. Thus, in **Chapter 4**, we combined the different merits of Ni-N-C and Fe-N-C catalysts to create a double metal atom catalyst to achieve both, a high selectivity and activity, simultaneously. In detail, we prepared atomically dispersed catalysts based on double metal atoms (Ni/Fe-N-C) through a simple pyrolysis of Ni and Fe co-doped Zn-based MOFs to achieve a high selectivity at a low overpotential towards CO_2 RR. The optimized dual-metal Ni/Fe-N-C catalyst showed an exclusive selectivity at a low overpotential. Our results prove that regulating the catalytic CO_2 RR performance via adjacent Ni and Fe active sites could potentially break the activity benchmark of single metal counterparts. In this way, we could draw the following conclusions:

• **Successful fabrication:** Through rationally controlling Ni and Fe additive amount in Zn-based IRMOF-3 through one-pot synthesis, instead of the tedious multi-step doping process, after the pyrolysis, a double-metal (Ni/Fe) active sites could be prepared.

• **Enhanced FE(CO) at a low overpotential:** The optimized Ni_7/Fe_3-N-C sample shows an almost exclusive selectivity to CO evolution (FE_{CO} is 98 %) at a low overpotential (390 mV vs. RHE), which are superior to both single metal counterparts (Ni-N-C and Fe-N-C) and other state-of-the-art M-N-C catalysts.

• **Computational insights unveiling the detailed reaction mechanism.** Via DFT calculations, we proved that regulating the catalytic CO_2 RR performance via adjacent Ni and Fe active sites in bimetallic Ni/Fe-N-C catalyst could potentially break the activity benchmark of single metal counterparts because the neighboring Ni and Fe active sites not only function in synergy to decrease the reaction barrier for the

formation of COOH* and desorption of CO* in comparison to their single metal counterparts, but also preventing the undesired hydrogen evolution reaction (HER).

The results gained from **Chapter 4** pave the way for the rational design of catalysts with bimetallic active sites for other reactions.

5.2 Outlook

During the past decades, many efforts have been done in order to achieve a high selectivity, large current density, low overpotential and robust stability in CO_2 RR. However, as a multi-path reaction, the reaction intermediates are complex during CO_2 RR. In this way, it is highly desirable to conduct studies for identifying the dynamic evolution of the catalysts and detecting intermediate states of the reaction processes. Therefore, in situ studies will play a more and more important role in the field of CO_2 reduction in the future. Through the real-time detection of the active sites and reaction intermediates, the dynamic process of the CO_2 RR will be able to be clearly revealed, which will be helpful to precisely understand the catalytic mechanisms and design efficient CO_2 catalytic systems. Moreover, the majority of the catalyst studies are performed in H-cells that suffer from massive CO_2 mass transport losses at the electrode interface. These mass transfer limitations are a barrier for the projection to large-scale CO_2 electrolyzer performance. Therefore, the subtle flow cell reactors should be exploited to diminish the mass transport limitations and achieve the industrial requirements. Moreover, the further combination of theoretical calculations should offer the most effective way to give deeper insights into both the stepwise elementary reaction mechanism and the local environment of catalysts. The insights obtained will thus contribute as the stepping-stone toward the clear identification of the nature of the catalytic sites and benefit for the further design of highly active catalysts for practical applications.

For MOF-based electrocatalysts, the low electrical conductivity and poor stability for most of them are still the bottleneck shadowing their applications. Therefore, in the future, an ideal MOF-based electrocatalysts should be design with high activity,

selectivity, conductivity, and structural stability. Meanwhile, in-depth mechanism studies on MOFs also should be focused to evaluate the possible change of active sites during the catalytic process, which will give more information on the structure-activity relationship and provide guidance to better design of suitable MOFs for their applications. Thus, there is still a long way for MOFs exploitation in the practical applications of renewable electrochemical energy-conversion devices.

For the single atom catalysts, over the past decade, although many encouraging results indicate that SACs hold a great promise, more efforts are still needed to push SACs-based commercial CO_2 electrolysis. This is due to the fact that most of the SACs produce CO as the major product, while a few of them can also convert CO_2 to formate, hydrocarbons, and oxygenates with considerable Faradaic efficiencies. On the other hand, CO_2 RR is a structure-sensitive reaction, its activity and selectivity are closely related to atomic structures and the local environments of the active sites. Similarly, fundamental understanding of the structure-performance correlations of the single atom catalyst will be important to guide the rational design of more active, selective, and stable CO_2 RR catalysts.

List of Publication:

1. **Ting Zhang**, Hong Liu, Xu Han, Martí Biset-Peiró, Yunhui Yang, Xuan Zhang, Fei Zhang, Pengyi Tang, Inhar Imaz, Teresa Andreu, Daniel Maspoch, Bo Yang,* **Joan Ramon Morante**,* **Jordi Arbiol*** Improvement of Carbon Dioxide Electroreduction by Crystal Surface Modification of ZIF-8. (***under review***)
2. **Ting Zhang**, Xu Han, Hong Liu, Xuan Zhang, Martí Biset-Peiró, Fei Zhang, Pengyi Tang,* Marc Heggen, Rafal E. Dunin-Borkowski, Bo Yang, Lirong Zheng,* **Joan Ramon Morante**,* **Jordi Arbiol*** Engineering FeN_4 Sites of Fe-N-C Catalyst via Bonded Oxygen for High-Efficient Electroreduction of Carbon Dioxide. (***under review***)
3. **Ting Zhang**, Xu Han, Hong Liu, Martí Biset-Peiró, Xuan Zhang, Pengyi Tang,* Bo Yang, Lirong Zheng,* **Joan Ramon Morante**, **Jordi Arbiol*** Quasi-Double-Star Nickel and Iron Active Sites for High-Efficient Carbon Dioxide Electroreduction. (***under review***)
4. Chaoqi Zhang, Ruifeng Du, Jordi Jacas Biendicho, Mingjie Yi, Ke Xiao, Dawei Yang, **Ting Zhang**, Xiang Wang, **Jordi Arbiol**, Jordi Llorca, Yingtang Zhou, **Joan Ramon Morante**, Andreu Cabot, Tubular CoFeP@CN as a Mott-Schottky Catalyst with Multiple Adsorption Sites for Robust Lithium-Sulfur Batteries, Advanced Energy Materials, 2021, DOI: 10.1002/aenm.202100432.
5. Junshan Li, Congcong Xing, Yu Zhang, **Ting Zhang**, Maria Chiara Spadaro, Qianbao Wu, Yunan Yi, Shenglan He, Jordi Llorca, **Jordi Arbiol**, Andreu Cabot, Chunhua Cui, Nickel Iron Diselenide for Highly Efficient and Selective Electrocatalytic Conversion of Methanol to Formate, **Small**, 2021, 17, 6, 2006623
6. Ahmad Ostovari Moghaddam, Evgeny Trofimov, **Ting Zhang**, **Jordi Arbiol**, Andreu Cabot, Phase Formation and Thermoelectric Properties of $Zn_{1+x}Sb$ Binary System, **Transactions of Nonferrous Metals Society of China**, 2021, 31, 753-763.
7. Mengyao Li, Yu Liu, Yu Zhang, Xu Han, **Ting Zhang**, Yong Zuo, Chenyang Xie, Ke Xiao, **Jordi Arbiol**, Jordi Llorca, Maria Ibáñez, Junfeng Liu, Andreu Cabot, Effect of the Annealing Atmosphere on Crystal Phase and Thermoelectric

Properties of Copper Sulfide, **ACS Nano**, 2021, 15, 4967-4978.

8. Junshan Li, Congcong Xing, Yu Zhang, **Ting Zhang**, Maria Chiara Spadaro, Qianbao Wu, Yunan Yi, Shenglan He, Jordi Llorca, **Jordi Arbiol**, Andreu Cabot, Chunhua Cui, Nickel Iron Diselenide for Highly Efficient and Selective Electrocatalytic Conversion of Methanol to Formate, **Small**, 2021, 17, 2006623.
9. Mauro Epifani, Saulius Kaciulis, Alessio Mezzi, **Ting Zhang**, **Jordi Arbiol**, Pietro Siciliano, Anton Landström, Isabella Concina, Abderrahim Moumen, Elisabetta Comini, Chu Xiangfeng, Rhodium as efficient additive for boosting acetone sensing by TiO2 nanocrystals. Beyond the classical view of noble metal additives, **Sensors and Actuators B: Chemical**, 2020, 319, 128338.
10. Congcong Xing, Yongpeng Liu, Yu Zhang, Xiang Wang, Pablo Guardia, Liang Yao, Xu Han, **Ting Zhang**, **Jordi Arbiol**, Lluís Soler, Yufen Chen, Kevin Sivula, Néstor Guijarro, Andreu Cabot, Jordi Llorca, A Direct Z-Scheme for the Photocatalytic Hydrogen Production from a Water Ethanol Mixture on $CoTiO_3/TiO_2$ Heterostructures, **ACS Applied Materials & Interfaces**, 2021, 13, 1, 449.
11. Yu Zhang, Yu Liu, Congcong Xing, **Ting Zhang**, Mengyao Li, Merce Pacios, Xiaoting Yu, **Jordi Arbiol**, Jordi Llorca, Doris Cadavid, Maria Ibáñez, Andreu Cabot, Tin Selenide Molecular Precursor for the Solution-Processing of Thermoelectric Materials and Devices, **ACS Applied Material & Interfaces**, 2020, 12, 24, 27104.
12. Yong Zuo, Junshan Li, Xiaoting Yu, Ruifeng Du, **Ting Zhang**, Xiang Wang, **Jordi Arbiol**, Jordi Llorca, Andreu Cabot, A SnS_2 Molecular Precursor for Conformal Nanostructured Coatings, **Chemistry of Materials**, 2020, 32, 5, 2097.
13. Xiaoting Yu, Zhishan Luo, **Ting Zhang**, Pengyi Tang, Junshan Li, Xiang Wang, Jordi Llorca, **Jordi Arbiol**, Junfeng Liu, Andreu Cabot, Stability of Pd_3Pb Nanocubes during Electrocatalytic Ethanol Oxidation, **Chemistry of Materials**, 2020, 32, 5, 2044.
14. Uriel Caudillo-Flores, Anna Kubacka, Taisiia Berestok, **Ting Zhang**, Jordi Llorca, **Jordi Arbiol**, Andreu Cabot, Marcos Fernández-García, Hydrogen

Photogeneration Using Ternary $CuGaS_2$-TiO_2-Pt Nanocomposites, **International Journal of Hydrogen Energy**, 2020, 45, 3, 1510.

15. Junshan Li, Xu Xijun, Xiaoting Yu, Xu Han, **Ting Zhang**, Yong Zuo, Chaoqi Zhang, Dawei Yang, Xiang Wang, Zhishan Luo, **Jordi Arbiol**, Jordi Llorca, Jun Liu, Andreu Cabot, Monodisperse CoSn and NiSn Nanoparticles Supported on Commercial Carbon as Anode for Lithium-and Potassium-ion Batteries, **ACS Applied Materials & Interfaces**, 2020, 12, 4, 4414.
16. Xuan Zhang, Yawei Zhang, Wei Guo, Kai Wan, **Ting Zhang**, **Jordi Arbiol**, Yong-Qing Zhao, Cai-Ling Xu, Maowen Xu, Jan Fransaer, A Yolk-Albumen-Shell Structure of Mixed Ni-Co Oxide with An Ultrathin Carbon Shell for High-Sensitivity Glucose Sensors, **Materials Advances**, 2020, 1, 908.
17. Xiaoting Yu, Chaoqi Zhang, Zhishan Luo, **Ting Zhang**, Junfeng Liu, Junshan Li, Yong Zuo, Jordi Jacas Biendicho, Jordi Llorca, **Jordi Arbiol**, **Joan Ramón Morante**, Andreu Cabot, A Low Temperature Solid State Reaction to Produce Hollow $Mn_xFe_{3-x}O_4$ Nanoparticles as Anode for Lithium-Ion Batteries, ***Nano Energy***, 2019, 66,104199.
18. Junfeng Liu, Xiaoting Yu, Ruifeng Du, Chaoqi Zhang, **Ting Zhang**, Jordi Llorca, **Jordi Arbiol**, Ying Wang, Michaela Meyns, Andreu Cabot, Chromium Phosphide CrP as Highly Active and Stable Electrocatalysts for Oxygen Electroreduction in Alkaline Media, **Applied Catalysis B: Environmental**, 2019, 256, 117846.
19. Ahmad Ostovari Moghaddam, Ali Shokuhfar, Yu Zhang, **Ting Zhang**, Doris Cadavid, **Jordi Arbiol**, Andreu Cabot, Ge-Doped ZnSb/β-Zn_4Sb_3 Nanocomposites with High Thermoelectric Performance, **Advanced Materials Interfaces**, 2019, 6, 1900467.
20. Yong Zuo, Yongpeng Liu, Junshan Li, Ruifeng Du, Xu Han, **Ting Zhang**, **Jordi Arbiol**, Nuria J. Divins, Jordi Llorca, Nestor Guijarro, Kevin Sivula, and Andreu Cabot, In Situ Electrochemical Oxidation of Cu_2S into CuO Nanowires as a Durable and Efficient Electrocatalyst for Oxygen Evolution Reaction, **Chemistry of Materials**, 2019, 331, 7732.

21. Chaoqi Zhang, Jordi Jacas Biendicho, **Ting Zhang**, Ruifeng Du, Junshan Li, Xuhui Yang, **Jordi Arbiol**, Yingtang Zhou, **Joan Ramon Morante**, Andreu Cabot, Combined High Catalytic Activity and Efficient Polar Tubular Nanostructure in Urchin-Like Metallic $NiCo_2Se_4$ for High-Performance Lithium-Sulfur Batteries, **Advanced Functional Materials**, 2019, 29, 1903842.
22. Kai Wan, Jiangshui Luo, Chen Zhou, **Ting Zhang**, **Jordi Arbiol**, Xihong Lu, Bing-Wei Mao, Xuan Zhang, Jan Fransaer, Hierarchical Porous Ni_3S_4 with Enriched High-Valence Ni Sites as a Robust Electrocatalyst for Efficient Oxygen Evolution Reaction, **Advanced Functional Materials**, 2019, 29, 1900315.
23. Junshan Li, Xijun Xu, Zhishan Luo, Chaoqi Zhang, Xiaoting Yu, Yong Zuo, **Ting Zhang**, Pengyi Tang, **Jordi Arbiol**, Jordi Llorca, Jun Liu, Andreu Cabot, Compositionally Tuned NixSn Alloys as Anode Materials for Lithium-Ion and Sodium-Ion Batteries with A High Pseudocapacitive Contribution, **Electrochimica Acta**, 2019, 304, 246.
24. Martí Biset-Peiró, Jordi Guilera, **Ting Zhang**, **Jordi Arbiol**, Teresa Andreu, On the Role of Ceria in Ni-Al_2O_3 Catalyst for CO_2 Plasma Methanation, **Applied Catalysis A: General**, 2019, 575, 223.
25. Junshan Li, Xijun Xu, Zhishan Luo, Chaoqi Zhang, Yong Zuo, **Ting Zhang**, Pengyi Tang, Maria F Infante-Carrió, **Jordi Arbiol**, Jordi Llorca, Jun Liu, Andreu Cabot, Co-Sn Nanocrystalline Solid Solutions as Anode Materials in Lithium-Ion Batteries with High Pseudocapacitive Contribution, **ChemSusChem**, 2019,12,1451.
26. Yong Zuo, Yongpeng Liu, Junshan Li, Ruifeng Du, Xiaoting Yu, Congcong Xing, **Ting Zhang**, Liang Yao, **Jordi Arbiol**, Jordi Llorca, Kevin Sivula, Néstor Guijarro, Andreu Cabot, Solution-Processed Ultrathin SnS_2-Pt Nanoplates for Photoelectrochemical Water Oxidation, **ACS Applied Materials & Interfaces**, 2019, 11, 6198.
27. Junshan Li, Yong Zuo, Junfeng Liu, Xiang Wang, Xiaoting Yu, Ruifeng Du, **Ting Zhang**, Maria F. Infante-Carrio, Pengyi Tang**, Jordi Arbiol**, Jordi Llorca, Zhishan Luo, Andreu Cabot, Superior Methanol Electrooxidation Performance of (110)-

Faceted Nickel Polyhedral Nanocrystals, **Journal of Materials Chemistry A**, 2019, 7, 22036.

28. Congcong Xing, Yongpeng Liu, Yu Zhang, Junfeng Liu, **Ting Zhang**, Pengyi Tang, **Jordi Arbiol**, Lluís Soler, Kevin Sivula, Néstor Guijarro, Xiang Wang, Junshan Li, Ruifeng Du, Yong Zuo, Andreu Cabot, Jordi Llorca*, Porous $NiTiO_3/TiO_2$ Nanostructures for Photocatatalytic Hydrogen Evolution, **Journal of Materials Chemistry A**, 2019, 7, 17053.
29. Xuan Zhang, Jiangshui Luo, Kai Wan, Dieter Plessers, Bert Sels, Jianxun Song, Liugang Chen, **Ting Zhang**, Pengyi Tang, Joan Ramon Morante, **Jordi Arbiol**, Jan Fransaer, From Rational Design of a New Bimetallic MOF Family with Tunable Linkers to OER Catalysts, **Journal of Materials Chemistry A**, 2019, 7, 1616.
30. Yu Zhang, Yu Liu, Khak Ho Lim, Congcong Xing, Mengyao Li, **Ting Zhang**, Pengyi Tang, **Jordi Arbiol**, Jordi Llorca, Ka Ming Ng, Maria Ibáñez, Pablo Guardia, Mirko Prato, Doris Cadavid, Andreu Cabot, Tin Diselenide Molecular Precursor for Solution-Processable Thermoelectric Materials, **Angewandte Chemie**, 2018,130, 17309.
31. Junshan Li, Zhishan Luo, Yong Zuo, Junfeng Liu, **Ting Zhang**, Pengyi Tang, **Jordi Arbiol**, Jordi Llorca, Andreu Cabot, NiSn Bimetallic Nanoparticles as Stable Electrocatalysts for Methanol Oxidation Reaction, **Applied Catalysis B: Environmental**, 2018, 234, 10.
32. Junfeng Liu, Michaela Meyns, **Ting Zhang**, **Jordi Arbiol**, Andreu Cabot, Alexey Shavel, Triphenyl Phosphite as the Phosphorus Source for the Scalable and Cost-Effective Production of Transition Metal Phosphides, **Chemistry of Materials**, 2018, 30, 1799.
33. Junshan Li, Zhishan Luo, Feng He, Yong Zuo, Chaoqi Zhang, Junfeng Liu, Xiaoting Yu, Ruifeng Du, **Ting Zhang**, Pengyi Tang, **Jordi Arbiol**, Jordi Llorca, Andreu Cabot, Colloidal Ni-Co-Sn Nanoparticles as Efficient Electrocatalysts for The Methanol Oxidation Reaction, **Journal of Chemistry A**, 2018, 6, 22915.